VWF binding and conformational changes under shear

Svenja Lippok

München 2014

VWF binding and conformational changes under shear

Svenja Lippok

Dissertation
durchgeführt an der Fakultät für Physik
der Ludwig–Maximilians–Universität
München

vorgelegt von
Svenja Lippok
aus Ludwigshafen

München, den 02.07.2014

Erstgutachter: Prof. Dr. Joachim Rädler
Zweitgutachter: Prof. Dr. Dieter Braun
Tag der mündlichen Prüfung: 14.08.2014

Blut ist ein ganz besondrer Saft.

Johann Wolfgang von Goethe (1808) (1)

ZUSAMMENFASSUNG

Der von Willebrand Faktor (VWF) ist ein multifunktionelles, multimeres Protein, das in der Blutgerinnung als Mechanosensor eine bedeutende Rolle spielt. Er vernetzt sich bei Verletzungen mit Thrombozyten und Kollagen, wodurch sich ein filamentöses Netzwerk ausbildet, das das verletzte Endothelgewebe bedeckt. Seit kurzem ist bekannt, dass viele Eigenschaften des VWF scherratenabhängig sind, insbesondere auch seine Spaltung durch die Metalloprotease ADAMTS13. Einzelmolekülkraftmessungen konnten zeigen, dass einige VWF Domänen Strukturen besitzen, die unter Scherspannung entfalten, wodurch neben Bindestellen auch die Spaltstelle freigelegt wird. Da zudem vermutet wird, dass die Multimergröße für die scherabhängige Funktionalität wichtig ist, ist vor allem die Spaltung des VWF maßgeblich für das Verständnis seiner mechanosensitiven Wirkung. Bislang gab es aber weder eine quantitative Beschreibung der Größenverteilung noch einen direkten Nachweis der Kraftabhängigkeit der ADAMTS13 Aktivität in Scherfluss. Um diese Lücke zu schließen, verwendeten wir in dieser Arbeit Fluoreszenzkorrelationsspektroskopie (FCS), wobei die Messungen der einzelnen Projekte durch weitere Techniken und Simulationen komplementiert wurden.

Im ersten Projekt gelang es uns die VWF Größenverteilung zu quantifizieren. In Zusammenarbeit mit der Gruppe von Prof. Schneppenheim, die uns rekombinante VWF-eGFP Konstrukte zur Verfügung stellte, konnten wir mit Hilfe von FCS nachweisen, dass die Größen des plasmatischen VWF exponentiell verteilt sind. Diese exponentielle Verteilung wurde mittels quantitativer Gelanalysen (Prof. Budde) und Interner Totalreflexionsfluoreszenzmikroskopie (Dr. Benoit) bestätigt. Sie ist in guter Übereinstimmung mit dem Polymerisierungsmodell eines schrittweisen Wachstums nach Flory, weshalb wir die Größenverteilung explizit anhand eines einzigen Parameters, dem Polymerisierungsgrad, beschreiben konnten. Tatsächlich ergab die Untersuchung einer VWF Mutante, dass der Polymerisierungsgrad ein Indikator für krankhafte Veränderungen der Größenverteilung ist, wodurch er als solcher klinische Anwendung finden könnte.

Mit Hilfe der nun bekannten Größenverteilung konnte daraufhin die Spaltung des VWF durch

ADAMTS13 quantifiziert werden. Die Kombination von FCS mit einer eigens entwickelten Scherzelle erlaubte es erstmals die Kinetik der VWF Spaltung als Funktion der Scherrate zu bestimmen, was ein spannendes Beispiel für eine mechanosensitive, biochemische Reaktion darstellt. Dabei entdeckten wir einen schaltähnlichen, sigmoidalen Anstieg der Enzymaktivität bei hohen Scherraten. In Zusammenarbeit mit der Gruppe von Prof. Netz konnten wir dieses Verhalten durch Brownsche Hydrodynamiksimulationen konsistent als scherratenabhängige Polymerentfaltung erklären, die auf einer kritischen Kraft für das Entfalten der Spaltdomäne als einzige Annahme aufbaute. Damit ergibt sich nun erstmals ein konsistentes Bild für das Zusammenspiel von Scherfluss, Entfaltung der VWF Multimere, Öffnung der Spaltdomänen und ADAMTS13 Aktivität, das notwendig ist um Vorhersagen über den Effekt von VWF Mutationen auf Gerinnungsstörungen treffen zu können.

Als Teil der Studie zur scherinduzierten ADAMTS13 Aktivität wurde eine VWF Mutante (G1629E) vermessen, die eine stark erhöhte Sensitivität für den ADAMTS13 Verdau aufwies. Dies weckte unsere Aufmerksamkeit, da die gängigen ADAMTS13-Aktivitätstests eine mangelnde Genauigkeit und Reproduzierbarkeit bei der Diagnose lebensbedrohlicher thrombotischer Erkrankungen aufweisen. Wir entwickelten einen Diagnosetest, der ein rekombinantes Fusionsprotein der hochsensitiven Mutante als Enzymsubstrat einsetzt. Mit dem Konstrukt rVWF-G1629E-eGFP und unter Verwendung von FCS konnten wir die Sensitivität gegenüber der bisher eingesetzten Tests um einen Faktor fünf erhöhen, was eine erhebliche Verbesserung zur Entwicklung adequater Therapien bedeutet. In Zusammenarbeit mit der Gruppe von Prof. Gräter, konnte die erhöhte Sensitivität der Mutante im Rahmen von Molekulardynamiksimulationen mit einer destablisierten Spaltdomäne begründet werden.

FCS wurde weiterhin genutzt um molekulare Wechselwirkungen des VWF zu untersuchen. So betrachteten wir neben der Multimerisierung auch die VWF Dimerisierung, die durch die Bildung von Disulfidbrücken im Endoplasmatischen Retikulum (ER) stattfindet. Mittels FCS und Thermophorese (MST) konnten wir zeigen, dass die Protein Disulfid Isomerase (PDI) spezifisch an die für die Dimerisierung verantwortliche VWF-CK Domäne bindet (K_D = 258 ± 104 nM). Ergänzend zu unseren Bindungsmessungen konnten Kolokalisierungsstudien ausgewählter VWF Mutanten (Dr. Brehm) die Rolle von PDI zusätzlich auf die VWF Dimerisierung einschränken und zeigen, dass PDI lediglich eine Nebenrolle bei der Korrektur fehlgefalteter Mutanten im ER spielt.

Zusätzlich betrachteten wir die Bindung des Gerinnungsfaktors VIII (FVIII) an Phosphatidylserin (PS)-haltige Thrombozyten, die zu einem späteren Zeitpunkt der Gerinnungskaskade auftritt. Mit Hilfe von FCS und MST konnten wir die Bindung von FVIII an PS-haltige Modellmembranen quantitativ beschreiben. Während für nicht-aktivierten FVIII das erwartete Bindungsverhalten zu sehen war, zeigte aktivierter FVIII (FVIIIa) eine starke Bindungsanomalie mit deutlichem Affinitätsmaximum bei dem physiologischem PS-Gehalt von Thrombozyten. Zudem wurde die FVIIIa Bindung durch Annexin A5 beeinflusst, welches den scheinbaren PS-Gehalt durch kompetetives Binden einstellt. Diese Studie demonstriert die regulatorische Funktion des PS-Gehalts in der Blutgerinnung.

Summary

The multimeric von Willebrand Factor (VWF) plays a pivotal role as a mechanosensitive protein in hemostasis. In succession of injury, VWF promotes adhesion of platelets to collagen as well as platelet aggregation, thereby forming a filamentous network, which covers the damaged epithelial tissue. Recently, it was discovered that most of VWF's functions are shear-dependent, in particular its cleavage by the protease ADAMTS13. Single-molecule force experiments revealed that the multimer possesses structural elements that unfold under flow-induced tension, exposing several binding and the cleavage site. Because the multimer size seems to be an important parameter for VWF's shear-dependent functionality, cleavage of VWF is a significant factor in hemostasis. However, there was hitherto neither a quantitative description of the size distribution of VWF nor a fundamental understanding of the effect of shear on ADAMTS13's activity. To close this gap, Fluorescence Correlation Spectroscopy (FCS) was used in this work, complemented with alternative experimental approaches or simulations, depending on the specific research question.

In a first study, we initially quantified the VWF size distribution. In cooperation with the group of Prof. Schneppenheim, who provided recombinant VWF-eGFP constructs, we found plasmatic VWF to exhibit an exponential size distribution using FCS. This finding was corroborated by quantitative gel analysis (Prof. Budde) and by single-molecule photo bleaching experiments using total internal reflection fluorescence microscopy (Dr. Benoit). We attributed the exponentially distributed sizes to a step-growth polymerization process during biosynthesis according to Flory. This biophysical characterization allows for an explicit description of the size distribution with a single parameter, namely the extent of polymerization, which might be used as disease marker for clinical applications.

With the identified size distribution it was then possible to quantify ADAMTS13-mediated cleavage of VWF in blood plasma. Combining the FCS setup with a custom-built shear cell, we measured the effect of shear flow on VWF cleavage kinetics for the first time, which provides a fascinating example for a mechanosensitive biochemical reaction. We found a

Hill-type behavior with a sigmoidal increase in activity with increasing shear. In cooperation with the group of Prof. Netz, brownian hydrodynamics simulations of polymers in shear flow were performed, which revealed that this behavior results from shear-dependent polymer unfolding. These results enable to draw a consistent picture of the interrelation of shear-flow, VWF unfolding, opening of the mechanosensitive cleavage domain, and ADAMTS13 activity, which is essential to enable predictions of hemostatic dysfunction of mutant VWF.

During these studies on shear-induced ADAMTS13 activity, we found that one VWF mutant (G1629E) is extremely susceptible to proteolysis. This attracted our interest, because reliable quantification of ADAMTS13 activity levels is important in clinical diagnostics but remains challenging with commonly used assays. Using a recombinant fusion construct of VWF-G1629E as enzyme substrate, we developed a highly sensitive ADAMTS13 activity assay. We found a five-fold increased sensitivity compared to commonly used assays, which implies a significant improvement for adequate therapies. Molecular dynamics simulations (Prof. Gräter) rationalized the increased sensitivity as a local structural destabilization due to the mutation G1629E that results in an increased accessibility of the A2 cleavage domain.

We also used FCS to quantitatively characterize molecular interactions of VWF. In the context of the multimerization study, we focused on VWF dimerization, which occurs in the endoplasmatic reticulum (ER) by formation of disulfide bonds. Using FCS and Microscale Thermophoresis (MST), we showed that protein disulfide isomerase (PDI) binds VWF exclusively within the VWF CK-domain, which is responsible for dimerization ($K_D = 258 \pm 104\ nM$). In addition to our binding studies, co-localization experiments of specific VWF-CK domain mutants were performed (Dr. Brehm), which elucidated the role of PDI in the initial VWF dimerization rather than in the repair of misfolded VWF in the ER.

Aside from studies involving VWF, we investigated the binding of the coagulation factor VIII (FVIII) to phosphatidylserine (PS)-expressing platelets, which is another important step in the coagulation cascade. Using FCS and MST, we established a quantitative description of FVIII binding to PS-containing vesicles. While non-activated FVIII showed the expected binding behavior, we found a pronounced binding anomaly for activated FVIII (FVIIIa) that is manifested in a sharp peak in binding affinity around the natural PS content of platelets. Moreover, annexin A5 effectively influenced FVIIIa binding, triggering the apparent PS content by shielding PS lipids via competitive binding. This study demonstrates the regulatory function of the PS content in blood coagulation.

Contents

1 Introduction

Blood coagulation has evolved as the body's own defense mechanism against bleeding. Under physiological conditions, the coagulation system is balanced in favor of anticoagulation, but is immediately activated in the event of vascular injury. Its exact regulation is of fundamental importance as a malfunction of the system either leads to dangerous blood loss or causes thrombotic disorders, which may result in stroke and heart attack. To avoid both severe pathological states, blood clotting has to be strictly prevented in uninjured blood vessels but has to work extremely precise and rapid, when a vessel ruptures.

Thereby, the initiation of coagulation is particularly difficult, as will be explained in the following, because shear flow increases dramatically at sites of injury. Local shear rates at vessel walls in the human microvasculature have been determined to be of the order of 100 to 8.000 1/s (2; 3). At vessel injuries, vasoconstriction[1], or stenotic compartments[2], the reduction of the vessel lumen can rise the shear rates to excessive levels above 50.000 1/s (4). At such high shear rates, wounds need to be plugged. However, high shear flow is naturally accompanied by an increase of lift forces. Thus, binding is usually hindered under shear. Therefore, well-functioning blood clotting needs a specialized mechanism to enable the required shear-induced absorption of clotting factors to the ruptured vessel wall.

Nature meets this challenge with a polymer called von Willebrand Factor (VWF) that exhibits an increased adhesion potential with increasing hydrodynamic shear stress (5). It initiates coagulation mediating the binding of platelets to the ruptured vessel wall (see Figure 1.1). More specifically, VWF is present in an inactivated state under physiological flow conditions. When shear flow increases, it becomes activated via a shear-induced globular-stretch transition, thereby exposing numerous formerly shielded tensile binding sites. In addition to the unfolding of the polymer chain, single force-sensing VWF domains open upon a certain shear force. The characteristic shear rate that is needed to induce VWF's conformational change exhibits a very sensitive size dependence, as smaller multimers are more resistant to shear forces

[1] contraction of the muscular wall of the vessels to reduce the amount of blood loss

[2] abnormal narrowed parts of the vessel

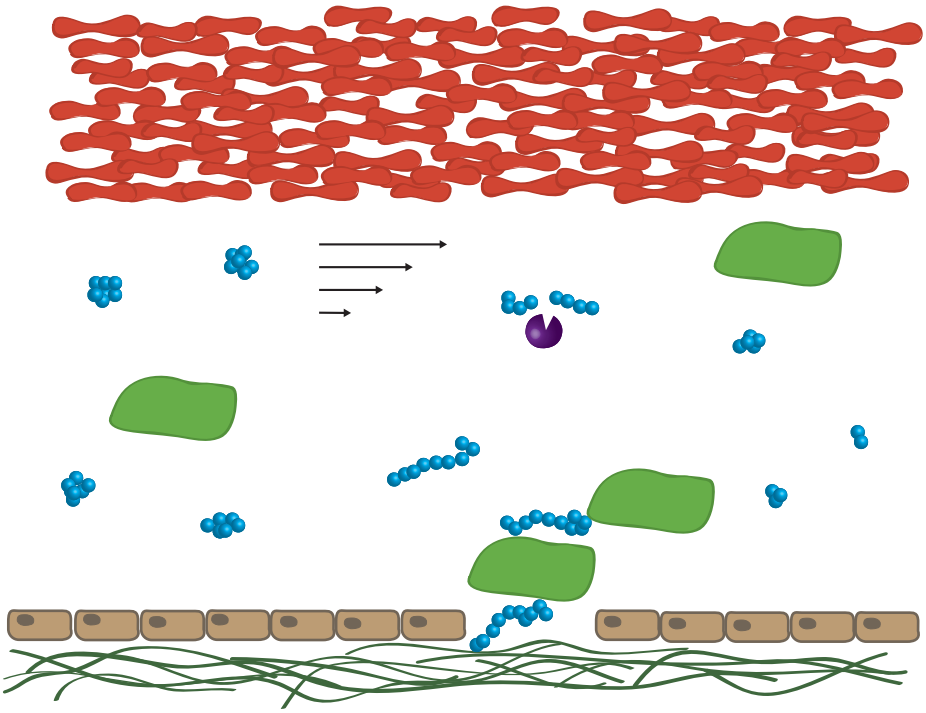

Figure 1.1: VWF in blood coagulation. Activated by shear flow, VWF (blue) binds to collagen (dark green) and platelets (green) via binding sites in its A1 and A3 domains, which initiates coagulation. Unfolded VWF can be cleaved in the A2 domain by the protease ADAMTS13 (purple).

than larger ones. This leads to a highly specialized regulatory potential of VWF function, because different sizes of VWF are present in the plasma, and the appearing size distribution can be permanently adjusted in the circulation by the enzyme ADAMTS13 (a disintegrin and metalloproteinase with a thrombospondin type 1 motif, member 13) (6). ADAMTS13 was shown to be the specific VWF cleaving protease in 2001 (8; 9; 10). By cleaving VWF multimers at a specific cleavage site in the A2 domain, it regulates the VWF size distribution and hence the binding capacity of VWF in the human vasculature. This A2 cleavage domain is mechanosensitive and opens under high shear forces (11). Thus, the size regulation depends on the shear rates in the vessel. This results in a feedback loop, which is adapted precisely to the requirements of coagulation and prevents both clotting and bleeding (see Figure 1.2): High shear rates increase the cleavage activity resulting in small VWF multimers. Small multimers cannot be stretched anymore, which downregulates cleavage.

Thus, VWF's cleavage as well as binding sites are activated by shear flow. Under shear, initially the VWF A1 domain opens, which possesses a binding site to platelets and collagen. Over time additionally the VWF A2 domain for cleavage by ADAMTS13 is activated (11; 12). Therefore, the initiation of clot formation (via VWF platelet interaction) is preferred over VWF inactivation (via cleavage by ADAMTS13) facilitating controlled coagulation under high shear flow conditions. In conclusion, VWF shows the counterintuitive behavior of shear-induced enhanced adhesion rates due to its multimeric and mechanosensitive structure and can be well controlled by its environment via its distributed sizes.

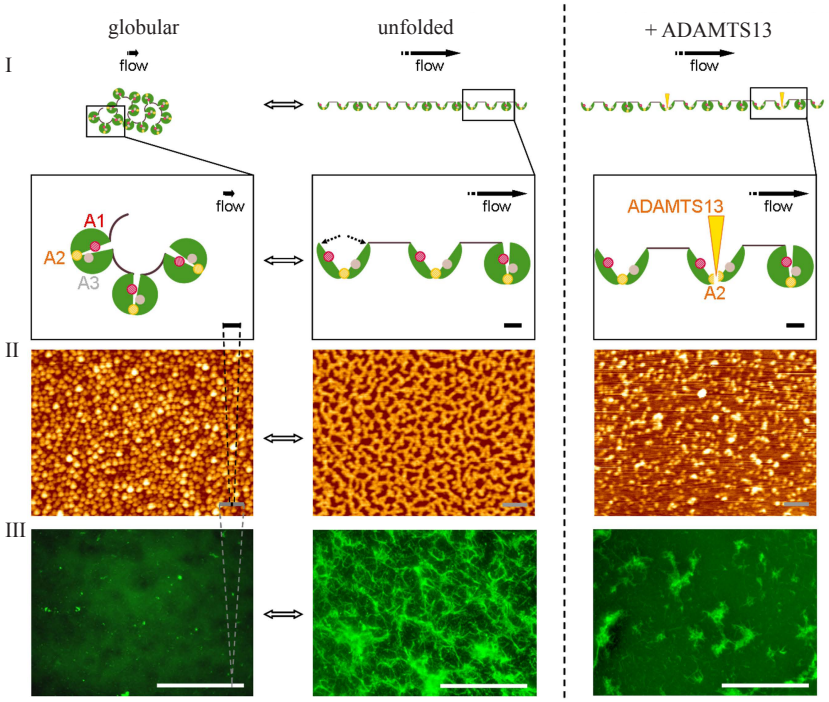

Figure 1.2: Shear flow and proteolytic cleavage maintain VWF activity balanced. (I) Under low shear conditions, inactivated VWF exists in a globular shape in the circulation (left). The A domains A1 (red) and A2 (yellow) are shielded. Shear flow unfolds long VWF multimers and the A domains become exposed (middle). Opening of the mechanosensitive A2 domain exposes a cleavage site for ADAMTS13. In the presence of ADAMTS13, unfolded VWF is degraded at the A2 domain (right). Scale bars correspond to 10 *nm*. **(II)** Height-coded atomic force microscopic images of VWF transition. Monomers appear as yellow dots covering the surface (left). Under shear flow, VWF monomers/dimers polymerize to a structured two-dimensional network (middle). In the presence of ADAMTS13, this network is efficiently degraded (right). Scale bars correspond to 100 *nm*. **(III)** Immunofluorescence images of VWF stained in green in the globular (left) and in the unfolded state (middle), in the absence or presence (right) of ADAMTS13. Scale bars correspond to 100 μm (reprinted with permission from (7)).

Discovery

The first hint towards the existence of VWF came from the discovery of bleeding patients who lacked it (13; 14). Erik Adolf von Willebrand, a Finnish internal specialist, studied several members of a family from Föglö, an island in the Åhland Archipelago in the Gulf of Bothnia (Figure 1.3) (15). He found a so far unknown form of bleeding disorder that showed an increased bleeding tendency but, in contrary to hemophilia[3], additionally an increased bleeding time[4]. Another significant difference to hemophilia was that the symptoms were mostly found in females. Von Willebrand called this serious bleeding tendency *pseudo-hemophilia* because he was not able to determine if it was caused by a defect in platelets, blood plasma, or the vasculature. In 1933, von Willebrand discovered further details of the disease, i.a. a re-

[3] clotting factor FVIII deficiency
[4] medical test to assess how long a person bleeds after causing a standardized cut in its forearm

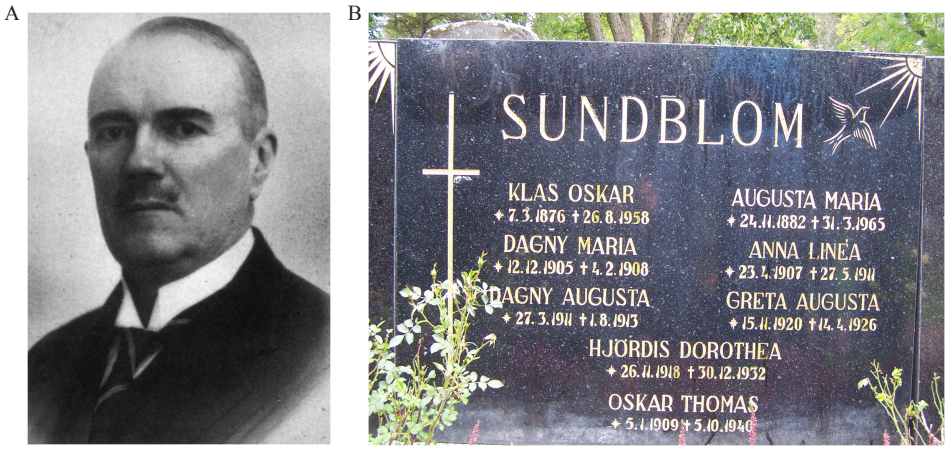

Figure 1.3: Discovery of von Willebrand disease. **A** Erik von Willebrand, a Finnish internal specialist, described the von Willebrand disease for the first time (adapted from (17)). **B** Von Willebrand studied the clinical picture of family Sundblom. Four girls of the family died from bleeding before the age of six (with courtesy of Reinhard Schneppenheim).

duced agglutination tendency of the thrombocytes, in cooperation with the German physician Rudolf Jürgens. From thereon, it was called *von-Willebrand-Jürgens syndrom* (16). Today, the international denotation "von Willebrand disease" (VWD) is used.

In the 1950s, an association between increased bleeding times and decreased levels of FVIII was found in patients with VWD and a *bleeding time-correcting plasma factor* was defined (18; 19; 20). In 1971, the factor was purified for the first time and called *FVIII-related antigen* (21). When it was shown that it is the product of a different gene on a different chromosome than FVIII, it was finally renamed in "von Willebrand Factor". The complete sequence of VWF was reported by several groups in 1985 (22).

VWF research

The last decades have seen considerable progress in understanding VWF assembly, the structural requirements for its function, and the molecular basis of VWD. However, the dependency of VWF's functionality on shear stress remained unexplored for a long time. Because the investigation of the effect of shear is crucial when examining our circulatory system, shear flow regulation of hemostasis recently came to the fore of research with the ultimate goal to bridge the gap between nanomechanics and clinical presentation. Focusing on the force sensing ability of VWF finally shifted VWF research to the field of biophysics. Using a rotating disk system combined with Atomic Force Microscopy (AFM), Siedlecki et al. observed in 1996 for the first time that VWF undergoes a shear-induced conformational transition from a globular to a stretched state (23). In 2007, Schneider et al. directly visualized this conformational change using fluorescently labeled VWF molecules, which were sheared by a SAW (surface acoustic waves)-driven flow chip (5). Moreover, they identified the shear-induced increase in binding affinity of VWF to collagen coated channels, unraveling this effective self-regulating repair mechanism of our body for the first time. In a recent work of Zhang et al., force was ap-

plied directly to single A2 cleavage domains using optical tweezers. This enabled to measure both the A2 domain opening force and the dependence of the catalytic rate on ADAMTS13 concentration (24).

These studies clearly elucidated the importance of conformational changes for the function of VWF. However, the exact dependence of VWF functionality on shear is still poorly understood. Yet, it is of eminent interest for the wider field of force sensing mechanisms in biology, since mechanosensitive polymers under flow conditions are hitherto rarely explored. Simultaneous measurements of hydrodynamic flow-induced unfolding at the single molecule level and the concomitant alteration of VWF's functionality, such as binding or enzymatic activity, remain difficult to access and have not been studied quantitatively. Above all, there is a need to perform measurements under blood plasma conditions, since VWF may easily alter its properties in an artificial environment. Nevertheless, most studies of VWF so far have been performed in buffer.

Technical challenges

The experimental realization of such studies, however, is challenging due to VWF's extremely heterogeneous size distribution, which includes orders of magnitudes in multimer size, and, moreover, due to its dependency on shear flow. As the latter results in both unfolding of the multimer and opening of single force-sensing domains, VWF research has to focus both on the multimer and on the domain level.

Studies under blood plasma conditions exclude the usage of a wide range of experimental techniques. Several techniques based on fluorescence microscopy can be used, though. Amongst others, Total Internal Reflection Fluorescence Microscopy (TIRFM), Laser Scanning Microscopy (LSM), Fluorescence Correlation Spectroscopy (FCS), Microscale Thermophoresis (MST), Förster resonance energy transfer (FRET), and Fluorescence Recovery After Photobleaching (FRAP) work well in bulk media (25; 26; 27; 28; 29; 30).

The need to study the dynamics of multimeric VWF on a molecular level, limits the number of potential approaches for VWF research considerably. In order to induce conformational changes, force has to be applied on the multimer. On the one hand, this can be done by directly using optical and magnetic tweezers, or AFM (31; 32; 33). On the other hand, shear flow can be applied. Although the former approaches are very well suited to study intramolecular forces and molecular stability, as well as conformational architecture and organization, the so applied forces are homogenous along the polymer chain and constant during application. However, simulations of VWF unfolding under shear flow reveal that the intramolecular forces in VWF are inhomogeneous and fluctuating (34; 35). Thus, it is expected that in VWF multimers under shear flow more and less susceptible intramolecular regions may exist, which in addition show a size dependent probability to appear. This cannot be imitated using techniques that apply forces directly. Therefore, shear flow is needed for studies of VWF in its natural environment.

There are several fluorescent techniques working well under flow conditions, e.g. FRET (36),

FCS (37), and MST (38). Accordingly, all these techniques come into consideration for VWF studies in a physiological environment. As FRET depends on very specific labeling, the analysis is limited to well defined two-component interactions or intramolecular studies. Experiments with the whole range of VWF sizes would highly increase the intricacy of a corresponding study. In particular, the observation of collective phenomena seems nearly impossible. However, MST averages over all molecules in the sample and is well suited for ensemble measurements. Thus, it can be used for all studies that are independent of VWF size. MST cannot resolve the single multimers within the solution, though.

Fluorescence Correlation Spectroscopy (FCS) allows for an accurate determination of macromolecular dynamics (39; 40; 41; 42; 43; 44). In particular, the diffusion coefficient, structural relaxation and interactions between different species can be measured (45). Moreover, since the required sample size is very small, FCS studies can easily be combined with microfluidic devices (37; 46). Because FCS is based on confocal microscopy and uses concentrations in the nanomolar regime, it achieves few molecule resolution, which allows for the distinction between molecules with different brightnesses and sizes. Therefore, it is suitable to study size dependent-functions using the full-length VWF distribution. Moreover, it is sensitive for VWF fragments consisting of single domains only. Thus, we chose FCS as the best suited technique for the VWF research questions addressed in this work. For some projects, complementary techniques were applied to strengthen the results obtained with FCS.

This work

The work presented in this thesis is motivated by the idea to quantitative measure VWF under blood plasma conditions and shear flow. It involves four VWF-related projects, namely VWF size distribution analysis (chapter 4), shear-induced VWF cleavage (chapter 5), an ADAMTS13 activity assay (chapter 6), and the interaction of Protein Disulfide Isomerase (PDI) with VWF (chapter 7). The first project provides a characterization of plasmatic full-length VWF samples. This paved the way for quantitative studies under shear with the full-length multimer. For experiments under shear flow, a microfluidic shear cell was built that was used in the second project to relate cleavage rates to VWF's shear dependent conformation. Based on this study, we developed a diagnostic approach to determine ADAMTS13 levels in patient's plasma in the third project. Finally, binding studies were performed, which elucidated the role of Protein Disulfide Isomerase (PDI) on VWF dimerization. We introduced both MST and FCS to this study and adapted the multicomponent FCS data analysis to quantify full-length VWF binding studies. Furthermore, a project focusing on a later step in the coagulation cascade is presented that investigates the mechanism of FVIII binding to platelets (chapter 8).

In summery, we introduced FCS as a promising method for VWF research and proved it to be well suited for investigations of VWF under shear and blood plasma conditions. We showed that it can be used as diagnostic approach for both quantitative defects in the VWF size distribution and ADAMTS13 deficiencies. Above all, we obtained a more precise picture of VWF as a force-sensing polymer by quantifying, for the first time, the shear-induced ADAMTS13 activity, which we explained consistently with the biophysical theory of polymer unfolding.

2 Experimental Methods

Fluorescence Correlation Spectroscopy (FCS) allows for accurate determination of molecular dynamics in bulk fluids and under flow conditions. It this work, FCS was employed for quantitative studies of VWF and its function in its natural environment, i.e. in blood plasma and under shear flow. In the first part of this chapter, the basic principles of FCS (2.1.1), its expansion to heterogeneous multimer samples (2.1.2), and the used instrumentation (2.1.3) are discussed in detail. For the size distribution analysis presented in chapter 4, quantitative gel analysis and Total Internal Reflection Fluorescence Microscopy (TIRFM) were used in addition to FCS. These techniques are briefly introduced in section 2.2 and 2.3. For studies of VWF under shear flow, a specialized setup was established, which had to generate constant shear flow in small sample volumes and to be combinable with the FCS setup. The properties of the built shear cell are discussed in section 2.4. As a complementary technique to FCS, Microscale Thermophoresis (MST) was used in chapters 7 and 8 for biomolecular interaction studies. In the last section of this chapter 2.5, the theory of MST and its experimental realization are described.

2.1 Fluorescence Correlation Spectroscopy (FCS)

2.1.1 Principle

FCS is an experimental technique with single-molecule sensitivity, which detects the dynamics of fluorescent molecules in solution (39; 40; 41). In particular, diffusion coefficients, structural relaxation and interactions between different species can be measured. FCS follows the intensity time trace I(t) of fluorescent molecules in a detection volume and gains information from temporal intensity fluctuations. The fluctuations result from changes in the particle number and/or alterations of the particle brightness (Figure 2.1 A,B), caused by their motion such as diffusion, rotation, and active transport, by enzymatic activity, and/or by photophysical

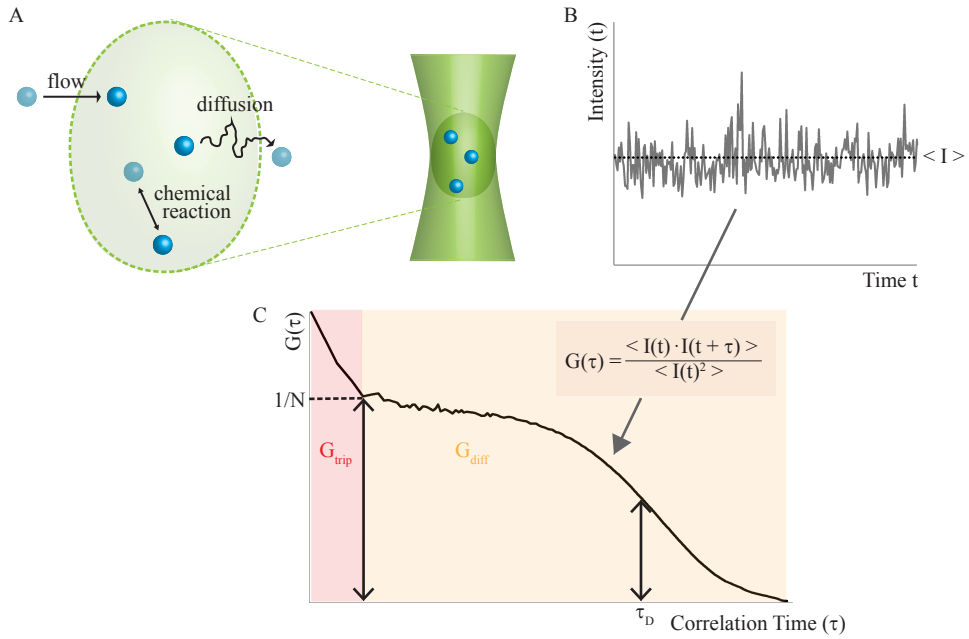

Figure 2.1: Conceptual basics of FCS. A A confocal microscope detects changes in fluorescence due to transport of fluorescent molecules into the confocal volume by flow, diffusion, or transitions of the molecules to different fluorescent states. **B** The resulting fluctuations in the fluorescence intensity I(t) are autocorrelated using G(τ). **C** The autocorrelation curve contains information about photophysical effects such as triplet kinetics, diffusion properties, and the number of fluorescent molecules in the detection volume.

or photochemical reactions, each of them appearing at a characteristic timescale (45).

The autocorrelation curve G(τ), derived from the intensity fluctuations, is used to extract these characteristics from the measurement signal. In particular, G(τ) is a measure of the self-similarity of the signal after a lag time τ. It represents the conditional probability to find a molecule in the confocal volume at a later time τ, given it was there at a time t (47). The normalized autocorrelation function is defined as:

$$G(\tau) = \frac{\langle I(t) \cdot I(t+\tau) \rangle}{\langle I(t)^2 \rangle} \tag{2.1}$$

where $\langle\rangle$ denotes the time average. For the systems studied in this thesis, photophysical effects due to triplet kinetics as well as diffusion dynamics of the fluorescent particles contribute to the autocorrelation function:

$$G(\tau) = 1 + G_{trip} \cdot G_{diff} \tag{2.2}$$

The first term, G_{trip}, considers the relatively high probability of fluorophores to enter a triplet state at the excitation intensities typically used for FCS. The resulting temporary dark states appear in the autocorrelation curve as an additional slope at timescales that are significantly

shorter than diffusion (Figure 2.1 C). This slope is described by an exponential decay (48):

$$G_{trip}(\tau) = \left(1 + \frac{f_{trip}}{1 - f_{trip}}\right) e^{-\frac{\tau}{\tau_{trip}}} \tag{2.3}$$

with fraction of molecules in the triplet state f_{trip} and triplet decay time τ_{trip}. Although triplet kinetics had to be included into the fitting routine, G_{trip} was not the subject of the studies presented here but rather used to obtain reliable results for G_{diff}.

G_{diff} accounts for the dynamics of the fluorescent particles diffusing through the detection volume and can be fitted by diffusion models to obtain parameters such as the diffusion constant or the particle concentration. For free diffusion of molecules in a three-dimensional Gaussian probe volume with radial dimension ω_r and axial dimension ω_z, G_{diff} is given by:

$$G_{diff}(\tau) = \frac{1}{N} \cdot \frac{1}{1 + \frac{\tau}{\tau_D}} \cdot \frac{1}{\sqrt{1 + \frac{\tau}{S^2 \cdot \tau_D}}} \tag{2.4}$$

where N denotes the average number of particles in the focus volume and the diffusion time τ_D the time, at which the autocorrelation function has decayed to one-half of its value. The structure parameter S is a measure for the ratio between the focus radii in axial and radial dimension, ω_z and ω_r, and depends on the optical properties of the setup and the sample solution: $S = \omega_z/\omega_r$. It is calibrated with a well-known fluorescent molecule before every experiment and kept fixed for data analysis. This leaves two fitting parameters describing the fluorescent sample: τ_D and N. The latter is used to determine the concentration of fluorescent particles c:

$$c = \frac{N}{V_{cf} \cdot N_A} \tag{2.5}$$

with Avogadro constant N_A and confocal detection volume V_{cf}, which amounts typically to about 0.2 fl. The diffusion time τ_D characterizes the average time that the molecules need to cross the focal width and allows for the determination of the diffusion coefficient D:

$$D = \frac{\omega_r^2}{4 \cdot \tau_d} \tag{2.6}$$

As τ_D depends on the size of the detection volume, the diffusion coefficient D is better suited to describe the characteristic diffusion properties of a molecule in a given solvent. D is a measure for the mobility of a particle and depends on its size, the viscosity of the fluid η, and the temperature T. For a perfectly spherical particle, the hydrodynamic radius r_{hyd} can be deduced from the Stokes-Einstein relation as follows:

$$D = \frac{k_B T}{6\pi\eta r_{hyd}} \tag{2.7}$$

with Boltzmann constant k_B. For a particle with cylindrical shape, D is given by:

$$D = A \cdot \frac{k_B T}{3\pi\eta L} \tag{2.8}$$

with cylinder length L, cylinder diameter d, and correction factor A:

$$A = ln(L/d) + 0.312 + 0.565/(L/d) - 0.1/(L/d)^2 \tag{2.9}$$

2.1.2 MULTICOMPONENT ANALYSIS

For measurements of an n-component mixture of non-interacting fluorescent particles, the overall autocorrelation function is a weighted sum of the autocorrelation functions $G_i(\tau/\tau_i)$ of all components (49):

$$G(\tau) = \frac{\sum_{i=1}^{n} q_i^2 N_i G_i(\tau/\tau_{Di})}{\left(\sum_{i=1}^{n} q_i N_i\right)^2} \tag{2.10}$$

where q_i denotes the brightness, N_i the number, and τ_{Di} the diffusion time of molecules of species i. For the heterogeneous VWF sample, multicomponent analysis was used. The adaption of equation 2.10 to the individual projects is described in the following.

SIZE DISTRIBUTION

In this thesis, a novel size distribution analysis approach, based on equation 2.10, was introduced to determine the size distribution of VWF multimer samples (see chapter 4). VWF multimers are organized as long linear chains consisting of a certain number of dimers i, which serve as the building block of the multimer. For known brightnesses q_i and diffusion times τ_{Di}, the size distribution N_i can be fitted with equation 2.10. In this work, a VWF-eGFP fusion construct was used, where each monomer is labeled with one eGFP molecule at the dimerization site of the multimer. Therefore, the brightness q_i scales with the number of dimers i. Quenching might occur for dimers with respect to monomers due to the binding site of eGFP. However, it is not expected for multimers among each other because there is no label at the multimerization site. As the brightness was counted dimer-wise, quenching was neglected for VWF and $q_i = i$ was used for analysis.

There exist several models for the diffusion times τ_{Di} of polymers consisting of i subunits. The simplest one is the Rouse model (50), which describes the conformational dynamics of an ideal chain consisting of i beads connected by harmonic springs. This model neglects excluded volume interactions between the beads, and each bead is subjected to a random thermal force as well as a drag force. This results in a diffusion coefficient $D_i = D/i$ and diffusion times $\tau_{Di,Rouse} = \tau_D \cdot i$. Zimm extended this model by the inclusion of hydrodynamic interactions

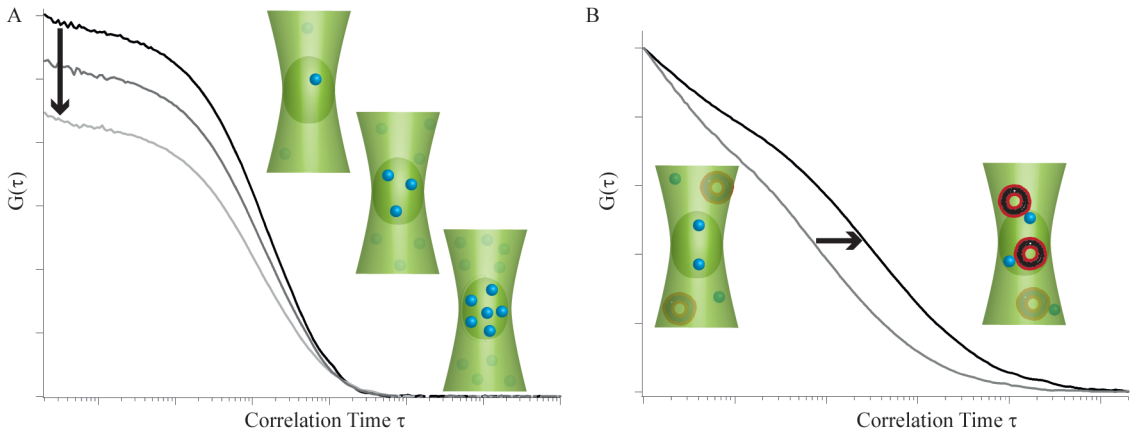

Figure 2.2: Illustration of the effect of cleavage and binding on G(τ). A Increasing concentration of fluorescent particles leads to lower amplitudes of the autocorrelation curve G(0). This effect is used to detect VWF cleavage. **B** Binding shifts the autocorrelation curves towards longer diffusion times due to increasing effective particle sizes.

among the beads due to forces that are caused by the motion of the solution itself (51). The Zimm model predicts a diffusion coefficient $D_i = D/\sqrt{i}$ and a diffusion time $\tau_{Di,Zimm} = \tau_D \cdot \sqrt{i}$. The diffusion time of a stiff cylinder lies in between these two models as shown in equation 2.8. As there is little known about the persistence length of the VWF polymer and its exact shape in the used buffer containing 1.5 *M* urea, we used the simple Rouse model, which worked sufficiently well for fitting.

Cleavage

The amplitude of the autocorrelation curve $G(0)$ is a measure for the particle concentration (Figure 2.2 A). For the concentration detection of a system with multiple species, the amplitude of the autocorrelation function is given by:

$$G(0) = \frac{\sum_{i=1}^{n} q_i^2 N_i}{(\sum_{i=1}^{n} q_i N_i)} \tag{2.11}$$

with number N_i and brightness q_i of molecules of species i. For species with varying brightnesses q_i, weighting with the brightness results in a systematic underestimation of the number of molecules in the detection volume. This underestimation can be analytically derived using equation 2.11. Thus, knowing both the size distribution and the brightness of the different species, allows to obtain quantitative results. In chapter 5, the equation was adapted to quantify the cleavage of VWF multimers. This was possible because recombinant VWF-eGFP molecules were used, where each monomer was labeled with one eGFP molecule. Thus, cleavage resulted in an increase in fluorescent molecules. For the VWF size distribution $N(i) = (p-1)p^{i-1}$ with $p = 0.64$ (see chapter 4), the underestimation due to distinct bright-

nesses of the molecules was calculated to:

$$\frac{G(0)}{G(0) - G(0)_{FCS}} = 40.4\% \tag{2.12}$$

We showed that the data correction $C = C_{FCS} \cdot 1.4$ is valid also for the cleaved sample within the used measurement times (for details see supplement B).

BINDING

With multicomponent analysis, also binding events can be analyzed assuming a two component mixture of free and bound fluorescent receptor molecules. Due to the increase in apparent size, binding to another molecule shifts the autocorrelation curves towards longer diffusion times (see Figure 2.2 B). If binding does not alter the brightness of the receptor molecule, i.e. $q_{bound} = q_{free}$, equation 2.10 can be simplified to:

$$G(\tau) = \frac{1}{N}\left[(1 - f) \cdot G(\tau/\tau_{free}) + f \cdot G(\tau/\tau_{bound})\right] \tag{2.13}$$

with the fraction of bound receptor molecules f and the total number of receptor molecules N. This form of the autocorrelation function allows for the analysis and discrimination of differences in the diffusion characteristics and can be applied to quantitatively determine the binding of small fluorescent particles to particles of larger sizes. For data analysis, the autocorrelation functions of both components, $G(\tau/\tau_{free})$ and $G(\tau/\tau_{bound})$, are determined separately and kept as fixed parameters. This proceeding reduces artifacts, leaving the number of particles and the fractions of bound and unbound particles as the only free fit parameters.

Measurements of binding to a multimer containing several binding sites poses the challenge that the brightness of the multimer depends on the number of bound fluorescent receptor molecules f_i. Furthermore, if the multimers are present in different sizes, as it is the case for the VWF multimers used in this work, the number of binding sites scales with the size of the multimer N_i. Thus, the brightness changes due to binding according to $q_i = f_i N_i$. For this scenario, we developed the following fitting formula, which is used in chapter 7:

$$G(\tau) = \frac{1}{N}\left[(1 - f) \cdot G(\tau/\tau_{free}) + f^3 \cdot \bar{i} G(\bar{\tau})\right] \tag{2.14}$$

with average multimer size $\bar{i}$ and average multimer diffusion time $\bar{\tau}$ (for details see chapter 7).

2.1.3 INSTRUMENTATION

FCS measurements were performed on an Axiovert 200 microscope with a ConfoCor 2 unit (Carl Zeiss, Jena, Germany) equipped with a 40x (NA = 1.2) water immersion apochromat

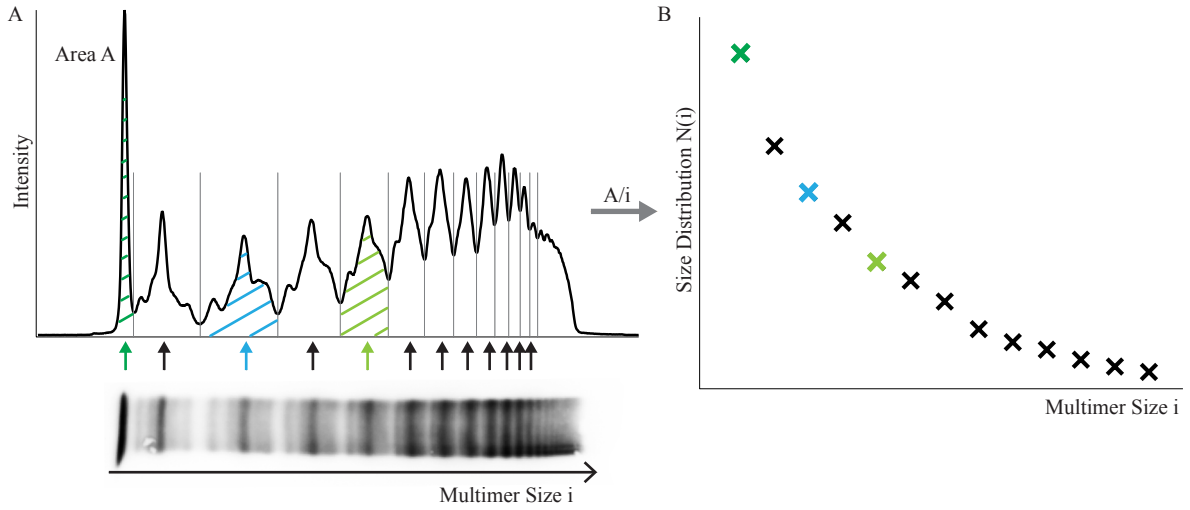

Figure 2.3: Quantitative Gel Analysis. A Multimer pattern of a VWF sample shows a ladder of multimers. Densitogram intensity is plotted versus multimer size and integrated over area A. **B** Intensities are normalized with the size of the multimer in the respective band, which provides the distribution of multimer sizes.

objective (Carl Zeiss, Jena, Germany). An argon laser (488 nm) and a HeNe-laser (633 nm) were used for illumination. Samples were measured in eight well LabTek I chamber slides (Nunc, Rochester, NY), except for measurements under shear flow, which were performed in a self-built sample holder (see section 2.4.1). For experiments at $37°C$, either a heating stage (ibidi GmbH, Martinsried, Germany) or a water bath (Julabo GmbH, Seelbach, Germany; shear experiments) was used. Correlation was performed with the ConfoCor 2 software. For FCS data analysis of the VWF size distribution and VWF binding, Labview routines were implemented. Fitting procedures were carried out using IgorPro.

2.2 Quantitative Gel Analysis

For the quantification of VWF size distributions, gels were analyzed in this thesis in addition to FCS measurements (see chapter 4). Although gel analysis is the most frequently used technique for VWF multimer analysis (52; 53; 54), gels have usually been compared qualitatively in the past. In order to quantitatively interpret gels in terms of size distributions, we introduced a new analysis method, which was applied to recombinant VWF samples as well as blood samples of patients. Therefore, sodium dodecyl sulfate agarose gels were provided by the group of Prof. Budde (Medilys Coagulation Laboratory Asklepios Klinic Altona, Hamburg). After separation of the multimers via gel electrophoresis, they were visualized by detecting their luminescent signal (see Figure 2.3). Thereby, proteins were labeled with horseradish peroxidase-conjugated antibodies that cleave a chemiluminescent agent causing luminescence that is proportional to the amount of protein. The gels were evaluated using lu-

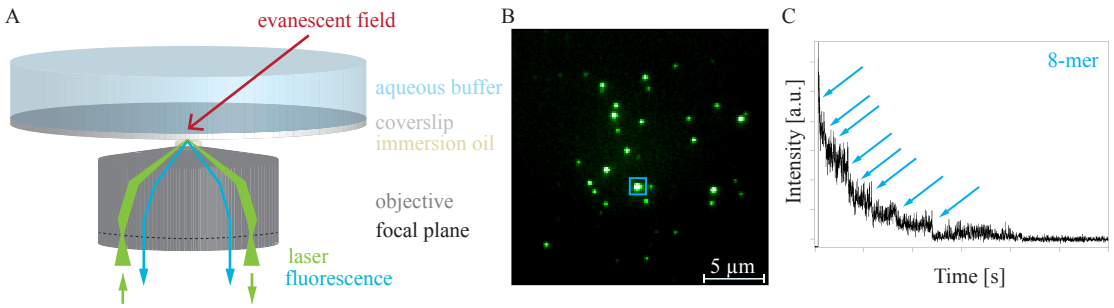

Figure 2.4: Total Internal Reflection Fluorescence Microscopy (TIRFM). A Schematic illustration of the used objective-type TIRFM. The laser beam (green) is focused on the periphery of the objective's back focal plane such that it reachs the glass-water interface under a total reflection angle, generating an evanescent field. **B** TIRFM image of VWF multimers immobilized on a glass surface. **C** Bleaching steps of the intensity time traces are used to determine the multimer size [B and C modified from (55)].

minescent immunoblotting, implying that the measured signal intensities in each band reflect the number of antibody labels (see Figure 2.3 A). As the number of antibody labels scales with the size of the multimers, the signal A was normalized by the number of dimers i, corresponding to the size of the multimers in the respective band (see Figure 2.3 B). The normalized intensities correspond to the molecular weights of the multimers. Thus, plotting A/i versus i directly illustrates the distribution of the multimer sizes $N(i)$.

2.3 TOTAL INTERNAL REFLECTION FLUORESCENCE MICROSCOPY

Total Internal Reflection Fluorescence Microscopy (TIRFM) is used for imaging fluorescent molecules on a transparent substrate with single molecule resolution (25; 56). Instead of direct illumination, the evanescent field of a totally internal reflected laser beam provides selective illumination of the sample (see Figure 2.4 A). The critical angle necessary for total reflection and the generation of a evanescent field is given by $\alpha_c = arcsin\left(\frac{n_2}{n_1}\right)$ with refraction indices $n_2 < n_1$. The resulting evanescent field decays exponentially with increasing distance to the interface:

$$I(z) = I_0 \cdot exp\left(-\frac{z}{d}\right) \tag{2.15}$$

with the depth of penetration:

$$d = \frac{\lambda_t}{4\pi\sqrt{n_1^2 sin^2\alpha - n_2^2}} \tag{2.16}$$

Thus, only fluorophores within typically 100 *nm* above the substrate surface are excited. This restriction of the sample illumination to a very thin layer ensures a high signal-to-noise ratio

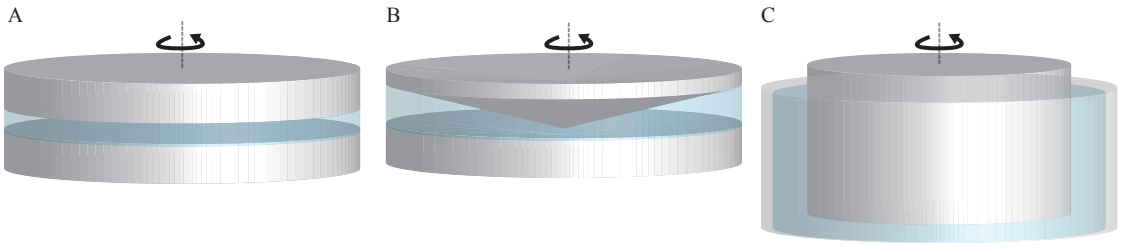

Figure 2.5: Geometries of rotary viscometers. A Plate-and-plate design built of two coaxial circular plates. Shear rates increase with increasing distance to the center. **B** Cone-and-plate design with a rotating cone above a static plate. Produces homogenous shear rates. **C** Couette-cell consisting of two coaxial cylinders. For narrow gaps between the cylinders, homogenous shear rates are generated.

of the detected fluorescence.

In this thesis, TIRFM was used to analyze the size distribution of fluorescent recombinant VWF-eGFP (see chapter 4). Under continuous excitation, the fluorescence signal of the sample was observed to decrease in discrete steps over time (see Figure 2.4 B). As these bleaching steps can be taken as a measure for the number of eGFP-tagged VWF monomers (57), counting the bleaching steps provided a means for analyzing the VWF size distribution (see Figure 2.4 C).

2.4 Microfluidic Shear Cell

In order to study VWF under defined shear flow, a shear cell was designed with the experimental requirement that it had to be combinable with the FCS setup and constantly produce homogenous shear rates over several hours. Rotary viscometers fulfill the second requirement of long-term studies as the rotational movement sustains the generated flow. In such devices, the fluid between two surfaces is sheared due to the rotation of one component. The resulting shear rates depend on the geometry of the components and can be adjusted via the rotational speed. The most frequently used geometries can be divided into three groups: plate-and-plate, cone-and-plate, and concentric cylindrical, also known as Couette-cell (Figure 2.5). The first consists of two coaxial circular plates, one of which is static and the other rotating (Figure 2.5 A). In this geometry, the resulting shear rates increase with increasing distance to the center. The cone and plate viscometer uses a cone of very shallow angle, which rotates at a short distance above a flat plate (Figure 2.5 B). With this design, homogenous shear rates are achieved throughout the whole sample volume. The Couette cell is built of two coaxial cylinders, which rotate relatively to each other (Figure 2.5 C). For very small distances between the two cylinders, the shear rates within this gap can be considered as homogeneous. We chose a combination of the latter ones.

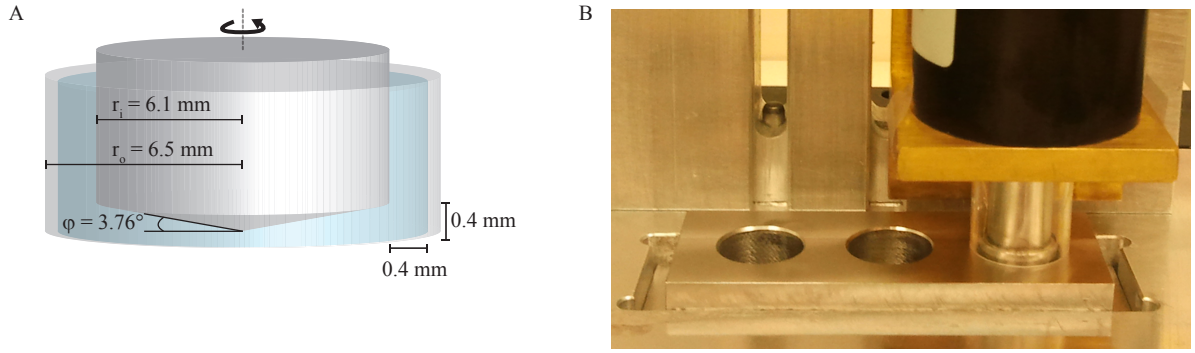

Figure 2.6: Mooney-type shear cell. A A combination of cone-and-plate and concentric cylindrical geometry was used to obtain constant shear rates within the whole sample volume. **B** A sample holder containing three wells serves as static outer cylinder. The rotating inner cylinder is connected to a brushless motor and generates shear rates from 10 to 10.000/s.

2.4.1 DESIGN

In this work, a Mooney-type shear cell was built (58). It consists of a combination of the cone-and-plate and the concentric cylindrical geometry and was designed in a way so that constant shear rates were provided within the whole sample volume (Figure 2.6). It is made of a stainless steel sample holder containing wells with radii $r_o = 6.5\ mm$, serving as static outer cylinders. Before the experiments, a coverslip (Carl Roth, Karlsruhe, Germany) is fixed with nail varnish to the bottom of the sample holder. The rotating inner cylinder (radius $r_i = 6.1\ mm$) is connected to a brushless motor with integrated controller (Faulhaber GmbH, Schönaich, Germany) and generates shear rates from $10 - 10.000/s$. The angle ϕ between cover glass and cone tip measures $\phi = arctan((r_o - r_i)/r_o) = 3.74°$. The sample volume is approximately 150 μl.

The value of the generated shear rates can be calculated based on the design parameters of the device. If the constriction $r_i/r_o > 0.97$ holds for a shear cell with radius r_i of the rotating inner and radius r_o of the static outer cylinder, the shear rate $\dot{\gamma}$ is given by:

$$\dot{\gamma} = \left|\frac{\Delta v}{\Delta r}\right| = \frac{v(r_i) - v(r_o)}{r_o - r_i} = \frac{\omega_i \cdot r_i}{r_o - r_i} \tag{2.17}$$

with surface velocity v and angular velocity ω. As both manufacture and alignment of such a narrow gap between inner and outer cylinder was technically not feasible ($r_i/r_a = 0.94$), a more elaborated formula had to be used. For power-law fluids with flow behavior index n, the shear rate is described by (59):

$$\dot{\gamma} = \frac{\omega_i \cdot (2/n) \cdot \epsilon^{2/n}}{\epsilon^{2/n} - 1} \tag{2.18}$$

where $\epsilon = r_o/r_i$. For Newtonian fluids ($n = 1$) equation 2.18 can be simplified to:

$$\dot{\gamma} = \frac{\omega_i \cdot 2 \cdot \epsilon^2}{\epsilon^2 - 1} \tag{2.19}$$

For shear-thinning fluids like blood, n is less than 1. As n strongly depends on patient-specific parameters such as hematocrit and cholesterol concentration, values for n in whole blood in literature range from 0.6 to 0.7 (60; 61). Here, for measurements in blood plasma (i.e. blood without cells), $n = 0.8$ was assumed.

2.4.2 Experiments under shear flow

Since FCS measurements rely on diffusion, shearing and FCS data sampling needed to be run in an alternating mode, where the solution was sheared for a certain time period, which was directly followed by a 15 minute long FCS detection period without shear. This approach allows to detect events that are stable in the absence of shear, such that the sample is not expected to change during the detection period. This was the case for the shear-induced VWF cleavage presented in chapter 5.

For measurements with VWF, both cylinders had to be coated to avoid sticking of VWF to the surface. Therefore, the shear cell was incubated for half an hour with ultra heat treated (UHT) milk and thereafter washed with buffer for at least ten times.

2.5 Microscale Thermophoresis (MST)

MST is a technology that measures the directed movement of molecules in a temperature gradient. Analyzing this phenomenon called thermophoresis allows for studies on binding affinities and kinetics of biomolecules (28; 62; 63).

2.5.1 Principle

In fluids, molecules with thermophoretic mobility D_T move in a temperature gradient ΔT with the velocity $v = D_T \cdot \Delta T$ (64). The thermophoretic movement induces differences in concentration c, which leads to diffusion. This results in a total flow density of:

$$\mathbf{j} = \mathbf{j}_D + \mathbf{j}_{D_T} = -\Delta c \cdot D - c \cdot \Delta T \cdot D_T \tag{2.20}$$

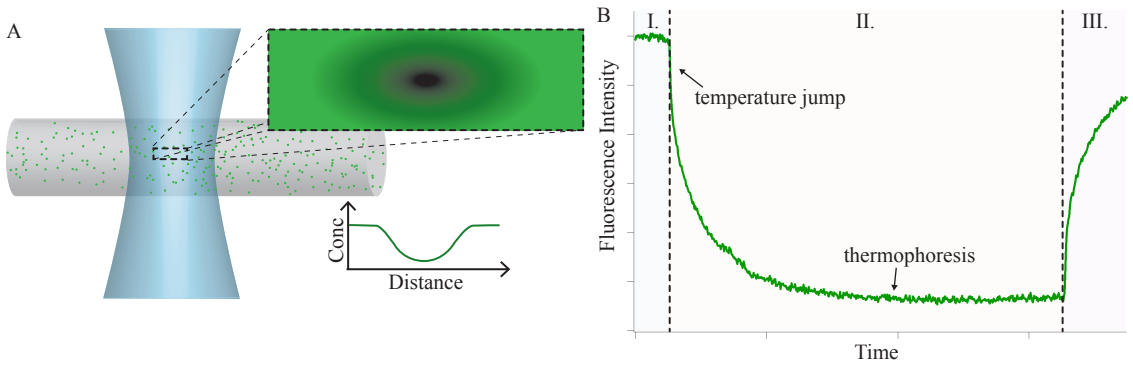

Figure 2.7: Microscale Thermophoresis (MST). A Fluorescence is detected from molecules in a probe chamber. After switching on a focused infrared-laser, a temperature gradient establishes, which generates directed motion of the molecules. This thermophoretic movement produces a concentration gradient inside the capillary. The concentration increases with increasing distance from the laser focus. **B** Detection of fluorescence over time monitors the thermophoretic movement. I. Cold fluorescence F^{cold} is detected, before the laser is switched on. II. After switching the laser on, a temperature jump is observed in fluorescence because of the temperature dependence of the fluorescent dyes. It is followed by the charateristic thermophoretic movement. F^{hot} is extracted from this fluorescence time course. III. After switching off the laser, backdiffusion starts.

with D being the diffusive mobility of the molecules. In equilibrium, thermophoresis is balanced by ordinary diffusion ($\mathbf{j} = 0$):

$$\frac{dc}{c} = -\frac{D_T}{D} \cdot dT \tag{2.21}$$

leading to an equilibrium concentration distribution of:

$$\frac{c(x)}{c_0} = exp[-(D_T/D) \cdot (T(x) - T(x_0))] \tag{2.22}$$

where c_0 denotes the concentration at position x_0. The ratio of the diffusive mobilities D_T/D is defined as Soret coefficient S_T and a measure for the strength of thermodiffusion in the steady state. For small, quasi-constant temperature steps, the concentration distribution due to thermophoretic movement may also be interrelated with a local change in the Gibbs free energy G using a Boltzmann distribution (65):

$$\frac{c(T_1)}{c(T_2)} = exp\left[-\frac{G(T_1) - G(T_2)}{k_B T}\right] \tag{2.23}$$

with Boltzmann constant k_B. Equation 2.22 and 2.23 directly relate the Soret coefficient to the overall entropy S:

$$S_T \cdot k_B T = \frac{\Delta G}{\Delta T} = -S \tag{2.24}$$

For single particles at constant pressure, S denotes the local negative entropy of the particle-solvent system. In water, the particle entropy is dominated by the entropy of ionic shielding and the entropy of hydration. This leads to:

$$S_T = \frac{A}{k_B T}\left(-s_{hyd} + \frac{\beta\sigma_{eff}^2}{4\epsilon\epsilon_0 T}\cdot\lambda_{DH}\right) \tag{2.25}$$

with the hydration shell s_{hyd} per surface area A, the effective surface charge density σ_{eff}, the Debye screening length λ_{DH}, the dielectric constant ϵ, and the electric constant ϵ_0. β gives the relative change of the solvent's dieletric constant $\epsilon(T)$ with temperature.

2.5.2 Soret Analysis

As depicted in equation 2.25, the Soret coefficient depends on size, conformation, charge, and solvation entropy of a particle. Binding to other molecules may alter all or some of these properties, which is used in MST to quantify the interaction of biomolecules because S_T determines the change in concentration in steady state:

$$c = c_0 \cdot exp(-S_T \cdot \Delta T) \tag{2.26}$$

with the temperature rise $\Delta T = T - T_0$ at the respective spot. In MST experiments, a low power infrared laser generates a temperature gradient inside a probe filled chamber, e.g. a capillary with solved molecules. Using fluorescent molecules allows for the visualization of the thermophoretic movement as a shift in the detected fluorescence intensity (see Figure 2.7 A). The thermophoretic depletion is thereby given by the ratio F^{hot}/F^{cold} of the average fluorescence intensity determined in the time periods when the laser is switched on (F^{hot}) and off (F^{cold}) (see Figure 2.7 B). In a typical experiment, the amount of unlabeled binding partners (called receptor in the following) is varied. Directly plotting the detected thermophoretic depletion against the receptor concentration results in a binding isotherm.

The binding isotherm can be analyzed applying the law of mass action. In a bimolecular binding process of binder molecule B and receptor molecule R, the complex RB associates with the rate k_{on} and dissociates with the rate k_{off}:

$$c_R^{free} + c_B^{free} \rightleftharpoons c_{RB} \tag{2.27}$$

The affinity between ligand and binder molecules is quantified by the dissociation constant K_D:

$$K_D = \frac{k_{off}}{k_{on}} = \frac{c_R^{free}\cdot c_B^{free}}{c_{RB}} = \frac{(c_R - c_{RB})(c_B - c_{RB})}{c_{RB}} \tag{2.28}$$

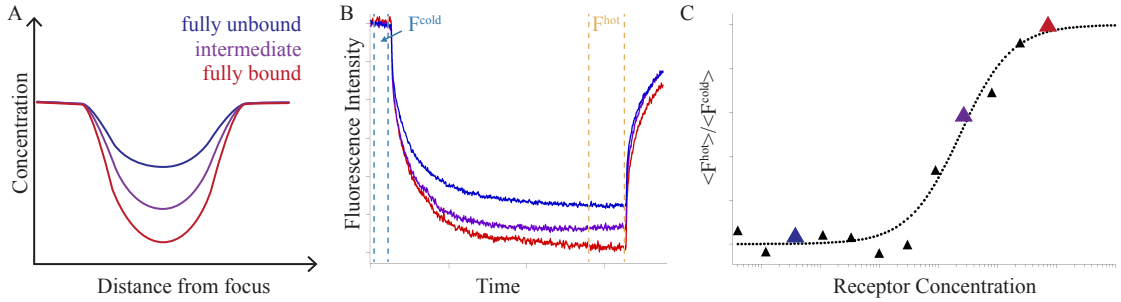

Figure 2.8: Soret Analysis. A The thermophoretic movement changes upon binding. **B** This results in differences in the fluorescence time traces. **C** Binding isotherms are obtained directly from the thermophoretic depletion. Fitting with equation 2.29 is indicated as dotted line.

with $c_R = c_R^{free} + c_{RB}$ and $c_B = c_B^{free} + c_{RB}$. Rearrangement of equation 2.28, leads to the expression used for data analysis:

$$\frac{c_{RB}}{c_B} = \frac{c_R + c_B + K_D - \sqrt{(c_R + c_B + K_D)^2 - 4c_R c_B}}{2c_B} \tag{2.29}$$

where c_{RB}/c_B denotes the fraction of occupied binding molecules, which is measured as thermophoretic depletion in the MST experiments (see Figure 2.8).

3 VWF: A Mechanosensitive Polymeric Blood Protein

The multimeric blood protein VWF is a key factor in primary hemostasis as it initiates coagulation by the promotion of platelet adhesion at sites of vascular injury. Remarkably, VWF possesses a shear-flow sensitive structure, and binding of various enzymes and coagulation factors, interacting with VWF, is activated by shear stress. Moreover, its function in primary hemostasis correlates with its size. The work presented in this thesis focuses on VWF as a multimeric, mechanosensitive protein, and on the shear-induced regulation of its functionality. Underlying medical and biological basics are presented in this chapter. Starting with a general overview of hemostasis (3.1), the biosynthesis of VWF (3.2), and its structure-function relationship (3.3) as well as the VWF-associated disease Thrombotic Thrombocytopenic Purpura (3.4) are discussed in detail. Finally, the protocol to produce recombinant fluorescent VWF-eGFP, as was used in this thesis, is described (3.5).

3.1 Hemostasis

Hemostasis is a complex pivotal process that stops bleeding at ruptured vessel walls. It can be divided into two steps: During the primary hemostasis, vasoconstriction along with the formation of a platelet plug initially occlude the vascular lesion. During the subsequent secondary hemostasis, the formation of fibrin clots ensures the final blood coagulation. Strict regulation of both parts is essential to prevent both heavy blood loss and clogged blood vessels (66).

Primary hemostasis has to be rapid, reliable, precise, and, moreover, effectively operating under high shear stress, which arises where injury occurs. It is initiated by constriction of the damaged blood vessel, minimizing the amount of blood that can be lost. Meanwhile, thrombocytes adhere to the exposed sub-endothelium collagen fibers. This adhesion is mediated by the blood protein VWF, which possesses binding sites for both collagen and the platelet receptor GPIb. Subsequent to adhesion, the thrombocytes are activated; they start to secret coagulation factors, undergo conformational changes, and form aggregates. The thereby evolved platelet

plug temporarily closes the rupture in the vessel wall.

In secondary hemostasis, the formed thrombus has to be stabilized. This is ensured by the interplay of various coagulation factors (termed Fx) and called blood coagulation cascade (66). Most of the coagulation factors are proteolytic enzymes, which exist in the plasma in an inactive form. Secondary hemostasis consists of three phases: the activation phase, which leads to the conversion of prothrombin to thrombin, the coagulation phase, where soluble fibrin monomers are built out of fibrinogen, and finally the retraction phase, where the thrombus is stabilized and contracted via fibronectin and thrombosthenin (67). When this stable, platelet- and fibrin-containing plot is built, repairing of the damaged vessel sets in.

The activation phase of the coagulation cascade consists of two pathways. Both result in activation of FX, which in turn initiates the formation of thrombin. The extrinsinc pathway uses a complex consisting of membrane-activated FVII, membrane-bound tissue factor, and calcium to do so. The intrinsic pathway works 50-fold more efficiently, and a dysfunction of this pathway leads to severe bleeding disorders. It is completed by a membrane-bound tenase complex that is built from activated FVIII and FIX. Hemophilia, the second most prevalent coagulation disorder, results from the absence or inactivity of either FVIII (hemophilia A, 85%) or FIX (hemophilia B) (67).

Within this complex network that was established as a defense mechanism against bleeding, one glycoprotein, the VWF, cannot be substituted. Deficiency or dysfunction of VWF, called von Willebrand disease, is the most common inherited bleeding disease (13). In addition to its essential role in primary hemostasis, VWF acts as carrier protein for FVIII, which is rapidly removed from the circulation in the absence of VWF. Consequently, patients who lack VWF suffer from severe bleeding disorders due to profound defects both in blood clotting and in the formation of platelet plugs at sites of vascular injury.

3.2 VWF: BIOSYNTHESIS AND SECRETION

VWF is a large, multimeric glycoprotein present in blood plasma, platelet α-granules, and subendothelial connective tissue. Its biosynthesis is a highly sophisticated process, leading to a molecular heterogeneity, which reaches from 500 kDa dimers to 40.000 kDa high molecular weight multimers (HMWM) (Figure 3.1). Synthesis starts in the cytoplasm by production of pre-pro-monomers, which are translocated to the endoplasmatic reticulum (ER). Here, glycosylation occurs, and dimers form via intermonomer disulfide bonds in the carboxy-terminal domain. Dimers with a molecular mass of 500 kDa represent the repeating unit of the VWF multimer. They are transported from the ER (pH = 7.4) to the Golgi apparatus (pH = 6.2). There, pH-dependent multimerization occurs by formation of linear multimers via interchain disulfide bonds at the amino-terminal, resulting in multimeric VWF (31; 68; 69). The VWF propeptide, which acts as an oxidoreductase to promote VWF multimerization, is then furin-

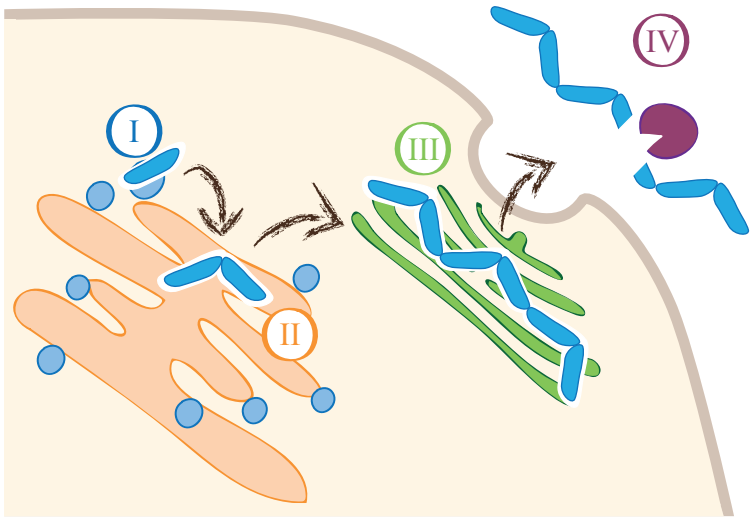

Figure 3.1: Schematic representation of plasma VWF biosynthesis and post-secretional size control. (I) VWF is synthesized in the cytoplasm, and originates from 360 kDa pre-pro-monomers. (II) Monomeric VWF is transported to the endoplasmic reticulum, where it is dimerized through intermonomer disulfide bonds. (III) Multimerization takes place in the Golgi apparatus, where the dimers form multimers, which are then secreted to the blood plasma. (IV) Size control in plasma is provided by the protease ADAMTS13. No further multimerization occurs after secretion to the plasma (modified from (55)).

cleaved for separate secretion (70; 71). The VWF multimers are either stored in Weibel-Palade bodies until release upon thrombotic stimuli or secreted constitutively to the plasma (72). After secretion to the blood plasma, no further multimerization takes place. VWF multimers are cleared with a halflife of about 12 h. The plasma concentration averages 10 $\mu g/ml$.

3.3 VWF: Biological Activities and Structure-Function Relationship

VWF possesses a multi-domain structure, which enables its versatile role in blood coagulation (Figure 3.2). The individual domains carry several binding sites, and VWF performs its hemostatic functions through binding to coagulation factor VIII (FVIII), platelets, and collagen. For FVIII, VWF acts as a transporter protein, preventing degradation of this important player of the coagulation cascade in the blood vessel. Initiating primary hemostasis, VWF furthermore mediates accelerated binding of platelets to collagen that is exposed at ruptured vessel walls, and to one another. While there are no binding sites for collagen present on platelets, there are two binding sites designed for VWF: Non-activated platelets bind VWF's A1-domain via the receptor GPIb, which is characterized by a fast association rate. After activation, binding to GPIb is followed by binding of the integrin GPIIb/IIIa to VWF's RGD binding sequence. Besides, VWF might facilitate platelet aggregation by forming networks via VWF intermolecular

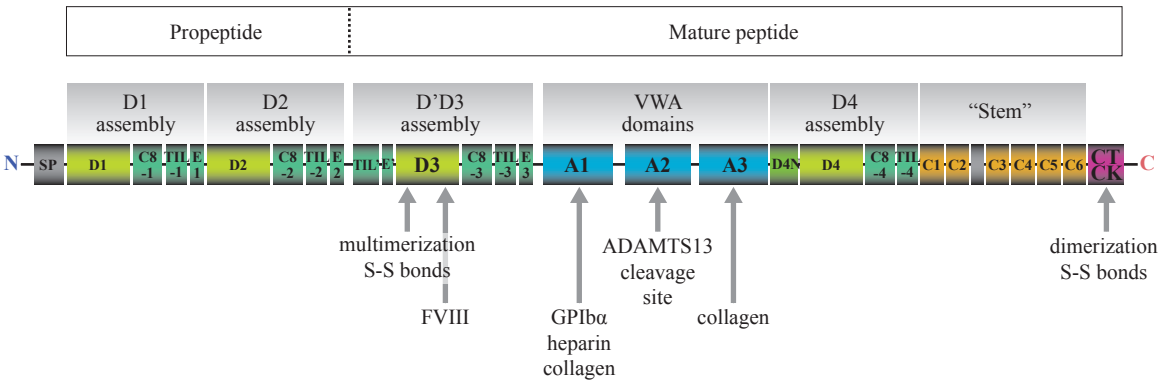

Figure 3.2: Multidomain structure of the VWF monomer and attributed binding sites (with courtesy modified from C. Baldauf).

binding (73). Moreover, there is a reasonable suspicion that unspecific interactions of VWF with endothelial cells exist (74; 75).

Due to its multimeric structure, there exists a wide range of mutations in the VWF coding gene causing von Willebrand disease (VWD), an inherited bleeding disorder. VWD is characterized by a prolonged bleeding time, which stems from quantitative and/or functional deficits of VWF. It is classified into three types: VWD type 1 and 3 are quantitative defects with depressed levels of VWF, either with regular functionality (type 1), or with almost complete absence of VWF (type 3). In contrast, VWD type 2 includes a wide variety of structural and/or functional defects of VWF, resulting from mutations in distinct domains of the molecule. The impact of these mutations are diverse, involving dimerization and multimerization defects, mechanical instabilities of individual domains, altered binding affinities, and modified proteolysis kinetics (76).

Remarkably, all VWF interactions, besides FVIII binding, are known to strongly depend on VWF's conformation and size (Figure 3.3) (5; 24; 77; 78). This represents a highly specialized regulation of VWF's functionality, which is particularly important in the arterial and microcirculation: In this environment, VWF is exposed to high shear forces with hydrodynamic shear rates ranging over several orders of magnitude from 10^{-1} to 10^{5} 1/s, which explains why VWF requires a specific mechanism to enable platelet adhesion and aggregation. This specific mechanism consists of two features: a multimeric structure and a force-sensing domain. At low shear rate, VWF exists in the blood in a globular form and performs a globular-stretch transition at a critical shear rate (5). In addition to this polymeric unfolding, VWF's A2 domain possesses a mechanosensitive structure, which opens at a critical force (24). Within this force-sensing A2 domain lies the cleavage site for ADAMTS13 (a disintegrin and metalloproteinase with a thrombospondin type 1 motif, member 13). The metalloproteinase was found to be the specific plasma protease, regulating the size of VWF, in 2001 (8; 9; 10). Because smaller multimers are more resistant to shear forces than larger ones, VWF functionality strongly depends on its size, and its shear-induced degradation by ADAMTS13 is a determining factor in hemostasis. Thereby, the size regulation by ADAMTS13 establishes, in

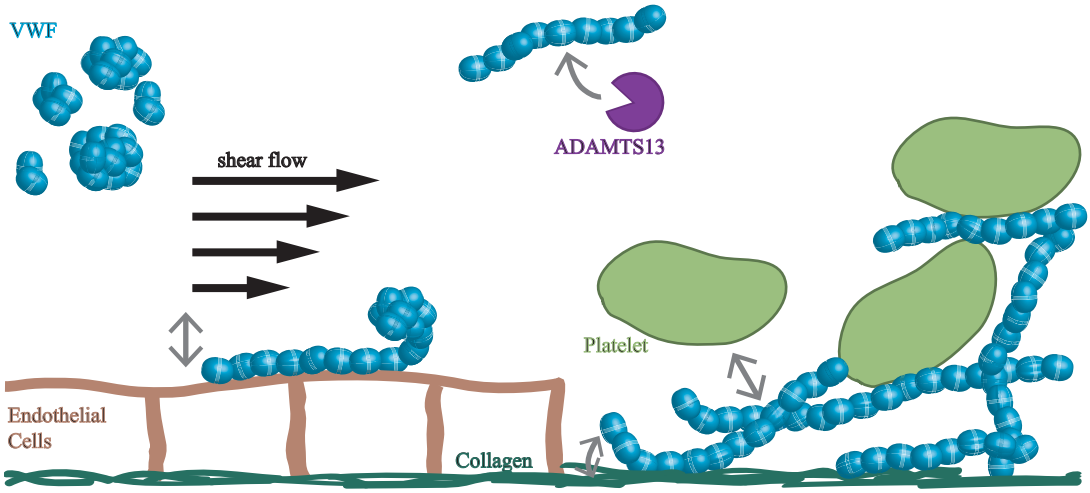

Figure 3.3: VWF in the blood vessel and during coagulation. Differently sized VWF multimers persist at low shear rates in an inactivated globular state. Shear stress elongates VWF, and binding sites are exposed. The metalloprotease ADAMTS13 regulates the VWF size distribution by shear-dependent proteolysis. VWF binds to endothelial cells, platelets, and collagen. VWF and platelets form networks during hemostasis, which cover the damaged epithelial tissue.

combination with shear flow, a unique feedback loop of VWF's activity: The higher the shear rate, the faster ADAMTS13 cleaves the polymer. The shorter the polymers, the less they are stretched, reducing ADAMTS13 cleavage potential.

3.4 Thrombotic Thrombocytopenic Purpura (TTP)

The hematological disorder thrombotic thrombocytopenic purpura (TTP) is a severe, occlusive, microvascular thrombotic microangiopathy. It is associated with acquired or congenital deficiency of the VWF cleaving protease ADAMTS13. In TTP, absence of functional ADAMTS13 leads to unusually large VWF multimers, which are hemostatically more active. This results in life-threatening depositions of thrombi in the microvasculature that consist of platelets and ultralarge VWF, leading to thrombocytopenia and bleeding episodes (79). Most cases of TTP in adults are caused by acquired autoantibodies that inhibit ADAMTS13 (80). Interestingly, the ADAMTS13 concentration fluctuates over a wide regime and patients with more than 10% of the physiological ADAMTS13 level can live without symptoms. Severely deficient ADAMTS13 activity occurs at ADAMTS13 levels of 5% and below (81). Although plasma exchange therapies are widely used to remove autoantibodies and replenish ADAMTS13, TTP still leads to a high morbidity rate and significant mortality (14). The detection of such low ADAMTS13 concentrations around 100 pM and below is technically challenging. Thus, measurements of ADAMTS13 activity in TTP and other pathological conditions remain in the focus of substantial clinical research effort.

3.5 EXPRESSION OF RECOMBINANT VWF-EGFP

For the used measurement techniques based on fluorescence microscopy (see chapter 2), a recombinant fluorescent VWF-enhanced green fluorescent protein (eGFP) fusion construct was produced. For cloning of the wild-type VWF-eGFP plasmid, the stop codon was eliminated from the plasmid pIRESneo2-vWF (Takara Bio Europe/Clontech, Saint- Germain-en-Laye, France) and an EcoRI restriction site was introduced. The eGFP sequence was cut out from the plasmid pEGFP-N2 (Takara Bio Europe/Clontech) by the restriction endonucleases EcoRI and NotI and inserted into the plasmid pIRESneo2 by using its EcoRI/NotI restriction sites (pIRESneo2-EGFP). Subsequently, VWF-cDNA from plasmid pIRESneo2-VWF, lacking the stop codon, was cut out by EcoRI and cloned into pIRESneo2-EGFP (pIRESneo2-VWF-EGFP).

Several mutations of the full-length recombinant VWF were used in this work. Plasmids of these mutants were produced as following:

rVWF-eGFP dimer: The pIRESneo2-vWF-delPro-EGFP was modified such that the signal peptide sequence plus the first three codons of the VWF propeptide were retained, while the rest of the propeptide, corresponding to codons 26-763 (delT26-R763), was cut out. Therefore, the VWF multimerization site was missing, and expression of this construct resulted in VWF monomers that assembled into carboxy-terminal dimers but could not multimerize at the amino-terminal.

rVWF-eGFP monomer: The plasmid pIRESneo2-vWF-delPro/C2771R-EGFP was produced by in vitro-mutagenesis of the VWF-delPro construct, producing VWF-eGFP dimers. The cystein codon 2771 was exchanged for arginine (p.C2771R), which presents a naturally occurring mutation. This mutation causes a severe dimerization defect in addition to the multimerization defect of the VWF-delPro construct. Thus, expression resulted in rVWF-eGFP monomers.

rVWF-eGFP-IIC: In the wild-type plasmid pIRESneo2-VWF-EGFP, the codon 1099 for cysteine was exchanged for tyrosine (p.C1099Y), which corresponds to another mutation found in patients. Expression of the plasmid PIRESneo2-vWF-C1099Y-EGFP did not result in quantitative defects in the expression of VWF. However, it generated a deficiency in large and medium-sized VWF multimers. In patients, this mutation is characterized as VWD type 2A, phenotype IIC.

rVWF-eGFP-G1629E: This construct carries a mutation in the mechanosensitive A2 domain that strongly destabilizes the domain. The plasmid of wild-type pIRESneo2-VWF-eGFP was modified by exchanging in codon 1629 glycine for glutamine (p.G1629E). Due to this mutation, the VWF cleavage site becomes permanently accessible, leading to highly increased cleavage rates and absence of long VWF multimers.

Human Embryonic Kidney (HEK) 293 cells were transiently transfected with full-length mVWF or wtVWF cDNA by liposomal transfer (Lipofectamine 2000; Invitrogen). 48 h after transfection, cells were trypsinized and grown until confluence in Dulbeccos modified Eagle medium, containing 10% fetal bovine serum and G418 at 500 mg/ml for selection. After further growth of an aliquot of the stable cell line until 70−80% confluence, cell culture medium was exchanged by OPTIPRO-SFM medium for serum-free expression. Cell culture medium was harvested after 72 h and concentrated by Amicon Ultrafree, MWCO 100.000 (Merck Millipore, Darmstadt, Germany).

4

Size Distribution Analysis of VWF

This chapter presents a study on the size distribution of the plasmatic polymer VWF. In primary hemostasis, the function of VWF is determined by its shear-flow sensitive structure and correlates with its size. From a polymer physics point of view, this size dependent functionality is of eminent interest, because the distribution of VWF sizes represents an important regulator of the influence of shear flow on its activity. Although it was well known that VWF forms multimers before being secreted to the blood plasma, there was hitherto no quantitative description on the size distribution.

We found exponentially distributed sizes using multiple experimental approaches, involving FCS, Quantitative Gel Analysis (Prof. Budde), and TIRFM (Dr. Benoit). Recombinant VWF constructs were provided by the group of Prof. Schneppenheim. We attributed the resulting size distribution to a step-growth polymerization process during VWF biosynthesis. As a consequence, the size distribution can be explicitly described by a single parameter, namely the extent of polymerization, which we found to be reduced for a disease-related VWF mutant. Using FCS, we measured shifts in the VWF sizes due to ADAMTS13-induced proteolysis and showed that the decreasing average VWF size is in agreement with the expected evolution of an exponential distribution under random cleavage. The quantitative assessment of the VWF size distribution in terms of an exponential might prove to be useful both as a valuable biophysical characterization and as a possible disease marker for clinical applications. Moreover, it allows for quantitative studies of full-length VWF rendering experiments with isolated VWF domains instead of the multimers unnecessary.

The experimental data and the resulting conclusions are presented in the following publication:

S. Lippok, T. Obser, J.P. Müller, V.K. Stierle, M. Benoit, U. Budde, R. Schneppenheim, J.O. Rädler. 2013. ”Exponential Size Distribution of von Willebrand Factor.” *Biophysical Journal* 105:1208-1216.

Exponential Size Distribution of von Willebrand Factor

Svenja Lippok,[†] Tobias Obser,[‡] Jochen P. Müller,[§] Valentin K. Stierle,[†] Martin Benoit,[§] Ulrich Budde,[¶] Reinhard Schneppenheim,[‡] and Joachim O. Rädler[†*]

[†]Faculty of Physics and Center for NanoScience, Ludwig Maximilian University, Munich, Germany; [‡]Department of Pediatric Hematology and Oncology, University Medical Center, Hamburg-Eppendorf, Hamburg, Germany; [§]Chair for Applied Physics, Ludwig Maximilian University, Munich, Germany; and [¶]Coagulation Lab, AescuLabor Hamburg, Hamburg, Germany

ABSTRACT Von Willebrand Factor (VWF) is a multimeric protein crucial for hemostasis. Under shear flow, it acts as a mechanosensor responding with a size-dependent globule-stretch transition to increasing shear rates. Here, we quantify for the first time, to our knowledge, the size distribution of recombinant VWF and VWF-eGFP using a multilateral approach that involves quantitative gel analysis, fluorescence correlation spectroscopy, and total internal reflection fluorescence microscopy. We find an exponentially decaying size distribution of multimers for recombinant VWF as well as for VWF derived from blood samples in accordance with the notion of a step-growth polymerization process during VWF biosynthesis. The distribution is solely described by the extent of polymerization, which was found to be reduced in the case of the pathologically relevant mutant VWF-IIC. The VWF-specific protease ADAMTS13 systematically shifts the VWF size distribution toward smaller sizes. This dynamic evolution is monitored using fluorescence correlation spectroscopy and compared to a computer simulation of a random cleavage process relating ADAMTS13 concentration to the degree of VWF breakdown. Quantitative assessment of VWF size distribution in terms of an exponential might prove to be useful both as a valuable biophysical characterization and as a possible disease indicator for clinical applications.

INTRODUCTION

The large plasma glycoprotein von Willebrand Factor (VWF) is essential for the initiation of blood coagulation as it promotes adhesion of platelets to the injured vessel wall as well as platelet aggregation (1,2). It is present in human blood and the secretory granules of endothelial cells and platelets. Plasma VWF plays a crucial role in early hemostasis as it binds rapidly and tightly to collagen whenever blood is exposed to injured tissues (3). Remarkably, VWF is a multimer that consists of several identical subunits and its function in primary hemostasis strictly correlates with its multimer size. Even though much research is being done on its size-dependent functionality, only little is known about the exact size distribution and its origin. Quantitative deficiency of plasma VWF causes von Willebrand disease (VWD) type 1, the most common congenital bleeding disorder (1). Although VWD is often caused by a lack of long multimers, an aberrantly increased activity of VWF due to larger than normal multimers is assumed to be a pathogenic factor in thrombotic thrombocytopenic purpura (2,4). The size-dependent functionality relates to the shear flow-sensitive structure of VWF, which responds to shear by expansion to an elongated form, thereby exposing binding sites for collagen and the platelet receptor GPIb (5). This process highly depends on the extent of multimerization of VWF because smaller multimers are more resistant to shear forces than larger ones and subsequently binding sites for their ligands are not as readily exposed (6,7). Consequently, the size of the multimeric VWF is a critical factor for VWF's functionality and the question arises, which size distribution is produced by VWF biosynthesis and how it is controlled in homeostasis. In polymer science, the problem of polymer size distribution has been addressed by the seminal work of Paul Flory in 1936, in which he calculated the exact size distribution of polymers based on the model of step-growth polymerization reaction (8). He showed that a theoretical prediction of a multimer size distribution is possible if the mechanism and the kinetics of the synthesis reaction are known. Vice versa, the size distribution provides clues with respect to the polymerization mechanism.

VWF is expressed as a proprotein (Fig. 1 *A*), which is translocated into the endoplasmatic reticulum, where it dimerizes via intermonomer disulfide bonds in the C-terminal domain (Fig. 1 *B*). The dimers with a molecular mass of 500 kDa represent the repeating unit of the VWF multimer. They are transported from the endoplasmatic reticulum (pH $\approx$ 7.4) to the Golgi (pH $\approx$ 6.2). This is the place where multimerization occurs by formation of linear multimers via interchain disulfide bonds at the N-terminal resulting in multimeric VWF with molecular masses of up to $>$ 40.000 kDa (Fig. 1 *C*) (9–11). In this process, VWF propeptide acts as an oxidoreductase to promote VWF multimerization (12–14). The propeptide is then cleaved for separate secretion (15,16). After multimerization, VWF is either secreted constitutively to the plasma or stored in Weibel-Palade bodies and released upon certain stimuli (e.g., thrombin, plasmin, fibrin) without further multimerization taking place in the plasma (17). For a postsecretion size regulation, circulating VWF undergoes cleavage by

Submitted April 3, 2013, and accepted for publication July 24, 2013.

*Correspondence: raedler@lmu.de

Editor: Ashok Deniz.

0006-3495/13/09/1208/9 $2.00

http://dx.doi.org/10.1016/j.bpj.2013.07.037

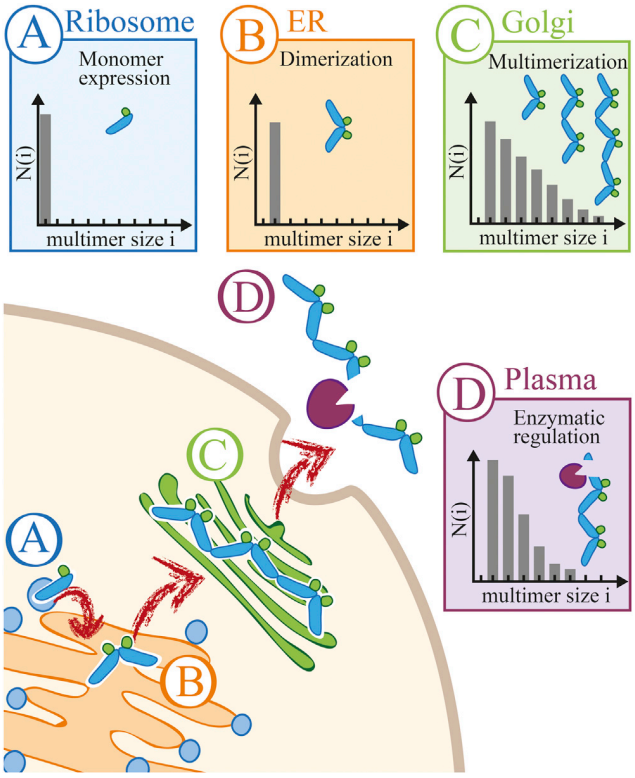

FIGURE 1 Schematic representation of plasma VWF size regulation. (*A*) VWF is synthesized by endothelial cells and megakaryocytes and originates from a 360 kDa monomer. (*B*) Monomeric VWF is transported to the endoplasmic reticulum where it is dimerized through intermonomer disulfide bonds. (*C*) Multimerization takes place in the Golgi apparatus, where the dimers form multimers with sizes ranging from 500 to 40.000 kDa, which are then secreted to the blood plasma. (*D*) Size control in plasma is provided by the protease ADAMTS13. No further multimerization occurs after secretion to the plasma.

the specific metalloprotease ADAMTS13, a disintegrin and metalloproteinase with a thrombospondin type 1 motif, member 13 (Fig. 1 *D*) (18). As known from bleeding disorders, defects in VWF multimer synthesis or size regulation have fundamental implications in hemostasis and exhibit defined patterns in VWF gel electrophoresis. Yet, the size distribution of VWF and its molecular causation has not been quantitatively studied so far.

Here, we investigate the size distribution of VWF using fluorescence correlation spectroscopy (FCS), quantitative gel analysis, and total internal reflection fluorescence microscopy (TIRFM). TIRFM allows for direct imaging of recombinant VWF-eGFP multimers including the assessment of VWF size by intensity analysis. Gel analysis is widely accepted in VWF diagnostics for screening patient samples for diseases. FCS measures the hydrodynamic size of fluorescently labeled species in solution. In contrast to gel analysis and TIRFM, FCS allows for measurements of fluorescent VWF-eGFP in blood plasma and is therefore well suited for VWF analysis in its native environment. We compare the size distribution of recombinant VWF and VWF-eGFP and its disease-related mutant VWF 2A (IIC), which is characterized by an increased concentration of dimers (19,20). We show that after secretion from VWF producing cells, VWF has an exponential size distribution in both healthy and pathologic form. The physiological and pathological distributions are distinct in the extent of polymerization characterizing the distribution. We also show that proteolytic cleavage by ADAMTS13 leads to non-exponential distributions that shift with time allowing for in situ monitoring of VWF cleavage under blood plasma conditions.

MATERIALS AND METHODS

Production of recombinant VWF

The recombinant fusion protein rVWF-eGFP was expressed and purified separately in its monomer, dimer, and multimer form as described in detail in the following:

Cloning of a VWF-enhanced green fluorescent protein (EGFP) Plasmid

From the plasmid pIRESneo2-vWF (Takara Bio Europe/Clontech, Saint-Germain-en-Laye, France) the stop codon was eliminated and an *Eco*RI restriction site was introduced. The EGFP sequence was cut out from the plasmid pEGFP-N2 (Takara Bio Europe/Clontech) by *Eco*RI and NotI and inserted into plasmid pIRESneo2 by using its *Eco*RI/NotI restriction sites (pIRESneo2-EGFP). Subsequently, VWF-cDNA from plasmid pIRESneo2-VWF lacking the stop codon was cut out by *Eco*RI and cloned into pIRESneo2-EGFP (pIRESneo2-VWF-EGFP).

pIRESneo2-VWF-EGFP was then used to produce three mutant constructs:

1) pIRESneo2-vWF-delPro-EGFP with the retained signal peptide sequence and the first three codons of the VWF propeptide but lacking the rest of the propeptide corresponding to codons 26–763 (delT26-R763). Expression of this construct will result in VWF monomers that assemble into carboxy-terminal dimers but not into larger multimers.
2) pIRESneo2-vWF-delPro/C2771R-EGFP, which was produced by in vitro-mutagenesis of construct 1), by exchanging codon 2771 for cysteine against the naturally occurring mutation to arginine (p.C2771R). Expression of this construct results in VWF monomers only, because p.C2771R causes a severe dimerization defect (R. Schneppenheim, unpublished) in addition to the multimerization defect of the VWF-delPro construct 1.
3) PIRESneo2-vWF-C1099Y-EGFP, which was produced by in vitro-mutagenesis of wild-type pIRESneo2-VWF-EGFP, by exchanging codon 1099 for cysteine against the naturally occurring mutation to tyrosine (p.C1099Y). Expression of this mutant results in near normal quantitative expression of mutant VWF, however, lacking large and medium sized VWF multimers as in the phenotype IIC of VWD type 2A.

Generation of stable cell lines constitutively secreting VWF

Transfection of 293 cells was carried out as described previously (21). 48 h after transfection cells were trypsinized and grown until confluence in Dulbecco's modified Eagle's medium buffer containing 10% fetal bovine serum and G418 at 500 μg/ml for selection. After further propagation of an aliquot of the stable cell line until 70–80% confluence, cell culture medium was changed to OPTIPRO-SFM medium for serum-free expression. Cell culture medium was harvested after 72 h and concentrated by Amicon Ultrafree (MWCO 100000 DA) if necessary.

Blood samples

The patient samples were sent to our laboratory for the evaluation of VWF multimers and subtyping of the already known VWD. Informed consent was obtained from all subjects.

Quantitative gel analysis

VWF multimer analysis was carried out in sodium dodecyl sulfate agarose gels combined with immunoblotting and luminescence visualization. The luminescent blot was stored on electronic media using photo imaging (FluorChem8000; Alpha Innotech, San Leandro, CA) (22). VWF multimers were separated via gel electrophoresis and visualized by detecting their luminescent signal. Electrophoretic bands were visualized by means of luminescent immunoblotting. Thereby, intensities were obtained by labeling the proteins with horseradish peroxidase-conjugated antibodies that cleave a chemiluminescent agent producing luminescence that is proportional to the amount of protein (23).

The multimer patterns of rVWF and rVWF-eGFP are taken from different gels, which were recorded on different days. Therefore, the run times vary from sample to sample. As the run times are not used for data analysis this does not have any influence on the analyzed data.

FCS

FCS detects the dynamics of fluorescently labeled molecules diffusing in and out of a confocal volume (24–28) and can be applied to multicomponent systems with different fluorescent species (29). It can be used for measurements in crowded media like blood plasma, thus enabling the study of molecules in their native environment (30). This ensures that the investigated molecules keep their natural properties, because these often change in bulk fluids acting as solvents and thereby reducing effects such as aggregation. FCS data analysis is described in detail in the Supporting Material.

For FCS measurements, an Axiovert 200 microscope with a ConfoCor 2 unit (Carl Zeiss, Jena, Germany) equipped with a 40× (NA = 1.2) water immersion apochromat objective (Carl Zeiss) was used. An argon laser (488 nm) was used for illumination. Samples were measured in eight-well LabTek I chamber slides (Nunc, Rochester, NY). All measurements were performed in 5 mM Tris-HCl, pH 8.0 with 1.5 M urea at a temperature of 37°C controlled by an ibidi heating stage (ibidi GmbH, Martinsried, Germany). At this urea concentration, VWF can be conceived as a semiflexible polymer as urea stretches it without affecting its basic structure. These conditions are widely used for VWF analysis if measurements with the stretched polymer have to be performed without shear flow (4,31). eGFP functionality was proved to be functional under this buffer condition in agreement with Alkaabi et al. (32). Measurements were performed for 10 × 60 s (eGFP, monomer and dimer) and 20 × 6 min (rVWF; rVWF-IIC). To ensure optimal fluctuation detection for multicomponent analysis, we chose long measurement times to obtain sufficient statistics while keeping concentrations low (20 nM for all samples). Correlation was performed using ConfoCor 2 software. For FCS data analysis, a Labview routine was implemented.

TIRFM

TIRFM is a suitable technique for imaging fluorescent molecules on a transparent substrate with single molecule resolution (33,34). The technique uses the evanescent field of a totally internal reflected laser beam exciting only fluorophores above the substrate surface within typically 100 nm. This provides a high signal/noise ratio of the collected fluorescence and is therefore well suited for direct imaging of fluorescent molecules.

For TIRFM measurements, rVWF was immobilized on epoxy silane-coated glass slides and imaged using the TIRFM setup presented in (35). For excitation in the total internal reflection mode, a 473 nm laser (iBeam smart, TOPTICA, Gräfelfing, Germany) was used at a power of 0.4 mW. The corresponding filter set consisted of a Chroma z 470/10, a Chroma z 470 RDC, and a Chroma HQ 525/50 (Chroma Technology GmbH, Olching, Germany). The emitted light signal was detected by a back-illuminated EMCCD camera (DU-860D, Andor, Belfast, Ireland). The EMCCD chip was operated at a temperature of −90°C and the electron multiplication gain was set to 300-fold. 3000 frames (21 × 21 μm^2) were taken per image sequence with a recording rate of 10 frames/s. All measurements were carried out in phosphate buffered saline. To minimize eGFP bleaching before the actual measurement, all adjustment procedures were carried out at low laser power (0.1 mW).

Data analysis was obtained with a step detection algorithm. As the routine cannot distinguish between on- and off-steps and fails in detecting steps that occur within a very short time slot, the obtained step number was corrected by eye for blinking and missed steps.

Proteolysis of full-length rVWF by ADAMTS13

Cleavage of recombinant VWF-eGFP by ADAMTS13 was achieved as reported in Pruss et al. (36). Cleaved samples were stored at −80°C until multimer analysis was performed.

RESULTS

Quantitative gel analysis of rVWF

Gel analysis is the most frequently used technique for VWF multimer analysis (22,23,36). By quantitative analysis of the intensity profiles obtained by antibody staining in gels (Fig. 2, *A*,*B* and *C*,*D*, respectively) we yield the size distribution of VWF, which in a semilogarithmic plot shows good agreement with an exponential (Fig. 2, *E* and *F*). Hereby we assume that antibody staining is proportional to the number of dimers in the VWF multimer. The gels were evaluated using luminescent immunoblotting implying that the measured luminescent signal intensities in each band reflect the number of antibody labels (Fig. 2, *C* and *D*). The signal was normalized by the number of dimers i corresponding to the size of the multimers in the respective band. These normalized intensities correspond to the molar distribution function and were plotted in a semilogarithmic diagram versus the multimer size given in number of dimers i (Fig. 2, *E* and *F*). We took gel data from both wild-type rVWF and rVWF-IIC and their eGFP fusion analogs (Fig. 2 *A*) as well as from VWF of normal plasma VWF-NP and patient plasma VWF-IIC (Fig. 2 *B*). For rVWF, clearly an exponential decay is found. One possible mechanistic explanation for such an exponential decay is the Flory theory of linear condensation polymers (8) that describes a step-growth polymerization process taking place in an enclosed reactor by the intermolecular reaction of bifunctional compounds (for details, see the Supporting Material). It predicts an exponential size distribution for step-growth polymerization resulting in a molar fraction of i-mers containing i subunits (8)

$$\frac{N_i}{N} = (1-p)p^{i-1}. \quad (1)$$

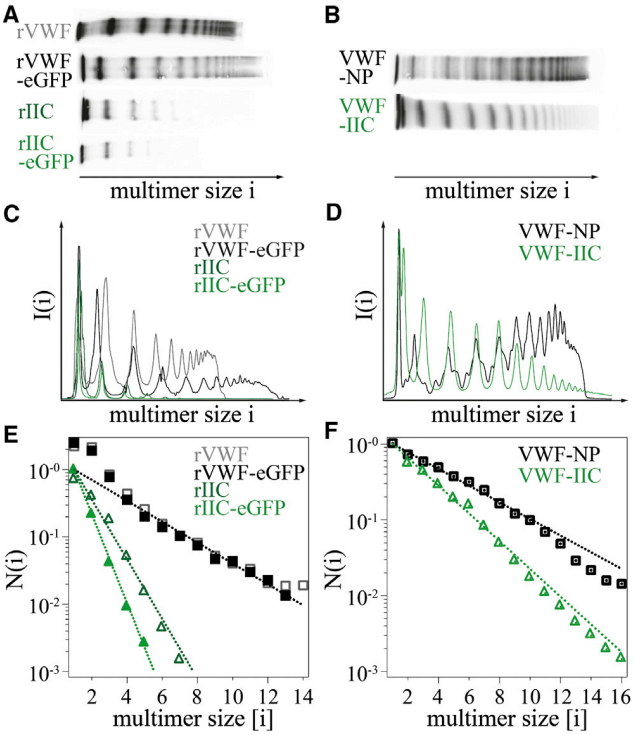

FIGURE 2 Quantitative gel analysis of recombinant and blood plasma VWF. (*A*) Multimer patterns of recombinant VWF distributions showing a ladder of multimers. (*B*) Multimer patterns of VWF distribution of normal plasma and of a patient with von Willebrand disease type IIC. (*C* and *D*) Densitogram intensity is plotted versus multimer size in terms of dimer number *i*. (*E*) Fits of normalized data show no significant difference in size distribution between rVWF (*gray squares*) and fluorescent rVWF-eGFP (*black squares*), stressing that the recombinant distribution with fused eGFP exhibits a normal multimerization behavior. Best fits to the gel data are obtained using an exponential function $N(i) = N_1 p^{i-1}$ with an extent of polymerization of $p = 0.70$ (*black dotted line*). For pathological rVWF-IIC (*green triangles*), a reduced extent of polymerization of $p = 0.36$ (*dark green dotted line*) for rVWF-IIC and $p = 0.22$ (*green dotted line*) for rVWF-IIC-eGFP is obtained. (*F*) Both plasma samples show likewise an exponential decay with a decreased $p = 0.66$ for pathological VWF-IIC (VWF-NP: $p = 0.78$). We observe a small, systematic deviation for large multimer sizes due to enzymatic cleavage in the plasma.

Here, N_i and N represent the number of i-mers and the total number of VWF molecules, respectively. p indicates the extent of polymerization, i.e., the number of polymerized subunits to the total number of subunits, N. We assume that VWF multimerization complies with the step-growth polymerization model insofar as the formation of disulfide bonds can be assumed to be independent of size and the reaction volume is finite, which is a reasonable assumption considering the fact that multimerization occurs in the Golgi Apparatus only. Fitting the measured size distribution by the exponential function $N(i) = N_1 p^{i-1}$ yields an extent of polymerization of $p = 0.70 \pm 0.02$ for rVWF. N_1 is a constant fitting parameter that contains information about the number of dimers available for polymerization (for details, see the Supporting Material). p describes the slope of the size distribution: high values of p indicate a slowly decaying size distribution with long multimers being more abundant, whereas small values of p indicate a steep decay with only a small amount of long multimers. The same exponential decay as for rVWF is found for rVWF-eGFP (*black squares*), showing that the shape of the distribution does not change significantly when fusing eGFP to VWF. The recombinant VWF-eGFP construct is therefore well suited for further studies employing fluorescence microscopy. The pathological rVWF-IIC appears only in a few bands of short sizes due to its lack of large multimers. Fitting yields an exponential, as for physiological VWF, yet with an extent of polymerization $p = 0.36 \pm 0.01$ for rVWF-IIC (*dark green*) and $p = 0.22 \pm 0.01$ for rVWF-IIC-eGFP (*green*).

Physiological VWF derived from blood samples also exhibits an exponential decrease (Fig. 2 *F*) with an extent of polymerization $p = 0.78 \pm 0.02$ for normal patients. However, the distribution function seems to exhibit a slight, but systematic deviation underrepresenting the larger fraction. This deviation can be attributed to ADAMTS13-induced cleavage that occurs in plasma and is depicted in the gels by the two satellite bands flanking the main bands that are known to be the products of proteolysis. Pathological VWF-IIC from plasma of patients suffering from von Willebrand disease type IIC shows an extent of polymerization $p = 0.66 \pm 0.01$.

FCS single-component analysis of rVWF

FCS allows for size measurements of fluorescently labeled VWF in solution and is in principle capable to resolve multiple species with varying diffusion properties. We find that the measured FCS autocorrelation functions of recombinant VWF-eGFP are consistent with an exponential size distribution. First, we investigate recombinant VWF-eGFP (rVWF) monomer and dimer. A single-component analysis provides diffusion times (diffusion coefficients) of $\tau_D = 322\ \mu s$ ($D = 31.9\ \mu m^2/s$) for the monomer and $\tau_D = 447\ \mu s$ ($D = 19.5\ \mu m^2/s$) for the dimer (Fig. 3 *A*). Fig. 3 *A* also shows purified eGFP as a control. The eGFP diffusion time of $\tau_D = 90\ \mu s$ is in agreement with previous results (37). Because VWF is a rather elongated protein (11) a crude approximation of the VWF monomer and the VWF dimer as cylinders with the same diameter and twice the length for the dimer is reasonable. With these assumptions, the measured diffusion coefficients correspond to a cylinder 3 nm in diameter and 85.3 nm (*dimer*) and 42.7 nm (*monomer*) in length (for details, see the Supporting Material). This is in accordance with experiments performed by tapping mode atomic force microscopy (38) and electron microscopy measurements (11).

The single-component analysis can also be used as a first approximation of the full VWF distribution. Because it averages over all the species within the sample, it cannot

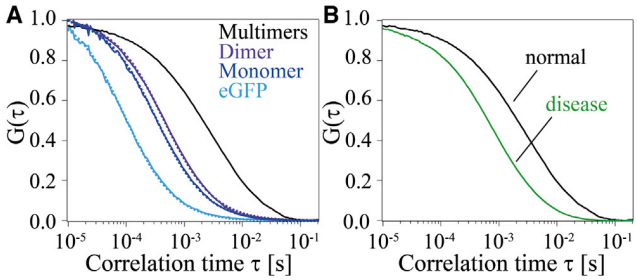

FIGURE 3 FCS measurements of recombinant VWF distributions and their building blocks. (*A*) Single-component fits of eGFP (*light blue*), rVWF monomer (*dark blue*), and rVWF dimer (*purple*) give correlation times τ_D of 90 μs, 322 μs, and 447 μs. Assuming a cylindrical shape for the dimer, the corresponding diffusion coefficient D = 19.5 $\mu m^2/s$ characterizes a cylinder with length l = 85.3 nm and d = 3 nm. A clear shift toward longer diffusion times can be seen for the multimer distribution rVWF (*black*). (*B*) Single-component analysis was used as a first estimate of the autocorrelation function of physiological rVWF (*black*). A clear shift can be seen for pathological rVWF-IIC (*green*) that allows distinguishing between normal and abnormal conditions. Average diffusion times of τ_D = 2244 ± 515 μs (rVWF) and τ_D = 712 ± 22 μs (rVWF-IIC) are obtained.

reflect the different species within the VWF size distribution. Thus, single-component analysis is not able to provide the actual size distribution $N(i)$. However, it provides an average VWF size and is suited to rapidly pinpoint differences between the physiological distribution of rVWF and of the pathological distribution rVWF-IIC (Fig. 3 *B*) showing an average diffusion time of τ_D = 2244 ± 515 μs (*black line*) for physiological and τ_D = 712 ± 22 μs (*green line*) for pathological rVWF. For rVWF, the diffusion time is in good agreement with measurements performed by Torres et al. (39) who detected an average diffusion time of 2.0–3.5 ms for VWF-NP bound to fluorescently labeled antibodies. For rVWF-IIC, the lack of large multimers explains the shift to shorter diffusion times in our measurements. Although this single-component analysis does not contain quantitative information about the size distribution of VWF, it is clearly sufficient to distinguish between the physiological and the investigated pathological VWF distribution (Fig. 3 *B*).

FCS multicomponent analysis of rVWF

To examine the nature of the VWF size distribution a multimer analysis was applied (Fig. 4) and found to be consistent with the exponential size distribution measured with quantitative gel analysis. The multimer analysis allows to compare the autocorrelation function expected for a given size distribution $N(i)$ with the experimental autocorrelation curve (see the Supporting Material, S1). Several distribution functions were tested for $N(i)$. Best results are achieved using an exponential function $N(i) = N_1 p^{i-1}$ in agreement with the data obtained with quantitative gel analysis. The base is found to be p = 0.64 for physiological rVWF (Fig. 4 *A*) and p = 0.18 for pathological rVWF-IIC (Fig. 4 *B*).

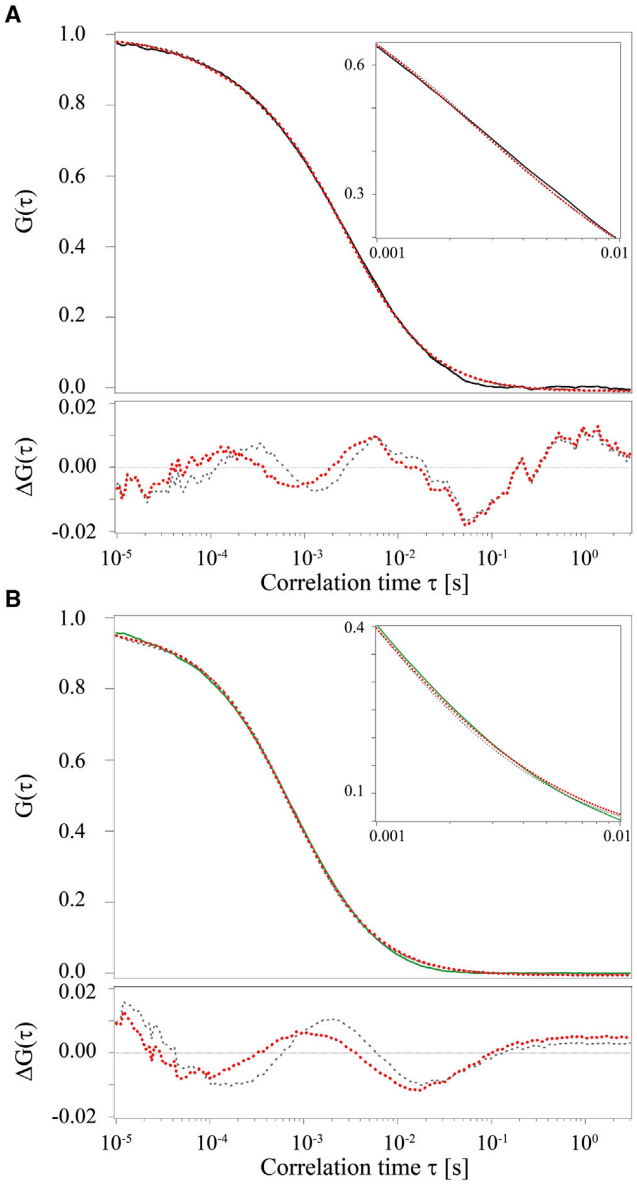

FIGURE 4 Multimer analysis of rVWF using FCS. (*A*) Multicomponent fit (*red dotted line*) of the autocorrelation function of physiological rVWF (*black line*) leads to a size distribution that decays with the base p = 0.64. Furthermore, the single-component analysis (*gray dashed line*) fits the distribution well, yielding an average multimer size of $\bar{i}$ = 6.3 ± 1.4 dimers. (*B*) With the multicomponent fit (*red dotted line*) for the pathological distribution rVWF-IIC (*green line*), the base is determined to be p = 0.18, indicating the lack of large VWF multimers. Single-component fit (*gray dashed line*) infers an average multimer size of $\bar{i}$ = 2.0 ± 0.1 dimers.

The best fit to the exponential distribution shows a small improvement over the initial single component analysis (Fig. 4). The fact that the multicomponent analysis is close to a single component fit is explained by the fact that the FCS autocorrelation function weights each molecule with its squared brightness (see the Supporting Material). For rVWF-eGFP the brightness scales with the number of dimers i, the resulting weighted size distribution

is $N'(i) = i^2\,N(i)$, which exhibits a sharp maximum at the average multimer size $\bar{i} = 4.7$. Due to the narrow weighted distribution function, the multicomponent fit appears to be close to the fit of a single species. The average multimer size is in good agreement with the average multimer size obtained with single-component analysis that yields $\bar{i} = 6.3 \pm 1.3$ for rVWF (for details see the Supporting Material S1). For the mutant rVWF-IIC with $p = 0.18$, an average multimer size of $\bar{i} = 1.5$ is calculated compared to $\bar{i} = 2.0 \pm 0.1$ measured with the single-component fit. However, it is important to note that the proper multicomponent analysis using the proposed exponential size distribution $N(i)$ describes the measured autocorrelation function the best within the experimental accuracy.

Direct imaging of VWF with TIRFM

The data presented so far reveals an exponential size distribution of VWF. Using TIRFM, we confirmed these results by direct imaging. Under continuous excitation, the fluorescence signal of rVWF-eGFP was observed to decrease in discrete steps over time. As described in (40) and explained in detail in the Supporting Material S3, the number of bleaching steps can be taken as a measure for the number of eGFP-tagged VWF monomers. Counting bleaching steps therefore provides a means for analyzing the VWF size distribution. Measurements of an rVWF dimer sample proved that this analysis method is indeed suitable for our samples (see the Supporting Material S3).

For localizing the rVWF multimers, an average image of the first 100 frames was calculated (Fig. 5 *A*) and regions of interest were selected. Bleaching steps in the intensity-time traces of these regions were identified with the step detection algorithm described in (41) (Fig. 5, *B* and *C*). The relative frequency for detecting a certain number of steps was plotted versus the number of steps (Fig. 5 *D*) and each step number was assigned to a certain multimer size. As we count the multimer size in number of dimers i but the bleaching steps scale with the number of monomers, two bleaching steps add up to an increase of one in the multimer size. Odd numbers of bleaching steps were round up to the next even number. The thereby obtained size distribution N(i) was plotted versus the multimer size in number of dimers i. Fitting yields an exponentially decaying size distribution $N(i) = N_1 p^{i-1}$ with a base $p = 0.29$ (Fig. 5 *D*), convincingly confirming the findings from quantitative gel analysis and FCS.

Effect of ADAMTS13 cleavage on VWF size distribution

The VWF size distribution is after secretion into the blood plasma dynamically controlled by the protease ADAMTS13 (Fig. 1 *D*) with defects in ADAMTS13 activity resulting in unusually large VWF that cause thrombotic thrombocytopenic purpura. We investigated this time-dependent evolution of the VWF size distribution with FCS and found systematic shifts to smaller multimer sizes that are no longer exponentially distributed. Various concentrations of ADAMTS13 were used to visualize different cleavage states. rVWF concentrated to 65% of normal plasma concentration (0.65 units/ml) was digested by 0.12, 0.25, and 1.00 units/ml ADAMTS13. As expected, the cleavage due to ADAMTS13 shifts the autocorrelation curves to higher particle numbers (lower amplitude) and shorter diffusion times (*steeper decay*). It is not possible to describe these autocorrelation curves with a multicomponent analysis with an exponentially decaying size distribution $N(i)$, indicating that the cleavage changes the shape of the distribution. Yet, using single-component analysis it is possible to extract average diffusion times of $\tau_D = 1045\ \mu s$, $813\ \mu s$, and $617\ \mu s$ (0.12, 0.25 and 1.00 units/ml ADAMTS13) (Fig. 6 *A*). We find an exponential dependence of the average multimer size in terms of dimer number i on the

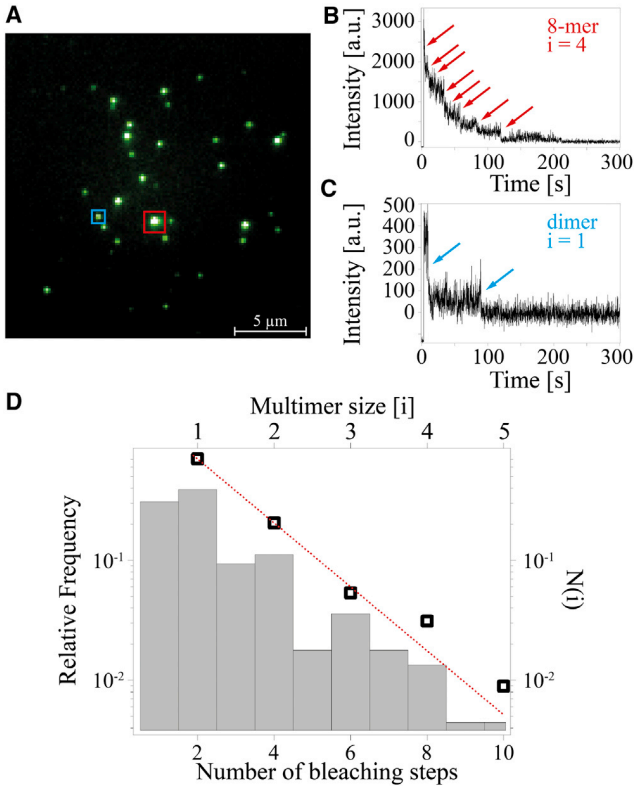

FIGURE 5 Direct imaging of rVWF using TIRFM. (*A*) TIRFM image of VWF multimers immobilized on a glass surface. The multimer size is determined by counting eGFP bleaching steps as each rVWF monomer is labeled with one eGFP. The intensity-time traces of the two highlighted molecules represent an 8-mer (*B*) and a dimer (*C*). The positions of the counted steps are indicated with arrows. (*D*) The relative frequency for detecting a certain number of steps in the intensity trace is shown as a bar chart. Size distribution analysis of $N(i)$ (*black squares*) yields, in good agreement with the results from quantitative gel analysis and FCS, an exponentially decaying size distribution $N(i) = N_1 p^{i-1}$ (*red dots*) with the base $p = 0.29$.

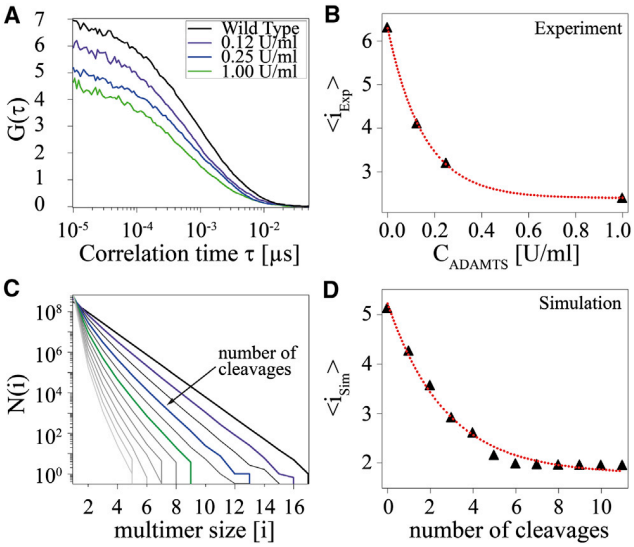

FIGURE 6 Multimer analysis after ADAMTS13-induced proteolytic cleavage. (*A*) Varying concentrations of ADAMTS13 are used to visualize different cleavage states. Correlation curves of rVWF distribution are shifted toward lower correlation times and higher particle concentrations (*lower* G(0)) with increasing protease concentration. (*B*) Single-component analysis indicates an exponential decay of the average multimer sizes with increasing ADAMTS13 concentration. (*C*) Simulation of a random cleavage process shows the changes in the size distribution due to ADAMTS13 cleavage. (*D*) Average multimer sizes decrease exponentially with an increasing number of cleavage steps per molecule. Comparing the decay constant in (*B*) and (*D*), ~0.1 units/ml ADAMTS13 and one cleavage step per molecule lead to a similar effect on the average multimer size.

ADAMTS13 concentration with $\bar{i} = 4.5$, 2.6, and 1.2, corresponding to 0.12, 0.25, and 1.00 units/ml concentration of ADAMTS13 (Fig. 6 *B*).

To get an estimate of the size distribution in the presence of ADAMTS13, the cleavage process was simulated based on a model that assumes random cleavage sites combined with equal cleavage probability for all multimer sizes (Fig. 6 *C*). Starting with the measured exponentially shaped multimer distribution, each iteration cuts each multimer once at a random site. For each iteration, the average multimer size of the generated size distribution is calculated and plotted against the number of cleavage steps (Fig. 6 *D*). Comparison of experiment and simulation (Fig. 6, *C* and *D*), shows that the average multimer size scales exponentially with the number of cleavages of each molecule, with ~0.1 units/ml ADAMTS13 and one cleavage step resulting in the same average multimer size. This means that a 0.1 units/ml ADAMTS13 concentration is necessary to cleave each molecule of a 0.65 units/ml VWF concentration once within 5 h.

DISCUSSION

In this article, we found independent evidence that the size of recombinant VWF is exponentially distributed. First quantitative gel analysis of VWF based on antibody staining indicates an exponential size distribution, second a FCS multicomponent analysis of recombinant VWF-eGFP proves consistent with the proposed distribution function, and finally the frequency distribution obtained from direct single molecule fluorescence imaging yields an exponential dependence for the first five VWF-eGFP multimer sizes. An exponential size distribution as such is not unexpected and well known for both equilibrium polymers (42) and linear condensation polymers (8). An equilibrium polymer forms by reversible association of subunits with mutual binding constant affinity. Prominent examples for equilibrium polymers are actin, microtubulin, and other cytoskeleton filaments (43). Linear condensation polymers are formed by irreversible growth mechanisms. It is well established that VWF is a covalently linked multimer as the VWF multimerization occurs via formation of disulfide bonds. Furthermore, it is understood that the VWF multimerization takes place in the Golgi, where the propeptide of VWF itself acts as oxidoreductase, thereby facilitating disulfide bond formation that allows VWF to polymerize in this compartment (12–14). An exponential size distribution results if the reactivity of subunits is independent of the segment size and takes place in a finite compartment. In this case, the molar fraction of segments containing i subunits is given by Eq. 1. The distribution is fully determined by a single parameter, the extent of polymerization, p. This extent of polymerization is limited both by the reaction rate of the VWF molecules to each other and by the reaction time, which is determined by the time the VWF remains in the Golgi. We find that the fraction of polymerized dimers is $p_{rVWF} = 0.70 \pm 0.02$ for rVWF and $p_{rVWF\text{-}IIC} = 0.22 \pm 0.01$ in case of the pathological form rVWF-IIC. It is noteworthy that for the disease mutant VWF-IIC, the exponentially decaying size distribution is maintained indicating that the mechanism of biosynthesis is the same. As aberrances in the size distribution of VWF-IIC are caused by mutations in the VWF propeptide that prevent multimerization in the Golgi (44), a decreased reaction rate can be assumed and explains the lower extent of polymerization.

The fact that the exponential VWF size distribution is in accordance with a step-growth reaction mechanism allows the quantification of a VWF distribution by a single parameter. Knowing the extent of polymerization p yields the entire range of multimers. An interesting finding is the fact that the extent of polymerization is in general fairly low with far less long multimers being formed than hitherto expected. For the physiological distribution rVWF, 30% of VWF dimers remain as non-polymeric species. Multimers consisting of five or more dimers account for only 24% of the total number of VWF molecules whereas multimers containing 10 or more dimers represent just 4%. Hence, the polymeric form of VWF that is supposed to be the one most relevant for VWF function is a minority species of VWF. Secondly, as characteristic for the base of an

exponential function, already small changes in p have a strong leverage on the multimer distribution and consequently a detrimental impact on the physiological state. A loss of 25% in the extent of polymerization reduces the number of 10mers by a factor of 100.

The size distribution of VWF is changed upon secretion to the blood plasma by ADAMTS13-induced cleavage. We used rVWF to mimic this cleavage process. Varied cleavage states represented by different concentrations of ADAMTS13 can be clearly distinguished from uncleaved rVWF. The exponentially shaped size distribution is not maintained during cleavage. Simulation of a random cleavage process allows us to relate the ADAMTS13 concentration to a certain number of cleavage steps. We show that cleavage with 0.1 units/ml ADAMTS13 concentration under partly denaturing condition in urea has the same effect on the average multimer size as cutting each VWF molecule once at a random site. In blood plasma, ADAMTS13-induced cleavage is assumed to require shear-induced stretching of VWF. We find that the size distribution of healthy patients exhibits almost the same exponential size dependence as recombinantly expressed VWF. Small deviations at larger size fractions could be indicative of extracellular ADAMTS13 activity in blood flow. Interestingly, the size distribution of patients exhibiting von Willebrand disease type IIC showed less deviation from the normal case as predicted from the recombinant expressed VWF-IIC. It must be assumed that the deficiency in the extent of polymerization is partly compensated, possibly by VWF expelled from Weibel-Palade bodies. Plasma VWF is essential for the initiation of blood coagulation but is immediately joined by VWF stored in the granules of endothelium cells (Weibel-Palade bodies) at the beginning of hemostasis so that long VWF multimers can be provided whenever needed.

From a measurement technique point of view, we showed that FCS is capable of following the evolution of VWF size distribution under blood plasma conditions. This opens up the possibility to use recombinant VWF-eGFP in combination with FCS as a diagnostic assay for ADAMTS13 activity in hematology. Moreover, FCS has the capability to use shear forces during measurement. Therefore, experiments with urea as a stretcher could become redundant and be replaced by measurements under shear flow in situ.

CONCLUSION

In this work, we reported on the exponential size distribution of recombinant and physiological VWF multimers. We found evidence that the exponential distribution is the generic outcome of VWF biosynthesis as disease-related VWF mutant VWF-IIC also exhibits an exponential size distribution, albeit with a smaller extent of polymerization. In light of this finding, we hypothesize that the disease-related mutation type IIC affects the polymerization reaction. We show that FCS allows for monitoring the change in VWF-eGFP size distribution under blood plasma conditions over time. In particular, ADAMTS13 activity was measured and it was shown that the decreasing average VWF size is in agreement with the expected evolution of an exponential distribution under random cleavage. We believe that the extent of polymerization, describing the size distribution of VWF, provides a valuable indicator in VWF-related disease diagnostics and that FCS proves valuable as a quantitative tool to follow the evolution of VWF size distribution in vitro over time.

SUPPORTING MATERIAL

Two figures, supporting analysis, and references (45,46) are available at http://www.biophysj.org/biophysj/supplemental/S0006-3495(13)00859-X.

We thank Hanna Engelke for fruitful discussions and reading the manuscript. Mathias Strackharn and Stephan Heucke are gratefully acknowledged for their support with the TIRFM setup.

This work was supported with seed funds from the Center for NanoScience and the priority network within the Deutsche Forschungsgemeinschaft SHENC (Shear Flow Regulation of Hemostasis - bridging the gap between Nanomechanics and Clinical presentation), DFG research unit FOR 1543. We thank all SHENC members, especially Maria A. Brehm. S.L. thanks the support by the Elite Network of Bavaria.

REFERENCES

1. Sadler, J. E. 1998. Biochemistry and genetics of von Willebrand factor. *Annu. Rev. Biochem.* 67:395–424.
2. Ruggeri, Z. M. 2001. Structure of von Willebrand factor and its function in platelet adhesion and thrombus formation. *Best Pract. Res. Clin. Haematol.* 14:257–279.
3. Ruggeri, Z. M. 1997. von Willebrand factor. *J. Clin. Invest.* 99:559–564.
4. Furlan, M., R. Robles, and B. Lämmle. 1996. Partial purification and characterization of a protease from human plasma cleaving von Willebrand factor to fragments produced by in vivo proteolysis. *Blood.* 87:4223–4234.
5. Siedlecki, C. A., B. J. Lestini, …, R. E. Marchant. 1996. Shear-dependent changes in the three-dimensional structure of human von Willebrand factor. *Blood.* 88:2939–2950.
6. Schneider, S. W., S. Nuschele, …, M. F. Schneider. 2007. Shear-induced unfolding triggers adhesion of von Willebrand factor fibers. *Proc. Natl. Acad. Sci. USA.* 104:7899–7903.
7. Zhang, X., K. Halvorsen, …, T. A. Springer. 2009. Mechanoenzymatic cleavage of the ultralarge vascular protein von Willebrand factor. *Science.* 324:1330–1334.
8. Flory, P. J. 1936. Molecular size distribution in linear condensation polymers. *J. Am. Chem. Soc.* 58:1877–1885.
9. Wagner, D. D. 1990. Cell biology of von Willebrand factor. *Annu. Rev. Cell Biol.* 6:217–246.
10. Singh, I., H. Shankaran, …, S. Neelamegham. 2006. Solution structure of human von Willebrand factor studied using small angle neutron scattering. *J. Biol. Chem.* 281:38266–38275.
11. Springer, T. A. 2011. Biology and physics of von Willebrand factor concatamers. *J. Thromb. Haemost.* 9 (*Suppl 1*):130–143.
12. Wise, R. J., D. D. Pittman, …, S. H. Orkin. 1988. The propeptide of von Willebrand factor independently mediates the assembly of von Willebrand multimers. *Cell.* 52:229–236.

13. Purvis, A. R., and J. E. Sadler. 2004. A covalent oxidoreductase intermediate in propeptide-dependent von Willebrand factor multimerization. *J. Biol. Chem.* 279:49982–49988.

14. Dang, L. T., A. R. Purvis, …, J. E. Sadler. 2011. Phylogenetic and functional analysis of histidine residues essential for pH-dependent multimerization of von Willebrand factor. *J. Biol. Chem.* 286:25763–25769.

15. McCarroll, D. R., E. G. Levin, and R. R. Montgomery. 1985. Endothelial cell synthesis of von Willebrand antigen II, von Willebrand factor, and von Willebrand factor/von Willebrand antigen II complex. *J. Clin. Invest.* 75:1089–1095.

16. Fay, P. J., Y. Kawai, …, V. J. Marder. 1986. Propolypeptide of von Willebrand factor circulates in blood and is identical to von Willebrand antigen II. *Science.* 232:995–998.

17. de Wit, T. R., and J. A. van Mourik. 2001. Biosynthesis, processing and secretion of von Willebrand factor: biological implications. *Best Pract. Res. Clin. Haematol.* 14:241–255.

18. Tsai, H. M. 1996. Physiologic cleavage of von Willebrand factor by a plasma protease is dependent on its conformation and requires calcium ion. *Blood.* 87:4235–4244.

19. Gaucher, C., J. Diéval, and C. Mazurier. 1994. Characterization of von Willebrand factor gene defects in two unrelated patients with type IIC von Willebrand disease. *Blood.* 84:1024–1030.

20. Schneppenheim, R., K. B. Thomas, …, B. Zieger. 1995. Identification of a candidate missense mutation in a family with von Willebrand disease type IIC. *Hum. Genet.* 95:681–686.

21. Schneppenheim, R., J. J. Michiels, …, U. Budde. 2010. A cluster of mutations in the D3 domain of von Willebrand factor correlates with a distinct subgroup of von Willebrand disease: type 2A/IIE. *Blood.* 115:4894–4901.

22. Schneppenheim, R., H. Plendl, and U. Budde. 1988. Luminography—an alternative assay for detection of von Willebrand factor multimers. *Thromb. Haemost.* 60:133–136.

23. Budde, U., R. Schneppenheim, …, I. Peake. 2008. Detailed von Willebrand factor multimer analysis in patients with von Willebrand disease in the European study, molecular and clinical markers for the diagnosis and management of type 1 von Willebrand disease (MCMDM-1VWD). *J. Thromb. Haemost.* 6:762–771.

24. Magde, D., E. Elson, and W. W. Webb. 1972. Thermodynamic fluctuations in a reacting system-measurement by fluorescence correlation spectroscopy. *Phys. Rev. Lett.* 29:705–708.

25. Elson, E. L., and D. Magde. 1974. Fluorescence correlation spectroscopy. I. Conceptual basis and theory. *Biopolymers.* 13:1–27.

26. Magde, D., E. L. Elson, and W. W. Webb. 1974. Fluorescence correlation spectroscopy. II. An experimental realization. *Biopolymers.* 13:29–61.

27. Rigler, R., Ü. Mets, …, P. Kask. 1993. Fluorescence correlation spectroscopy with high count rate and low background: analysis of translational diffusion. *Eur. Biophys. J.* 22:169–175.

28. Petrov, E. P., and P. Schwille. 2008. State of the art and novel trends in fluorescence correlation spectroscopy. *In* Standardization and Quality Assurance in Fluorescence Measurements II. U. Resch-Grenger, editor. Springer, pp. 145–197.

29. Thompson, N. L. 1991. Fluorescence correlation spectroscopy. *In* Topics in Fluorescence Spectroscopy, Vol. 1. J. R. Lakowicz, editor. Plenum Press, New York, pp. 337–378.

30. Engelke, H., I. Dorn, and J. O. Rädler. 2009. Diffusion and molecular binding in crowded vesicle solutions measured by fluorescence correlation spectroscopy. *Soft Matter.* 5:4283–4289.

31. Zanardelli, S., A. C. K. Chion, …, D. A. Lane. 2009. A novel binding site for ADAMTS13 constitutively exposed on the surface of globular VWF. *Blood.* 114:2819–2828.

32. Alkaabi, K. M., A. Yafea, and S. S. Ashraf. 2005. Effect of pH on thermal- and chemical-induced denaturation of GFP. *Appl. Biochem. Biotechnol.* 126:149–156.

33. Axelrod, D. 1981. Cell-substrate contacts illuminated by total internal reflection fluorescence. *J. Cell Biol.* 89:141–145.

34. Kufer, S. K., M. Strackharn, …, H. E. Gaub. 2009. Optically monitoring the mechanical assembly of single molecules. *Nat. Nanotechnol.* 4:45–49.

35. Gumpp, H., S. W. Stahl, …, H. E. Gaub. 2009. Ultrastable combined atomic force and total internal fluorescence microscope. *Rev. Sci. Instrum.* 80:063704–063705.

36. Pruss, C. M., C. R. P. Notley, …, D. Lillicrap. 2008. ADAMTS13 cleavage efficiency is altered by mutagenic and, to a lesser extent, polymorphic sequence changes in the A1 and A2 domains of von Willebrand factor. *Br. J. Haematol.* 143:552–558.

37. Petrásek, Z., and P. Schwille. 2008. Precise measurement of diffusion coefficients using scanning fluorescence correlation spectroscopy. *Biophys. J.* 94:1437–1448.

38. Seyfried, B. K., G. Friedbacher, …, P. L. Turecek. 2010. Comparison of plasma-derived and recombinant von Willebrand factor by atomic force microscopy. *Thromb. Haemost.* 104:523–530.

39. Torres, R., J. R. Genzen, and M. J. Levene. 2012. Clinical measurement of von Willebrand factor by fluorescence correlation spectroscopy. *Clin. Chem.* 58:1010–1018.

40. Ulbrich, M. H., and E. Y. Isacoff. 2007. Subunit counting in membrane-bound proteins. *Nat. Methods.* 4:319–321.

41. Opfer, J., and K.-E. Gottschalk. 2012. Identifying discrete states of a biological system using a novel step detection algorithm. *PLoS ONE.* 7:e45896.

42. Hill, T. L. 1987. Linear aggregation theory in cell biology. Springer-Verlag, New York.

43. Howard, J. 2001. Mechanics of motor proteins and the cytoskeleton. Sinauer Associates, Sunderland, MA.

44. Sadler, J. E., U. Budde, …, A. B. Federici; Working Party on von Willebrand Disease Classification. 2006. Update on the pathophysiology and classification of von Willebrand disease: a report of the Subcommittee on von Willebrand Factor. *J. Thromb. Haemost.* 4:2103–2114.

45. Rouse, Jr., P. E. 1953. A theory of the linear viscoelastic properties of dilute solutions of coiling polymers. *J. Chem. Phys.* 21:1272–1280.

46. Inoué, S., O. Shimomura, …, P. T. Tran. 2002. Fluorescence polarization of green fluorescence protein. *Proc. Natl. Acad. Sci. USA.* 99:4272–4277.

5 Shear-Induced Cleavage of VWF

In this chapter, a study on full-length VWF cleavage under shear flow is presented. Due to the size dependent functionality of VWF, its degradation by the metalloprotease ADAMTS13 is a determining factor in hemostasis. ADAMTS13 cleaves VWF within the mechanosensitive A2 domain, which is believed to open under shear flow. Quantifying the effect of shear is essential in order to enable predictions of hemostatic dysfunctions of mutant VWF. Therefore, the interrelation of shear-flow, VWF unfolding, opening of the mechanosensitive A2 domain, and ADAMTS13 activity is currently a highly debated topic. Yet, the enzymatic activity of ADAMTS13 on full-length VWF had not been measured under flow conditions.

Here, FCS was used in combination with a custom-built microfluidic shear cell to investigate ADAMTS13-mediated cleavage of full-length VWF as a function of shear rate. This novel approach allowed, for the first time, to quantify the effects of shear on the kinetics of VWF cleavage in blood plasma. The presented measurements reveal a remarkable Hill-type behavior with a sigmoidal increase in activity with increasing shear. The data are in good agreement with Brownian hydrodynamics simulations of shear-dependent polymer unfolding, which were performed by the group of Prof. Netz. Besides, a strong increase in ADAMTS13 activity under blood plasma conditions was observed, suggesting the involvement of hitherto unknown accessory factors in the blood plasma. This study combined a novel biophysical methodology with theoretical simulations and clinically relevant VWF mutations to quantify VWF cleavage. In addition, the findings represent a significant contribution to the general understanding of shear-induced unfolding of multimeric proteins, with important implications for ADAMTS13 and VWF-related hemostatic dysfunctions.

The experimental data and the resulting conclusions are presented in the following manuscript:

S. Lippok, M. Radtke, T. Obser, L. Kleemeier, R. Schneppenheim, R.R. Netz, J.O. Rädler. ”Shear dependency of ADAMTS13-mediated cleavage measured on full-length VWF under blood plasma conditions.” *PNAS, under review*

Shear dependency of ADAMTS13-mediated cleavage measured on full-length VWF under blood plasma conditions

Svenja Lippok[a], Matthias Radtke[b], Tobias Obser[c], Lars Kleemeier[a], Reinhard Schneppenheim[c], Roland R. Netz[b], and Joachim O. Rädler[a,1]

[a] Faculty of Physics and Center for NanoScience, Ludwig Maximilian University, 80539 Munich, Germany

[b] Department of Physics, Freie Universität Berlin, 14195 Berlin, Germany

[c] Department of Pediatric Hematology and Oncology, University Medical Center Hamburg-Eppendorf, 20246 Hamburg, Germany

[1] Corresponding author: phone: +49 89 2180 2438, email: raedler@lmu.de

Short Title: Shear dependency of ADAMTS13-mediated cleavage

Classification

BIOLOGICAL SCIENCE: Biophysics and Computational Biology

Keywords: mechanosensitive proteins, polymer physics, enzyme kinetics, hemostasis, thrombotic microangiopathies

ABSTRACT

Proteolysis of the multimeric hemostatic protein von Willebrand Factor (VWF) by ADAMTS13 is crucial for prevention of microvascular thrombosis. ADAMTS13 cleaves VWF within the mechanosensitive A2 domain, which is believed to open under shear flow. Yet, the enzymatic activity of ADAMTS13 on full-length VWF has not been measured under flow conditions. Here, we combine Fluorescence Correlation Spectroscopy (FCS) and a microfluidic shear cell to monitor real-time kinetics of full-length VWF proteolysis as a function of shear stress. Without shear, ADAMTS13 cleaves wild-type VWF with Michaelis-Menten type activity ($K_M = 171 \pm 85$ nM) only under partially denaturing conditions (1.5 M urea), while cleavage of the pathological mutant VWF-G1629E occurs in the absence of denaturants. Under shear, ADAMTS13 activity on wild-type VWF exhibits a sigmoidal increase with half-maximum shear rate $\dot{\gamma}_{1/2} = 5360$/s and cooperativeness coefficient n = 5. Brownian hydrodynamics simulations quantitatively reproduce the observed shear dependence in terms of the shear-induced tension profile along VWF multimers. Experiments under physiological conditions show five-fold increased cleavage rates in comparison to buffer, while cleavage is inhibited in patient blood containing anti-ADAMTS13 antibodies. Our findings for the first time quantify the flow-rate dependence of ADAMTS13 activity in blood plasma, which, in case of mutant forms of VWF, is relevant to the prediction of hemostatic dysfunction.

SIGNIFICANCE

Mechanosensitive degradation of multimeric von Willebrand Factor (VWF) by ADAMTS13 is crucial for hemostasis. Hydrodynamic shear is thought to make its A2 domain susceptible to proteolysis. Quantification of this effect in wild-type VWF in combination with biophysical modeling is essential to enable prediction of hemostatic dysfunction of mutant VWF. We report the first characterization of full-length VWF cleavage by ADAMTS13 as a function of shear rate, including the Michaelis-Menten constants in buffer and blood plasma. The shear-dependence is rationalized by hydrodynamic modeling of shear-dependent polymer unfolding. As well as providing the first quantitative evidence for dependence of proteolysis on shear-induced opening of VWF, the work represents a methodological advance, which will facilitate future studies on VWF mutations in coagulation disorders.

INTRODUCTION

In the event of vascular injury, the multimeric plasma protein von Willebrand Factor (VWF) mediates platelet adhesion, aggregation and crosslinking to maintain hemostasis [1,2]. VWF is either constitutively secreted into the circulation or is stored in Weibel-Palade bodies and released in the form of ultralarge multimers in response to physiological and pathophysiological stimuli [3]. A carefully controlled balance of VWF binding and crosslinking, and VWF degradation and cleavage by ADAMTS13 (a disintegrin and metalloprotease with thrombospondin type 1 motif, member 13) [4-6], is required for hemostasis. Here, fluid shear stress plays a key role: It initially activates the binding of the VWF A1 domain to platelets, and regulates over time additionally VWF degradation by opening the A2 domain, exposing the cleavage site for ADAMTS13 [7,8]. Hence, force-controlled activation and cleavage of VWF is part of a feedback loop that balances hemostasis. Absence of ADAMTS13 causes the life-threatening disease thrombotic thrombocytopenic purpura (TTP), which is characterized by uncontrolled microvascular thrombosis [5,9]. ADAMTS13 may also control the size distribution of VWF in the circulation, since the effect of shear stress depends on the hydrodynamic drag and hence on the size of VWF multimers [10].

The mechanism of shear-induced unfolding of VWF has been explored in several studies in the recent past [11,12]. VWF is cleaved by breakage of the Tyr1605-Met1606 bond in its A2 domain, which is a deeply buried cleavage site [13,14]. The interaction of immobilized VWF or VWF fragments with ADAMTS13 fragments or variants has been characterized in buffer using ELISAs [7,15]. Recognition of recombinant VWF fragments by recombinant ADAMTS13 has been examined under both denaturing [16] and non-denaturing conditions [17]. In a seminal study by Zhang et al. using laser tweezers, force was applied directly to single A2 domains in buffer and the dependence of the catalytic rate on the enzyme concentration was measured [14]. Pulling at the ends of polymeric molecules results in a homogenous force profile along the polymer chain under equilibrium conditions. However, simulations of unfolding under shear flow reveal that the intramolecular forces in VWF are inhomogenous and fluctuating [18,19]. Therefore, cleavage probabilities under shear flow are expected to show a size dependence and more and less susceptible intramolecular regions may exist. In particular, ADAMTS13 is not expected to act on the full-length protein in the same fashion as on isolated fragments.

We have recently shown that Fluorescence Correlation Spectroscopy (FCS) allows one to measure the size distribution of VWF [20]. In addition, FCS can be used to monitor binding in complex fluids such as blood plasma [21] and provides information on macromolecular dynamics [22-24]. This is of particular interest for studies of VWF, since it is assumed that unidentified enhancers of ADAMTS13 activity are present in plasma, whose effects cannot be mimicked in experiments performed in buffer [25]. Moreover, since the sample size required is very small, FCS studies can easily be combined with microfluidic devices [26,27].

In this paper, we study the cleavage of VWF by ADAMTS13 under shear flow in aqueous buffer and in blood plasma. Using FCS, we detect the breakdown of VWF-eGFP by

measuring the increase in VWF number concentration. A specially designed shear cell, combined with an FCS setup, allows us to monitor the cleavage of recombinant full-length VWF-eGFP as a function of shear flow. With this approach, we analyzed VWF cleavage under denaturing conditions as a reference and the observed Michaelis Menten constant was compared with that obtained for the disease-related mutant VWF-G1629E, which is abnormally sensitive to proteolysis [17]. We showed that cleavage of rVWF under shear flow in blood plasma can be followed over time. In normal plasma, enhanced proteolytic activity was found, presumably due to hitherto unknown accessory factors. We then determined cleavage rates as a function of shear rate. In agreement with Brownian hydrodynamics simulations, the shear dependence exhibited a Hill-type sigmoidal with a half-maximum shear rate $\dot{\gamma}_{1/2} = 5360/s$ and a cooperativeness coefficient of n = 5. Theoretical modeling enabled us to calculate the degree of flow-induced polymer unfolding and extract the probability of opening of the A2 domain from the distribution of tension along the coarse-grained polymer model of VWF.

RESULTS

Cleavage of full-length rVWF follows Michaelis-Menten kinetics. In this study, we adopted a novel approach to study VWF proteolysis, based on the use of recombinant VWF-eGFP (rVWF) fusion as substrate. Each VWF monomer is thus labeled with a single eGFP unit, and therefore cleavage of the rVWF-eGFP multimers results in an increase in the number of fluorescent molecules. We monitor this increase using the amplitude of the fluorescence correlation signal, G(0), which is inversely proportional to the average particle number N in the detection volume (see Figure 1 and Supporting Information S1). To test this concept, we performed cleavage experiments in denaturing buffer that unfolds VWF (Figure 2). Figure 2A displays the decrease in G(0) with cleavage over time, which reflects an increase in the molar concentration of rVWF (C_{VWF}). The rVWF concentration increased linearly, with the cleavage rate dC_{VWF}/dt depending on the ADAMTS13 concentration used (Figure 2B). For constant amounts of ADAMTS13, the cleavage rates increased hyperbolically as a function of the VWF concentration (Figure 2C). We fitted the curves with Michaelis-Menten kinetics $dC_{VWF}/dt = v_{max}C_{VWF}/(C_{VWF}+K_M)$ imposing the constraint that the K_M value does not depend on the enzyme concentration. With this global fitting, we obtain $K_M = 171 \pm 85$ nM and $v_{max} = 358 \pm 118$ pM/min for the physiological ADAMTS13 concentration (1 µg/ml), designated here as 1 U/ml. A tenfold increase in protease concentration (10 U/ml) resulted in a doubling of the maximum cleavage rate ($v_{max} = 584 \pm 193$ pM/min). The goodness of fit for v_{max} is, however, limited, and this might explain the lower than expected increase in this parameter at the higher ADAMTS13 concentrations. Autoproteolysis of ADAMTS13 at high concentrations may also play a role.

Shear-induced rVWF cleavage. A shear cell was built that could be mounted on a microscope stage in combination with an FCS setup. We chose a Mooney-type design for the shear cell, consisting of a cylindrical container and a rotating inner cylinder with a conical tip, which generates constant shear rates throughout the sample volume of 150µl (see Figure 3A). This device allowed us to monitor enzyme activity under shear flow with shear rates up to 10.000/s. Since FCS measurements rely on diffusion, shearing and FCS data sampling had to

be run in an alternating mode: The solution was sheared and VWF cleaved for 15 min, and this was followed by a 15-min FCS detection period in the absence of shear, during which the VWF concentration was determined (Figure 3A). A typical experiment consisted of 16 such cycles. At zero shear rate, $\dot{\gamma}$ = 0/s, cleavage rates were very low, less than 2pM/min. However, higher shear rates did indeed results in increasing rVWF concentrations (Figure 3B). The full shear rate dependence was studied for cleavage of 10 nM rVWF at two different ADAMTS13 concentrations in buffer, with applied shear rates ranging from 0/s to 10.000/s (Figure 3C,D). The data show negligible enzymatic activity at low shear rates, with cleavage rates equivalent to that at zero shear, which is at the limit of resolution of the experiment. Significantly lower cleavage rates were detected for 1 U/ml ADAMTS13 compared to 10 U/ml. The increase in ADAMTS13 activity with shear could be described by an exponential $dC/dt(\dot{\gamma}) = \alpha \exp\left(\dot{\gamma}/\tilde{\dot{\gamma}}\right)$, in which case a characteristic shear rate $\tilde{\dot{\gamma}}$ = 1090 ± 44 s^{-1} is obtained (Figure 3C,D dashed lines). However, better agreement with data is found when fitting a power law $dC/dt(\dot{\gamma}) = a\dot{\gamma}^n$ with exponents n_{U1} = 2.7 and n_{U10} = 3.6 (see bold dotted lines in Figure 3C,D). At even higher shear rates, above 5000/s, a new regime appears, where FCS correlation curves detect aggregation of the VWF multimers. This process appears to be irreversible and the aggregates impede determination of reliable cleavage rates. Details of the course of aggregation, which might be due to shear-induced opening of intermolecular binding sites, are given in Supporting Information S2.

Cleavage of the mutant rVWF-G1629E. Next, we asked whether ADAMTS13 cleaves disease-related VWF mutants with altered kinetics. We studied VWF-G1629E, which carries a mutation within the A2 domain near the site cleaved by ADAMTS13, as schematically depicted in Figure 4A. The G1629E mutation is believed to keep the domain permanently unfolded [17]. In agreement with this assumption, strong ADAMTS13 activity was detected even at zero shear. In order to compare the cleavage rates with those for wild-type rVWF, we plotted the mutant data together with the ADAMTS13 activity previously measured under denaturing conditions. Strikingly, although the enzyme concentration used in the mutant case is 200-fold lower (0.05 instead of 10 U/ml), the rates are comparable (Figure 4B). This confirms that the mutant VWF is far more susceptible to proteolysis than the wild type, leading to the loss of large multimers and ultimately to the significant bleeding symptoms seen in patients with the mutation G1629E.

Hydrodynamic Computer Simulations. Our experiments show that rates of cleavage by ADAMTS13 in the regime of elevated shear rates very sensitively depend on the precise shear rate and that, in agreement with the general belief, mutations in the A2 domain can dramatically lower the shear rate at which cleavage becomes significant. In order to corroborate the concept of shear-induced opening of the A2 cleavage domain, we compared the measured shear-dependent cleavage rates with simulations of the tension profile in unfolded VWF. To this end, we modeled the VWF polymer as a chain of weakly aggregating beads connected by stiff springs and performed Brownian dynamics simulations including hydrodynamic interactions [18,28,29]. In our simulation model, spherical beads of radius a represent VWF's repeating units (dimers), which interact with a cohesive strength ε. Rescaled shear rates $\gamma\tau$ were used, with the characteristic diffusion time of a single bead being given

by $\tau=6\pi\eta a^3/kT$. Thus, the simulation results apply to arbitrary values of radius and viscosity. In order to obtain physical units, we chose to set a=45nm and $\eta=1.2\text{x}10^{-3}$ Pas. The remaining free parameter is the cohesive strength ε, which strongly influences the shear rate at which unfolding sets in. This parameter was set at 1.2 kT, such that, in the absence of shear flow, the polymer is collapsed, and the unfolding transition occurs at a shear rate close to the experimental data. A different choice for the radius would shift the unfolding transition to different shear rates and the cohesive strength could be altered to reproduce the experimentally observed data. We calculated tension profiles along the chain of beads under shear flow as a function of polymer size and shear rate (Figure 5). Figure 5A shows the profile of the average tension along the VWF polymer for a representative polymer size of 20 beads (tension profiles of 10mer and 30mer are depicted in Supporting Information S3). The distribution exhibits a flattened profile with minimal tension at the ends and its curvature increases with increasing shear rate. Strong fluctuations are indicated by the high standard deviation σ shown for $\dot{\gamma}$ = 15.000/s. Typical snapshots of the 20mer unfolded by shear flow are illustrated in Figure 5B. In order to connect the tension profile with the cleavage activity, we make the key assumption that there exists a critical tension, above which a single subunit opens and becomes accessible for cleavage by ADAMTS13. To illustrate this point, the normalized tension distribution P(f) of a single bead (i=10) in a 20mer is shown in the inset of Figure 5C. With increasing shear, the tension distribution broadens and shifts toward higher tension. The opening probability for a single bead is obtained by calculating the fraction $P_i(f>f_c)$ that exceeds a critical force f_c. We define the opening probability for the whole multimer as the probability that at least one cleavage site is accessible, $P_{open}(\dot{\gamma})=1-\prod_1^N\left(1-P_i(f>f_c)\right)$, and plot the results for different VWF sizes N in Figure 5C. The shear dependence of the open fraction is well described by a Hill-type sigmoidal $P(\dot{\gamma})=\frac{1}{1+\left(\dot{\gamma}/\dot{\gamma}_{1/2}\right)^{-n}}$ (Figure 5C, dotted lines). Here, $\dot{\gamma}_{1/2}$ denotes the half-maximum shear rate, at which half of the polymers are open and n the cooperativeness coefficient. We obtain increasing values for $\dot{\gamma}_{1/2}$ with decreasing polymer size N ($\dot{\gamma}_{1/2}$(N=10) = $4.3\cdot10^4$ s^{-1}, $\dot{\gamma}_{1/2}$(N=20) = $2.4\cdot10^4$ s^{-1}, $\dot{\gamma}_{1/2}$(N=30) = $2.0\cdot10^4$ s^{-1}) and cooperativeness coefficients n_{10} = 4.9, n_{20} = 5.3, and n_{30} = 6.1. In the simulation, a critical opening force of f_c = 2.9 pN was chosen to ensure that a vanishing opening probability of well below 1% is obtained for low shear rates. A lower critical force leads to higher opening probabilities at low shear but does not affect the characteristic increase for high shear rates (see Supporting Information S4).

Shear-induced cleavage in blood plasma. We were particularly interested in characterizing the shear dependence of VWF proteolysis in blood plasma (Figure 6). Therefore, rVWF-eGFP was added to patient's blood plasma and studied in the FCS-shear cell. In this case, no ADAMTS13 is added, since normal plasma contains natural ADAMTS13. In this setting, both the recombinant VWF as well as the endogenous unlabeled VWF serve as substrates for ADAMTS13. For data analysis, we estimate the concentration of unlabeled VWF to be 3 nM (see Supporting Information S1). Figure 6A shows the cleavage rate as a function of VWF

concentration under denaturing conditions in 25% normal plasma (NP) (0.25 U/ml ADAMTS13). For comparison, the plot also shows the data for (1 U/ml) ADAMTS13 in buffer (taken from Figure 2C). Straight lines indicate fits with the same K_M = 171 nM value, but different v_{max} = 505 ± 37 pM/min (NP) and v_{max} = 358 ± 118 pM/min (buffer), respectively. The patient's plasma used in Figure 6B contained anti-ADAMTS13 autoantibodies (AB plasma) and cleavage rates are considerably reduced (3.13 ± 1.5 pM/min instead of 18.24 ± 2.0 pM/min). Figure 6C shows the cleavage rate as a function of shear. Importantly, we did not find any evidence for VWF aggregation in experiments with blood plasma. We were therefore able to measure VWF cleavage in blood plasma up to $\dot{\gamma}$ = 10.000/s. In order to exclude the possibility that VWF concentration might increase under high shear over time due to solvent evaporation, we carried out a control experiment on pure eGFP protein, which shows only a small concentration increase of 6% in buffer subjected to a shear rate of $\dot{\gamma}$ = 8400/s over 2.5h. Under shear, rVWF in 50% NP exhibits, as predicted by the simulation, a Hill-type sigmoidal increase with increasing shear rates. For the 50% AB plasma with reduced ADAMTS13 activity, we find the same sigmoidal dependence on shear, but overall reduced cleavage rates. The experimentally determined dependence on shear rate is in good agreement with the hydrodynamic model. Assuming that the cleavage rate k_{CR} is proportional to the shear-dependent unfolding probability: $k_{CR} = k_{\max} \cdot P_{open}(\dot{\gamma})$, the straight lines in Figure 6C are best fits with optimized prefactors $k_{max,NP}$ = 243 ± 20 pM/min and $k_{max,AB}$ = 101 ± 26 pM/min, respectively. Using a Hill-type function for $P_{open}(\dot{\gamma})$ as before, we obtain the half maximum shear rate $\dot{\gamma}_{1/2}$ = 5358 ± 41 s^{-1} and cooperativeness coefficient n = 4.8 ± 0.2 s^{-1}. The opening probability is calculated based on the Brownian hydrodynamic model using a fixed parameter set (a = 90 nm, f_c = 2.9 pN). Here, we average P_{open} over three different sizes N, as shown in Figure5C, and weight according to the size distribution ~p^{N-1} with p=0.64 [20].The fact that the shear dependence of cleavage in both NP and AB plasma has the same shape is a strong indication that VWF unfolding is the determining mechanism, while the concentration of available ADAMTS13 just sets the prefactor.

DISCUSSION:

Using FCS and recombinant rVWF-eGFP, we have measured the ADAMTS13 activity in real-time. In denaturing buffer, we observed Michaelis-Menten kinetics with K_M^{VWF} = 171 nM. At first glance, this value seems rather low by comparison with those obtained in recent experiments performed with VWF fragments: Zanardelli et al. measured K_M = 1.61 µM by high pressure liquid chromatography for cleavage of a 16.9 kDa fragment of the VWF A2 domain [30]. In experiments using gel analysis and ELISA, Gao et al. obtained K_M = 1.7 µM for cleavage of an A2 domain fragment consisting of amino acid residues Asp^{1596}-Arg^{1668} [7]. Both values seem to reflect lower proteolytic activities than found in our work. However, our data, for the first time, yield rates of full-length VWF cleavage. Consequently, our K_M is expressed in terms of the molar concentration of *multimeric* VWF. If converted into molar concentration of VWF cleavage sites, using an average number of 12.6 monomers per VWF molecule [20], we obtain an effective monomer Michaelis-Menten constant K_M^{mono} = 2.1 µM, in good agreement with the results for VWF fragments.

The unfolding of VWF under shear is known as a globular-stretch transition and it has long been speculated that its susceptibility to proteolysis is modulated by force-induced extension. We find that the shear dependence in experiment is accurately described by Brownian dynamics simulations. Experiment and theory both exhibit an Hill-type sigmoidal dependence on shear with half maximum shear rate $\dot{\gamma}_{1/2}$ = 5358/s and cooperativeness coefficient n = 4.8. These findings are in line with earlier observation of abrupt onset of VWF unfolding as a function of shear rate using fluorescence microscopy and small-angle neutron scattering [11,12]. The relationship between VWF unfolding and cleavage activity can be accounted for by assuming that the A2 domain opens when the force exerted on it exceeds a critical value. Using Brownian hydrodynamics simulations, we determined the tension induced by shear flow along the backbone of unfolded VWF multimers. By comparison with the cleavage data, we yield a critical force f_c = 2.9 pN for the opening of the A2 domain. This parameter has also been calculated by molecular dynamics (MD) simulations [8] and independently measured with optical tweezers [14]. The former yielded values of up to 1000 pN, and are likely to be significantly overestimated, owing to the short (nanosecond) time-scale of MD simulations. In contrast, the unfolding forces measured with optical tweezers are in the same range (5-20 pN) as those presented here. However, optical tweezers apply homogenous forces to VWF, while shear flow leads to an inhomogeneous force distribution with strong fluctuations. Since mutations in VWF's A2 domain are known to affect the opening force, a model of shear-induced-opening might be constructed, which could relate mutations directly to hemostatic dysfunction. Future work may thus close the gap between the atomistic models and the coarse-grained hydrodynamic model used in this work.

Measurement of ADAMTS13 activity in its natural environment, namely blood plasma, is of clinical importance, and fluorescence-based assays have the advantage of being readily applicable to body fluids. In this work, we determined the kinetics of rVWF-eGFP cleavage in 25% normal blood plasma and found that the rate of proteolysis is increased more than five-fold relative to experiments performed in buffer. This finding corroborates a previous hypothesis, which suggested that certain components found in blood, such as coagulation factor VIII, increase VWF's susceptibility to cleavage [31]. The enhancement of proteolysis is attributed, *inter alia*, to the conformational change induced in VWF by the binding of factor VIII [32]. Other cofactors and their effects on VWF have not yet been studied, but might provide novel therapeutic targets. FCS-based measurements of rVWF-eGFP cleavage may also have diagnostic potential. Determination of levels of ADAMTS13 activity in plasma is, for example, required for differential diagnostics in microangiopathies. The sensitivity of the conventionally used assays is hitherto limited, especially at clinically relevant, pathologically low ADAMTS13 levels. FCS combined with recombinant VWF-eGFP added to patient samples permits detection of extremely low levels of ADAMTS13 activity. Even higher detection limits, well below 5%, can be achieved, if the extremely proteolysis-sensitive rVWF-G1629E is employed as a substrate. However, as indicated by the mechanism of shear-induced unfolding and opening, ADAMTS13 concentration is only one determinant of pathology, while mutant forms of VWF itself are likely to make a much greater contribution to hemostatic dysfunctions. FCS can help to quantify the effect of mutations and assess the impact of potential drugs. In this context, the ability to measure specific cleavage activity on

VWF in native blood samples constitutes a valuable extension of available methods, as it provides insight into the dynamics of the hemostatic network.

MATERIALS AND METHODS

Protein expression: The recombinant fusion protein rVWF-eGFP was expressed and purified as described in detail before [20]. For the mutant VWF-G1629E, the plasmid PIRESneo2-VWF-G1629E-eGFP was used, which was produced by *in vitro* mutagenesis of wild-type pIRESneo2-VWF-eGFP by replacing wild-type codon 1629 for glycine with the naturally occurring mutant codon specifying glutamic acid (p.Gly1629Glu). Wild type rhuADAMTS13 used was produced as described in [17].

Plasma samples were taken from normal volunteer donors and collected in S-monovettes, coagulation sodium citrate (Sarstedt, Germany), incubated at room temperature (30 min), and centrifuged (10 min, 2300 rpm). The supernatant was aliquoted and stored at −80°C until use. Informed consent was obtained from all subjects.

Fluorescent Correlation Spectroscopy (FCS) measurements were performed on an Axiovert 200 microscope with a ConfoCor 2 unit (Carl Zeiss, Jena, Germany), equipped with a 40x (NA = 1.2) water-immersion Apochromat objective (Carl Zeiss). A 488 nm argon laser was used for illumination. For calibration, eGFP was measured for 20x60 s in the corresponding buffer. Experiments without shear flow were carried out in eight-well LabTek I chamber slides (Nunc, Rochester, NY) on rVWF for 20x15 min and on rVWF-G1629E for 20x9 min, (owing to its higher sensitivity to proteolysis). Correlation analysis was performed using the ConfoCor 2 software. The FCS data analysis is described in detail in Supporting Information S1.

Shear cell: A custom-made shear cell was used to apply shear forces consisting of a combined cone-and-plate and concentric cylindrical design, called Mooney system [33]. A coverslip (Carl Roth, Karlsruhe, Germany) was fixed with nail varnish to a stainless steel sample holder containing wells of radii $r_o = 6.5$ mm, serving as outer cylinders. The inner rotating cylinder (radius $r_i = 6.1$ mm) was connected to a brushless motor with integrated controller (Faulhaber GmbH, Schönaich, Germany). Before use, both cylinders were first incubated for 30 min with UHT milk to avoid sticking of the sample to the surface, and then washed with buffer for at least ten times. For shear-flow measurements, periods of applied shear stress (15 min) without FCS recording alternated with measuring periods (5x3 min) without shear flow.

Cleavage protocol: Measurements were conducted in either buffer or blood plasma. The cleavage buffer contained 5 mM Tris-HCl (pH 8.0) with 10 mM $BaCl_2$ for ADAMTS13 activation [34,35]. For measurements without shear flow, 1.5 M urea was added to partially denature VWF based on the commonly used protocol [30,34,36]. For measurements in blood plasma, the plasma was diluted to the desired concentration with 5 mM Tris-HCl (pH 8.0). For all measurements, the temperature was set to 37°C (without shear: heating stage, ibidi GmbH, Martinsried, Germany; with shear: water bath, Julabo GmbH, Seelbach, Germany).

Simulation methods: Brownian dynamics simulations were performed using a discretized Langevin equation, where hydrodynamic interactions are taken into account via the Rotne-Prager tensor [37] (for details, see Supporting Information S3). The VWF was modeled as a homopolymer consisting of N beads, which interact via Lennard-Jones potentials of depth

$\varepsilon = \tilde{\varepsilon} / k_B T = 1.2$, and are connected in a linear chain by harmonic bonds with a rescaled spring constant $k = \tilde{k} / \left(k_B T a^2\right) = 200$. Tensile forces acting along each bond $f_i = -k\left(r_{i,i+1} - 2\right)$ are recorded during the course of simulation. To compare the dimensionless quantities used in the simulation to physical values (marked by the tilde), we use the dimer radius a = 45nm, the viscosity η = 1.2x10^{-3}Pas, and the temperature T = 310K.

Acknowledgements:

We thank Thomas Ligon and Carolin Leonhardt for reading the manuscript. This work was supported with seed funds from the Center for NanoScience, and by DFG research unit FOR 1543,which is funded by the the Deutsche Forschungsgemeinschaft . We gratefully acknowledge all SHENC members, especially Frauke Gräter for fruitful discussions. S.L. thanks the Elite Network of Bavaria for its support.

REFERENCES

[1] Sadler JE (1998) Biochemistry and genetics of von Willebrand factor. *Annual review of biochemistry* 67(1): 395-424.

[2] Ruggeri ZM (2001) Structure of von Willebrand factor and its function in platelet adhesion and thrombus formation. *Best Practice & Research Clinical Haematology* 14(2): 257-279.

[3] Romani de Wit T, van Mourik JA (2001) Biosynthesis, processing and secretion of von Willebrand factor: biological implications. *Best Practice & Research Clinical Haematology* 14(2): 241-255.

[4] Zheng X et al. (2001) Structure of von Willebrand factor-cleaving protease (ADAMTS13), a metalloprotease involved in thrombotic thrombocytopenic purpura. *Journal of Biological Chemistry* 276(44): 41059-41063.

[5] Levy GG et al. (2001) Mutations in a member of the ADAMTS gene family cause thrombotic thrombocytopenic purpura. *Nature* 413(6855): 488-494.

[6] Soejima K et al. (2001) A Novel Human Metalloprotease Synthesized in the Liver and Secreted into the Blood: Possibly, the von Willebrand Factor-Cleaving Protease? *Journal of Biochemistry* 130(4): 475-480.

[7] Gao W, Anderson PJ, Majerus EM, Tuley EA, Sadler JE (2006) Exosite interactions contribute to tension-induced cleavage of von Willebrand factor by the antithrombotic ADAMTS13 metalloprotease. *Proceedings of the National Academy of Sciences* 103(50): 19099-19104.

[8] Baldauf C et al. (2009) Shear-induced unfolding activates von Willebrand factor A2 domain for proteolysis. *Journal of Thrombosis and Haemostasis* 7(12): 2096-2105.

[9] Tsai HM (2003) Is severe deficiency of ADAMTS-13 specific for thrombotic thrombocytopenic purpura? Yes. *Journal of Thrombosis and Haemostasis* 1(4): 625-631.

[10] Tsai H-M (2003) *Shear stress and von Willebrand factor in health and disease*. Seminars in thrombosis and hemostasis, Copyright © 2003 by Thieme Medical Publishers, Inc., New York.

[11] Schneider SW et al. (2007) Shear-induced unfolding triggers adhesion of von Willebrand factor fibers. *Proceedings of the National Academy of Sciences* 104(19): 7899.

[12] Singh I, Themistou E, Porcar L, Neelamegham S (2009) Fluid shear induces conformation change in human blood protein von Willebrand factor in solution. *Biophysical journal* 96(6): 2313-2320.

[13] Dent JA, Berkowitz SD, Ware J, Kasper CK, Ruggeri ZM (1990) Identification of a cleavage site directing the immunochemical detection of molecular abnormalities in type IIA von Willebrand factor. *Proceedings of the National Academy of Sciences* 87(16): 6306-6310.

[14] Zhang X, Halvorsen K, Zhang CZ, Wong WP, Springer TA (2009) Mechanoenzymatic cleavage of the ultralarge vascular protein von Willebrand factor. *Science* 324(5932): 1330.

[15] Majerus EM, Anderson PJ, Sadler JE (2005) Binding of ADAMTS13 to von Willebrand factor. *Journal of Biological Chemistry* 280(23): 21773-21778.

[16] Zanardelli S et al. (2006) ADAMTS13 substrate recognition of von Willebrand factor A2 domain. *Journal of Biological Chemistry* 281(3): 1555-1563.

[17] Hassenpflug WA et al. (2006) Impact of mutations in the von Willebrand factor A2 domain on ADAMTS13-dependent proteolysis. *Blood* 107(6): 2339.

[18] Alexander-Katz A, Schneider MF, Schneider SW, Wixforth A, Netz RR (2006) Shear-flow-induced unfolding of polymeric globules. *Physical review letters* 97(13): 138101.

[19] Sing CE, Alexander-Katz A (2011) Dynamics of collapsed polymers under the simultaneous influence of elongational and shear flows. *J. Chem. Phys.* 135(1): 014902.
[20] Lippok S et al. (2013) Exponential Size Distribution of von Willebrand Factor. *Biophysical journal* 105(5): 1208-1216.
[21] Engelke H, Dorn I, Rädler JO (2009) Diffusion and molecular binding in crowded vesicle solutions measured by fluorescence correlation spectroscopy. *Soft Matter* 5(21): 4283-4289.
[22] Lumma D, Keller S, Vilgis T, Rädler JO (2003) Dynamics of large semiflexible chains probed by fluorescence correlation spectroscopy. *Physical review letters* 90(21): 218301.
[23] Scalettar BA, Hearst JE, Klein MP (1989) FRAP and FCS studies of self-diffusion and mutual diffusion in entangled DNA solutions. *Macromolecules* 22(12): 4550-4559.
[24] Sukhishvili SA et al. (2000) Materials science: Diffusion of a polymer 'pancake'. *Nature* 406(6792): 146-146.
[25] Tao Z et al.(2005) Cleavage of ultralarge multimers of von Willebrand factor by C-terminal-truncated mutants of ADAMTS-13 under flow. *Blood* 106(1): 141-143.
[26] Guttenberg, Z et al. (2004) Flow profiling of a surface-acoustic-wave nanopump. *Physical Review E* 70:5, 056311.
[27] Dittrich PS, Schwille P (2002) Spatial two-photon fluorescence cross-correlation spectroscopy for controlling molecular transport in microfluidic structures. *Analytical Chemistry* 74:17, 4472-4479.
[28] Sendner C, Netz RR (2009) Single flexible and semiflexible polymers at high shear: Non-monotonic and non-universal stretching response. *The European Physical Journal E* 30:(1), 75-81.
[29] Radtke M, Netz R (2014) Shear-induced dynamics of polymeric globules at adsorbing homogeneous and inhomogeneous surfaces. *The European Physical Journal E* 37(3):1-11.
[30] Zanardelli S et al. (2009) A novel binding site for ADAMTS13 constitutively exposed on the surface of globular VWF. *Blood* 114(13): 2819-2828.
[31] Cao W, Krishnaswamy S, Camire RM, Lenting PJ, Zheng XL (2008) Factor VIII accelerates proteolytic cleavage of von Willebrand factor by ADAMTS13. *Proceedings of the National Academy of Sciences* 105(21): 7416-7421.
[32] Skipwith CG, Cao W, Zheng XL (2010) Factor VIII and platelets synergistically accelerate cleavage of von Willebrand factor by ADAMTS13 under fluid shear stress. *Journal of Biological Chemistry* 285(37): 28596-28603.
[33] Barnes HA, Hutton JF, Walters K (1989) *An introduction to rheology*, Elsevier. Amsterdam.
[34] Kokame K, Nobe Y, Kokubo Y, Okayama A, Miyata T (2005) FRETS-VWF73, a first fluorogenic substrate for ADAMTS13 assay. *British journal of haematology* 129(1): 93-100.
[35] Pruss CM, Notley CRP, Hegadorn CA, O'Brien LA, Lillicrap D (2008) ADAMTS13 cleavage efficiency is altered by mutagenic and, to a lesser extent, polymorphic sequence changes in the A1 and A2 domains of von Willebrand factor. *British journal of haematology* 143(4): 552-558.
[36] Furlan M, Robles R, Lamie B (1996) Partial purification and characterization of a protease from human plasma cleaving von Willebrand factor to fragments produced by in vivo proteolysis. *Blood* 87(10): 4223-4234.
[37] Rotne J, Prager S (2003) Variational treatment of hydrodynamic interaction in polymers. *The Journal of Chemical Physics* 50(11): 4831-4837.

FIGURES

Figure 1

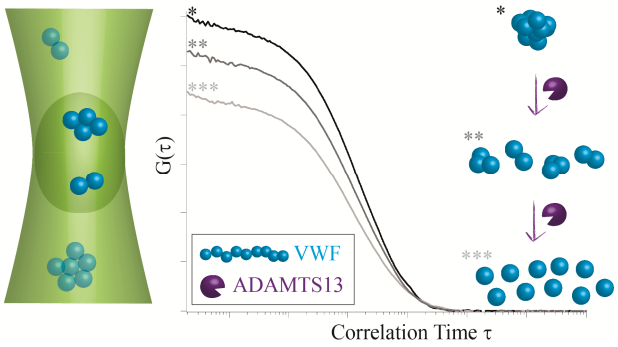

Figure 1: FCS analysis of the kinetics of VWF proteolysis. The correlation curve G(τ) at time 0 is proportional to the reciprocal of the number of fluorescent molecules in the detection volume N = 1/G(0), i.e. the molar concentration of VWF. For multimeric rVWF-eGFP with one eGFP molecule attached to each VWF monomer, cleavage by ADAMTS13 results in an increase in the number of fluorescent molecules. This increase in N concomitantly reduces the value of G(0) and can be detected in real-time.

Figure 2

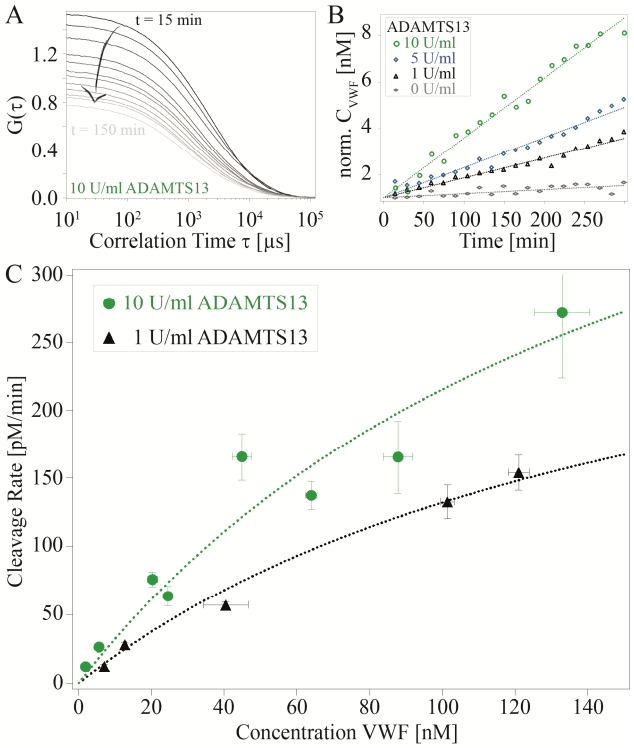

Figure 2: Cleavage of full-length rVWF in buffer follows Michaelis-Menten kinetics. **A** Representative autocorrelation curves showing that proteolysis of VWF is reflected in a progressive decrease in amplitude G(0) with time. **B** Molar concentration of rVWF molecules increases linearly over time and the cleavage rates depend on ADAMTS13 concentration. **C** The hyperbolic dependence of cleavage rate on VWF concentration was fitted with the Michaelis-Menten equation (dotted lines). Constraining a Michaelis-Menten constant independent of the enzyme concentration, we obtained K_M = 171±85 nM, v_{max} = 358±118 pM/min (1 U/ml ADAMTS13), and v_{max} =584 ±193 nM (10 U/ml ADAMTS13).

Figure 3

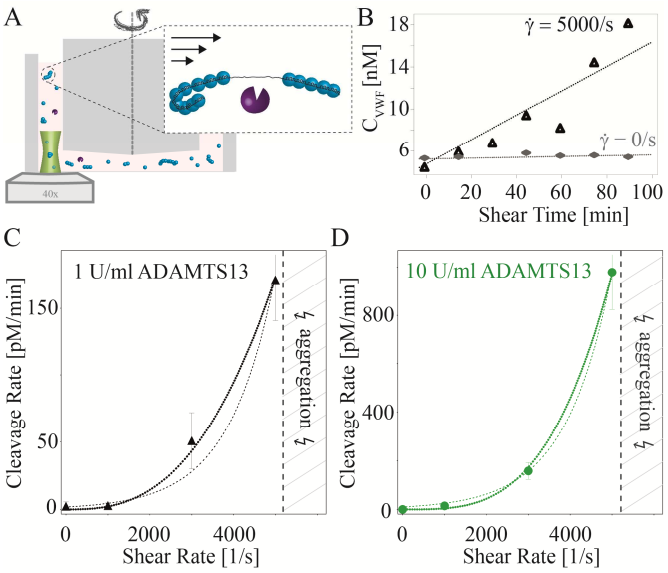

Figure 3: Shear-induced cleavage of rVWF. **A** Cartoon illustrating VWF proteolysis under shear flow. The shear cell generates constant shear rates throughout the whole sample volume. Above a certain threshold, VWF unfolds, the A2 domains open and cleavage sites for ADAMTS13 are exposed. **B** Molar VWF concentrations at the end of each shear period are plotted as a function of the total duration of shear as shown here for $\dot{\gamma}$ = 0/s and 5000/s. **C** rVWF cleavage rates (1 U/ml ADAMTS13) as a function of applied shear rates. **D** Use of a tenfold higher protease concentration (10 U/ml) significantly increases cleavage rates. Exponential (dashed lines) and power law (bold dotted lines) fits are plotted; better agreement is found for the power law. For shear rates $\dot{\gamma}$ > 5000/s, VWF aggregation becomes dominant over VWF cleavage.

Figure 4

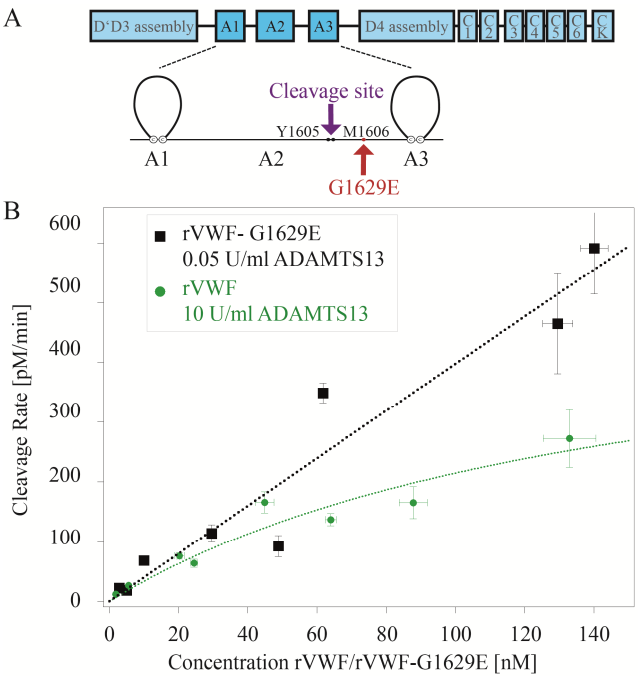

Figure 4: Proteolysis of the disease-related mutant rVWF-G1629E. **A** Schematic drawing of the multidomain structure of a VWF monomer. The G1629E mutation is located close to the site cleaved by ADAMTS13 and results in constitutive opening of the A2 domain. **B** Kinetics of mutant cleavage in the absence of shear. In buffer without urea, the mutant exhibits significantly increased susceptibility to proteolysis as compared to rVWF in denaturing buffer. Note that cleavage rates in both cases are comparable, even though a 200-fold lower ADAMTS13 concentration (0.05 U/ml) was used in case of the mutant. Best Michaelis-Menten kinetic fits are shown as dotted lines.

Figure 5

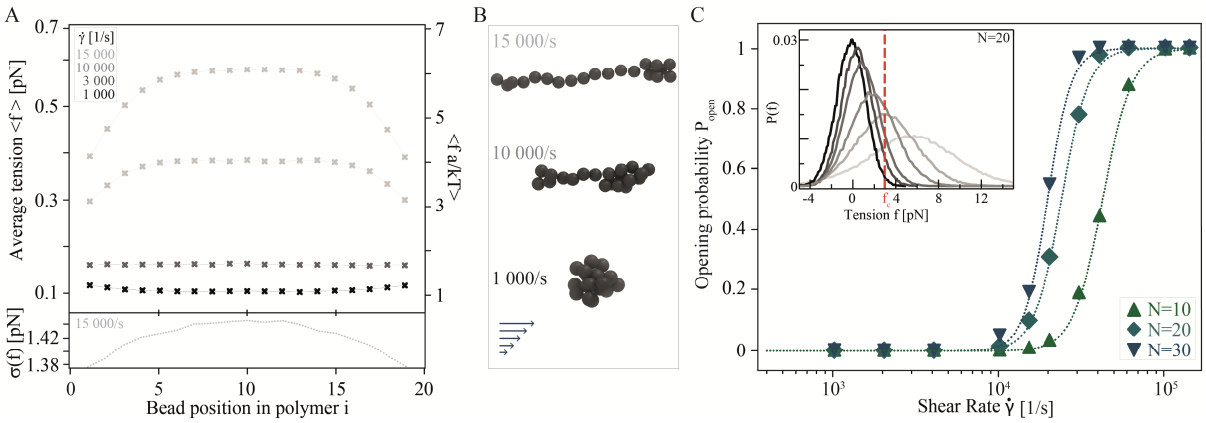

Figure 5: Results of hydrodynamic simulations of polymer response to shear flow. **A** The average tension <f> is plotted as a function of bead position i along a polymer of size N = 20. The tension exhibits a flat profile with a decrease at each end of the chain and increases with increasing shear rate $\dot{\gamma}$. The standard deviation σ, plotted at the bottom for $\dot{\gamma}$= 15.000/s, indicates a broad distribution of the tensile forces. **B** Snapshots of typical polymer configurations obtained at different shear rates as indicated. **C** Opening probability P_{open} as a function of shear rate, obtained from the tension distribution P(f) of individual beads. P(f) for a single bead is shown in the inset (with increasing shear from dark to light). The opening probability of a single bead is defined as the probability that tension exceeds a critical value (f_c) of 2.9 pN (indicated by a red dashed vertical line in the inset). The opening probability P_{open} for the multimer is the probability that at least one cleavage site is accessible. It exhibits a Hill-type sigmoidal increase with increasing shear rates (sigmoidal fit: dotted lines).

Figure 6

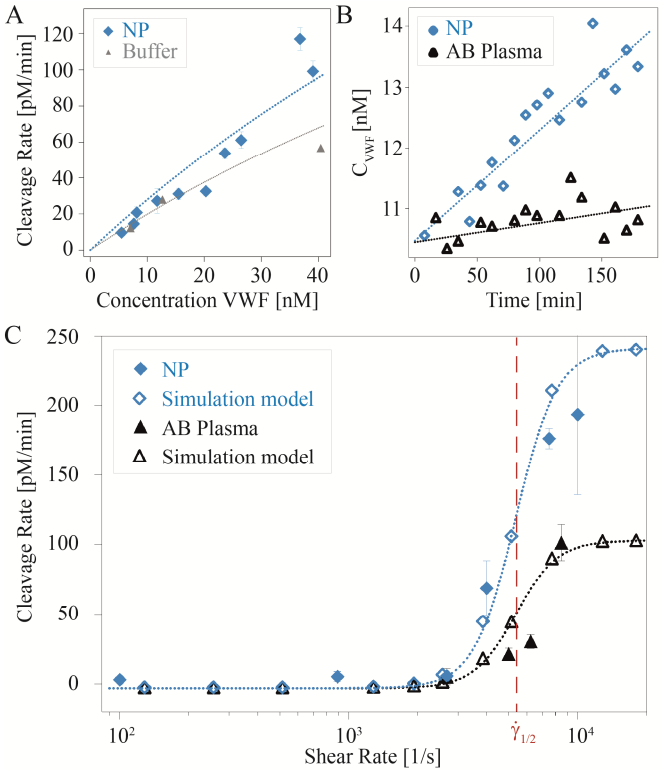

Figure 6: VWF proteolysis in blood plasma. **A** Kinetic analysis of rVWF cleavage in 25% NP (0.25 U/ml ADAMTS13) yields v_{max} = 505 ± 37 nM at a fixed K_M = 171 nM (Michealis-Menten fit: blue dotted line). For comparison, the (lower) enzyme activity in buffer (1 U/ml ADAMTS13) is shown (grey). **B** Protease activity in normal versus patient's AB plasma. The patient's plasma exhibited a six-fold reduced protease activity under denaturing conditions. **C** Shear-flow induced cleavage in blood plasma. For both NP and AB plasma, cleavage rate increases following a Hill-type sigmoidal with increasing shear ($\dot{\gamma}_{1/2}$ = 5358/s, n = 4.8, sigmoidal fit: dotted lines). Decreased proteolytic activity was found for AB plasma. This is in good agreement with the hydrodynamic simulation model assuming that the cleavage rate k_{CR} is proportional to the shear-dependent probability of opening: $k_{CR} = k_{max} \cdot P_{open}(\dot{\gamma})$ (open markers) with enzyme activity dependent k_{max} = 243 pM/min (NP) and k_{max} = 101 pM/min (AB).

6

Destabilized recombinant VWF as Substrate for ADAMTS13 Activity Assays

ADAMTS13 activity assays are the key laboratory finding in TTP diagnostics. In these assays, the enzymatic activity is indirectly detected via the cleavage of substrate VWF. However, this poses the challenge that the A2 cleavage domain of full-length VWF needs to be open to provide access for ADAMTS13, as demonstrated in the previous chapter. Thus, either VWF fragments or denaturing buffers are commonly used. Under these constraints, standard coagulation tests for the detection of ADAMTS13 activity are still limited by reproducibility and insufficient sensitivity for ADAMTS13 concentrations of less than 5 % of the physiological plasma level. Yet, these low concentrations are known to result in TTP. Thus, exact quantification is needed for adequate therapies.

We established an assay that applies a recombinant fusion protein of the destabilized mutant VWF-G1629E as enzyme substrate. We analyzed the increased sensitivity in terms of enzyme kinetics and found cooperative Hill-type behavior in addition to a highly increased affinity to ADAMTS13 compared to VWF-wt. Using the mutant enabled us to detect ADAMTS13 activity levels down to 0.5 %, which is 5- to 10-fold more sensitive than commonly used assays. Molecular Dynamics Simulations (Prof. Gräter/ Dr. Baldauf) identified local structural changes in the mutated A2 cleavage domain that induce destabilization, which presumably keeps the cleavage site accessible even in the absence of shear. The increased sensitivity of rVWF-G1629E-eGFP as an ADAMTS13 substrate provides a significant improvement both in analytical sensitivity and in accuracy that might enhance TTP diagnostics. Moreover, recombinant fluorescent proteins as substrates allow for fast and cost-efficient read-out. Further specialized VWF mutants might be used to enhance coagulation diagnostics.

The experimental data and the resulting conclusions are presented in the following manuscript:

S. Lippok, C. Aponte-Santamaría, T. Obser, R. Schneppenheim, C. Baldauf, F. Gräter, U. Budde, J.O. Rädler. "Destabilized recombinant VWF as substrate for highly sensitive ADAMTS13 activity assays." *to be submitted to Journal of Thrombosis and Haemostasis*

Destabilized recombinant VWF as substrate for highly sensitive ADAMTS13 activity assays

S. Lippok[a], C. Aponte-Santamaría[b], T. Obser[c],

R. Schneppenheim[c], C. Baldauf[d], F. Gräter[b], U. Budde[e], J.O. Rädler[a,1]

[a] Faculty of Physics and Center for NanoScience, Ludwig Maximilian University, 80539 Munich, Germany

[b] Molecular Biomechanics, Heidelberger Institut für Theoretische Studien, 69118 Heidelberg, Germany

[c] Department of Pediatric Hematology and Oncology, University Medical Center Hamburg-Eppendorf, 20246 Hamburg, Germany

[d] Fritz-Haber-Institut, Max-Planck-Gesellschaft, 14195 Berlin, Germany

[e] MEDILYS Laborgesellschaft mbH, Hemostaseology, Asklepios Klinik Altona, 22763 Hamburg, Germany

[1] Corresponding author: phone: +49 89 2180 2438, email: raedler@lmu.de

Keywords: VWF-G1629E, VWF-cleaving protease, TTP, Fluorescence Correlation Spectroscopy

ABSTRACT

The protease ADAMTS13 plays an essential role in haemostasis as it cleaves the large multimeric glycoprotein von Willebrand Factor (VWF). Deficiency of ADAMTS13 with plasma activity levels of 5 % and below leads to the severe coagulation disorder thrombotic thrombocytopenic purpura (TTP). Reliable quantification of the ADAMTS13 activity levels in patient's blood is important in clinical diagnostics, but remains challenging with commonly used assays. Because the ADAMTS13 activity is detected via breakdown of substrate VWF, limitations arise partly from the fact that the cleavage site of VWF is only accessible upon opening at high shear rates or under denaturing conditions. Here, we show that a fast and sensitive ADAMTS13 assay can be set up employing the recombinant mutant VWF-G1629E-eGFP as a fluorescent enzyme substrate. Using Fluorescence Correlation Spectroscopy (FCS), we followed online the ADAMTS13-meditated breakdown of the fluorescent substrate both *in vitro* and in patient's blood samples. We obtained a 5-fold improved detection limit than that achieved with commonly used assays. *In vitro* data affirm cooperative enzyme kinetics with Hill coefficient n = 2.3 as well as a linear rate response to ADAMTS13. Molecular dynamics simulations (MDS) suggest that the enhanced responsiveness to ADAMTS13 arises from a local structural destabilization of the mutation G1629E that results in an increased accessibility of the A2 cleavage domain. The elevated signal-to-noise ratio achieved with the mutant provides a significant improvement both in analytical sensitivity and in accuracy in laboratory tests that facilitates diagnosis of TTP as well as difficult to detect mild ADAMTS13 deficiencies.

INTRODUCTION

The multimeric protein von Willebrand Factor (VWF) is essential for the initiation of blood coagulation as it promotes the binding of platelets to ruptured vessel walls [1,2]. The size distribution of VWF is regulated by the protease ADAMTS13 (a disintegrin and metalloprotease with thrombospondin type 1 motif, member 13). The enzymatic cleavage by ADAMTS13 represents a crucial control mechanism in hemostasis [3]. A severe deficient ADAMTS13 activity (5 % of that in normal plasma) leads to increased amounts of ultralarge, highly-active VWF multimers that cause a thrombotic microangiopathy, which is commonly referred to as thrombotic thrombocytopenic purpura (TTP) [4-6]. TTP is caused either by mutations of the ADAMTS13 gene or by acquired autoantibodies that inhibit ADAMTS13 activity [7]. The ADAMTS13 specific cleavage site is located at the peptide bond Tyr1605-Met1606 and deeply buried in the VWF A2 domain [8,9]. This domain has been shown to be mechanosensitive and its opening *in vivo* is induced by shear flow, for instance arising at ruptured vessel walls. Only the opened A2 domain allows access to its cleavage site [10,11]. Moreover, we showed recently that the opening mechanism of the A2 domain has a huge impact on the resulting cleavage rates [Lippok et al., 2014, submitted].

The quantification of ADAMTS13 activities below 5 % is the key laboratory finding to diagnose TTP [12]. Although numerous activity assays already exist, there are hitherto limitations in sensitivity and reproducibility [12,13]. In particular, the extremely low disease-

related ADAMTS13 activity levels are difficult to measure. A critical impediment is that assays using full-length VWF as substrate rely on the opening of the A2 domain. Therefore, in many cases only VWF fragments are used [13-15], or cleavage is conducted in denaturing buffer containing 1.5 M urea [16-19]. This makes it difficult to identify whether the detected amount of ADAMTS13 is functional in circulation. Moreover, denaturing substances only partly destabilize the VWF multimer, which decreases the detected cleavage rates and considerably reduces the achieved signal-to-noise ratio.

There are several naturally occurring mutations in the A2 domain, which induce increased VWF proteolysis in patients. In a broad study, Hassenpflug et al. investigated the impact of 13 different VWD type 2A mutations on ADAMTS13-dependent proteolysis [20]. 11 of them showed increased specific proteolysis compared to VWF wild-type (VWF-wt). For four mutants, this holded true even in the absence of urea. In particular one mutant, namely VWF-G1629E, was found to result in very strongly increased sensitivity to proteolysis under nondenaturing conditions. Moreover, this mutant showed no quantitative defects in the expression and exhibited the physiological VWF size distribution.

Here, we use the mutant VWF-G1629E as enzyme substrate to measure the ADAMTS13 activity in patient's plasma. As shown recently, Fluorescence Correlation Spectroscopy (FCS) is capable to detect full-length VWF cleavage on-line under blood plasma conditions using recombinant VWF-eGFP fusion proteins [Lippok et al., 2014, submitted]. FCS collects intensity fluctuations that arise from fluorescent proteins diffusing through a laser focus to assess the number density of detected molecules. Using FCS and the fluorescent fusion protein rVWF-G1629E-eGFP, we quantified ADAMTS13 activity levels down to 0.5 % in buffer, i.e. with a 5- to 10-fold higher detection limit than most commercially available assays. Moreover, we investigated the elevated cleavage rates of the mutant by enzyme kinetics in 0.5 % normal plasma (NP) and found a cooperative behaviour with Hill coefficient $n = 2.3$ in contrast to non-cooperative Michaelis-Menten type kinetics published recently for denatured wild-type VWF [Lippok et al., 2014, submitted]. In particular, we show that cleavage rates of the mutant were 20-fold increased compared to cleavage with denatured VWF-wt. The elevated sensitivity of rVWF-G1629E is supported by Molecular Dynamics Simulations (MDS) showing a destabilization of the mutated A2 domain, which suggests a facilitated access to the cleavage site. We discuss possible applications of the mutant rVWF-G1629E as enzyme substrate for standard coagulation tests in clinical laboratories.

MATERIALS AND METHODS

Protein expression: Recombinant fusion proteins were produced as described in [21]. Full-length ADAMTS13 cDNA was cloned into the expression vector pIRES neo2 for stable transfection of HEK 293 cells by liposomal transfer under selective pressure 48h after transfection [20]. Wild-type rhuADAMTS13, secreted to the medium, was used for cleavage experiments.

Plasma samples were collected from normal volunteer donors in S-monovettes, coagulation sodium citrate (Sarstedt, Germany). After incubation at room temperature for 30 min, samples

were centrifuged (10 min, 2300 rpm). The supernatant was stored at -80°C until further use. Informed consent was obtained from all subjects.

FCS measurements were run on an Axiovert 200 microscope with a ConfoCor 2 unit (Carl Zeiss, Jena, Germany), equipped with a 40x (NA = 1.2) water-immersion Apochromat objective (Carl Zeiss) and a 488 nm argon laser for illumination. Experiments were carried out in 8-well LabTek I chamber slides (Nunc, Rochester, NY) in 5 mM Tris-HCl (pH 8.0) containing 10 mM $BaCl_2$ for 10x6 min on rVWF-G1629E and for 20x9 min on rVWF (owing to the decreased cleavage). For measurements in blood plasma, the plasma was diluted to the desired concentration with Tris-HCl buffer. For wild-type rVWF, 1.5 M urea was added, based on the commonly used protocol [3,14,22]. The setup was calibrated measuring eGFP for 20x60 s in the corresponding buffer. The temperature was set to 37°C (heating stage, ibidi GmbH, Martinsried, Germany). Correlation analysis was performed using the ConfoCor 2 software. FCS data was analyzed as described in detail before [Lippok et al., 2014, submitted].

MDS were carried out starting from the solvated conformation of the VWF A2 domain (taken from its X-ray structure PDB ids. 3GXB [23]). Simulations were carried out with the GROMACS package [24-26] (4.5.5 version) following the procedure described in [27], both for the wild type domain (5 runs of 200 ns each for 1 μs concatenated simulated time) and for the mutant G1629E (4 runs of 200 ns each for 0.8 μs concatenated simulated time). The PyMOL software was used [28].

A PCA was carried out to identify changes in the conformational dynamics of the domain induced by the mutation G1629E. It consists in the calculation and diagonalization of the covariance matrix of the atomic positions of the backbone atoms [29]. Concatenated trajectories of both wt and mutant domains were used for the PCA calculation. The RMSF of the atomic positions was computed by concatenating separately the simulations of the wt and the mutant domain. An FDA analysis [30] was performed to monitor changes in the internal stress of the protein upon mutation. Time-averaged pair-wise forces $<F_{ij}>$ were computed for all residue pairs (i,j) of the A2 domain, in its wild-type ($<F_{ij}(wt)>$) and mutated ($<F_{ij}(G1629E)>$) forms. The absolute value of the difference $\Delta F_{ij}=|<F_{ij}(wt)>-<F_{ij}(G1629E)>|$ was subsequently calculated as a measure of the change in internal stress after mutation. $|\ |$ denotes absolute values.

RESULTS

FCS measurements of rVWF-G1629E cleavage. We established an assay to investigate ADAMTS13-mediated cleavage of mutant VWF-G1629E (Figure 1A). The mutant was provided as recombinant VWF-G1629E-eGFP fusion protein (rVWF-G1629E) in buffer and added to the blood plasma (Figure 1B). In this construct, one eGFP molecule is bound to each VWF monomer. Thus, cleavage of one rVWF-G1629E protein results in two fluorescent molecules. FCS detects the increasing protein number on-line by means of the amplitude of the autocorrelation curve G(0), which is inversely proportional to the number of fluorescent molecules in the confocal volume, G(0) 1/N [31].

Figure 2A illustrates cleavage of 6 nM rVWF-G1629E by ADAMTS13 at a concentration of 0.3 U/ml, which corresponds to 30 % of the physiological ADAMTS13 amount in normal plasma (NP). The graph depicts the shift of the autocorrelation curves towards lower amplitudes during cleavage over time. Note, that neither denaturing substances nor shear flow were applied for these experiments. Nevertheless, a decrease in the amplitude is clearly visible over time. The corresponding increase in particle number is plotted in the inset of Figure 2A. The steepness of this curve defines the cleavage rate dC/dt, which is the increase in molar VWF concentration over time. The cleavage rate depends on the applied enzyme concentration and is used as a measure for the ADAMTS13 activity.

Enzyme kinetics of rVWF-G1629E. To quantify the sensitivity of the mutant to cleavage, we investigated the enzyme kinetics of ADAMTS13-mediated cleavage at 0.5% NP (Figure 2B). We find a cooperative Hill-type behaviour. Fitting with $dC/dt = v_{max}/(1+(K_A/C)^n)$ yields a cooperativity coefficient $n = 2.3 \pm 0.2$, a maximum cleavage rate $v_{max} = 143.2 \pm 0.4$ pM/min, and a VWF-G1629E concentration producing half maximum cleavage $K_A = 11.5 \pm 0.5$ nM. For cleavage of denatured VWF-wt, non-cooperative Michaelis-Menten kinetics were observed [Lippok et al., 2014, submitted]. Moreover, a 15-fold reduced K_M was found compared to the K_A value for rVWF-G1629E cleavage.

Linear rate response to ADAMTS13 concentration. Figure 3A shows the cleavage rates for a constant rVWF-G1629E concentration (6 nM) as a function of ADAMTS13 concentration in buffer. We used this substrate concentration, because it is in the most sensitive concentration regime for FCS measurements. We detect the expected linear response within the entire investigated ADAMTS13 concentration regime. ADAMTS13 concentrations in the range of 5 to 30 % are easily detectable with commonly used assays. Fitting this concentration range with a linear fit, we get an increase of the cleavage rate with ADAMTS13 concentration of 1.61 ± 0.08 nM/min (red dotted line). Fitting only the low concentration range as depicted in the inset (0.5 - 5 %), which is hardly accessible with commonly used diagnostic assays, we achieve 1.50 ± 0.04 nM/min. This demonstrates that the assay is highly sensitive for rVWF-G1629E cleavage by ADAMTS13 at activities down to 0.5 % of the physiological level. Hence, we gain a resolution limit that is significantly lower than that of most commonly used assays, which lies between 2.5 and 5 % [32,33].

Accuracy of rVWF-G1629E cleavage detection in plasma samples. Next, we performed FCS measurements under blood plasma conditions to test the accuracy of our assay (see Figure 3B). For diagnostics, direct measurements in blood plasma are an essential requirement in order to avoid purification steps. Therefore, recombinant rVWF-G1629E was added to varying concentrations of normal plasma (NP) of a healthy volunteer (Figure 3A). ADAMTS13 activity was quantified in highly diluted plasma samples, containing only 1-5 % NP. We show that adding a higher amount of rVWF-G1629E (24 nM instead of 6 nM) increased the cleavage rates, so that we achieved a significantly better signal-to-noise ratio. The resulting cleavage rate at 1 % NP (400 pM/min) is well above the detection limit (about 2 pM/min). This demonstrates that the assay has not yet reached its detection limit at the applied ADAMTS13 concentrations. Moreover, for both rVWF-G1629E concentrations, the expected linear increase in the cleavage rate with increasing ADAMTS13 concentration is visible. Thus, the mutant allows for highly accurate measurements under blood plasma

conditions.

Comparison of rVWF-G1629E and rVWF-wt. To quantify the increase in accuracy, we compared the sensitivity of the mutant to proteolysis with that of rVWF-wt as shown in Figure 3B. For rVWF-wt, a denaturing buffer had to be used to partially denature the rVWF-eGFP fusion protein. Otherwise, the cleavage site would not be accessible for ADAMTS13 and cleavage activity could not be detected [Lippok et al., 2014, submitted]. Moreover, threefold prolonged measurement times were needed for the wild-type compared to those of the mutant to achieve a reliable signal-to-noise ratio. With these requirements, we were able to detect ADAMTS13 concentrations down to 1 % NP. However, we found that the cleavage rates are more than 20-fold reduced for rVWF-wt, which results in a considerable loss in accuracy. This is probably due to the fact that the urea-containing buffer only partly destabilizes VWF and does not completely open the A2 cleavage domain [34]. To verify this, we measured the diffusion coefficients of rVWF-wt dimer in nondenaturing and denaturing buffer, and rVWF-G1629E dimer (data not shown). We obtained $D_{Dimer,wt} = 20.1\ \mu m^2/s$ (nondenaturing conditions), $D_{Dimer,wt} = 19.5\ \mu m^2/s$ (denaturing conditions), and $D_{Dimer,mutant} = 18.9\ \mu m^2/s$. These data confirm the conception of only partly opening due to urea, while the mutation induces an increased destabilization, which we measure in terms of increased cleavage rates.

Altogether, using the mutant instead of wild-type VWF as substrate offers the possibility to detect more than 20-fold lower ADAMTS13 plasma levels without losing accuracy. In addition, measurement times are significantly reduced and the experiments can be performed without adding denaturing agents, which might alter the studied reactions.

Molecular Dynamics Simulations of the VWF A2 domain with and without mutation G1629E. To monitor the conformational changes induced by the G1629E mutation, which provide the increased cleavage rates, we performed MD simulations (Figure 4). MDS allow to ellucidate changes on the structure, dynamics and mechanical stability of proteins. We performed simulations of the wt and mutant VWF A2 domain for hundreds of nanoseconds. Within this time regime, the A2 domain remained folded in both its wild type and its mutant form, maintaining its globular shape, which keeps the ADAMTS13 cleavage site Y1605-M1606 shielded. This suggests that larger conformational changes, which increase the mutant's cleavage, occur on a longer time scale than the simulated time.
However, the simulations allowed us to capture local distabilizations, which may make the domain more prone to unfold in a shorter time when mutated. By performing principal component analysis (PCA), we identified two collective motions of the domain that covered 31% of the total positional fluctuations of the protein. We found that the wild type domain sampled two main region in the subspace consituted by these two vectors (Figure 4A). The mutated domain did not only populate these two but also further regions. This indicates that the mutated domain adopted a broader range of conformations than the wt domain, depicting higher conformational dynamics.

To further identify the parts of the domain that display the largest conformational changes upon mutation, we computed the round mean square fluctuations (RMSF) of the A2 domain (Figure 4B). We observe a broader conformational variability for the mutant due to local

fluctuations at the helix H5 and the loop L3-4. The former is positioned near the residue G1629. Interestingly, the loop L3-4, which connects the helix H3 with the strand B4, is not in direct contact with the G1629 residue, but also presented an increment in the RMSF. In contrast, the knotted C-terminal part of the protein (residues < 1580) presented small RMSF both for the wild type and the mutant. This implies a high structural stability for this region and is in concordance with previous computational studies [11]. In terms of RMSF, no affects were seen for the cleavage site located at the strand B4.

Finally, we analyzed whether the mechanical integrity of the protein was changed upon mutation. To this end, we performed a FDA analysis to compute the internal stress of the protein in wt and mutant. We observed that the mutation induced drastic changes in many of the residue pair-wise forces, which provide a measure of the internal stress. (Figure 4C). These changes were not only observed locally at the mutation site, but also extended to other distant parts of the protein including the ones hiding the ADAMTS13 cleavage site. In addition, pairs that are not involved in the mutation site also showed alterations, presumably to counteract for the perturbation imparted by the mutation to maintain the overall mechanical stability of the protein.

These data strengthens the theory of a destabilized structure that leads to a highly increased proteolysis, a reduced number of long multimers and finally to significant bleeding symptoms in patients with the mutation G1629E. Although we could not observe full unfolding of the domain due to the simulated time scale of merely hundreds of ns, we identified local structural changes and a wide-spread change in the internal stress of the protein. Such changes may act as destabilization factors that make the mutated A2 domain more prone to unfold.

DISCUSSION

We studied the fluorescent VWF mutant rVWF-G1629E as a new substrate for fast and accurate laboratory tests of ADAMTS13 activity in patient samples. Using FCS, we investigated the increased sensitivity of the mutant with enzyme kinetic studies that exhibited strongly increased cleavage rates and a cooperative Hill-type behaviour. Cooperativeness was not observed for cleavage of denatured VWF-wt [Lippok et al., 2014, submitted]. Due to the destabilized structure of the mutant, several binding sites might be accessible at the same time, which may lead to cooperative binding of the protease with prolonged dwell times at each of the multimers.

We showed that using rVWF-G1629E as substrate allows to detect ADAMTS13 activities down to 0.5 % of the physiological level, which is 5-fold more sensitive than most commonly used assays. MDS showed that the G1629E mutation induced local structural variations of the A2 domain, hence corroborating the hypothesis that the mutated regions allows facilitated access to the cleavage site. In addition to its high sensitivity, the application of the mutant renders shear flow as well as denaturing agents unnecessary, while still allowing for measurements with full-length VWF.

Recently, Lotta et al. presented a similarly sensitive assay based on SELDI-TOF mass

spectroscopy [13]. Instead of full-length VWF, they used a VWF fragment (VWF73) as substrate, which was fixed to a surface, to measure the residual plasmatic activity of ADAMTS13 in TTP patients. The cleavage reaction was performed for 16 hours. Further frequently used, well-established diagnostic ADAMTS assays, rely on either denaturing VWF substrate or on subsequent labeling via antibodies against VWF [12]. In contrast, the assay presented here does not require surface immobilization, which minimizes possible sources of error. Moreover, subsequent treatments such as washing, purification, or labeling are unnecessary, and the assay merely runs for an hour.

The use of a recombinant fluorescent substrate is advantageous in many ways. Recombinant proteins are applicable as a reliable standard for activity tests, which in principle might also allow absolute calibration of ADAMTS13 level. Moreover, the self-fluorescence of the substrate allows for fast read-out of the full blood assay without additional labeling or purification steps, which may strongly accelerate currently used approaches, while avoiding possible sources of error. This includes the possibility of fluorescent read-out of quantitative gel electrophoresis, which renders the use of expensive fluorescent antibodies for detection unnecessary.

We presented here one VWF mutant that is suited for ADAMTS13 detection due to its increased sensitivity to ADAMTS13. However, there are much more naturally occurring mutations known to be sensitive for distinct VWF functions and binding partners. While these mutants lead to diseases in patients, they might provide opportunities to increase sensitivity and specificity in diagnostics. This may open a wide field of enhancements not only for the diagnostics of TTP.

Acknowledgements: This work was supported with seed funds from the Center for NanoScience and the priority network within the Deutsche Forschungsgemeinschaft SHENC (Shear Flow Regulation of Hemostasis - bridging the gap between Nanomechanics and Clinical presentation), DFG research unit FOR 1543. We grateful acknowledge all SHENC members. S.L. thanks the support by the Elite Network of Bavaria.

REFERENCES

1. Sadler, J. E., Biochemistry and genetics of von Willebrand factor. *Annual review of biochemistry* 1998, 67, (1), 395-424.

2. Ruggeri, Z. M., Structure of von Willebrand factor and its function in platelet adhesion and thrombus formation. *Best Practice & Research Clinical Haematology* 2001, 14, (2), 257-279.

3. Furlan, M.; Robles, R.; Lamie, B., Partial purification and characterization of a protease from human plasma cleaving von Willebrand factor to fragments produced by in vivo proteolysis. *Blood* 1996, 87, (10), 4223-4234.

4. Furlan, M.; Robles, R.; Galbusera, M.; Remuzzi, G.; Kyrle, P. A.; Brenner, B.; Krause, M.; Scharrer, I.; Aumann, V.; Mittler, U., Von Willebrand factor-cleaving protease in thrombotic thrombocytopenic purpura and the hemolytic-uremic syndrome. *New England Journal of Medicine* 1998, 339, (22), 1578-1584.

5. Tsai, H.-M.; Lian, E. C.-Y., Antibodies to von Willebrand factor-cleaving protease in acute thrombotic thrombocytopenic purpura. *New England Journal of Medicine* 1998, 339, (22), 1585-1594.

6. Bianchi, V.; Robles, R.; Alberio, L.; Furlan, M.; Lämmle, B., Von Willebrand factor-cleaving protease (ADAMTS13) in thrombocytopenic disorders: a severely deficient activity is specific for thrombotic thrombocytopenic purpura. *Blood* 2002, 100, (2), 710-713.

7. Sadler, J. E., Von Willebrand factor, ADAMTS13, and thrombotic thrombocytopenic purpura. *Blood* 2008, 112, (1), 11-18.

8. Dent, J. A.; Berkowitz, S. D.; Ware, J.; Kasper, C. K.; Ruggeri, Z. M., Identification of a cleavage site directing the immunochemical detection of molecular abnormalities in type IIA von Willebrand factor. *Proceedings of the National Academy of Sciences* 1990, 87, (16), 6306-6310.

9. Zhang, X.; Halvorsen, K.; Zhang, C. Z.; Wong, W. P.; Springer, T. A., Mechanoenzymatic cleavage of the ultralarge vascular protein von Willebrand factor. *Science* 2009, 324, (5932), 1330-1334.

10. Gao, W.; Anderson, P. J.; Majerus, E. M.; Tuley, E. A.; Sadler, J. E., Exosite interactions contribute to tension-induced cleavage of von Willebrand factor by the antithrombotic ADAMTS13 metalloprotease. *Proceedings of the National Academy of Sciences* 2006, 103, (50), 19099-19104.

11. Baldauf, C.; Schneppenheim, R.; Stacklies, W.; Obser, T.; Pieconka, A.; Schneppenheim, S.; Budde, U.; Zhou, J.; Gräter, F., Shear-induced unfolding activates von Willebrand factor A2 domain for proteolysis. *Journal of Thrombosis and Haemostasis* 2009, 7, (12), 2096-2105.

12. Studt, J.-D.; Böhm, M.; Budde, U.; Girma, J.-P.; Varadi, K.; Lämmle, B., Measurement of von Willebrand factor-cleaving protease (ADAMTS-13) activity in plasma: a multicenter comparison of different assay methods. *Journal of Thrombosis and Haemostasis* 2003, 1, (9), 1882-1887.

13. Lotta, L. A.; Wu, H. M.; Mackie, I. J.; Noris, M.; Veyradier, A.; Scully, M. A.; Remuzzi, G.; Coppo, P.; Liesner, R.; Donadelli, R., Residual plasmatic activity of ADAMTS13 is correlated with phenotype severity in congenital thrombotic thrombocytopenic purpura. *Blood* 2012, 120, (2), 440-448.

14. Kokame, K.; Nobe, Y.; Kokubo, Y.; Okayama, A.; Miyata, T., FRETS-VWF73, a first fluorogenic substrate for ADAMTS13 assay. *British journal of haematology* 2005, 129, (1), 93-100.

15. Kato, S.; Matsumoto, M.; Matsuyama, T.; Isonishi, A.; Hiura, H.; Fujimura, Y., Novel monoclonal antibody-based enzyme immunoassay for determining plasma levels of ADAMTS13 activity. *Transfusion* 2006, 46, (8), 1444-1452.

16. Furlan, M.; Robles, R.; Solenthaler, M.; Lämmle, B., Acquired deficiency of von Willebrand factor-cleaving protease in a patient with thrombotic thrombocytopenic purpura. *Blood* 1998, 91, (8), 2839-2846.

17. Gerritsen, H. E.; Turecek, P. L.; Schwarz, H. P.; Lämmle, B.; Furlan, M., Assay of von Willebrand factor (vWF)-cleaving protease based on decreased collagen binding affinity of degraded vWF: a tool for the diagnosis of thrombotic thrombocytopenic purpura (TTP). *Thrombosis and Haemostasis* 1999, 82, (5), 1386-1389.

18. Böhm, M.; Vigh, T.; Scharrer, I., Evaluation and clinical application of a new method for measuring activity of von Willebrand factor-cleaving metalloprotease (ADAMTS13). *Annals of hematology* 2002, 81, (8), 430-435.

19. Obert, B.; Tout, H. l. n.; Veyradier, A. s.; Fressinaud, E.; Meyer, D.; Girma, J.-P., Estimation of the von Willebrand factor-cleaving protease in plasma using monoclonal antibodies to vWF. *Thrombosis and Haemostasis* 1999, 82, (5), 1382-1385.

20. Hassenpflug, W. A.; Budde, U.; Obser, T.; Angerhaus, D.; Drewke, E.; Schneppenheim, S.; Schneppenheim, R., Impact of mutations in the von Willebrand factor A2 domain on ADAMTS13-dependent proteolysis. *Blood* 2006, 107, (6), 2339-2345.

21. Lippok, S.; Obser, T.; Müller, J. P.; Stierle, V. K.; Benoit, M.; Budde, U.; Schneppenheim, R.; Rädler, J. O., Exponential Size Distribution of von Willebrand Factor. *Biophysical journal* 2013, 105, (5), 1208-1216.

22. Zanardelli, S.; Chion, A. C. K.; Groot, E.; Lenting, P. J.; McKinnon, T. A. J.; Laffan, M. A.; Tseng, M.; Lane, D. A., A novel binding site for ADAMTS13 constitutively exposed on the surface of globular VWF. *Blood* 2009, 114, (13), 2819-2828.

23. Zhang, Q.; Zhou, Y.-F.; Zhang, C.-Z.; Zhang, X.; Lu, C.; Springer, T. A., Structural

specializations of A2, a force-sensing domain in the ultralarge vascular protein von Willebrand factor. *Proceedings of the National Academy of Sciences* 2009, 106, (23), 9226-9231.

24. Spoel, D. V. D.; Lindahl, E.; Hess, B.; Groenhof, G.; Mark, A. E.; Berendsen, H. J. C., GROMACS: fast, flexible, and free. *Journal of Computational Chemistry* 2005, 26, (16), 1701-1718.

25. Hess, B.; Kutzner, C.; van der Spoel, D.; Lindahl, E., GROMACS 4: Algorithms for highly efficient, load-balanced, and scalable molecular simulation. *Journal of Chemical Theory and Computation* 2008, 4, (3), 435-447.

26. Pronk, S.; Páll, S.; Schulz, R.; Larsson, P.; Bjelkmar, P.; Apostolov, R.; Shirts, M. R.; Smith, J. C.; Kasson, P. M.; van der Spoel, D.; Hess, B.; Lindahl, E., GROMACS 4.5: a high-throughput and highly parallel open source molecular simulation toolkit. *Bioinformatics* 2013, 29, (7), 845-854.

27. Grässle, S.; Huck, V.; Pappelbaum, K. I.; Gorzelanny, C.; Aponte-Santamaría, C.; Baldauf, C.; Gräter, F.; Schneppenheim, R.; Obser, T.; Schneider, S. W., Von Willebrand factor directly interacts with DNA from neutrophil extracellular traps. *Arteriosclerosis, Thrombosis, and Vascular Biology* 2014, 34, (7), 1382-1389.

28. Schrödinger, L. L. C., The PyMOL Molecular Graphics System, Version~1.3r1 2010.

29. Amadei, A.; Linssen, A. B. M.; Berendsen, H. J. C., Essential dynamics of proteins. *Proteins: Structure, Function, and Genetics* 1993, 17, (4), 412-425.

30. Costescu, B. I.; Gräter, F., Time-resolved force distribution analysis. *BMC Biophysics* 2013; 6, (1), 5.

31. Elson, E. L.; Magde, D., Fluorescence correlation spectroscopy. I. Conceptual basis and theory. *Biopolymers* 1974, 13, (1), 1-27.

32. Jin, M.; Cataland, S.; Bissell, M.; Wu, H. M., A rapid test for the diagnosis of thrombotic thrombocytopenic purpura using surface enhanced laser desorption/ionization time-of-flight (SELDI-TOF)-mass spectrometry. *Journal of Thrombosis and Haemostasis* 2006, 4, (2), 333-338.

33. Jin, M.; Casper, T. C.; Cataland, S. R.; Kennedy, M. S.; Lin, S.; Li, Y. J.; Wu, H. M., Relationship between ADAMTS13 activity in clinical remission and the risk of TTP relapse. *British journal of haematology* 2008, 141, (5), 651-658.

34. Singh, I.; Themistou, E.; Porcar, L.; Neelamegham, S., Fluid shear induces conformation change in human blood protein von Willebrand factor in solution. *Biophysical journal* 2009, 96, (6), 2313-2320.

FIGURES

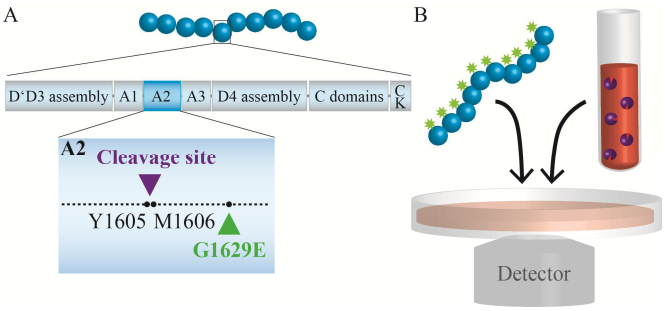

Figure 1: ADAMTS13 activity assay using enzyme substrate rVWF-G1629E and FCS. A The mutant rVWF-G1629E exhibits a mutation close to the ADAMTS13 specific cleavage site that facilitates opening of the VWF A2 domain. **B** FCS measures the number density of eGFP labeled rVWF-G1629E added to patient plasma samples containing ADAMTS13 and hence allows for on-line monitoring the cleavage mediated by ADAMTS13.

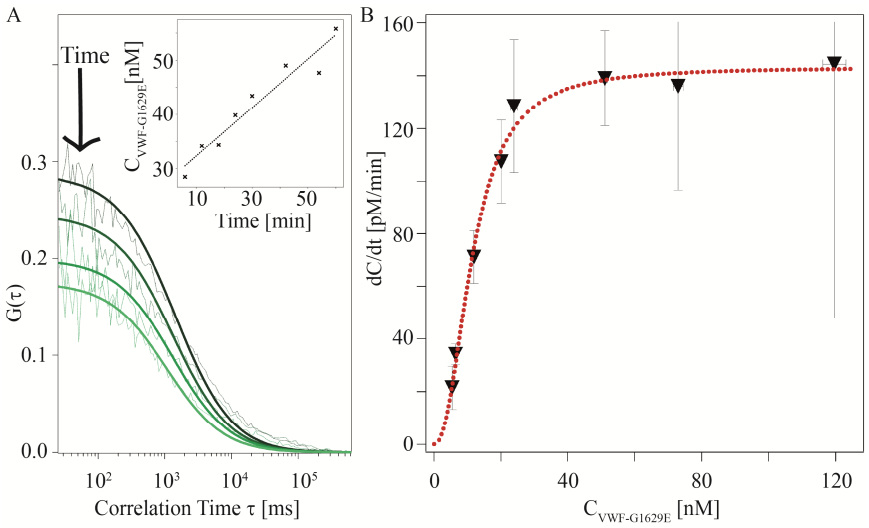

Figure 2: FCS-based assay for rVWF-G1629E cleavage detection. A Cleavage detection via FCS. The amplitude of the autocorrelation curve G(0) is inversely proportional to the number of fluorescent molecules N in the detection volume and decreases during cleavage according to $G(0) \propto N$. Inset: The increase in particle concentration is plotted over cleavage time. The slope of the curve defines the cleavage rate dC/dt. **B** Enzyme kinetics of rVWF-G1629E in 0.5% NP. We measured Hill-type activity with cooperativity coefficient n = 2.3. A half maximum cleavage rate at 11.5 nM rVWF-G1629E indicates strongly increased cleavage compared to VWF-wt.

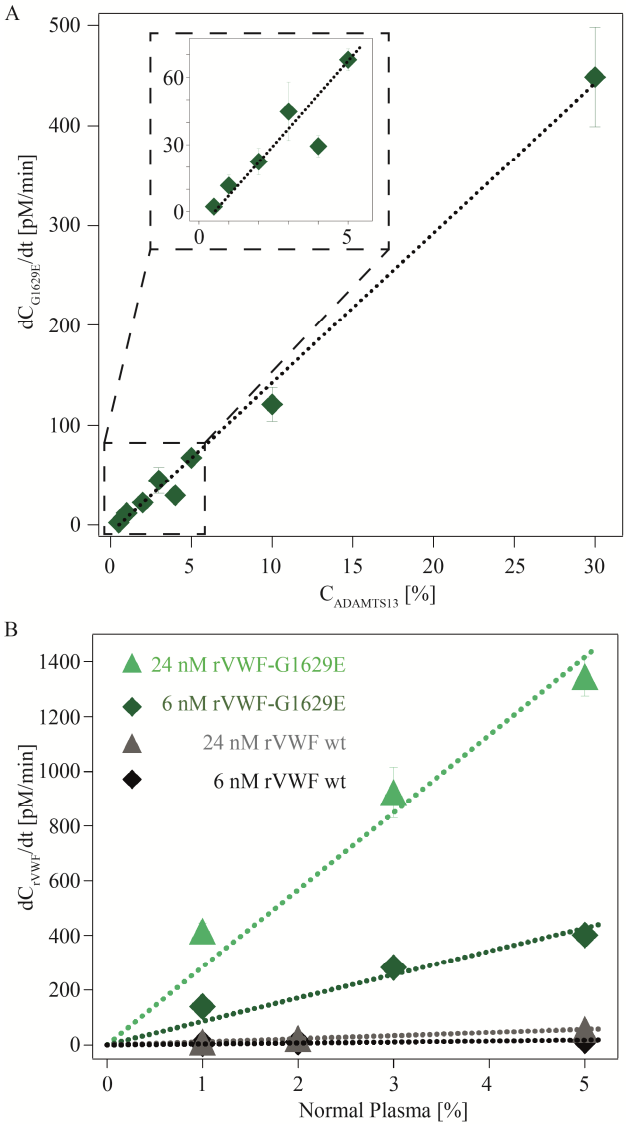

Figure 3: Linear rate response to ADAMTS13 concentration. A ADAMTS13 activity in buffer. Cleavage rates increase linearly with ADAMTS13 concentration, depicted in % of the level in normal plasma. The assay quantifies cleavage rates down to ADAMTS13 concentrations of 0.5 %, as highlighted in the inset. **B** Cleavage of rVWF-G1629E and rVWF-wt in normal plasma. rVWF-G1629E cleavage is clearly quantifiable down to 1 % NP concentration (green). For a 4-fold increased substrate concentration of 24 nM (green triangles), the signal-to-noise ratio is considerably increased and the measured cleavage rate at 1% NP is well above the detection limit of about 2 pM/min. Cleavage of wild-type rVWF results in more than 20-fold decreased cleavage rates (grey and black), which significantly reduces the signal-to-noise ratio at disease-related low ADAMTS13 concentrations. Additionally, for cleavage of wild-type rVWF, increased measurement times and denaturing buffer conditions had to be used. Fits are indicated as dotted lines.

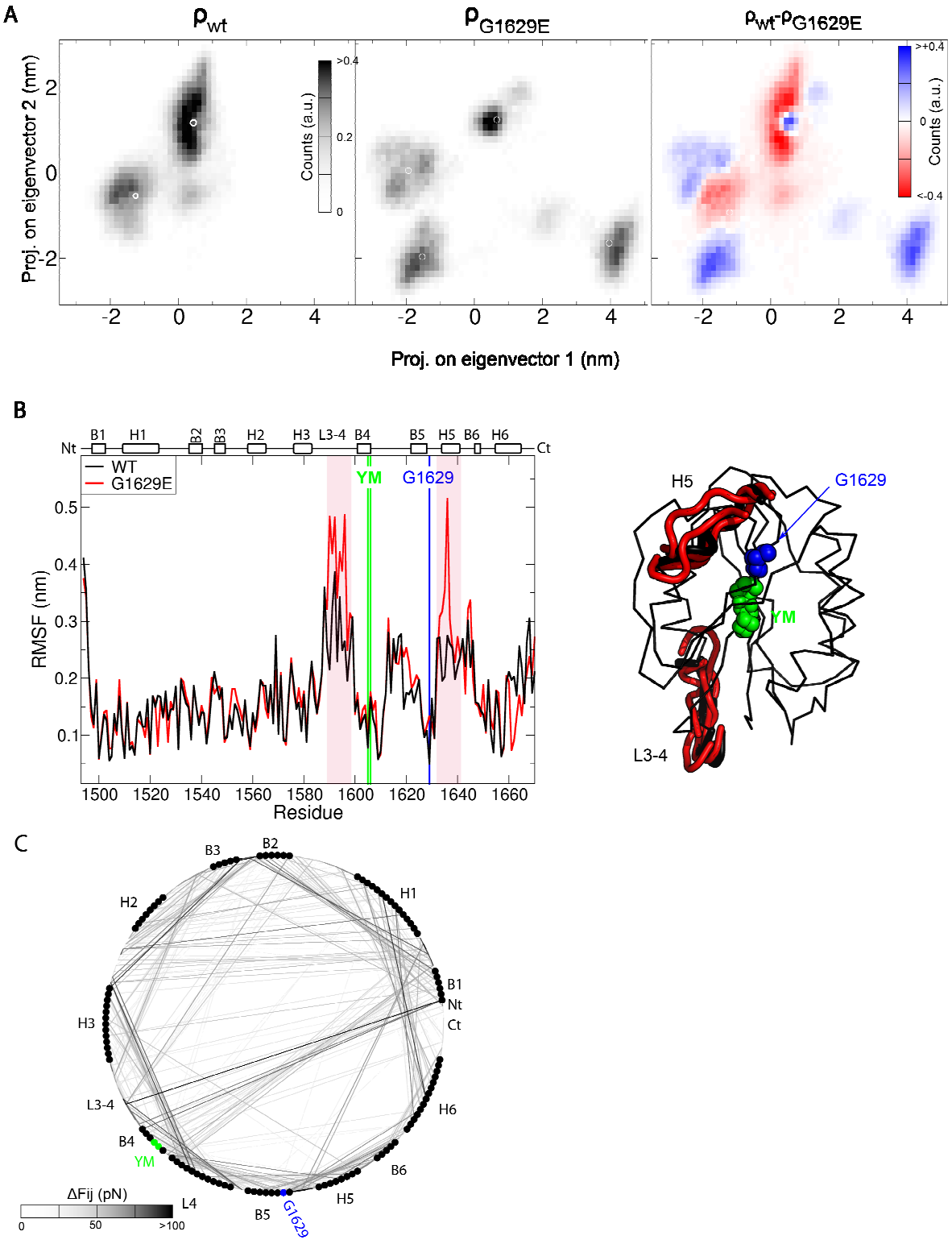

Figure 4: MD simulations reveal structural and mechanical changes in the VWF A2 domain upon G1629E mutation. A PCA analysis of the A2 domain yielded two main collective eigenvectors. Populated regions of the subspace constituted by these two vectors are shown for wt (left) and mutant (middle). Differences in population density are depicted according to the color scales. Regions in red correspond to areas only visited by the wt and regions in blue visited by the mutant domain. The mutation induced a broader

range of conformations than measured for the wt. **B Left** RMSF of each residue of wt (black) and mutant (red). The secondary structure of the A2 domain is indicated at the upper part, highlighting the N- and C-terminus (Nt and Ct, respectively), the strands (B1...B6), the helices (H1...H6), and the loop connecting H3 with B4 (L3-4). The RMSF for G1629 is highlighted in blue, the one for the ADAMTS13 cleavage site Y1605-M1606 (YM) in green. For the mutant, a broader conformational variability due to local fluctuations is observed at the helix H5 and the loop L3-4 (accentuated in red). **Right** Structure of the A2 domain (ribbon representation). The YM cleavage site (green) and residue G1629 (blue) are highlighted as spheres. Various representative conformations are shown for the regions with increased RMSF for the mutant compared to the wild type domain (L3-4 and B5, tubes). **C** Changes in the internal stress of the protein upon G1629E mutation recovered by FDA. The secondary structure of the protein is spanned around the circle. Each point of the circle corresponds to a residue, ranging from the N-terminus at 0 degree to the C-terminus at 360 degree. The cleavage site is highlighted in green and G1629 in blue. Each line connecting two points of the circle corresponds to the difference Δf_{ij} for the residue pair (i,j). Here, $\Delta f_{ij}=|\langle F_{ij}(wt)\rangle-\langle F_{ij}(G1629E)\rangle|$, with $\langle F_{ij}(wt)\rangle$ the time-averaged pair-wise force of the residue pair (i,j) in its wild type form and $\langle F_{ij}(wt)\rangle$ in its mutated form. Δf_{ij} is displayed according to the color scale at the bottom, varying from no change (white) to substantial change (black) in the internal stress. The mutation perturbed the internal stress, both locally at the mutation site and at distant parts, see e.g. lines connecting the region near G1629 with structure elements L4, B5, H5 and H1.

7

Binding of PDI to VWF and its Role on Dimerization

The biosynthesis of VWF multimers is a highly sophisticated process that is organized by spatial separation of each step in different cellular compartments due to varying pH value requirements. It is known that VWF dimerization occurs in the endoplasmatic reticulum (ER), where intermolecular disulfide bonds in the VWF CK domains are formed. However, the identity of the enzyme facilitating this disulfide bond formation had not yet been identified. While investigating the localization of VWF mutants within the ER, our cooperation partners recently observed co-localization of VWF with protein disulfide isomerase (PDI), an essential catalyst and chaperone for protein folding within the ER (82). Thus, we hypothesized that PDI might be involved in VWF dimerization.

To confirm this hypothesis, we performed binding studies with FCS and MST and measured specific binding of PDI to VWF wildtype with $K_D = 236 \pm 66\ nM$. We showed that PDI binds VWF exclusively within the CK-domain since binding of PDI to the isolated CK domain exhibits a similar K_D value ($258 \pm 104\ nM$). Together with immunofluorescence data of VWF with selected CK-domain mutations (Dr. Brehm), we found that the PDI binding site is located N-terminally of Cys2773. Co-localization measurements of pathologically relevant CK-domain mutants, which were performed in the group of Prof. Schneppenheim, showed that an additional ER polymerase, namely ERp57, is a key player in the repair of misfolded VWF mutants. This indicates the role of PDI in VWF dimerization rather than in the repair of misfolded VWF. Altogether, our findings show for the first time a direct binding of VWF and PDI. Moreover, we shed light on the mechanism of VWF dimerization both in VWF wt and in CK-domain mutants. This might help to answer open questions in the context of the physiological relevance of PDI in hemostasis that are currently debated.

The experimental data and the resulting conclusions are presented in the following manuscript:

S. Lippok, G. König, T. Obser, R. Schneppenheim, J.O. Rädler, M.A. Brehm. "The (patho)-physiological Relevance of Protein Disulfide Isomerase Binding to von Willebrand Factor." *to be submitted to Journal of biological chemistry*

The (patho)-physiological relevance of Protein Disulfide Isomerase binding to von Willebrand Factor

Svenja Lippok[1], Gesa König[2], Tobias Obser[2],

Reinhard Schneppenheim[2], Joachim O. Rädler[1], Maria A. Brehm[2,*]

[1] Faculty of Physics and Center for NanoScience, Ludwig Maximilian University, Munich, Germany

[2] Department of Paediatric Haematology and Oncology, University Medical Centre Hamburg-Eppendorf, Hamburg, Germany

*Corresponding author: Phone: +49 (040) 7410- 58523; E-mail: m.brehm@uke.de

Keywords: von Willebrand factor; Protein disulfide isomerase, dimerization

Running title: *PDI-VWF-interaction*

ABSTRACT

Multimeric von Willebrand factor (VWF) plays a pivotal role in primary hemostasis mediating binding of platelets to the ruptured vessel wall. Its biosynthesis occurs in spatially separated steps due to varying pH value requirements. The dimerization takes place at neutral pH in the endoplasmatic reticulum (ER) by the formation of three intermolecular disulfide bonds between the CK-domains of two VWF monomers. Here, we investigated the role of protein disulfide isomerase (PDI), an essential catalyst and chaperone of protein folding within the ER, in VWF dimerization. Binding studies based on Fluorescence Correlation Spectroscopy (FCS) and Microscale Thermophoresis (MST) identified specific binding of PDI to wildtype (wt) VWF with a dissociation constant of $K_D = 236 \pm 66$ nM. The interaction of PDI and the isolated VWF CK-domain exhibited a similar K_D value (258 ± 104 nM) indicating that PDI binds solely to the CK domain where dimerization occurs. Moreover, our immunofluorescence studies revealed that VWF CK-domain mutants are associated with von Willebrand disease (VWD) type 2A/IID through two mechanisms: either inhibition of PDI-catalyzed disulfide bond formation, or inhibition of PDI binding due to misfolding. The here described direct binding of PDI to VWF indicates PDI as the VWF dimerizing enzyme, and sheds new light on the mechanism of dimerization and the pathophysiological consequences of its inhibition by genetic alterations.

INTRODUCTION

Von Willebrand factor (VWF) is an essential glycoprotein for platelet-dependent primary hemostasis. The shear-induced transition between a globular and a stretched conformation of VWF high molecular weight multimers (HMWM) leads to exposition of binding sites for VWF partners and thus the initiation of platelet adhesion and aggregation. Because smaller multimers are more resistant to shear forces than larger ones, VWF's shear flow-activated functions are dependent on its multimeric structure.

The biosynthesis of VWF-HMWM's is a highly sophisticated multistep process, which involves spatial separation of each step in order to optimize for distinct pH value conditions. It is initiated in the cytoplasm by the translation of the VWF pre-pro-monomers. N-glycosylation and quantitative dimerization occur in the endoplasmic reticulum (ER). Processing of high mannose glycans and sulfation as well as O-glycosylation, multimerization, pro-peptide cleavage, and tubulation take place in the Golgi apparatus. Until stimulated release, the HMWM's are stored in Weibel-Palade bodies [1-3].

Multimerization as well as dimerization are established by the formation of intermolecular disulfide bonds. The C-terminal cysteine knot (CK) domain contains 11 cysteines [4]. Recently, crystal structure analysis revealed that eight of these cysteines form intra-chain disulfide bonds, while three, namely, Cys2771, Cys2773, and Cys2811, mediate the inter-chain connections for dimerization [5]. The latter are encased in the intra-chain cysteine knots resulting in a rigid structure that is resistant to the high shear forces, which affect VWF in the circulation. Mutations of the cysteines present in the CK-domain can lead to the bleeding

disorder von Willebrand disease (VWD) type 2A/IID. C-terminal dimerization is strongly disturbed in these mostly heterozygous patients leading to odd-numbered multimers by attachment of mutant monomers to wildtype multimers by N-terminal disulfide bond formation [6].

The assembly of mature VWF-HMWM by multimerization is well understood [7]. It occurs in the acidic environment of the trans-Golgi network where dimers are multimerized by formation of interchain disulfide bonds between the D'-D3 domains of VWF dimers. The formation of these N-terminal disulfide bonds is facilitated by the VWF pro-peptide that contains two D domains that both harbor a CGLC protein disulfide isomerase consensus sequence, which have been shown to be essential for multimerization. The activation of this intrinsic isomerase is strongly pH-dependent. Enabled by the lower pH of the Golgi apparatus, it is activated by protonation of histidine residues adjacent to the CGLC sequence. Interestingly, mutations within the CGLC sequences in the propeptide inhibit multimerization but do not affect dimerization [8,9]. The relevance of a third CGLC consensus sequence in the D4 domain has not been elucidated yet. However, genetic alterations within this sequence neither influence multimerization nor dimerization [unpublished data R. Schneppenheim and U. Budde]. Therefore, dimerization does not seem to be performed by an intrinsic protein disulfide isomerase activity within VWF. To date it is not known, though, which protein catalyzes the highly complex formation of these bonds. Since dimerization occurs within the ER, it requires an ER-localized protein disulfide isomerase. Allen et al. showed that calnexin and ERp57, two proteins specialized in glycoprotein folding, weekly co-localize with VWF and are involved in VWF processing. Moreover, mutations within the VWF propeptide prolong ER localization and increase interaction with calnexin and ERp57 [10]. These data indicate that calnexin and ERp57 are involved in the initial folding of VWF and the correction of VWF misfolding. Protein disulfide isomerase (PDI) is one of the few members of the PDI family that is known to catalyze both disulfide formation as well as isomerization. Although it is an essential folding catalyst and chaperone of the ER [11-14], the role of PDI in VWF dimerization has not yet been investigated.

Since it has previously been described that VWF co-localizes with PDI, merely, to prove VWF ER-localization, we further investigated if PDI is the required protein for VWF dimerization. We performed extensive binding studies employing immunoprecipitation, Microscale Thermophoresis (MST), and Fluorescence Correlation Spectroscopy (FCS) and showed that PDI directly binds to VWF. Using Immunofluorescence studies, we investigated co-localization of selected VWF CK-domain mutants and PDI or ERp57. Our data indicate the role of PDI rather in VWF dimerization than in the repair of misfolded VWF.

MATERIALS AND METHODS

Cell culture and expression of wtVWF and VWF mutants in HEK293 cells. HEK293 cells were cultured in Dulbecco Modified Eagle Medium (DMEM, Invitrogen) with 10 % [v/v] fetal bovine serum (Invitrogen) and 1 % penicillin/streptavidin (Invitrogen) at 37°C and 5 % CO_2. For immunofluorescence, HEK293 cells were seeded in Ibidi treat 8-well µ-slides (Ibidi, Martinsried, Germany) 24h prior transfection with Lipofectamine LTX (Invitrogen) and VWF-plasmid-constructs in vector pcDNA3 [15].

Immunofluorescence was performed as previously described [16] 48h post transfection. Antibodies used were: rabbit anti-VWF (DAKO; 1:1,000), mouse anti-PDI (abcam, 1:100), mouse anti-ERp57 (Santa Cruz, 1:100) goat anti-rabbit AF488 (Invitrogen, 1:5,000), goat anti-mouse AF 546 (Invitrogen, 1:5,000). Images were captured at RT with a confocal microscope (LSM 510; Carl Zeiss, Jena, Germany) using a Plan Apochromat 63×/1.4 oil DIC objective, ZEN 2009 software (Carl Zeiss), and the following settings: image size of 1776 × 1776 and 8 bit, laser power of the 543 and 488 lasers was set to 100 % and 24 %, respectively. After image capturing, the original LSM files were converted into TIFF files with the LSM Image browser software (Carl Zeiss).

Co-Immunoprecipitation. Lysates were prepared from HEK293 cells in M-PER Mammalian Protein Extraction Reagent (Thermo Fisher Scientific Inc., Rockford, IL, USA) supplemented with Complete Protease Inhibitor cocktail (Roche, Penzberg, Germany) according to the manufacturer's instructions. To reduce background caused by nonspecific adsorption of proteins, 50 µl of protein G-agarose suspension (Roche, Penzberg, Germany) was added per 1 ml lysate and incubated for 3 h at 4°C on a rocking platform. Beads were pelleted by centrifugation (20 s at 12,000xg), and supernatant was transferred into a fresh tube. Then, 2 µg of rabbit anti-VWF (DAKO, Germany) were added to 1 ml lysate each and incubated for 1 h at 4°C on a rocking platform. After addition of 50 µl protein G-agarose beads, incubation was continued overnight. Agarose-bead-antibody-antigen complexes were collected by centrifugation (20 s at 12,000xg), and the supernatant was discarded. Beads were washed for 10 min in washing buffer 1 [50 mM Tris-HCl (pH 7.5), 150 mM NaCl, 1 % Nonidet P40 (v/v), 0.5 % sodium deoxycholate (w/v) supplemented with Complete Protein Inhibitor cocktail (Roche, Penzberg, Germany)] at 4°C. Supernatant was removed after centrifugation and the wash was repeated once with washing buffer 1, twice with washing buffer 2 [50 mM Tris-HCl (pH 7.5), 500 mM NaCl, 0.1 % Nonidet 40 (v/v), 0.05 % sodium deoxycholate (w/v)], and twice with washing buffer 3 [50 mM Tris-HCl (pH 7.5), 0.1 % Nonidet P40 (v/v), 0.05 % sodium deoxycholate (w/v)]. Pelleted beads and 1 µg of input lysate were resuspended separately in SDS sample buffer, incubated 10 min at 95°C, separated by SDS-PAGE, and transferred onto a PVDF membrane using standard Western blotting techniques. PDI was detected by mouse anti-PDI antibody (Cell Signaling). The secondary goat anti-mouse antibody was conjugated with HRP (DAKO).

Sample preparation for binding studies. PDI human (Genway Biotech. Inc, San Diego, CA) was labeled with Alexa Fluor 647 carboxylic acid, succinimidyl ester (Life Technologies GmbH, Darmstadt, Germany). Measurements were conducted in 5 mM Tris buffer containing

500 mM NaCl and 2.5 mM $CaCl_2$ at 21°C. A fixed concentration of labeled PDI (MST: 25 nM, FCS: 3 nM) was titrated against varying rVWF, rVWF monomers (p.Cys2771Arg), and rVWF-CK-domain concentrations. Samples were incubated for 30 minutes at room temperature before measurement.

Microscale Thermophoresis. Thermophoresis is the directed flow of molecules in a temperature gradient. This thermophoretic movement is opposed by mass diffusion resulting in a stationary spatial concentration distribution [17,18]

$$C/C_0 = \exp(-S_T(T - T_0))$$

in the temperature rise $\Delta T = T\text{-}T_0$ at the respective spot. It is described by the Soret coefficient S_T, a measure of the strength of the thermophoretic flow compared with ordinary diffusion, which depends on size, charge, solvation entropy and conformation of the molecules. MST detects this movement to analyze the interactions of proteins [19,20].
Data analysis was conducted as described in detail elsewhere [19,20]. In short: The thermophoretic depletion, i.e. the fraction warm fluorescence F^{II}/cold fluorescence F^{I}, reports the fraction of bound receptor molecules. The binding of ligands to a specific receptor is described by the dissociation constant K_D, a measure for the affinity of the binding reaction under equilibrium conditions. To obtain the dissociation constant from the MST data, the binding curves were fitted by a function derived from the law of mass action:

$$\frac{C_{BL}}{C_{B_0}} = \frac{\left(C_{L_0} + C_{B_0} + K_D\right) - \sqrt{\left(C_{L_0} + C_{B_0} + K_D\right)^2 - 4C_{L_0}C_{B_0}}}{2C_{B_0}}$$

with the total concentration of receptor C_{B0} (PDI), the total amount of added ligand at each point C_{L0} (VWF binding sites), and the concentration of bound receptor molecules C_{BL} (PDI bound to VWF).
For MST experiments, a Monolith NT.115 system (NanoTemper Technologies, Munich, Germany) was used. 15% IR-laser and 20% LED power were applied for generating local temperature gradients and illumination, respectively. Laser on and off times were set at 60 s and 10 s. Cold fluorescence was averages over 5 s before the temperature jump while the warm fluorescence signal was averaged over 30 s starting 5 s after the temperature jump. About 5 µl sample volumes were filled into standard treated capillaries (Nanotemper Technologies) for measurements.

Fluorescence Correlation Spectroscopy. Fluorescence Correlation Spectroscopy (FCS) measures the dynamics of fluorescently labeled molecules diffusing in and out of a confocal volume due to Brownian motion. It analyzes the time-dependent fluctuations of the fluorescence intensity [21-25] using the autocorrelation function $G(\tau)$ of the intensities I(t):

where $\langle\ \rangle$ denotes the time average. For molecules diffusing freely in a Gaussian-shaped probe volume with radial dimension ω_r and axial dimension ω_z, $G(\tau)$ is derived analytically to [22]:

$$G(\tau) = \frac{1}{N}\left(1+\frac{\tau}{\tau_D}\right)^{-1}\left(1+\frac{\tau}{(\omega_z/\omega_r)^2\tau_D}\right)^{-1/2}$$

with the average number of molecules in the confocal volume N and the diffusion time τ_D, the time a molecule requires crossing the focal width. This analysis allows for calculation of the characteristic diffusion coefficient $D = \omega_r^2/\tau_D$.

Data analysis: In a system composed of multiples of distinct species, the autocorrelation function can be generalized by summing the autocorrelation functions $g_i(\tau)$ of all species:

$$G(\tau) = \frac{\sum q_i^2 N_i g_i(\tau)}{\left(\sum q_i N_i\right)^2}$$

with brightness q_i and particle number N_i of species i. Binding events can be analyzed assuming a two component mixture of free and bound fluorescent receptor molecules. If binding does not change the brightness of the receptor molecule, i.e. $q_{bound} = q_{free}$, this equation can be simplified to:

$$G(\tau) = \frac{1}{N}\left[(1-f)\cdot g(\tau_{free}) + f\cdot g(\tau_{bound})\right]$$

where f denotes the fraction of bound receptor molecules and N the total number of receptor molecules [26,27]. This equation is used to analyze binding of PDI to VWF-p.Cys2771Arg and rVWF CK domain, which possess a constant number of binding sites. In the case of PDI binding to rVWF, the number of rVWF binding sites scales with the number of monomers, i.e., the rVWF size. Therefore, the brightness q_i of a PDI-rVWF complex depends on the number of PDI molecules bound to the rVWF molecule. This number scales both with the fraction bound and with the size of the rVWF molecule $q_i = fiN(i)$ with the VWF size distribution $N(i)=(p-1)p^{i-1}$ that was published recently [28]. As shown in Lippok et al., 2013, FCS analysis of the VWF size distribution can be simplified using single component analysis approach with the average diffusion time and for the brightness the average VWF size $\bar{i}$. With this, equation () can be written in its normalized form as:

$$G(\tau) = (1-f)g(\tau_{free}) + f^3\bar{i}\,g(\tau_{bound})$$

which was used for fitting binding of PDI to rVWF.

FCS experiments were performed on an Axiovert 200 microscope with a ConfoCor 2 unit (Carl Zeiss, Jena, Germany) equipped with an 40x (NA=1.2) water immersion appochromat objective (Carl Zeiss Jena). For sample illuminations a HeNe-laser 633 laser was used. Samples were measured in eight well LabTek I chamber slides (Nunc, Rochester, NY) three times for 10x180 s.

RESULTS

PDI binds to VWF exclusively within its CK-domain. In multiple publications, the co-localization of VWF and PDI has merely been used to illustrate ER localization of VWF [29,30] but the physiological relevance of this potential interaction has not been elucidated yet. Since co-localization per se does not prove direct interaction of two proteins, we performed extensive binding studies employing three independent approaches to determine if PDI actually binds to VWF. Co-immunoprecipitation of PDI and wtVWF (Figure 1A, wt) showed that both proteins are part of the same protein complex. To further prove a direct interaction of VWF and PDI, we performed Microscale Thermophoresis (MST) and Fluorescence Correlation Spectroscopy (FCS) using recombinant fluorescently-labeled PDI and recombinant wtVWF (Figure 1B-G). The dissociation constants were determined to be $K_D = 236 \pm 66$ nM and $K_D = 282 \pm 123$ nM by MST and FCS, respectively. Therefore, the K_D values measured by these two methods were in agreement to each other and prove direct binding of PDI to VWF.

VWF is a glycoprotein rich in cysteine residues that determine the tertiary structure of the VWF A1, A3 and C domains by formation of disulfide bonds. In the C-terminal CK-domain, cysteines are not only bonded to form structural intramolecular disulfide bonds but also to dimerize monomers through intermolecular disulfide bonds [5]. To investigate whether PDI is involved in protein folding - which would require binding to all VWF domains - or specifically in dimerization of the CK-domains, we further performed MST of PDI and the CK-domain only. Binding to the isolated CK-domain results in a K_D of 258 ± 104 nM (MST) (Figure 1D). Since the interaction of PDI with both the isolated CK domain and full-length VWF exhibit similar K_D values, our data indicate that PDI exclusively binds to the CK-domain of VWF.

Effect of CK-domain mutations on PDI-VWF-interaction. The recently solved crystal structure of the VWF CK-domain revealed that the three disulfide bonds Cys2771-2773', Cys2771'-2773 and Cys2811-2811' are formed to dimerize two VWF monomers [5], but the enzyme essential for this bond formations has not been determined yet. To gain a more detailed insight into the mechanism of dimerization and its mutation-induced inhibition, we investigated the effect of dimerization inhibiting mutations on VWF-PDI-interaction.

In VWD type 2A/IID patients carrying the heterozygous mutation p.Cys2771Arg, the formation of odd-numbered multimers due to N-terminal disulfide bonding to wt multimers was observed [31]. Homozygous expression yields N-terminally connected dimers only, showing a complete inhibition of the C-terminal dimerization in the CK-domain. To investigate the mechanism of the inhibitory effect of this mutation in dimerization, we performed co-localization and binding studies with the recombinant mutant. Compared to wtVWF (Figure 2A), mutant p.Cys2771Arg showed normal co-localization with PDI (Figure 2B). The dissociation constants of p.Cys2771Arg binding to PDI, determined by both MST and FCS, exhibited K_D values comparable to those of wtVWF-PDI-binding ($K_D = 235 \pm 92$ nM (MST) and $K_D = 350 \pm 75$ nM (FCS)). This shows that binding of PDI to VWF is not affected by this mutation.

The insertion of an additional cysteine residue at position 2775 surprisingly has a strong inhibitory effect on dimerization. Although all three of the cysteines required for dimerization are present, mutant p.Ser2775Cys only yields dimers and some tetramers. When we investigated the intracellular localization of this mutant, we found a markedly reduced co-localization with PDI compared to wtVWF (Figures 2A,C and 3A,C), indicating a disturbed binding of PDI to p.Ser2775Cys.

Normal co-localization of PDI and a VWF mutant that exhibits a frameshift after amino acid 2772 (p.Cys2773Alafs*76) (Figure 2D, 3D) further points to an initial binding event between PDI and a binding domain within VWF N-terminally of Cys2773.

Effect of CK-domain mutations on protein folding. To determine whether decreased binding of PDI to p.Ser2775Cys is caused by misfolding, we investigated co-localization of this mutant with the ER-localized oxidoreductase ERp57 that is involved in repair of glycoprotein folding. As shown in Figure 4, we found co-localization of wtVWF as previously described [10] (Figure 4A). Mutants p.Cys2771Arg (Figure 4B) and p.Ser2775Cys (Figure 4C) showed the same week co-localization with ERp57 as wtVWF. In the latter case, an increase in ERp57 staining was observed that points to an increased expression of ERp57 when p.Ser2775Cys is expressed. These data indicate that p.Ser2775Cys undergoes more extensive refolding mediated by ERp57 than wtVWF and p.Cys2771Arg.

DISCUSSION

Here, we investigated the (patho)-physiological role of PDI in VWF processing. Employing different methods, we found independent evidence that PDI binds to VWF with a strong affinity in the nM regime. Moreover, we localized the CK-domain as the only PDI binding domain within VWF. These data revealed that PDI is involved in the dimerization of VWF in the ER.

Our co-localization studies of VWD-associated VWF mutants might offer insights into the detailed VWF dimerization process. We hypothesize that dimerization starts with initial binding of PDI to VWF N-terminally of Cys2773 because the binding characteristics did not change for mutant p.Cys2771Arg. Additionally, a frameshift mutant that possesses only Cys2771 out of the three cysteines necessary for dimerization and an altered amino acid composition C-terminally of residue 2772 still co-localizes with PDI. This proves that, the dimerization defect of p.Cys2771Arg originates from the missing cysteine in contrast to a missing interaction with PDI. Cys2771 is the most N-terminal cysteine that is involved in two of the three disulfide bonds that are formed to connect VWF monomers. It has previously been described that mutant p.Cys2773Arg, which is also associated with VWF 2A/IID leads to odd-numbered multimers in heterozygous patients [32]. However, homozygous expression reduces only formation of high molecular weight multimers showing merely a partial dimerization defect. The intracellular localization and co-localization with PDI was found to be normal. Therefore, PDI seems to be able to at least use Cys2771 and Cys2811 to form residual dimers. No pathological mutations have been identified to far that show missense mutations of Cys2811, which further promotes the hypothesis that PDI needs to recognize

Cys2771 to initiate dimerization. In case of mutant p.Ser2775Cys, all cysteines required for dimerization are present but an additional cysteine residue has been introduced. The fact that this mutant shows decreased co-localization with PDI and additionally increases expression of ERp57, points to misfolding of the protein that inhibits initial binding of PDI. Altogether, the inability of PDI to perform proper VWF dimerization in CK-domain mutants has pathophysiological consequences manifesting in VWD.

On further physiological relevance of the PDI-VWF-interaction could be speculated in the context of tissue factor (TF) activation. TF is involved in secondary hemostasis through complex formation with coagulation factor VIIa. It was found recently, that PDI is associated with TF and implicated in the regulation of TF activity [33-35]. In particular, Langer et al. showed that TF decryption requires oxidation of cell surface PDI [33]. However, how PDI is delivered to the surface of endothelial cells remains an open question [36]. Our findings lead to the suspicion that VWF might be an anchor for PDI on the surface of endothelial cells where VWF strings are exposed upon endothelial cell activation. This would not only offer a regulatory system for PDI exposition on endothelial cells, but moreover depict an indirect involvement of VWF in secondary hemostasis.

Furthermore, it has been shown that PDI is localized in close proximity to the GP1b receptor on the plasma membrane of platelets and that VWF binding to platelets decreases by addition of anti-PDI antibody [37]. Two possible explanations may be suggested to explain these findings: 1) PDI modifies the conformation of GPIb to expose VWF binding sites, 2) PDI enhances recruitment of VWF by additional binding events in the CK-domain. However, further measurements need to be performed to confirm these hypotheses.

Summarizing, our data for the first time showed binding of VWF to PDI and shed light on the mechanism of VWF dimerization. Inhibition of either PDI binding or PDI-catalyzed disulfide bond formation was rationalized with studies of selected mutants that are known to result in hemostatic disorders. Additional physiological relevance of PDI in primary and secondary hemostasis has been proposed previously by other groups. Our finding that PDI interacts with VWF may help answering open questions in this context.

REFERENCES

1. Wagner, D. D., Cell biology of von Willebrand factor. *Annual review of cell biology* 1990, 6, (1), 217-242.

2. Haberichter, S. L.; Fahs, S. A.; Montgomery, R. R., Von Willebrand factor storage and multimerization: 2 independent intracellular processes Presented in abstract form at the 41st Annual Meeting of the American Society of Hematology, New Orleans, LA, December 3-7, 1999. *Blood* 2000, 96, (5), 1808-1815.

3. Metcalf, D. J.; Nightingale, T. D.; Zenner, H. L.; Lui-Roberts, W. W.; Cutler, D. F., Formation and function of Weibel-Palade bodies. *Journal of Cell Science* 2008, 121, (1), 19-27.

4. Katsumi, A.; Tuley, E. A.; Bodó, I.; Sadler, J. E., Localization of disulfide bonds in the cystine knot domain of human von Willebrand factor. *Journal of Biological Chemistry* 2000, 275, (33), 25585-25594.

5. Zhou, Y.-F.; Springer, T. A., Highly reinforced structure of a C-terminal dimerization domain in von Willebrand factor. *Blood* 2014, blood-2013-11-523639.

6. Schneppenheim, R.; Brassard, J.; Krey, S.; Budde, U.; Kunicki, T. J.; Holmberg, L.; Ware, J.; Ruggeri, Z. M., Defective dimerization of von Willebrand factor subunits due to a Cys-> Arg mutation in type IID von Willebrand disease. *Proceedings of the National Academy of Sciences* 1996, 93, (8), 3581-3586.

7. Voorberg, J.; Fontijn, R.; van Mourik, J. A.; Pannekoek, H., Domains involved in multimer assembly of von willebrand factor (vWF): multimerization is independent of dimerization. *EMBO Journal* 1990, 9, (3), 797-803.

8. Purvis, A. R.; Sadler, J. E., A covalent oxidoreductase intermediate in propeptide-dependent von Willebrand factor multimerization. *Journal of Biological Chemistry* 2004, 279, (48), 49982-49988.

9. Wise, R. J.; Pittman, D. D.; Handin, R. I.; Kaufman, R. J.; Orkin, S. H., The propeptide of von Willebrand factor independently mediates the assembly of von Willebrand multimers. *Cell* 1988, 52, (2), 229-236.

10. Allen, S.; Goodeve, A. C.; Peake, I. R.; Daly, M. E., Endoplasmic reticulum retention and prolonged association of a von Willebrand's disease-causing von Willebrand factor variant with ERp57 and calnexin. *Biochemical and biophysical research communications* 2001, 280, (2), 448-453.

11. LaMantia, M.; Lennarz, W. J., The essential function of yeast protein disulfide isomerase does not reside in its isomerase activity. *Cell* 1993, 74, (5), 899-908.

12. Laboissiere, M. C. A.; Sturley, S. L.; Raines, R. T., The essential function of protein-disulfide isomerase is to unscramble non-native disulfide bonds. *Journal of Biological Chemistry* 1995, 270, (47), 28006-28009.

13. Wilkinson, B.; Gilbert, H. F., Protein disulfide isomerase. *Biochimica et Biophysica Acta (BBA)-Proteins and Proteomics* 2004, 1699, (1), 35-44.

14. Freedman, R. B.; Dunn, A. D.; Ruddock, L. W., Protein folding: a missing redox link in the endoplasmic reticulum. *Current biology* 1998, 8, (13), R468-R470.

15. Schneppenheim, R.; Michiels, J. J.; Obser, T.; Oyen, F.; Pieconka, A.; Schneppenheim, S.; Will, K.; Zieger, B.; Budde, U., A cluster of mutations in the D3 domain of von Willebrand factor correlates with a distinct subgroup of von Willebrand disease: type 2A/IIE. *Blood* 2010, 115, (23), 4894-4901.

16. Brehm, M.; Schenk, T.; Zhou, X.; Fanick, W.; Lin, H.; Windhorst, S.; Nalaskowski, M.; Kobras, M.; Shears, S.; Mayr, G., Intracellular localization of human Ins (1, 3, 4, 5, 6) P5 2-kinase. *Biochemical Journal* 2007, 408, 335-345.

17. Duhr, S.; Braun, D., Thermophoretic depletion follows Boltzmann distribution. *Physical Review Letters* 2006, 96, (16), 168301.

18. De Groot, S. R.; Mazur, P., *Non-equilibrium thermodynamics.* DoverPublications. com: 1962.

19. Wienken, C. J.; Baaske, P.; Rothbauer, U.; Braun, D.; Duhr, S., Protein-binding assays in biological liquids using microscale thermophoresis. *Nature communications* 2010, 1, 100.

20. Lippok, S.; Seidel, S. A. I.; Duhr, S.; Uhland, K.; Holthoff, H.-P.; Jenne, D.; Braun, D., Direct detection of antibody concentration and affinity in human serum using microscale thermophoresis. *Analytical chemistry* 2012, 84, (8), 3523-3530.

21. Magde, D.; Elson, E.; Webb, W. W., Thermodynamic fluctuations in a reacting system--measurement by fluorescence correlation spectroscopy. *Physical Review Letters* 1972, 29, (11), 705-708.

22. Elson, E. L.; Magde, D., Fluorescence correlation spectroscopy. I. Conceptual basis and theory. *Biopolymers* 1974, 13, (1), 1-27.

23. Magde, D.; Elson, E. L.; Webb, W. W., Fluorescence correlation spectroscopy. II. An experimental realization. *Biopolymers* 1974, 13, (1), 29-61.

24. Rigler, R.; Mets, Ü.; Widengren, J.; Kask, P., Fluorescence correlation spectroscopy with high count rate and low background: analysis of translational diffusion. *European Biophysics Journal* 1993, 22, (3), 169-175.

25. Petrov, E. P.; Schwille, P., *State of the art and novel trends in fluorescence correlation spectroscopy.* Standardization and Quality Assurance in Fluorescence Measurements II 2008, 145-197.

26. Rusu, L.; Gambhir, A.; McLaughlin, S.; Rädler, J., Fluorescence correlation spectroscopy studies of peptide and protein binding to phospholipid vesicles. *Biophysical Journal* 2004, 87, (2), 1044-1053.

27. Engelke, H.; Lippok, S.; Dorn, I.; Netz, R. R.; Rädler, J. O., FVIII binding to PS membranes differs in the activated and non-activated form and can be shielded by annexin A5. *The Journal of Physical Chemistry B* 2011, 115, (44), 12963-12970.

28. Lippok, S.; Obser, T.; Müller, J. P.; Stierle, V. K.; Benoit, M.; Budde, U.; Schneppenheim, R.; Rädler, J. O., Exponential Size Distribution of von Willebrand Factor. *Biophysical journal* 2013, 105, (5), 1208-1216.

29. Michaux, G.; Hewlett, L. J.; Messenger, S. L.; Goodeve, A. C.; Peake, I. R.; Daly, M. E.; Cutler, D. F., Analysis of intracellular storage and regulated secretion of 3 von Willebrand disease-causing variants of von Willebrand factor. *Blood* 2003, 102, (7), 2452-8.

30. Wang, J. W.; Valentijn, K. M.; de Boer, H. C.; Dirven, R. J.; van Zonneveld, A. J.; Koster, A. J.; Voorberg, J.; Reitsma, P. H.; Eikenboom, J., Intracellular storage and regulated secretion of von Willebrand factor in quantitative von Willebrand disease. *Journal of Biological Chemistry* 2011, 286, (27), 24180-8.

31. Brehm MA, H. V., Aponte-Santamaria C, Obser T, Grässle S, Oyen F, Budde U, Schneppenheim S, Baldauf C, Gräter F, Schneider SW, Schneppenheim R., von Willebrand disease type 2A phenotypes IIC, IID and IIE: A day in the life of shear-stressed mutant von Willebrand factor. *Thrombosis and haemostasis* 2014, 112: E-pub ahead of print. 10.1160/TH13-11-0902.

32. Wang, J. W., Groeneveld, D. J., Cosemans, G., Dirven, R. J., Valentijn, K. M., Voorberg, J., Reitsma, P. H., and Eikenboom, J. (2012) Biogenesis of Weibel-Palade bodies in von Willebrand's disease variants with impaired von Willebrand factor intrachain or interchain disulfide bond formation. *Haematologica* 97, 859-866

33. Langer, F.; Spath, B.; Fischer, C.; Stolz, M.; Ayuk, F. A.; Kröger, N.; Bokemeyer, C.; Ruf, W., Rapid activation of monocyte tissue factor by antithymocyte globulin is dependent on complement and protein disulfide isomerase. *Blood* 2013, 121, (12), 2324-2335.

34. Reinhardt, C.; von Brühl, M.-L.; Manukyan, D.; Grahl, L.; Lorenz, M.; Altmann, B.; Dlugai, S.; Hess, S.; Konrad, I.; Orschiedt, L., Protein disulfide isomerase acts as an injury response signal that enhances fibrin generation via tissue factor activation. *The Journal of clinical investigation* 2008, 118, (3), 1110-1122.

35. Versteeg, H. H.; Ruf, W., Tissue factor coagulant function is enhanced by protein-disulfide isomerase independent of oxidoreductase activity. *Journal of Biological Chemistry* 2007, 282, (35), 25416-25424.

36. Langer, F.; Ruf, W., Synergies of phosphatidylserine and protein disulfide isomerase in tissue factor activation. *Thrombosis and Haemostasis* 2014, 111, (4), 590-7.

37. Burgess, J. K.; Hotchkiss, K. A.; Suter, C.; Dudman, N. P.; Szollosi, J.; Chesterman, C. N.; Chong, B. H.; Hogg, P. J., Physical proximity and functional association of glycoprotein 1balpha and protein-disulfide isomerase on the platelet plasma membrane. *Journal of Biological Chemistry* 2000, 275, (13), 9758-66.

FIGURES

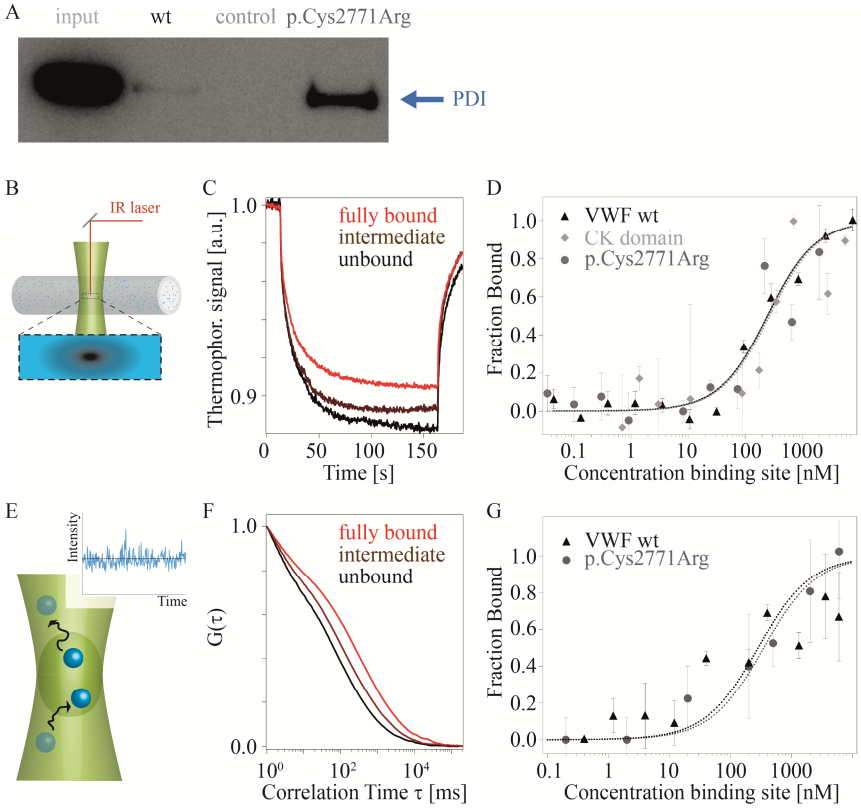

Figure 1: PDI binds VWF. A HEK293 cell lysates of non-transfected cells (input), wtVWF (wt), and p.Cys2771Arg overexpressing cells were incubated with rabbit anti-VWF antibody. Co-immunoprecipitating proteins were separated by SDS-gelelectrophoresis and PDI was detected with a mouse anti-PDI antibody. In a control without anti-VWF antibody, no PDI was detected (control). **B** MST uses the movement of molecules in a temperature gradient to analyze the interaction of biomolecules. **C** Binding of the fluorescently labeled PDI to VWF was detected as a decrease in thermophoretic depletion. **D** PDI binds to wtVWF, the isolated CK domain and p.Cys2771Arg with a very similar affinity (K_D = 240 ± 100 nM). **E** FCS was applied complementary to MST. It detects the diffusive dynamics of molecules. **F** Binding results in prolonged diffusion times visualized by a shift of the autocorrelation curve G(τ). **G** In agreement with the MST measurements, we detect similar affinities for wtVWF and mutant p.Cys2771Arg (K_D = 300 ± 100 nM).

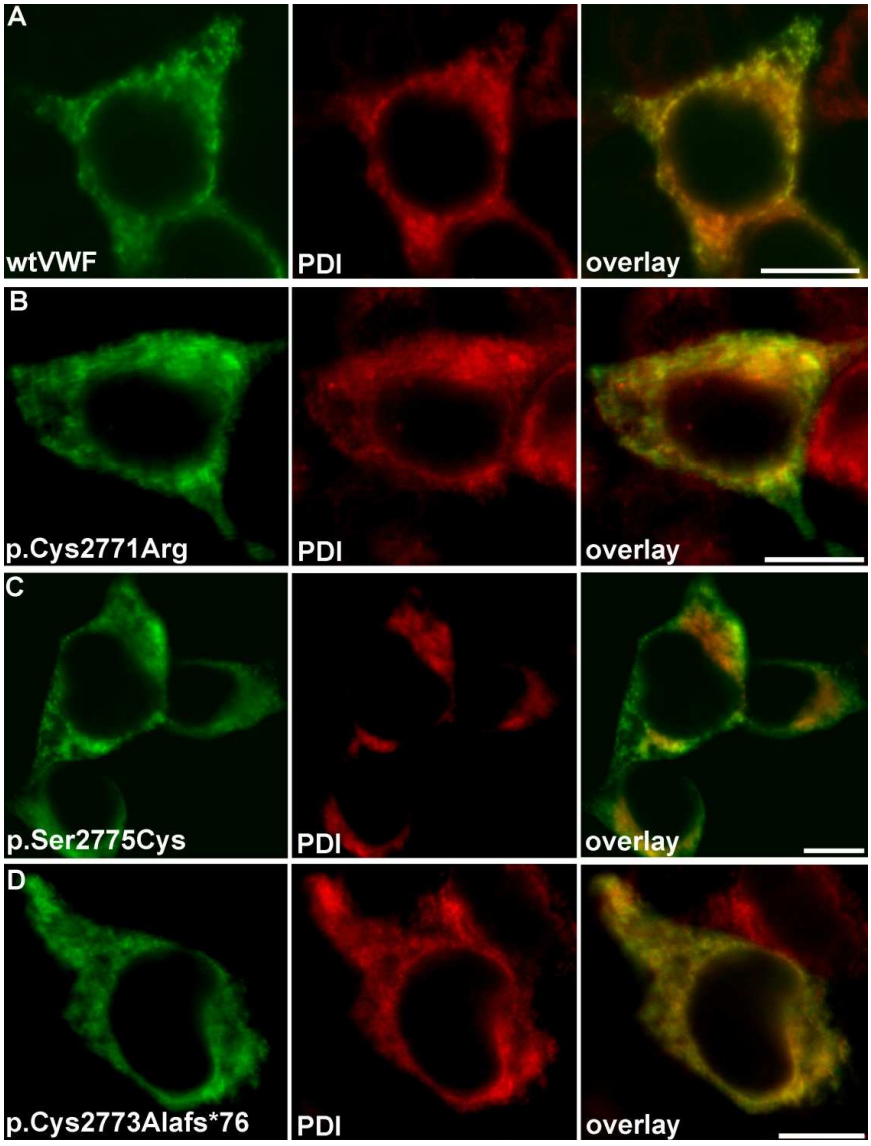

Figure 2: ER localization of VWF and PDI. A wtVWF, **B** VWF mutant p.Cys2771Arg, **C** p.Ser2775Cys, and **D** p.Cys2773Alafs*76 were transiently expressed in HEK293 cells. 48 h after transfection cells were fixed and VWF proteins and PDI were detected by indirect immunofluorescence employing rabbit anti-VWF and mouse anti-PDI antibodies. VWF-PDI-co-localization appears yellow in the overlays. Scale bars represent 10 µm.

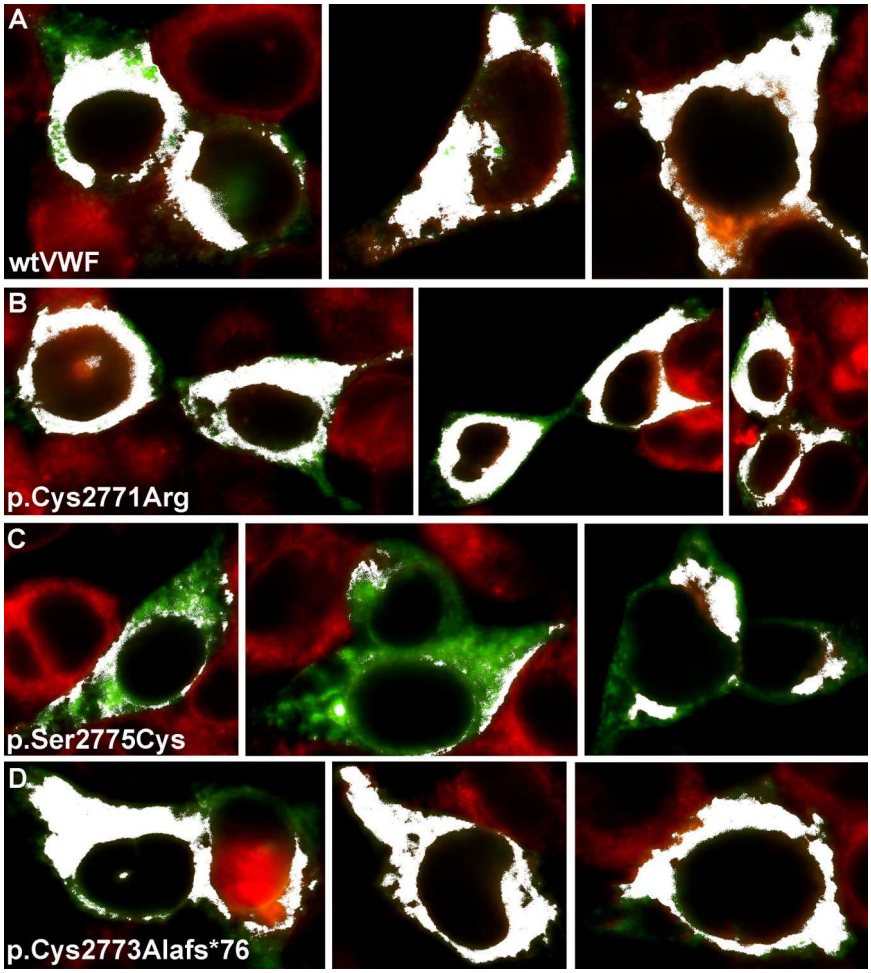

Figure 3: Co-localization of VWF and PDI. Co-localization of wt or mutant VWF with PDI was visualized employing the co-localization plugin of ImageJ. Co-localization is shown in white for PDI and **A** wtVWF, **B** p.Cys2771Arg, **C** p.Ser2775Cys, and **D** p.Cys2773Alafs*76.

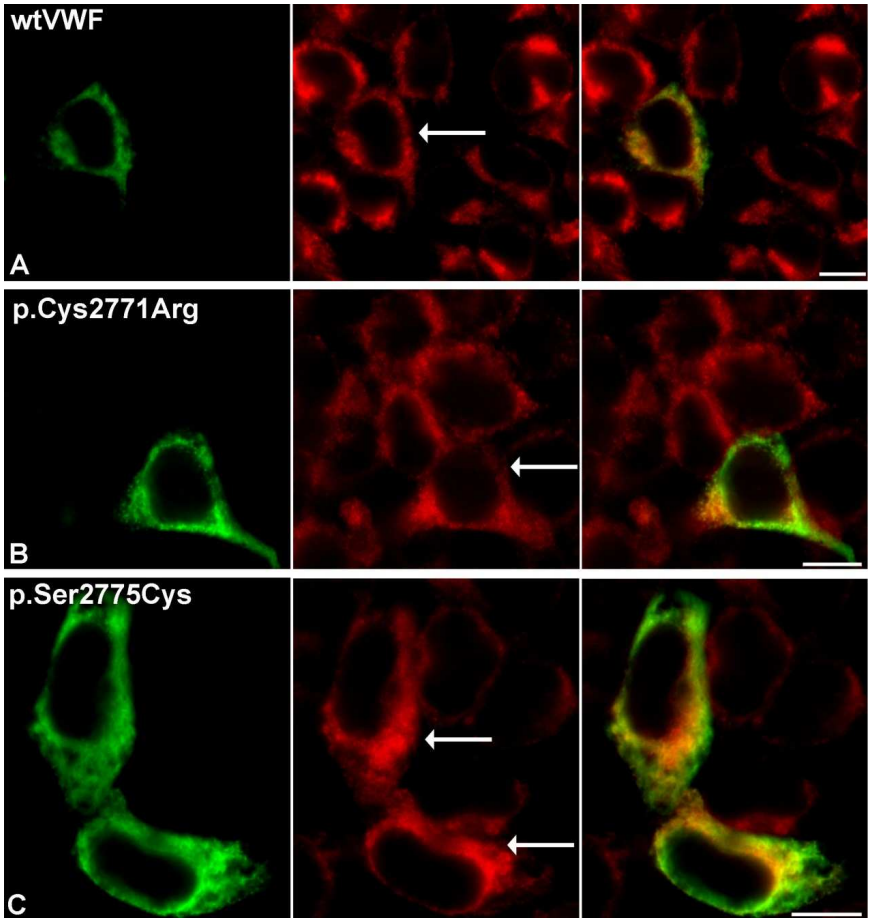

Figure 4: Co-localization of VWF and ERp57. A wtVWF, **B** VWF mutant p.Cys2771Arg and **C** p.Ser2775Cys were transiently expressed in HEK293 cells. 48 h after transfection, cells were fixed and VWF proteins and ERp57 were detected by indirect immunofluorescence employing rabbit anti-VWF and mouse anti-ERp57 antibodies. VWF-ERp57-co-localization appears yellow in the overlays. White arrows point to transfected cells to highlight increase in ERp57 expression in p.Ser2775Cys overexpressing cells. Scale bars represent 10 µm.

8

FVIII Binding to PS Membranes and its Regulation by Annexin A5

In this chapter, binding of FVIII to phosphatidylserine (PS)-containing membranes is investigated, and the impact of annexin A5 on this interaction is shown. Binding of activated FVIIIa to PS-expressing platelets is an essential process further downstream in the coagulation cascade. It is required to avoid severe bleeding disorders and known to be influenced by many cofactors. However, the exact binding mechanism had not been studied quantitatively, and it remained an open question whether and how it is influenced by annexin A5, which has been proposed to compete for PS-binding sites in the initiation of coagulation.

Using FCS and MST, we established a quantitative description of FVIII and FVIIIa binding to PS-containing vesicles, which served as model platelets. Non-activated FVIII showed the expected exponential increase in binding as a function of PS content of the vesicles. In contrast, FVIIIa exhibited a pronounced binding anomaly that consisted of a sharp peak in binding affinity around the natural PS content of platelets (11%). We showed that annexin A5 strongly influences the FVIIIa binding behavior, both reducing and increasing it, depending on whether the relative PS content exceeds the maximum binding value. This behavior was reproduced by an extended inhibition model, assuming that annexin A5 effectively reduces the PS content by shielding PS lipids upon binding. This study exemplifies the important role of the PS content as a regulatory signal within the blood coagulation cascade. The possible function of annexin A5 as a passive regulator of the effective PS level in platelets suggests its use as a potential drug for manipulation of the hemostatic function.

The experimental data and the resulting conclusions are presented in the following publication:

H. Engelke, S. Lippok, I. Dorn, R.R. Netz, J.O. Rädler. 2011. "FVIII Binding to PS Membranes Differs in its Activated and Non-Activated Form and can be Shielded by Annexin A5." *J. Phys. Chem. B* 115:12963-12970.

THE JOURNAL OF PHYSICAL CHEMISTRY B

ARTICLE

pubs.acs.org/JPCB

FVIII Binding to PS Membranes Differs in the Activated and Non-Activated Form and Can Be Shielded by Annexin A5

Hanna Engelke,[†] Svenja Lippok,[†] Ingmar Dorn,[‡] Roland R. Netz,[§] and Joachim O. Rädler*[,†]

[†]Center for NanoScience (CeNS) and Fakultät für Physik, Ludwig-Maximilians-Universität, Geschwister-Scholl-Platz 1, D-80539 München, Germany

[‡]Bayer Technology Services GmbH, 51368 Leverkusen, Germany

[§]Technische Universität München, 85748 Garching, Germany

Supporting Information

ABSTRACT: Binding of Factor VIII to phosphatidylserine (PS)-expressing platelets is a key process in the intravascular pathway of the blood coagulation cascade. Activated by thrombin, FVIIIa acts as a cofactor on the surface of platelets. It is under debate whether and how annexin A5 influences FVIIIa binding to platelets. Here, we investigate FVIII binding to PS-containing vesicles as model platelets and its interplay with annexin A5 in buffer using fluorescence correlation spectroscopy (FCS). We find that activated FVIIIa, in contrast to inactivated FVIII, exhibits a striking binding anomaly as a function of PS content, marked by a sharp maximum of the binding constant around 11% PS, which is close to the natural PS content of platelets. Furthermore, we show that the addition of annexin A5 can both increase or decrease this FVIIIa binding depending on whether the relative PS content is lower or higher than the maximum binding value. We demonstrate in theory that the observed binding diagram supports the hypothesis that annexin shields PS, indicating a possible indirect regulatory role of annexin A5 in blood coagulation. The overall PS- and annexin-dependent binding behavior of activated FVIIIa is preserved in experiments in blood plasma, confirming the validity of our results under more physiological conditions.

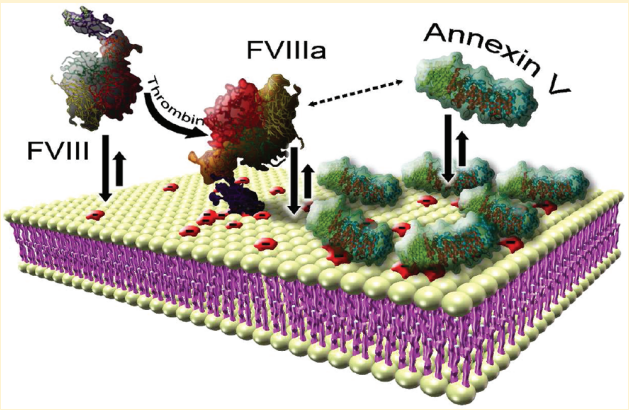

INTRODUCTION

Factor VIII is a key cofactor in the blood coagulation cascade. Its inherited deficiency in humans causes a severe dysfunction in hemostasis, leading to the bleeding disorder known as hemophilia A. A decisive event in the blood coagulation cascade is the binding of activated FVIIIa to phosphatidylserine (PS)-exposing platelets. FVIII is activated by thrombin, which releases FVIII from its carrier, the von Willebrand factor by cleaving off its B-domain. FVIIIa subsequently forms the tenase complex on the surface of the platelet membrane with the enzyme factor IX. Recently, it was found that activated FVIIIa exhibits enhanced binding affinity to platelets, as compared to its inactive form.[1] One important blood protein, that is believed to influence blood coagulation, is annexin A5, which binds to PS-containing membranes in a calcium dependent manner.[2−5] Annexin A5 binds to endothelial cells, leading to immediate effects on thrombin formation.[6] It was shown that antiphospholipid antibodies, which inhibit annexin A5 binding to phospholipids, accelerate plasma coagulation.[7] Furthermore, the inhibitory effect of annexin A5 on the binding of FVIII to platelets seems to be specific to activated FVIIIa and not significant for inactivated FVIII.[8] Additional evidence has been reported regarding the anticoagulant effect of annexin A5, although the mechanism of this effect remains unclear.[2] It was proposed that the formation of a two-dimensional annexin A5 crystal lattice leads to a reduction of lateral movement of membrane-bound coagulation factors, and hence a reduction of the kinetic rates in the membrane-based coagulation pathway.[9] Alternatively, annexin A5 is suggested to compete with coagulation factors for binding sites on the platelet membrane, thereby inhibiting their membrane-based interaction, as schematically depicted in Figure 1.

Therefore, a quantitative understanding of FVIII and annexin-A5 binding to platelet membranes and their possible interference is important for quantitative modeling of the coagulation cascade. Generally, a systems biology approach to hemostasis has the potential to leverage medical and pharmaceutical research.[10] However, the complexity of the biochemical network represents a formidable challenge. Prerequisites for quantitative modeling

Received: May 25, 2011
Revised: September 28, 2011
Published: September 28, 2011

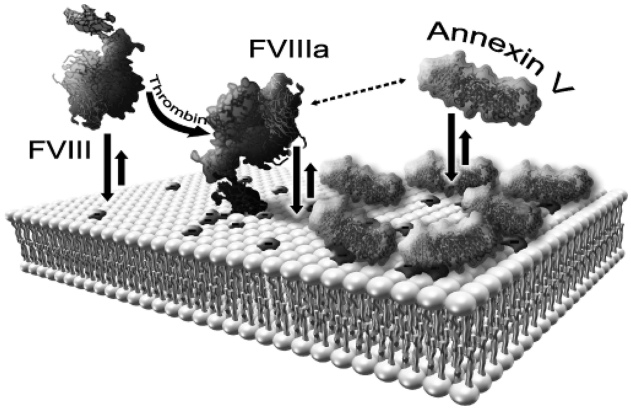

Figure 1. Schematic illustration of FVIII activation and binding to a phosphatidylserine (PS)-containing membrane. Annexin A5 is shown to compete for PS binding sites.

are the knowledge of the binding constants and reaction rates. Here, we focus on the lipid membrane related reactions of FVIII in the blood coagulation cascade. For such protein−membrane interactions, lipid membrane composition and local lipid phase segregation play a regulatory role. This kind of regulation by spatial organization has been shown, for instance, for binding to membranes containing the polyvalent acidic lipid phosphatidylinositol-4,5-bisphosphate (PIP_2) and on T-cell membranes, which form microdomains induced by protein binding.[11,12,22] However, these parameters are not fully captured in the current simulations and models. Binding of inactivated FVIII to PS-model membranes occurs in a charge dependent manner through a region in the C2 domain, which is enriched by four basic and three hydrophobic residues.[13,14] For activated FVIIIa, however, binding and, particularly, its dependence on negative charge, i.e., the PS content, has not yet been investigated. Likewise, there is no support by quantitative data for the hypothesis of competitive binding of FVIII and annexin to negatively charged membranes.

In this Article, we measure the binding of FVIII and FVIIIa to PS-containing membranes as well as investigate the mechanism of how annexin influences FVIIIa binding to membranes, as schematically shown in Figure 1. We use fluorescence correlation spectroscopy (FCS) to study FVIII and FVIIIa interacting with PS-containing vesicles as model membranes. FCS measures diffusion times and can discriminate freely diffusing from vesicle-bound proteins based on the size dependence of diffusion, as further explained in the Supporting Information.[15,16] We measure binding isotherms of FVIII binding to vesicles in consecutive titration experiments and study the binding characteristics of FVIII and FVIIIa as a function of the PS content of the membrane. For inactivated FVIII, we find a continuous increase of the binding constant with increasing PS content. In contrast, for activated FVIIIa, an anomaly in binding and an extremely enhanced sensitivity to the PS content was observed at the physiological PS content of activated platelets. The underlying molecular mechanism can be explained by binding of charged lipids to discrete protein binding sites and repulsion from neutral protein sites. As we will show in this Article, the binding anomaly of FVIIIa allows for an efficient regulatory role of annexin A5, if annexin A5 competes for binding to PS and hence changes the effective PS concentration sensed by FVIIIa.

EXPERIMENTAL PROCEDURES

Sample Preparation. Recombinant FVIII (Kogenate-FS) was obtained from Bayer HealthCare and labeled using Alexa 488-tagged ESH2 antibodies (American Diagnostica). (For additional information, see the Supporting Information.) This labeling method avoids aggregates that we found to be introduced by direct labeling of FVIII, and it allows for flexible labeling without direct chemical modification of the protein. Prior to labeling, FVIII was activated through a 30 min incubation with human thrombin at 37 °C, as described in Ahmad et al.[8] Antibody binding tests (see the Supporting Information) showed that activation was successful. FVIII and antibodies were diluted at concentrations of 110 and 10 nM, respectively, in citrate buffer (50 mM, pH 6.7, with 1 mM $CaCl_2$, 40 μg/mL Tween 80). 100 nm unilamellar vesicles were prepared by the extrusion of 1-palmitoyl-2-oleoyl phosphatidylcholine (POPC) and 1-palmitoyl-2-oleoyl-*sn*-glycero-3-phosphatidylserine (POPS) (Avanti Polar Lipids) in citrate buffer.

For experiments with annexin A5, annexin (Sigma Aldrich) was mixed with vesicles in citrate buffer with $CaCl_2$ added at a concentration of 12.5 mM. Control experiments were performed, which proved that FVIII binding does not change upon addition of this amount of $CaCl_2$. Annexin A5 (Sigma Aldrich) was incubated with vesicles and $CaCl_2$ for 2 min prior to the addition of FVIII. Cross-correlation experiments were performed with Alexa 647-labeled annexin A5 (Invitrogen) on supported lipid bilayers, which were prepared using the sonication technique.[21] FVIII-deficient plasma in citrate buffer (American Diagnostica) was added to the buffer solution, yielding a 1:1 buffer:plasma mixture. FXa inhibitor (Tenstop, American diagnostica) was added to prevent possible tenase complex formation on the vesicles.

Instrumentation. FCS measurements were performed on an Axiovert 200 microscope equipped with a ConfoCor 2 unit (Carl Zeiss, Jena, Germany). For excitation, an argon ion laser at 488 nm with an average power of 15 μW on the sample was used. Fluorescence emission was filtered from the excitation light using a 525/25 bandpass filter. The objective used was a 40× (NA = 1.2) water immersion appochromat (Carl Zeiss Jena, Germany). Samples were measured in eight well LabTek I chamber slides (Nunc, Rochester, NY). For cross-correlation experiments with Alexa 647-labeled annexin A5, a HeNe laser (633 nm) and a long-pass 650 filter were added to the setup. Correlation and analysis were performed using the ConfoCor 2 software. FCS data analysis is in accordance with Rusu et al.,[16] and is described in greater detail in the Supporting Information.

RESULTS

FVIII and FVIIIa Binding to PS Vesicles. We measured binding of FVIII and FVIIIa to vesicles containing different PS concentrations, as shown in Figure 2a. In FCS, fluorescence intensity fluctuations are recorded from the diffusion of fluorescently labeled proteins through an open focal illumination volume. The autocorrelation function of the fluorescence time series exhibits a characteristic decay representing the average time the molecules need to diffuse across the focal volume (Figure 2b). For proteins binding to the 100 nm vesicles, which are larger than the freely diffusing proteins, the diffusion time increases. This leads to the evolution of the autocorrelation functions depicted in Figure 2b. Each of the intermediate autocorrelation functions

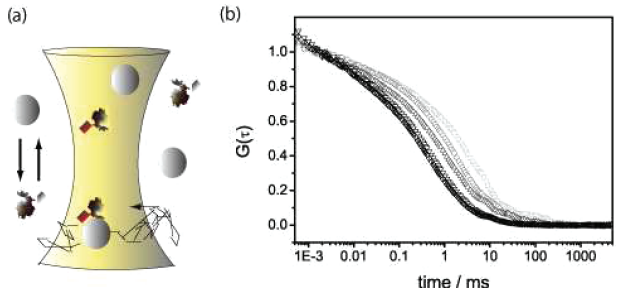

Figure 2. (a) Fluorescence correlation spectroscopy (FCS) detects FVIII binding to vesicles through the measurement of the diffusion time of fluorescently labeled FVIII across an open illumination volume. (b) Evolution of the time autocorrelation functions of FVIIIa as vesicles with 10% PS mol fraction are added. The fraction of vesicle-bound, slowly diffusing FVIIIa to the freely diffusing FVIIIa increases with lipid concentration from dark to light gray.

can be fitted by a sum of two autocorrelation functions corresponding to the fraction of bound and unbound proteins.[16] Consequently, the fraction of bound proteins can be obtained from the measured correlation function using appropriate fits (for details, refer to the Supporting Information). For FCS measurements, the protein needs to be fluorescently labeled. Here, FVIII was indirectly tagged using the fluorescently labeled antibody ESH2, which binds to FVIII without obstructing the capability of FVIII to bind PS-containing membranes.[17] As a control, we also used FVIII tagged with the antibody ESH8. We measured the fraction of bound FVIII and FVIIIa as a function of lipid concentration. Figure 3a shows an example of an isotherm that was obtained from a measurement on FVIII binding to vesicles of 10% PS content. These isotherms were recorded for lipid compositions with varying amounts of PS. In each case, we find binding isotherms described by

$$f_{\mathrm{bound}}(L) = \frac{K(\mathrm{PS})\cdot L}{1 + K(\mathrm{PS})\cdot L} \qquad (1)$$

where $K(\mathrm{PS})$ denotes the molar partition coefficient and L the molar lipid concentration in solution. $K(\mathrm{PS})$ describes the distribution of free and bound FVIII, and hence its binding constant to the lipid membrane as a function of its relative PS content. Note that the binding isotherm is sometimes fitted with reference to a bimolecular binding model, assuming a discrete number of lipids per binding site.[13] In the binding site description, the concentration of binding sites $L^* = L/n$ is related to the lipid concentration through the number of lipids per binding site, n. Consequently, the dissociation constant, K_D, according to the discrete binding model and $K(\mathrm{PS})$ are related by $n\cdot K_D = K^{-1}(\mathrm{PS})$. The PS content dependence of FVIII binding to membranes is plotted on a semilog scale in Figure 3b. The molar partition coefficient increases with increasing strength of binding, showing that binding increases continuously with increasing PS content for inactivated FVIII. For vesicles without PS, no significant binding could be detected within the range of concentrations studied. The measured $K_{\mathrm{FVIII}}(\mathrm{PS})$ values are in exact agreement with the previously reported data by Gilbert et al. using resonance energy transfer.[13] The line represents a fit indicating an exponential increase within the range of PS contents studied.

Interestingly, binding of activated FVIIIa notably deviates from this behavior. Figure 3b shows the strongly peaked dependence of FVIIIa binding on the membrane PS content. Binding sharply

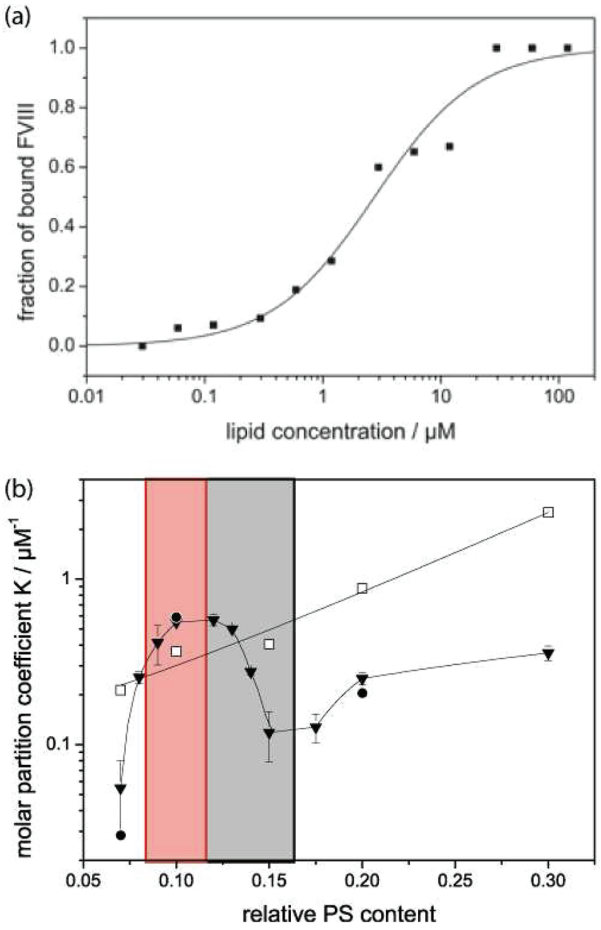

Figure 3. (a) Binding isotherm of FVIII binding to vesicles of 10% PS content. (b) The molar partition coefficient (binding constant), $K(\mathrm{PS})$, of activated (filled triangles) and nonactivated (open squares) FVIII. The black round data points indicate control experiments with activated FVIIIa labeled with ESH8 instead of ESH2. The range of physiological mol percentage of PS in activated platelets is marked in red. The region of the anomalous decrease in the binding constant with increasing PS content is indicated by the gray region. Comparison of the FVIII and FVIIIa data shows the strong deviation of FVIIIa from common binding behavior.

increases up to $K_{\mathrm{FVIIIa}}(\mathrm{PS}) = 0.6\ \mu\mathrm{M}^{-1}$ at a relative PS concentration of 11%, which exceeds the binding of inactivated FVIII by 100%. Surprisingly, the binding constant of activated FVIII decreases beyond this point, and reaches a minimum at about 17% PS content ($K_{\mathrm{FVIII}}(\mathrm{PS}) = 0.1\ \mu\mathrm{M}^{-1}$). This behavior must be considered anomalous, since the general understanding implies that binding increases with PS content due to electrostatic interaction. In order to confirm this result, we have measured the binding constant using optical thermophoresis as an independent second technique and obtained agreement within the experimental accuracy (see the Supporting Information). It is remarkable that the observed anomaly falls within the physiological range of PS content on the outer membrane of activated platelets. A comparison of the molar partition coefficients of inactivated and activated FVIII reveals that activated FVIII shows weaker binding than inactivated FVIII over most of the PS content range, except for this narrow region of the peak between 8 and 14%.

dx.doi.org/10.1021/jp2048579 |J. Phys. Chem. B 2011, 115, 12963–12970

Theoretical Modeling of FVIIIa Binding. The binding behavior of FVIII differs remarkably depending upon whether it is activated or not. In particular, the affinity of FVIIIa exhibits a maximum as a function of PS content, which is unusual, as it implies that beyond an optimal PS content the protein membrane interaction, that has a significant attractive electrostatic contribution, decreases despite the increasing surface charge of the lipid membrane. In electrostatic theory, the interactions of oppositely charged bodies, i.e., protein and membrane, increase monotonously with increasing charge of either component. This is indeed the case for the interaction of inactivated FVIII with PS membranes.[1,19] The existence of a maximum for FVIIIa is hence a principal challenge to the mechanism of FVIII binding to PS membranes. In the following, we present a simple statistical model that describes this phenomenon. It is well-known that the electrostatic interaction of the PS moiety in the lipid membrane plays a key role in FVIII binding. First, crystallography data show three residual positive charges on the membrane facing side of the protein. Second, when the protein binds to the membrane, its surface covers a distinct area of the membrane, which can be estimated to correspond to about 25 lipids. A fraction Φ of the lipids are charged PS lipids, and it is assumed that the binding energy is composed out of the binding energy of these charged constituents. The situation is depicted schematically in Figure S1 of the Supporting Information. We now introduce the very assumption that discriminates the activated and inactivated form in our model. In the nonactivated form, we assume that the electrostatic charge of the protein is equally distributed over the contact area and hence all $M = 25$ lipid sites have the same chemical free energy for a PS lipid. The reason for this could be that charges are buried by the B-domain of the protein or that there is a water layer between the protein and lipid bilayer. In contrast, in the case of activated FVIII, we assume the existence of three discrete binding sites for PS, as depicted in Figure S1 of the Supporting Information. In both cases, the binding constant, K, of the protein is determined from the statistical mean of the free energy, F, considering all possible configurations of charged lipids underneath the protein.

$$K = N \exp(-F/kT) = N \cdot Z(\tilde{\mu}) = N \cdot \sum_{m=1}^{M} P_M(m) e^{m\tilde{\mu}} \qquad (2)$$

where N is a constant normalization factor and $Z(\tilde{\mu})$ denotes the partition function, with $P_M(m)$ being the probability that m lipids in the contact area are charged and $\exp(m\tilde{\mu})$ its statistical weight (for the explicit presentation of $P_M(m)$, see the Supporting Information).

For the electrostatic binding of inactivated FVIII to membranes, we assume that each charged lipid under the protein contributes an equal amount of $\tilde{\mu} kT$ to the binding energy. Hence, binding increases with an increasing amount of charged lipids underneath the protein. The fit in Figure S2 of the Supporting Information with only the energy contribution per lipid $\tilde{\mu}$ and the normalization factor N as free fit parameters shows that this model reveals the PS dependence of the inactivated FVIII well.

The discrete binding of activated FVIII is modeled by discrimination of the energy contributions of charged lipids at charge binding sites and those at neutral sites of the protein.

Negatively charged lipids at charge binding sites are attracted and hence contribute a positive amount of $\tilde{\mu}_1 kT$ to the binding energy. Charged lipids, which are not at these sites, are repulsed and their contribution $\tilde{\mu}_2 kT$ to the binding energy is negative. The reason for this could be the entropic confinement of the counterions. The contribution of the charged lipids at charge binding sites leads to an increase of binding with increasing fraction of charged lipids at low PS concentrations up to a certain value, beyond which the repulsion at neutral sites dominates, resulting in a decrease of binding with increasing PS content of the membrane. The discrimination of these two different energy contributions leads to one additional parameter, $\tilde{\mu}_2$, and the probability function $P_M(m)$ splits into the probabilities $P_K(k)$ to find k charged lipids at the K charge binding sites and $P_L(l)$ to find l charged lipids at the $L = M - K$ neutral sites (for details, see the Supporting Information). Figure S2 of the Supporting Information shows that this discrete binding model reproduces the peak in the PS dependence of activated FVIII with only one additional parameter as compared to the model for inactivated FVIII. However, it reveals only the peak and it fails to describe the increase of the binding constant at high PS contents. This increase signals cooperative effects, which we implement in the model by addition of a quadratic term $l^2\varepsilon$ in the binding energy per charged lipid at noncharge binding sites. The dashed line in Figure S2 of the Supporting Information, which was obtained by the model including this extension, reveals the increase of binding at high PS contents. The experimental data for FVIIIa are more sharply peaked around the maximum than the theoretical model. The agreement could be improved by including higher order terms also for the PS lipids underneath charge sites, which we did not pursue in this paper.

Annexin A5 Can Both Reduce and Increase Binding of FVIIIa to PS Membranes. As annexin-A5 is supposed to affect the binding of FVIII to platelets, we study its influence on the binding of FVIII to membranes quantitatively by incubating the vesicles with annexin-A5 prior to the binding experiments with FVIII. In the case of inactivated FVIII, annexin-A5 had a weak but by trend decreasing influence on the binding. In contrast, FVIIIa binding was strongly influenced by the presence of annexin A5 even at low annexin concentrations of 4 μM. In fact, the full binding diagram as a function of both PS content and annexin concentration revealed a multifaceted behavior, as shown in Figure 4a. We note that the addition of annexin can both reduce and increase the binding of FVIIIa, depending on the PS content of the membrane. The binding of FVIIIa to vesicles containing 10% PS is continuously reduced with increasing annexin concentration up to full inhibition (Figure 4b). When vesicles of a relative PS content of 15% were used, however, the inhibition characteristic disappears. In this case, preincubation of the vesicles with annexin enhances binding up to a maximum value. At concentrations higher than this maximum, a reduction of FVIIIa binding to the vesicles is again observed (Figure 4c). Separate experiments on annexin binding to vesicles showed that this does not lead to vesicle aggregation and hence does not lead to these results by interfering with the FCS measurements.

Quantitative Model of Annexin Interaction. This change in the FVIIIa binding behavior in the presence of annexin A5 can be explained by an extended competetive inhibition model. It is generally assumed that annexin competes with FVIII for binding to PS lipid. We first demonstrate that, however, ordinary competitive binding does not fully describe the data. Competitive inhibition describes the interaction of a ligand and a receptor in the presence of a second ligand competing for binding to the same receptor. The competition for binding sites is based on

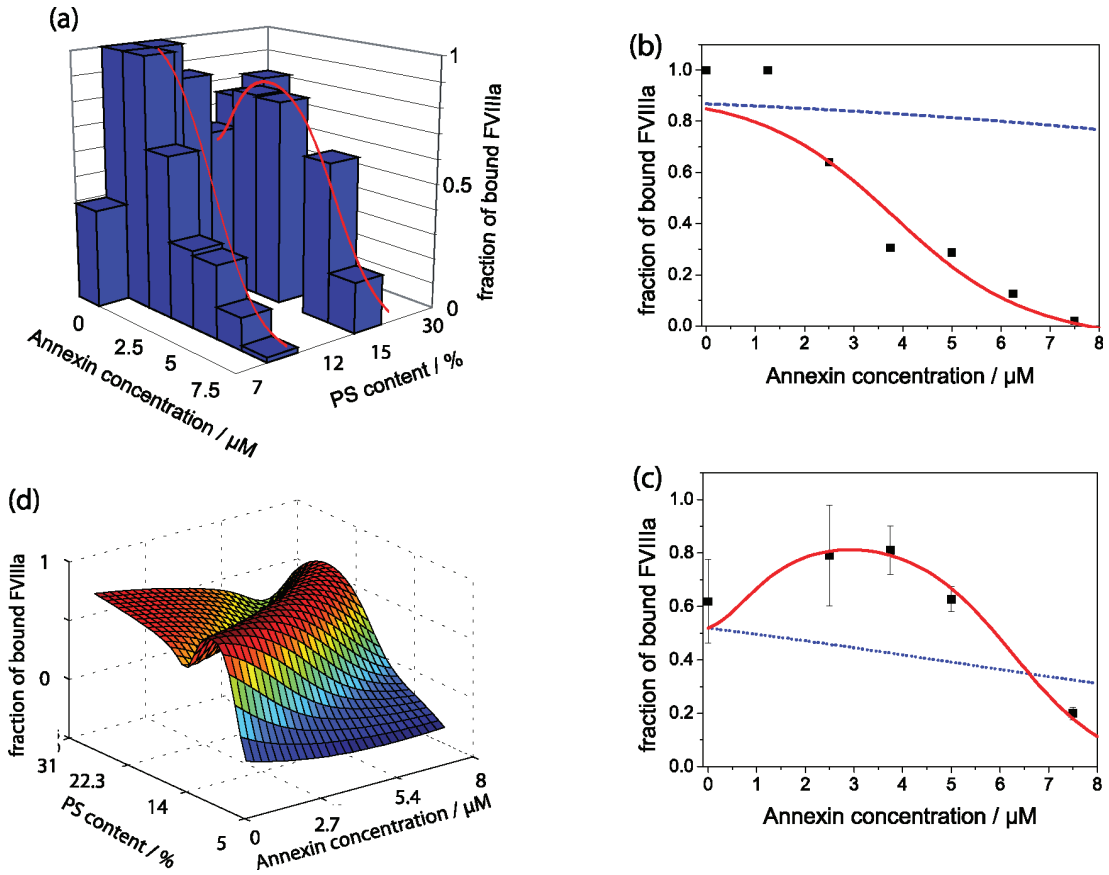

Figure 4. (a) 3D plot of the measured fraction of membrane-bound FVIIIa as a function of PS mol fraction and annexin A5 concentration. Cross-sectional plot of part a showing the influence of annexin A5 on FVIIIa binding to PS membranes at a PS content of 10% (b) and 15% (c). The blue dashed lines indicate a fit according to the simple competitive model, while the red full lines represent a fit following the extended shielding model. (d) Three-dimensional binding plot showing shielding model simulations of the PS content and annexin A5 concentration dependence of FVIIIa binding to membranes at a constant lipid concentration.

mass action, and hence, in our case, the binding of annexin A5 to PS reduces the absolute number of available PS binding sites for FVIIIa. This leads to an effectively reduced lipid concentration, $L_{\mathrm{eff}}(A) = L - L_{\mathrm{A}}$, with L_{A} being the number of lipids shielded by annexin A5. Replacing L by $L_{\mathrm{eff}}(A)$ in eq 1, we obtain the fraction bound of FVIII for competitive inhibition. This model, however, fails to describe the strong inhibition we measured for membranes with 10% PS content quantitatively, as seen in Figure 4b, where the blue dashed line represents a fit according to the competitive inhibition model. Moreover, the standard inhibition model can only explain the decrease in binding but not the enhanced binding measured for membranes with 15% PS content (Figure 4c).

We introduce now an extended competitive inhibition model, which assumes that annexin-A5 also modifies the binding constant $K_{\mathrm{FVIIIa}}(\mathrm{PS})$ due to the fact that PS lipid is shielded. The modified binding constant $K_{\mathrm{FVIIIa}}(\mathrm{PS}_{\mathrm{eff}}(A))$ is described by an effective PS content, $\mathrm{PS}_{\mathrm{eff}}(A) = \mathrm{PS}_0 \cdot (1 - \alpha A_{\mathrm{b}})$, where the amount of annexin bound (A_{b}) is given by the binding constant, K_{A}, of annexin A5 to the membrane (see the Supporting Information). In addition, the molar shielding efficiency, α, was introduced to quantify the efficiency of relative PS content reduction per mol annexin. A shielding efficiency of $\alpha = 0.1\ \mu\mathrm{M}^{-1}$, for instance, implies that 1 μM annexin reduces the relative PS content by 10%. Due to the sensitivity of FVIIIa binding to the PS content of membranes described above, a reduction of the relative PS content induces dramatic changes to the binding constant $K_{\mathrm{FVIIIA}}(\mathrm{PS})$, causing either the enhanced or reduced binding of FVIIIa. A quantitative description of the fraction of bound FVIIIa as a function of annexin A5 is given by

$$f_{\mathrm{bound}}(\mathrm{PS}, A) = \frac{K(\mathrm{PS}_{\mathrm{eff}}(A)) \cdot L_{\mathrm{eff}}(A)}{1 + K(\mathrm{PS}_{\mathrm{eff}}(A)) \cdot L_{\mathrm{eff}}(A)} \qquad (3)$$

Note that eq 3 contains only one unknown parameter, since we can use both the measured dependence, $K_{\mathrm{FVIIIA}}(\mathrm{PS})$, and the measured binding constant of annexin, K_{A}, which determine the effective quantities (for more details, refer to the Supporting Information). Equation 3 consistently describes the measured concentration dependence of the bound fraction (solid lines, Figure 4b and c). The strength of the model is the fact that only one adjustable parameter, the shielding efficiency α, is required, and has to be consistent with all measurements. The fact that both 10% PS and 15% PS data sets are well-described using the same α confirms the validity of the model. To further elaborate on the full phase diagram of the binding behavior, we plotted the theoretical landscape of binding as a function of PS and annexin A5 concentration (Figure 4d). The anomaly of the PS dependence of FVIIIa binding to membranes allows for inhibition and enhancement of binding, which occurs upon the reduction of the effective PS

dx.doi.org/10.1021/jp2048579 |J. Phys. Chem. B 2011, 115, 12963–12970

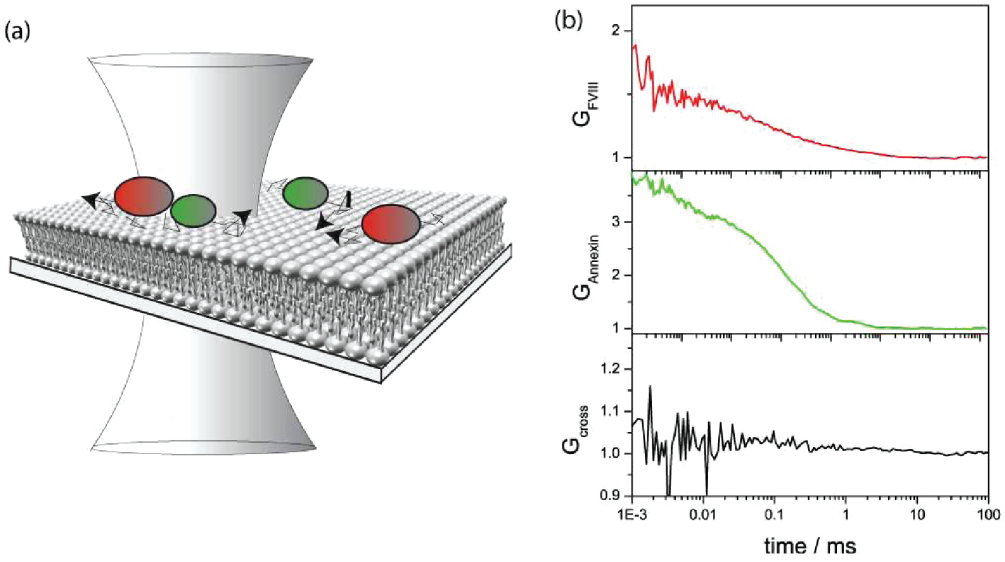

Figure 5. (a) Schematic diagram of the two-dimensional two-color cross-correlation FCS measurement on a supported membrane. (b) Autocorrelation curves of activated FVIII (red line) and annexin A5 (green line) on a supported lipid bilayer. No cross-correlation (black line) between annexin A5 and activated FVIII can be detected, indicating that these do not directly interact. The diffusion coefficient of activated FVIII is not influenced by annexin A5, and is measured to be approximately 10 $\mu m^2\ s^{-1}$ for both.

content through the addition of annexin. The shielding model is thus able to qualitatively and quantitatively explain the mechanism of interaction of annexin and FVIIIa binding to membranes.

Cross-Correlation Experiments. A key component of the inhibition model is the assumption that there is no direct interaction between annexin and FVIIIa. All annexin interference occurs indirectly via PS shielding, which then modulates the binding affinity of the membrane to FVIII. In order to test this hypothesis, we performed dual color cross-correlation experiments on supported membranes, as schematically depicted in Figure 5a. In this experiment, FVIIIa is labeled with green fluorescent-tagged antibody, while annexin is labeled with a red fluorescent-tagged antibody. Fluorescence cross-correlation, through the two-color coincidence, can differentiate between the diffusion of free proteins and correlated protein clusters through the focal spot. Distinct autocorrelation curves are obtained for both annexin and FVIIIa, yielding a diffusion coefficient of about 10 $\mu m^2\ s^{-1}$. This is approximately equal to the diffusion coefficient of lipids in the membrane (Figure 5b). Nevertheless, the cross-correlation shows a flat time dependence, indicating that the diffusion of annexin and of FVIIIa are not correlated. Comparison of the diffusion coefficients of each protein on a membrane in the presence and absence of the other indicates that the diffusion of one is not influenced by the other. Furthermore, the homogeneity of the intensity signal obtained in these experiments shows the absence of aggregates and their possible influence on the binding. Addition of calcium and chelation of calcium with EDTA lead to a change of the ratio of bound FVIIIa and bound annexin A5, whereas addition of neither EDTA nor calcium changed the amount of bound FVIIIa in the absence of annexin A5. This was used to fine-tune the concentrations of bound FVIIIa and annexin A5 in the cross-correlation experiments and is a further proof of the modulation of FVIIIa binding by annexin A5.

Experiments in Plasma. To see if our experimental results are valid under *in vivo* conditions, we repeated the experiments in FVIII-deficient blood plasma. Since plasma is a strongly scattering, crowded medium, FCS measurements face an experimental hurdle that needs to be addressed in the analysis. We have recently described a procedure on the required corrections for both the scattering and crowding effects in FCS data analysis.[18] Taking these effects into account, we were able to measure FVIII binding to vesicles containing 15% PS (see the Supporting Information). The first satisfying finding is that the molar partition coefficients of FVIIIa binding to LUVs (in the absence of annexin A5) in plasma are consistent with those obtained in buffer. Second, preincubation of the membranes with annexin A5 in plasma leads to the same characteristic enhancement and inhibition behavior observed in buffer. However, the absolute concentration of annexin A5 necessary to reach the same level of inhibition differs in plasma and buffer by a factor of 4, as shown by the rescaling of the theoretical prediction for the data in buffer (solid line, Figure 6) by a factor of 4 (dashed line, Figure 6).

DISCUSSION

We studied the binding of inactivated and activated FVIII to PS-containing phospholipid model membranes. The molar partition coefficient of inactivated FVIII is found to exhibit an exponential increase as a function of mol percentage PS, which is consistent with data from Gilbert et al.[13] and Bardelle et al.[19] This increase is caused by electrostatic interaction, which is proportional to the mol percentage PS in cases where there is low surface charge density.[20] The molar partition coefficients for FVIIIa, in contrast, were found to exhibit a pronounced binding anomaly consisting of a peaked binding affinity in the region of about 12% PS. This anomaly is reported for the first time, and a possible molecular mechanism is presented employing binding of charged lipids to a discrete number of protein binding sites.

Factor VIII is activated by thrombin through the site-specific cleavage of both the heavy and light chains, resulting in the separation of the A1 and A2 domains, as well as the release of the B-domain. *In vivo*, these conformational changes lead to the

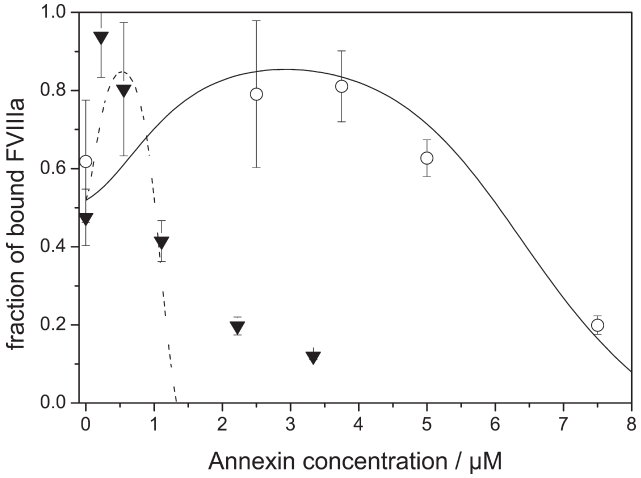

Figure 6. Comparison of the regulation of FVIIIa binding by annexin A5 in buffer (open circles) and in plasma (full triangles). The experiments in buffer are fitted according to the shielding model (full line), while the data in plasma can be described by the same theoretical dependence, when it is rescaled by a factor of 4 (dashed line).

dissociation of FVIII from the von Willebrand factor.[1] It is also believed that FVIII undergoes a conformational change in the C2 membrane-binding domain. We assumed that the release of the B-domain and possibly the associated conformational changes lead to exposition of the charge binding sites to the membrane and consequently to the observed enhancement of FVIIIa binding to membranes with an approximate composition of 12% molar content PS. It is noteworthy to mention that this binding characteristic of FVIIIa is also observable in blood plasma. The fact that binding of activated FVIII exceeds the binding of FVIII only in a narrow region of PS content, which coincides with the physiological PS content, might be important, since it allows for the selective binding of FVIIIa when injury occurs.

The experimental data of FVIIIa binding in the presence of annexin A5 seem to support an extended inhibition model proposed here, which assumes that annexin effectively reduces the PS content by shielding PS lipids upon binding. The partition coefficient of FVIIIa is shifted according to the reduced PS content, which, due to the unusual nature of the binding isotherm, results in an increase or decrease in binding affinity, depending on the actual PS concentration. The question arises if the characteristic of FVIIIa binding to vesicles also holds true for binding to platelets in circulation. Ahmad et al.[8] measured FVIII and FVIIIa binding to platelets corresponding to molar partition coefficients of 0.56 and 0.8 μM^{-1}, respectively, close to the values reported here for liposomes having a PS content approximately comparable to the physiological levels (10%). Our finding that FVIIIa exhibits stronger binding compared to FVIII in the physiological range is also consistent with results obtained for platelet binding.[1,8] Furthermore, FVIIIa binding to platelets is inhibited by annexin A5, which is in accordance with the findings from our model system. These results collectively confirm that PS-containing vesicles serve as a suitable model system for platelets, and that charge shielding, which reduces the effective charge of the membrane for FVIIIa, could be a mechanism for the involvement of annexin A5 in blood coagulation. Such a shielding mechanism explains the anticoagulant effect of annexin under nonpathological physiological conditions, and predicts a possible procoagulant effect for platelets exhibiting PS levels exceeding 12%.

We demonstrate that our competition model describes an indirect influence of annexin A5 on the binding of FVIIIa via the effective concentration of PS. It is likely that this scheme can be extended to the interplay of many cofactors. Here, we presented first indications that the effect of annexin A5 on FVIIIa binding to model membranes is enhanced in the presence of blood plasma. This enhancement might be due to other cofactors such as Factor IX. Ahmad et al.,[8] for example, reported an enhanced effect of annexin on FVIIIa binding to platelets in the presence of EGR-FIXa and FX. FCS allows for binding measurements in both buffer and plasma, and hence serves as a powerful tool for combinatorial binding studies. Such studies may ultimately allow the multidimensional cofactor landscape mapping of the membrane binding potential. This interplay of cofactor binding in membrane-based biochemical networks would be an important prerequisite to systems modeling of the blood coagulation cascade.

In conclusion, we have shown that the interaction of FVIIIa with PS membranes exhibits a highly unusual binding characteristic, which can be modulated by the presence of annexin. The binding of FVIII and FVIIIa is qualitatively described by a statisticial binding model and in addition its modulation by annexin by an extended competition inhibition model. Our study thus exemplifies the importance of PS content as a regulatory signal within the blood coagulation cascade and the possible role of annexin as a passive regulator of the effective PS level in platelets. Measurements of FVIIIa binding in blood plasma are feasible using FCS and would allow the competitive or cooperative binding of other cofactors to be studied. A complete and quantitative description of the entirety of membrane-mediated cofactor interdependencies will be the subject of further research.

■ ASSOCIATED CONTENT

Supporting Information. FCS analysis, antibody labeling, control experiments using optical thermophoresis, model of FVIII binding, and quantitative modeling of annexin regulation. This material is available free of charge via the Internet at http://pubs.acs.org.

■ AUTHOR INFORMATION

Corresponding Author
*E-mail: joachim.raedler@lmu.de.

■ ACKNOWLEDGMENT

Support from Bayer HealthCare, Berkeley, is gratefully acknowledged. H.E. also gratefully acknowledges the Elite Netzwerk Bayern for funding. J.O.R. and R.R.N. acknowledge support by the DFG through the excellence cluster NIM.

■ REFERENCES

(1) Saenko, E.; Scandella, D.; Yakhyanev, A.; Greco, J. *J. Biol. Chem.* **1998**, *273*, 27918–27926.
(2) Van Genderen, H.; Kenis, H.; Hofstra, L.; Narula, J.; Reutelingsperger, C. *Biochim. Biophys. Acta* **2008**, *1783*, 953–963.
(3) Posokhov, Y.; Rodmin, M.; Lu, L.; Ladokhin, A. *Biochemistry* **2008**, *47*, 5078–5087.

(4) Gerke, V.; Creutz, C.; Moss, S. *Nat. Rev. Mol. Cell Biol.* **2005**, *6*, 449–461.
(5) Tait, J.; Gibson, D.; Smith, C. *Anal. Biochem.* **2004**, *329*, 112–119.
(6) Van Heerde, W.; Poort, S.; van t'Veer, C.; Reutelingsperger, C.; de Groot, P. *Biochem. J.* **1994**, *302*, 305–312.
(7) Rand, J.; Wu, X.; Andree, H.; Ross, J.; Rusinova, E.; Gascon-Lema, M.; Calandri, C.; Harpel, P. *Blood* **1998**, *92*, 1652–1660.
(8) Ahmad, S.; Scandura, J.; Walsh, P. *J. Biol. Chem.* **2000**, *275*, 13071–13081.
(9) Andree, H.; Stuart, M.; Hermens, W.; Reutelingsperger, C.; Hemker, H.; Frederik, P.; Willems, G. *J. Biol. Chem.* **1992**, *267*, 17907–17912.
(10) Hockin, M.; Jones, K.; Everse, S.; Mann, K. *J. Biol. Chem.* **2002**, *277*, 18322–18333.
(11) McLaughlin, S.; Murray, D. *Nature* **2005**, *438*, 605–611.
(12) Golebiewska, U.; Gambhir, A.; Hangyas-Mihalyne, G.; Zaitseva, I.; Rädler, J. O.; McLaughlin, S. *Biophys. J.* **2006**, *91*, 588–599.
(13) Gilbert, G.; Furie, B.; Furie, B. *J. Biol. Chem.* **1990**, *265*, 815–822.
(14) Stoilova-McPhie, S.; Villoutreix, B.; Mertens, K.; Kernball-Cook, G.; Holzenburg, A. *Blood* **2002**, *99*, 1215–1223.
(15) Rhoades, E.; Ramlall, T.; Webb, W.; Eliezer, D. *Biophys. J.* **2006**, *90*, 4692–4700.
(16) Rusu, L.; Gambhir, A.; McLaughlin, S.; Rädler, J. *Biophys. J.* **2004**, *87*, 1044–1053.
(17) Griffin, B. D.; Micklem, L. R.; McCann, M. C.; James, K.; Pepper, D. S. *Thromb. Haemostasis* **1986**, *55*, 40–46.
(18) Engelke, H.; Dorn, I.; Rädler, J. *Soft Matter* **2009**, *5*, 4283–4289.
(19) Bardelle, C.; Furie, B.; Furie, B.; Gilbert, G. *J. Biol. Chem.* **1993**, *268*, 8815–8824.
(20) Ben-Tal, N.; Honig, B.; Peitzsch, R.; Denisov, G.; McLaughlin, S. *Biophys. J.* **1996**, *71*, 561–575.
(21) Sackmann, E. *Science* **1996**, *271*, 43–48.
(22) Douglass, A.; Vale, R. *Cell* **2005**, *121*, 937–950.

9 Conclusion and Outlook

For the underlying work, FCS was employed as a novel experimental approach for VWF research. Until now, studies on polymeric VWF faced manifold challenges, which were difficult to overcome: First of all, VWF is a blood plasma protein that is known to behave differently in buffer than in blood plasma supposably due to hitherto unknown helper proteins in the plasma. Thus, reliable quantitative data assessment requires experiments performed in blood plasma. Moreover, most of VWF's functions are known to be shear-dependent, because VWF possesses structural elements that open under flow-induced tension. Therefore, defined flow conditions have to be guaranteed in experiments. Finally, the multimer size is an important parameter for VWF's shear-dependent functionality. Because the exact size distribution of VWF was unknown, previously quantitative studies were virtually impossible with the full-length protein.

The here presented application of FCS paves the way for quantitative assessment of VWF properties. In this thesis, it was shown that FCS is well-suited to investigate VWF under blood plasma conditions and it proved to be sensitive to characterize disease-related VWF mutants. Moreover, the combination with a self-built microfluidic device allowed for studies of the full-length protein under shear flow. Due to the complexity of FCS read-out, diverse issues were successfully adressed, such as size distribution analysis, shear-induced cleavage, an enzyme activity assay, and binding studies. All studies were performed with FCS. Additionally, the different projects were complemented by alternative experimental approaches or computer simulations.

Extent of polymerization as disease indicator

In a first study, VWF's size distribution was quantified. Prior to this, commonly used assays only qualitatively determined the total amount of VWF as well as the relative amount of large VWF multimers. We showed that VWF has characteristic, exponentially distributed sizes and can be described by a single parameter, the extent of polymerization. This parameter was reduced for the disease related mutant VWF-IIC (VWF-C1099Y), and we proposed it as a

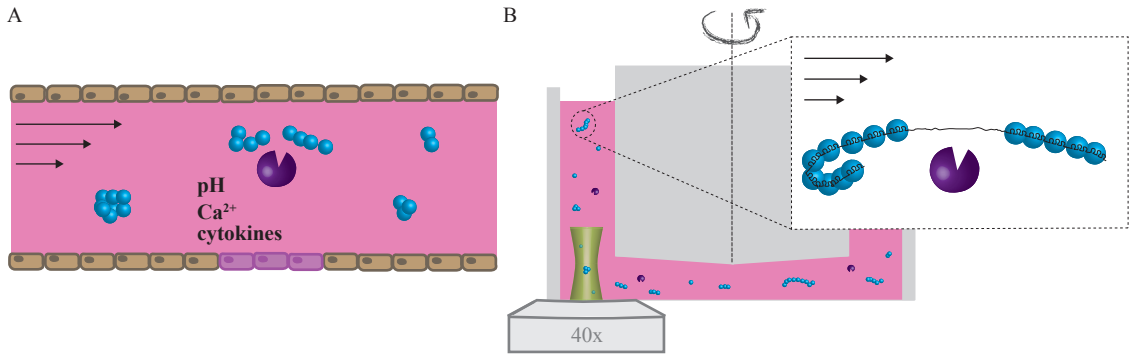

Figure 9.1: VWF in inflammation. **A** Ruptures of the blood vessel induce inflammatory reactions such as shifts of the pH and the Ca^{2+} concentration, and the secretion of cytokines. **B** The inflammatory milieu might influence both ADAMTS13 activity and shear-dependent VWF unfolding. This may be measured with the shear assay that was established in this work. (B modified from chapter 5)

potential disease indicator. There are various other VWF mutations that are known to result in different multimer patterns, causing hemostatic disorders in patients. Application of the presented assay to patient samples might help to quantify the disease-related shifts in VWF sizes by proposing the extent of polymerization as a valuable indicator for diagnosis of VWF-related diseases.

Model of shear-induced opening

In order to study VWF at defined shear rates, FCS was combined with a self-built shear cell. With this setup, VWF cleavage was measured in blood plasma and under shear flow. The assay enabled quantitative assessment of cleavage rates for VWF and VWF-G1629E mutant, and the investigation of VWF degradation as a function of shear-dependent VWF unfolding. Thereby, we found the unfolding transition and the opening of the A2 domain to be the crucial parameters for VWF degradation.

While it is known that ADAMTS13 concentrations reduced to 10% of the physiological level do not yet lead to critical symptoms, altered VWF unfolding transitions are likely to make a much greater contribution to hemostatic dysfunctions. Single mutations in the A2 cleavage domain can induce partly or even completely unfolded polymers. Thus, it would be of great interest to predict the impact of VWF mutations on VWF unfolding and the contribution of this unfolding transition to VWF proteolysis. Combining the here described approach, which involves FCS and Brownian Hydrodynamics Simulation, with Molecular Dynamics Simulations, might allow to construct such a complex model of shear-induced VWF opening. This model could relate VWF mutations directly to hemostatic dysfunction, closing the gap between atomistic VWF domain models and the coarse-grained hydrodynamic model proposed by us. This would not only lead to a more general understanding of VWF's shear-dependence, but moreover facilitate therapeutic VWF administration.

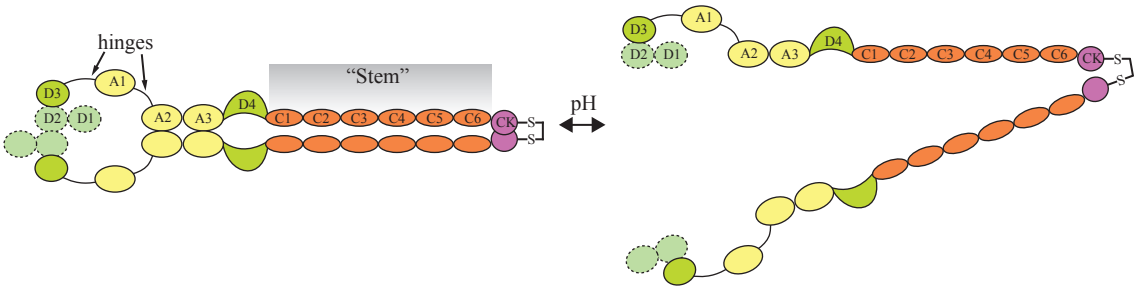

Figure 9.2: VWF dimer conformation. VWF possesses a pH-regulated dimeric stem, which might open after secretion to blood plasma at pH 7.4 (with courtesy of C. Baldauf, modified).

VWF proteolysis in inflammation

Interestingly, VWF proteolysis occurs not only under physiological conditions, as studied here, but also under pathophysiological conditions (see Figure 9.1). This is due to the fact that ruptures in the blood vessel simultaneously stimulate the initiation of the coagulation cascade and evoke inflammatory reactions. The resulting inflammatory milieu with acidic pH and altered Ca^{2+} concentrations might influence both ADAMTS13 activity and shear-dependent VWF unfolding. However, studies on VWF degradation under inflammatory conditions are lacking to date. Moreover, large amounts of VWF molecules are stored in intraendothelial Weibel-Palade bodies (WPB). There, VWF is colocalised with several proinflammatory proteins and chemokines, such as interleukin-8, P-selectin, and angiopoeitin-2. Upon endothelial cell activation, caused for example by an injury, hypoxia, or inflammatory stimuli, the contents of the WPBs are exposed to the blood flow. It is not known, whether the inflammatory proteins affect VWF's behavior, although there is the reasonable suspicion that VWF might work as a carrier for angiopoeitin-2. Angiopoeitin-2 is involved with controlling microvascular permeability, vasodilation, and vasoconstriction by signaling smooth muscle cells surrounding vessels. This poses the question whether and how VWF influences the regulation of vascular permeability under flow conditions. Using our established shear setup and the introduced data analysis, one could easily close these scientific gaps by solely modifying the surroundings, thereby providing insight into VWF's role and reactivity in inflammatory environments.

VWF stem conformation

We showed that VWF's mechanosensitive conformation plays a crucial role in its degradation. In addition to this, its flexible structure is essential for its overall functionality as it accounts for its accessibility for binding partners. Current research mainly focused on opening of recombinant VWF A domains and unfolding of the full-length protein. However, the role of the VWF C domains, the so called *stem*, has not been studied yet (see Figure 9.2). Recent publications show first evidence of a pH-regulated dimeric bouquet in VWF's structure and indicate that the C domains might induce an opening of the stem structure (84). Nevertheless, whether the dimers are in solution present with an open or closed stem remains an open ques-

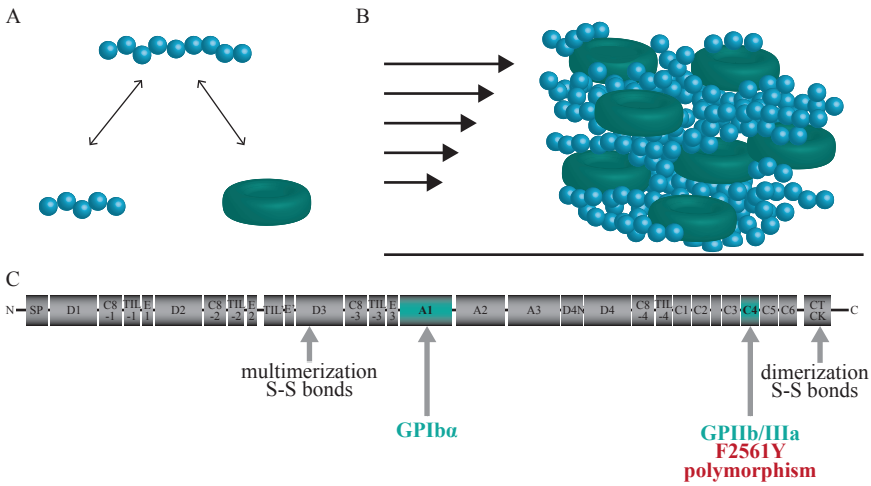

Figure 9.3: Formation of VWF-induced networks. **A** VWF (blue) self-assembles and binds to thrombocytes (green) via two glycoprotein receptor complexes, namely GPIbα and GPIIb/IIIa. **B** Under shear flow, VWF is streched and forms networks via crosslinking and binding to thrombocytes. **C** VWF with C4 domain polymorphism F2561Y is related to increased network formation. The polymorphism is located next to the GPIIb/IIIa binding site.

tion. Studying VWF's dimer conformation in terms of hydrodynamic radii as a function of pH and mutations might contribute to understanding the impact of VWF structure and flexibility on its function.

C4-domain polymorphism and network formation

In this context, an interesting mutation was recently discovered by the group of Prof. Schneppenheim (UKE, Hamburg): Preliminary results indicate that a C4 domain polymorphism (F2561Y) might be associated with an increased risk for myocardial infarction in young women. The underlying mechanisms, however, are completely unknown. Still, it was shown, that the polymorphism affects VWF-platelet network formation (see Figure 9.3 A,B). This leads to the suspicion that the polymorphism facilitates both aggregation of VWF molecules and binding to thrombocytes, resulting in higher order networks in the blood vessel, which might induce myocardial infarcts. Thus, both an increased affinity to thrombocytes and favored VWF cross-linking are assumed for VWF-F2561Y. As the C4 domain might have an impact on the stem formation, these properties are presumed to result from changes in stem flexibility due to the polymorphism, especially since the GPIIb/IIIa binding site for platelets on VWF is located next to the polymorphism site (see Figure 9.3 C). Thus, mutations in this domain could heavily influence GPIIb/IIIa binding. This hypothesis may be proved by exploring the interaction of C4 domains both with each other and with full-length VWF wt and mutant using FCS. In addition, binding affinities of VWF wt and mutants to GPIIb/IIIa may be analyzed. Performing the experiments under flow conditions would allow to correlate the binding affinities with the observation of collective network formation under shear flow and finally lead to a description of the kinetics of the network formation for VWF wt and mutant as a function of shear stress. This might elucidate the role of VWF in widespread conditions

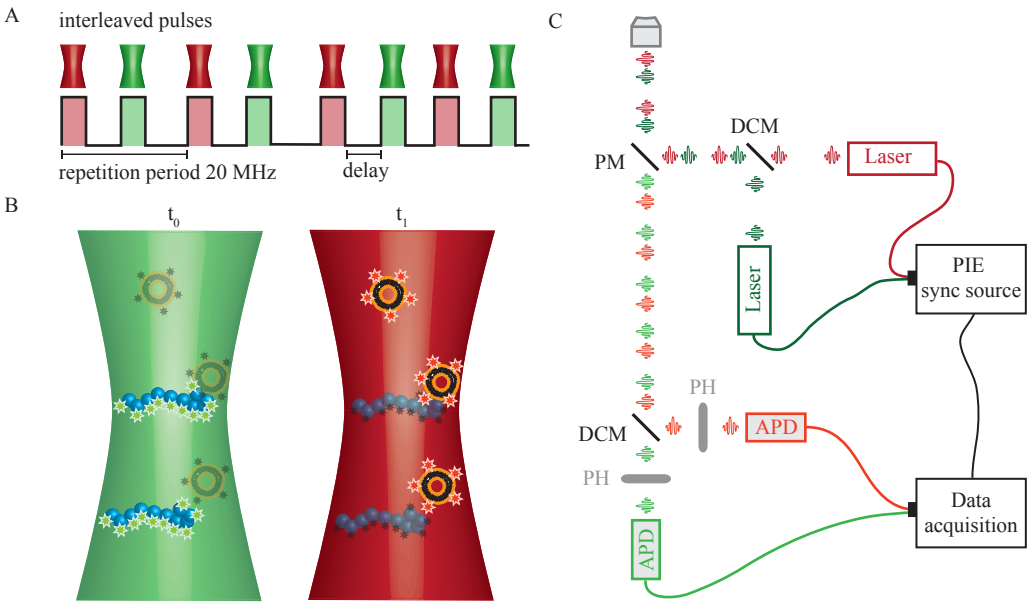

Figure 9.4: Pulsed Interleaved Excitation (PIE) - FCCS. A Two excitation sources are interleaved so that the fluorescence emission generated from one pulse is completed before the next excitation pulse arrives. **B** Due to different labels, FCS can distinguish between the time-resolved fluorescence emission of binder and receptor molecule, while spectral crosstalk is eliminated. **C** Schematic of a dual-color confocal microscope with pulsed interleaved excitation sources. In the diagram, APD refers to avalanche photodiode, DCM to dichroic mirror, PM to polychroic mirror, and PH to pinhole.

such as stroke or cardiac infarction.

Binding studies under flow

In this thesis, an analysis routine was implemented for quantitative, FCS-based binding studies on full-length VWF. Binding of VWF-wt and -mutants to PDI showed that PDI is the enzyme that facilitates VWF dimerization in the endoplasmatic reticulum. Although this study confirms that FCS is well suited for VWF binding studies under static conditions, the analysis of binding under flow requires further enhancement of the FCS, which cannot be based on determining diffusion times anymore. In 2005, Pulsed Interleaved Excitation (PIE) has been introduced to meet this challenge (85). In PIE, multiple excitation sources are interleaved so that the fluorescence emission generated from one pulse is completed before the next excitation pulse arrives (see Figure 9.4). Hence, the excitation source for each detected photon is known. Using PIE with FCS would allow to distinguish between the time-resolved fluorescence emission of binder and receptor molecule, if they were labeled with different colors; cross correlation of both signals would designate the fraction of bound molecules. Thereby, spectral crosstalk is eliminated, and the method is also sensitive for weak interactions. As shear flow essentially influences VWF's behavior, the establishment of a PIE-FCS would enable a whole slew of medically relevant and biophysically intriguing experiments.

Conclusion

The multifaceted role of shear stress in the regulation of VWF function and mutation-related dysfunction poses manifold experimental challenges and many open questions. In the here presented work, we found PDI to assist with dimerization of VWF in the ER. We established a model for the polymerization of these dimers based on the resulting size distribution. Following the multimer size after secretion to the blood plasma, we helped to unravel the mechanisms of shear-regulated activation of VWF cleavage and the influence of blood plasma conditions and VWF mutations on these characteristics. Encouraged by this study, we developed a highly sensitive assay to detect ADAMTS13 activity in patient samples. However, although these studies unraveled many open questions, further research has to be done to establish a coherent picture that relates the shear sensitive molecular structure to nano-mechanical properties of VWF and links dysfunction of VWF mechanistically to its outcome in clinical presentation. The realization of this picture represents a fascinating overlap of single molecule studies with collective phenomena in a research area that is of paramount medical importance.

A

Supporting Material for "Exponential Size Distribution of von Willebrand Factor"

Exponential Size Distribution of von Willebrand Factor

Supporting Material

Svenja Lippok[*], Tobias Obser [†], Jochen P. Müller[‡], Valentin K. Stierle*, Martin Benoit[‡], Ulrich Budde[§], Reinhard Schneppenheim[†], Joachim O. Rädler[*]

[*] Faculty of Physics and Center for NanoScience, Ludwig Maximilian University, Munich, Germany

[†] Department of Pediatric Hematology and Oncology, University Medical Center Hamburg-Eppendorf, Hamburg, Germany

[‡] Chair for Applied Physics, Ludwig Maximilian University, Munich, Germany

[§] Coagulation Lab, AescuLabor Hamburg, Hamburg, Germany

S1: FCS data analysis

FCS measures the dynamics of molecules in solution by analyzing the time-dependent fluctuations of the fluorescence intensity collected from a confocal detection volume (Figure S1A,B). The normalized autocorrelation function G(τ) of the intensities I(t) is defined as:

$$G(\tau) = \frac{\langle I(t) I(t+\tau) \rangle - \langle I(t) \rangle^2}{\langle I(t) \rangle^2}$$

where $\langle\ \rangle$ denotes the time average. For free diffusion of molecules in a three-dimensional Gaussian probe volume with radial dimension ω_r and axial dimension ω_z, G(τ) is derived analytically to (1):

$$G(\tau) = \frac{1}{N} \frac{1}{1+\frac{\tau}{\tau_D}} \frac{1}{\sqrt{1+\frac{\tau}{\left(\omega_z / \omega_r\right)^2 \tau_D}}}$$

wherein N is the average number of particles in the focus and τ_D, the diffusion time, the time the molecules need to cross the focal width. This single-component analysis allows for the determination of diffusion coefficient $D=\omega_r^2/4\tau_D$ and concentration N of molecules of the same species. For a perfectly spherical particle, the hydrodynamic radius is given by $r_{hyd} = k_B T/6\pi\eta D$ with Boltzmann constant k_B and viscosity η.

For a particle with cylindrical shape, the diffusion coefficient D is given by $D = Ak_BT/3\pi\eta L$ with cylinder length L and correction factor A: $A = \ln(L/d)+0.312+0.565/(L/d)-0.1/(L/d)^2$ with diameter d. According to (2,3), the dimer has a cylindrical shape. With this equations and the assumption that the VWF monomer can be described with the same diameter but half the length of the dimer, we get the length l_D = 85.3 nm and the diameter a_D = 3 nm for the VWF dimer (see Figure S1C).

For measurements of an n-component mixture of noninteracting fluorescent particles, multicomponent analysis is applied based on the fact that the overall autocorrelation function is a weighted sum of the autocorrelation functions of all components (4):

$$G(\tau) = \frac{\sum_{i=1}^{n} q_i^2 N_i G_i\left(\tau / \tau_{Di}\right)}{\left(\sum_{i=1}^{n} q_i N_i\right)^2}$$

where q_i denotes the brightness, N_i the number and τ_{Di} the diffusion time of molecules of species i. As VWF multimers are organized as long linear chains comprised of a certain number of dimers, VWF dimer serves as the building block of the distribution, and the multimer size is given in number of dimers i. To calculate the diffusion time τ_{Di} of a VWF polymer that consists of i subunits, we use the simple Rouse model (5) that describes the

conformational dynamics of an ideal chain by: $\tau_{Di} = \tau_{a_D} \cdot i$ with the diffusion time τ_{aD} of the building block of the polymer. We choose this simple model as there is little known about the persistence length of the VWF polymer and its exact shape in the used buffer containing 1.5 M urea. The diffusion time of the rVWF dimer is obtained from FCS measurements as τ_{aD} = 447µs (see Figure 3A). The brightness q_i scales with the number of dimers i as each VWF monomer is labeled with one eGFP molecule. Quenching is possible for dimers with respect to monomers due to binding of eGFP at the dimerization site but unexpected for multimers among each other as there is no label at the multimerization site. Since we measure in units of brightness per dimer, quenching is neglected (q_i = i). If there was quenching among the multimers, we would expect it to be a constant resulting in a brightness q_i =s*i with quenching factor s. In our fit formular, the brightness appears multiplied with the number of multimers N_i : q_i*N_i = i*s*N_1*p^{i-1} where N_1 denotes a constant fitting parameter. With the constant quenching factor s, a new fitting factor $N_1' = N_1$*s would be used and s would not affect fitting of the extent of polymerization. For this reason it would not alter our results.

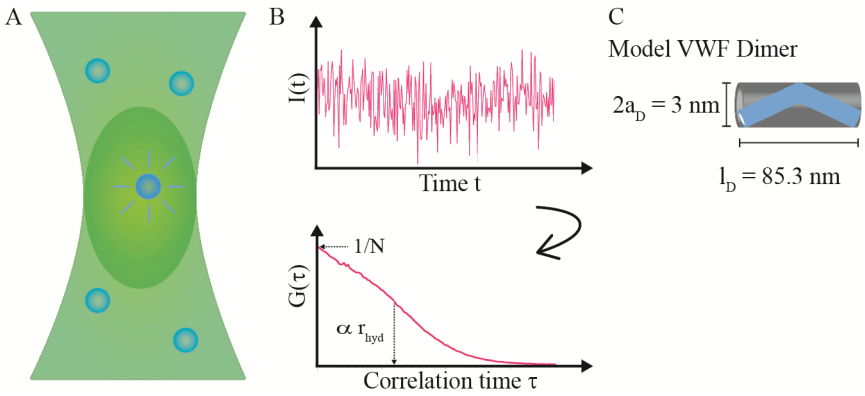

Fig. S1 Principles of Fluorescence Correlation Spectroscopy (FCS) and model of rVWF dimer. (A) FCS measures the dynamics of fluorescently labeled molecules diffusing in and out of a observation volume created by a confocal microscope. (B) Correlation analysis of the detected intensity trace provides information about particle size and concentration. (C) Cylindrical shape of the VWF dimer.

S2: Step-growth polymerization model

In 1936, Flory defined a step-growth polymerization model for polymers which have a functional group that reacts independently of the size of the molecule to which it is attached, and polymerize in an enclosed reactor as a linear chain (6). As VWF polymerizes in the Golgi Apparatus as a linear chain through the formation of disulfide bonds between the dimers, the exponential size distribution VWF shows can be explained by assuming the step-growth polymerization model presented by Flory.

For better understanding, we present an abbreviated derivation based on Flory's Paper in the following:

N_0 is the total number of dimers, N_{pol} is the number of polymerized segments, $p=N_{pol}/N_0$ is the extent of reaction, i.e. the fraction of the total number of segments that are polymerized (= extent of polymerization). A polymer is defined by containing two or more segments. An i-mer is a polymer that exists of i segments (here: VWF dimers).

For b being a possible polymerization site within a large group of partially polymerized segments, the probability that polymerization occurs at any particular b is p, and the probability that no polymerization takes place is 1-p. There are i possible configurations which fulfill the condition that a segment is part of an i-mer and each i-mer has i-1 polymerized sites as well as 2 unreacted possible polymerization sites. Thus, the probability that any of the i configurations exists is $\Pi_i = i*p^{i-1}*(1-p)^2 = (i*N_i)/N_0$. Π_i determines the fraction of segments which exist as component of i-mers.

Therefore the **number of i-mer molecules** is given by: $\mathbf{N_i = N_0\, p^{i-1}*(1-p)^2}$. As we do not know the total number of dimers N_0 that is present in the Golgi during polymerization, we define a constant fit parameter $N_1 = N_0*(1-p)^2$. This results in our fit formula: $\mathbf{N_i = N_1*p^{i-1}}$ which fits the extent of polymerization p.

The total number of molecules is given by $N = N_0*(1-p)$. Therefore the molar fraction of i-mers containing i subunits is $N_i/N = (p-1)p^{i-1}$.

S3: Size Distribution Analysis with TIRFM and rVWF dimer as a control

For measuring the VWF size distribution, we monitor two-step photo bleaching of the rVWF molecules. We cannot simply use the overall intensity of molecules for our size distribution analysis, as the intensity of eGFP fluorescence depends on the orientation of the chromophore relative to the polarization of the exciting beam (7). In our experiment, the VWF-eGFP was immobilized via free amino groups on an epoxysilane (3-glycidyloxypropyltrimethoxysilan) coated glass slide. This binding of eGFP molecules on the surface restricts the rotational degrees of freedom of eGFP which influences the effective excitation and thus the intensity of the emitted light of the chromophore. Therefore, the steps in the intensity traces do not have the same height.

There is the trend that the first step is larger than the last steps. For a constant excitation of a chromophore, the time until photo bleaching occurs (= emission time) follows an exponential distribution. An increase in the excitation intensity, which is correlated to the emission intensity, shifts this distribution to shorter emission times. High intensities are therefore by trend correlated to short emission times and vice versa. Thus, the first steps of the intensity-time-traces, i.e. the photo bleaching events of chromophores with a short emission time, are more likely to come along with a high emission intensity. Therefore, early bleaching steps tend to be higher.

To proof the ability of measuring rVWF size distribution by counting the bleaching steps of the rVWF molecules, we studied rVWF dimers that contain two eGFPs; one fused to each monomer (Figure S3). We detected one and two step events but no intensity trace with more than two bleaching steps. Therefore, a clear distinction can be made between the rVWF dimer and multimer sample.

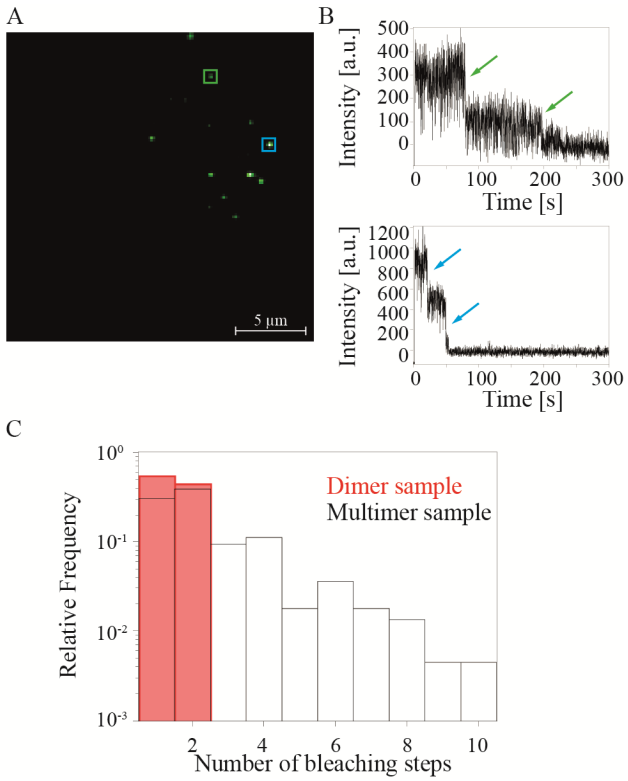

Fig. S3 TIRFM analysis of rVWF dimer sample. (A) TIRFM image of rVWF dimers. (B) Intensity-time traces were analyzed to count bleaching steps as indicators for the number of eGFP-tagged VWF monomers. In (C) the relative frequencies of the number of bleaching steps are shown for the dimer and the multimer sample. Whereas in the multimer sample multiple bleaching steps were detected, the dimer sample shows only one or two bleaching steps.

Supporting References:

1. Elson, E.L., and D. Magde. 1974. Fluorescence correlation spectroscopy. I. Conceptual basis and theory. Biopolymers. 13:1-27.

2. Springer, T.A. 2011. Biology and physics of von Willebrand factor concatamers. Journal of Thrombosis and Haemostasis. 9:130-143.

3. Seyfried, B.K., G. Friedbacher, H. Rottensteiner, H.P. Schwarz, H. Ehrlich, G.n. Allmaier, and P.L. Turecek. 2010. Comparison of plasma-derived and recombinant von Willebrand factor by atomic force microscopy. Thrombosis & Haemostasis. 104:523-530.

4. Thompson, N.L. 1991. Fluorescence Correlation Spectroscopy. In Topics in Fluorescence Spectroscopy, Vol.1. J.R. Lakowicz, editor. Plenum Press, New York. 337-378.

5. Rouse Jr, P. E. 1953. A theory of the linear viscoelastic properties of dilute solutions of coiling polymers. The Journal of Chemical Physics. 21: 1272-1280.

6. Flory, P.J. 1936. Molecular Size Distribution in Linear Condensation Polymers1. Journal of the American Chemical Society. 58:1877-1885.

7. Inoué, S., O. Shimomura, M. Goda, M. Shribak, and P. T. Tran. 2002. Fluorescence polarization of green fluorescence protein. Proceedings of the National Academy of Sciences. 99:4272-4277.

B

Supporting Information for "Shear-dependency of ADAMTS13-mediated cleavage measured on full-length VWF under blood plasma conditions"

Shear-dependency of ADAMTS13-mediated cleavage measured on full-length VWF under blood plasma conditions

Supporting Information

Svenja Lippok[a], Matthias Radtke[b], Tobias Obser[c], Lars Kleemeier[a], Reinhard Schneppenheim[c], Roland R. Netz[b], and Joachim O. Rädler[a,1]

[a] Faculty of Physics and Center for NanoScience, Ludwig Maximilian University, 80539 Munich, Germany

[b] Department of Physics, Freie Universität Berlin, 14195 Berlin, Germany

[c] Department of Pediatric Hematology and Oncology, University Medical Center Hamburg-Eppendorf, 20246 Hamburg, Germany

S1 Analysis of the VWF concentration using FCS

FCS uses a confocal fluorescent microscope to analyze the diffusion of fluorescently labeled molecules by correlating the intensity fluctuations within the confocal volume over time [1-3]. For identical fluorescent particles undergoing Brownian motion in a three-dimensional Gaussian focus volume element with radial dimension ω_r and axial dimension ω_z, the autocorrelation curve can be described by [2]:

$$G(\tau) = \frac{1}{N} \frac{1}{1+\frac{\tau}{\tau_D}} \frac{1}{\sqrt{1+\frac{\tau}{\left(\omega_z / \omega_r\right)^2 \tau_D}}}$$

The diffusion time τ_D, which states the time the molecules need to cross the focal width, is used to determine diffusion constants and hydrodynamic radii as described elsewhere [4,5]. In addition, the amplitude of the correlation curve at correlation time $\tau = 0$ s is a measure for the molar particle concentration: the particle number $N = 1/G(0)$ indicates the average number of fluorescent molecules within the confocal volume. Calibration of the confocal volume V_{con} with a known substrate (e.g. eGFP) allows calculating the molar particle concentration $C = \frac{N}{V_{con} \cdot N_A}$, with Avogadro constant N_A.

FCS can be used in crowded media such as blood plasma, thus enabling the investigation of blood proteins in their natural environment [6]. Moreover, fast measurement times allow the online detection of kinetics processes that occur within the minute scale.

In this study, the molar particle concentration of VWF is determined using FCS. This is possible because the amplitude of the correlation curve at correlation time $\tau = 0$ s, G(0), is a measure for the particle number N within the confocal volume: $1/G(0) = N$ [1-3]. To assure that this holds for the VWF distribution, we measured a serial dilution of rVWF in buffer (Figure S1A). This measurement validates that the particle number increases linearly with the rVWF concentration.

However, FCS weigths the molecules according to their brightness. In our measurements, each monomer is labeled with one eGFP molecule. Therefore, the brightness q_i of each VWF polymer scales with its size i. As a consequence, G(0) is given by $G(0) = \frac{\sum_i q_i^2 N_i}{\left(\sum_i q_i N_i\right)^2}$ with brightness $q_i = i$ and particle number N_i for a polymer with size i [7]. During cleavage, the VWF distribution changes its shape, shifting from longer to shorter polymer sizes. Before cleavage, N_i is exponentially distributed [5]: $N_0 = \sum_i N_i = \sum_i (p-1)p^{i-1}$ with the extent of polymerization being $p = 0.64$. After complete proteolysis, only dimers are present [8]. Thus, the particle number increases to $N_{end} = i(p-1)p^{i-1}$. Analytical assessment of the shift in

concentration due to complete cleavage yields (i = 1-20): $\frac{C_{end}}{C_0} = \frac{\sum_i i(1-p)p^{i-1}}{\sum_i (1-p)p^{i-1}} = 2.78$. For FCS analysis, the initial particle number N_0 is slightly underestimated and N_{end}/N_0 yields $\frac{G(0)_0}{G(0)_{end}} = \frac{N_{end}}{N_0} = \frac{\sum_i i^2 p^{i-1}}{\sum_i i^3 p^{i-1}} \cdot \left(\frac{\sum_i i^2 p^{i-1}}{\sum_i i p^{i-1}} \right)^2 = 3.10$. FCS experiments of complete cleavage, however, detected $N_{end}/N_0 = 2.9$ (Figure S1B). Thus, the theoretical error due to the brightness-weighted particle numbers lies within the measurement accurancy and the used FCS analysis seems applicable.

Nevertheless, to optimize our data analysis, we simulated VWF cleavage based on the assumption of random cleavage sites combined with an equal cleavage probability for all polymer sizes. These conditions are reasonable for cleavage in a denaturizing buffer [5]. The resulting particle number N_{Sim} was plotted versus the number of cleavage steps (Figure S1C). For each cleavage step, we calculated the FCS signal $N_{FCS} = 1/G(0)$ that would be generated by the corresponding size distribution. The percentaged deviation of the FCS signal N_{FCS} and the simulated particle number N_{Sim} is depicted in the inlet. For the first three cleavage steps, which is the regime we use for the data evaluation, the error amounts to 37.02 ± 4.5 %. This means that there is a general underestimation of the VWF concentration, which we have to take into account to assess the absolute concentration. As we can exactly calculate this underestimation for the uncleaved VWF distribution to be $\frac{N_0 - N_{0,FCS}}{N_0} = 40.4\%$, we correct all C_{VWF} values accordingly (red curves, S1C). In contrast, cleavage rates do not have to be corrected, as here the underestimation remains sufficiently constant within the relevant regime (S1C, inlet, red curve).

For the VWF cleavage induced by shear flow, the cleavage sites in middle of the polymer might be slightly favored. In order to estimate the case of the fastest possible size shift, we simulated the cleavage of the VWF distribution cutting each polymer in the middle (Figure S1D, black lines). For the resulting size distribution, the FCS output is calculated (Figure S1D, grey lines). This cleavage occurs faster; five cleavage steps are sufficient to cleave the physiological VWF distribution to dimers. Therefore, the FCS data equals the simulated particle number from cleavage step four onwards (Figure S1D, inlet). However, FCS data correction by adding the brightness-induced underestimation works very well for the first two cleavage steps. Because this is the regime, where maximal cleavage rates can be measured, we use it for our data analysis and correct the VWF concentrations accordingly.

Thus, we correct the systematic underestimation of 40.4 % for the VWF concentration in all analysis data. Although there is still a slight difference to the absolute concentration, the correction minimizes the error in the concentration detection. Moreover, a small shift in the VWF concentration has a negligible impact on our relevant fitting parameter, the Michaelis-Menten constant. Therefore, using the corrected FCS data, the precision of the Michaelis-Menten constant is limited by the measurement accurancy only. For the measurements in

blood plasma, we furthermore add the physiological VWF concentration of 3 nM to the measured concentration considering the unlabeled VWF within the plasma.

With these corrections and the benefits of our approach, including avoidance of purification and immobilization, defined labeling with fluorescent proteins, and fast and easy data analysis, this method is a promising and sensible assessment of the VWF cleavage rates.

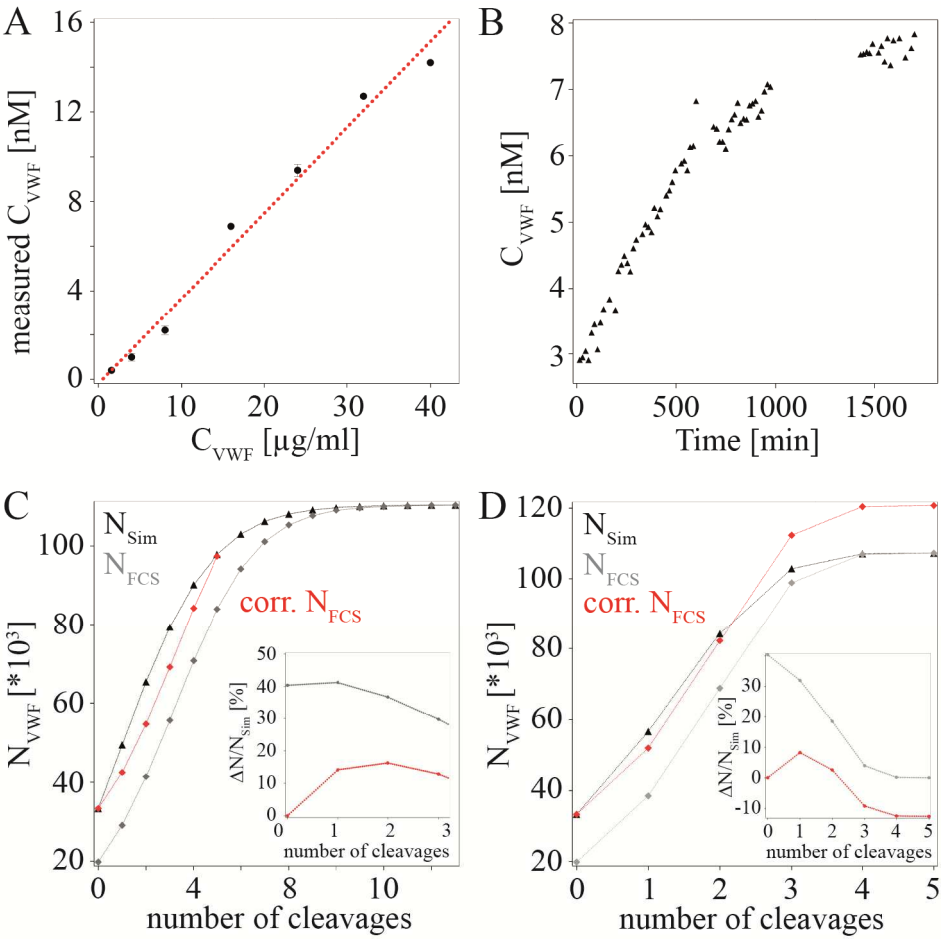

S1 VWF concentration detection using FCS. **A** Dilution series of rVWF in buffer measured with FCS. **B** Changes in VWF concentration during complete rVWF proteolysis. **C** Comparison of the simulated particle number N_{Sim} (black) during random cleavage of VWF and the particle number 1/N = G(0) (grey) generated using FCS. Red curves show the particle number after correction of the FCS data. **D** Particle numbers originating from VWF cleavage that cuts the molecules in the middle. Data correction (red) shifts the FCS data (grey) towards the simulated particle numbers (black). **Inlets:** Percentaged error of the FCS data analysis with (red) and without (grey) correction.

S2 VWF aggregation at high shear rates exceeds ADAMTS13 cleavage

For high shear rates, ADAMTS13 cleavage seems to compete with VWF aggregation. For the physiological ADAMTS13 concentration (1 U/ml), we detected VWF aggregation to appear at a shear rate $\dot{\gamma}$ = 7500/s (Figure S2A). After 30 minutes of shearing, aggregates with hydrodynamic radii of up to 1 µm formed. Within two and a half hours of shearing, the protease could not destroy these aggregates. However, after 135 minutes, the particle concentration recovered to 0.3 nM, corresponding to one twentieth of the initial concentration. At a tenfold higher ADAMTS13 concentration, aggregation was detected at $\dot{\gamma}$ = 10000/s (Figure S2B). After half an hour of shearing, the formed aggregates reached similar hydrodynamic radii of maximally 1µm but appeared at a significantly lower number. The particle concentration recovered to approximately one third of its origin within the next 105 minutes of shearing, probably due to augmented proteolytic activity.

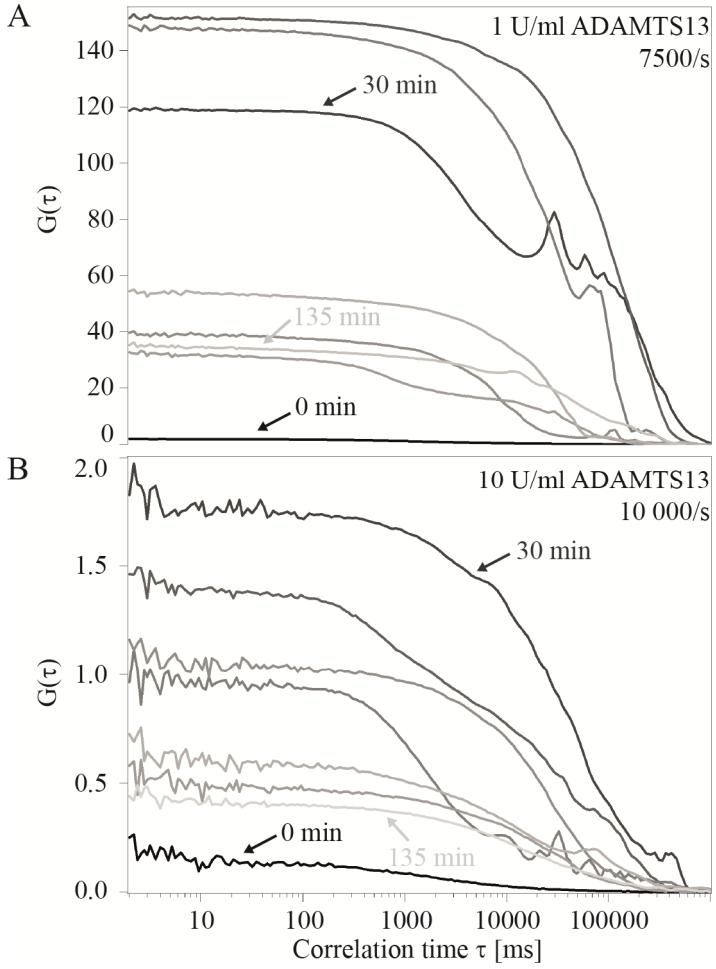

S2 VWF aggregation at high shear rates. **A** Applying 1 U/ml ADAMTS13 and $\dot{\gamma}$ = 7500/s, VWF aggregates formed. Although, the number of aggregates decreased over time, it stayed at high levels. **B** The tenfold protease concentration and a higher shear rate caused a significantly stronger increase in VWF concentration over time. Shearing time increases with diminishing brightness of the curves.

S3 Brownian dynamic simulation

Brownian hydrodynamics simulations were performed using the discretized Langevin equation

$$\vec{r}_i(t+\Delta t)-\vec{r}_i(t)=\left(\vec{\mu}_{ii}\dot{\gamma}z_i\hat{x}-\sum_{j=1}^{N}\vec{\mu}_{ij}\cdot\nabla_{\vec{r}_j}U(t)\right)\Delta t+\vec{\xi}_i(t),$$

which describes the displacement of bead i at position $\vec{r}_i$ after the time step Δt. Note that all quantities used are made dimensionless by rescaling lengths $r=\tilde{r}/a$ by the monomer radius a, energies $U=\tilde{U}/k_BT$ by thermal energy, and times $t=\tilde{t}/\tau$ by the characteristic monomer diffusion time $\tau=a^2/\mu_0 kT=6\pi\eta a^3/kT$, where μ_0 is the Stokes mobility and η the solvent viscosity. The first term in the Langevin equation represents a linear shear flow with rate $\dot{\gamma}=\tilde{\dot{\gamma}}\tau$, and $\hat{x}$ is the unit vector in x-direction. The second term accounts for the direct force acting on particle i itself as well as the hydrodynamic flow-field created by forces acting on all other particles $j\neq i$. Hydrodynamic interactions are taken into account via the mobility matrix approximated by the Rotne-Prager tensor [9]:

$$\vec{\mu}_{ij}=\tilde{\vec{\mu}}_{ij}/\mu_0=\begin{cases}\dfrac{3}{4r_{ij}}\left(\left(1+\dfrac{2}{3r_{ij}^{\,2}}\right)\vec{1}+\left(1-\dfrac{2}{r_{ij}^{\,2}}\right)\dfrac{\vec{r}_{ij}\vec{r}_{ij}}{r_{ij}^{\,2}}\right); r_{ij}\geq 2\\ \left(1-\dfrac{9r_{ij}}{32}\right)\vec{1}+\dfrac{3r_{ij}}{32}\dfrac{\vec{r}_{ij}\vec{r}_{ij}}{r_{ij}^{\,2}}; r_{ij}<2\end{cases}$$

with $\vec{r}_{ij}=\vec{r}_i-\vec{r}_j$ and $r_{ij}=\left|\vec{r}_{ij}\right|$. The stochastic contribution $\vec{\xi}_i$ is given by Gaussian random vectors with correlations according to the fluctuation-dissipation theorem $\left\langle\vec{\xi}_i(t)\vec{\xi}_j(t')\right\rangle=6\vec{\mu}_{ij}\Delta t\,\delta(t-t')$ and vanishing mean. The simulation time step is typically chosen as $\Delta t = 10^{-4}$.

The VWF is modeled as a homopolymer consisting of N beads, which interact via Lennard-Jones potentials of depth $\varepsilon=\tilde{\varepsilon}/k_BT=1.2$ and are connected in a linear chain by harmonic bonds with a rescaled spring constant $k=\tilde{k}/\left(k_BTa^2\right)=200$; the total potential reads

$$U=\varepsilon\sum_{i<j}\left(\left(2/r_{ij}\right)^{12}-2\left(2/r_{ij}\right)^{6}\right)+\frac{k}{2}\sum_i\left(r_{i,i+1}-2\right)^2.$$

Tensile forces acting along each bond, $f_i=-k\left(r_{i,i+1}-2\right)$, are recorded during the course of simulation. In order to compare the dimensionless simulation values to physical units, we use for the dimer radius a = 45 nm, the viscosity $\eta = 1.2\text{x}10^{-3}$ Pas, and temperature T = 310K and obtain a characteristic monomer diffusion time $\tau = 4.8\text{x}10^{-4}$s. The cohesive strength of the polymer is chosen as ε = 1.2 such that the polymer is collapsed in the absence of shear and the

unfolding transition occurs at a shear rate comparable to the experimental value of $\tilde{\dot{\gamma}}$ = 3000/s.

The average tensile force profiles for three different chains length N=10,20,30 are shown in Figure S3. For low shear rate, $\dot{\gamma}$ = 0.5, the polymers are collapsed and low tensile forces only stem from thermal fluctuations. The unfolding transition, which can be determined by the variance of the chain extension (data not shown), occurs around $\dot{\gamma}$ = 1.5. Note that the value of this shear rate also depends on the chain length. The tension increases with increasing shear rate due to flow induced unfolding and exhibits a flattened profile with minimal forces at the chain ends. At high shear rates the maximal tensions along unfolded, long polymers does not strongly depend on their length. The standard deviation for $\dot{\gamma}$ = 7.5 indicates a broad distribution of the tensile forces.

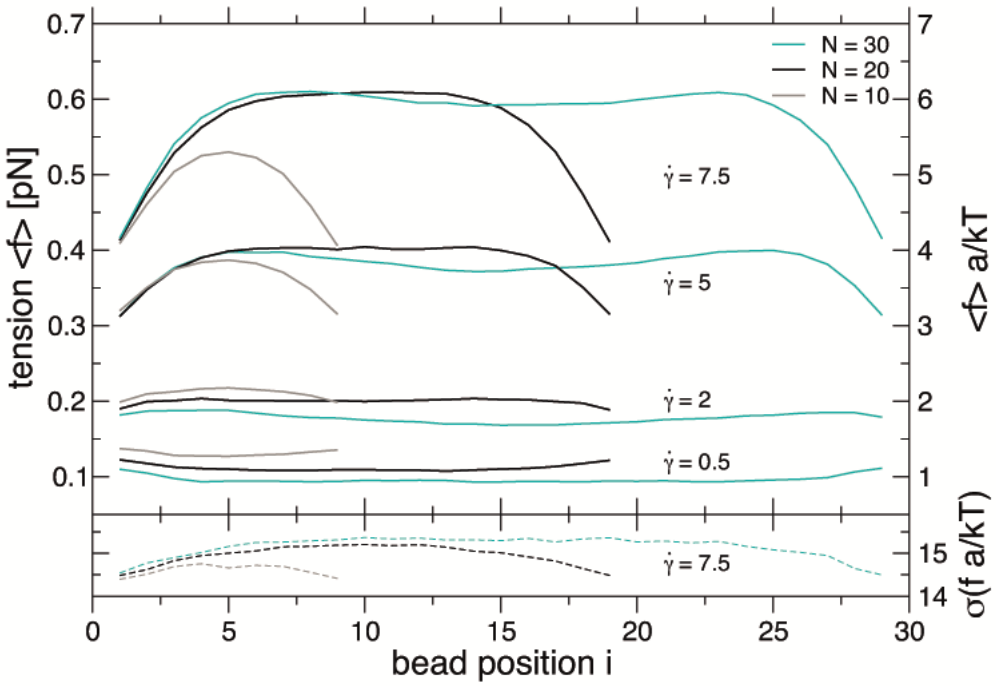

Figure S3: Average tensile force as a function of bead position along the polymer. Different colored profiles correspond to different chain length N; tension increases for increasing rescaled shear rate $\dot{\gamma}$. The standard deviation σ(f) is shown on a separate scale as dashed lines for $\dot{\gamma}$ = 7.5.

From the tension distribution of a single bead, e.g. the middle bead i=N/2, we obtain the opening probability for a single cleavage site, defined by the probability $P_i(f>f_c)$ that the

tension exceeds a critical value f_c. Considering the whole multimer, we define the opening probability as the probability that at least one of the N cleavage sites is accessible:

$$P_{open} = 1 - \prod_{i}^{N} (1 - P_i(f > f_c))$$

In Figure S4A, we plot the opening probability as a function of shear rate for the whole multimer P_{open} (black lines) as well as the probability $P_i(f>f_c)$ for a single bead to become accessible (grey lines). We show these data for two different values of the critical force f_c. Compared to P_i (single bead), P_{open} for the multimer rises much steeper and quickly saturates. In the main text, we choose f_c=30 (solid lines) because it yields a vanishing opening probability for low shear rates. As shown in Figure S3A, a lower critical force f_c=20 leads to higher opening probabilities for low shear and slightly shifts the characteristic increase toward lower shear rates. In Figure S4B, we illustrate the dependence of P_{open} on the multimer size. With increasing multimer size N, the opening probability increases. The red line in Figure S4 B constitutes the weighted average of $P_{open}(N)$ for N=10,20,30 with weights according to the VWF size distribution p^{N-1} with base p=0.64 [5].

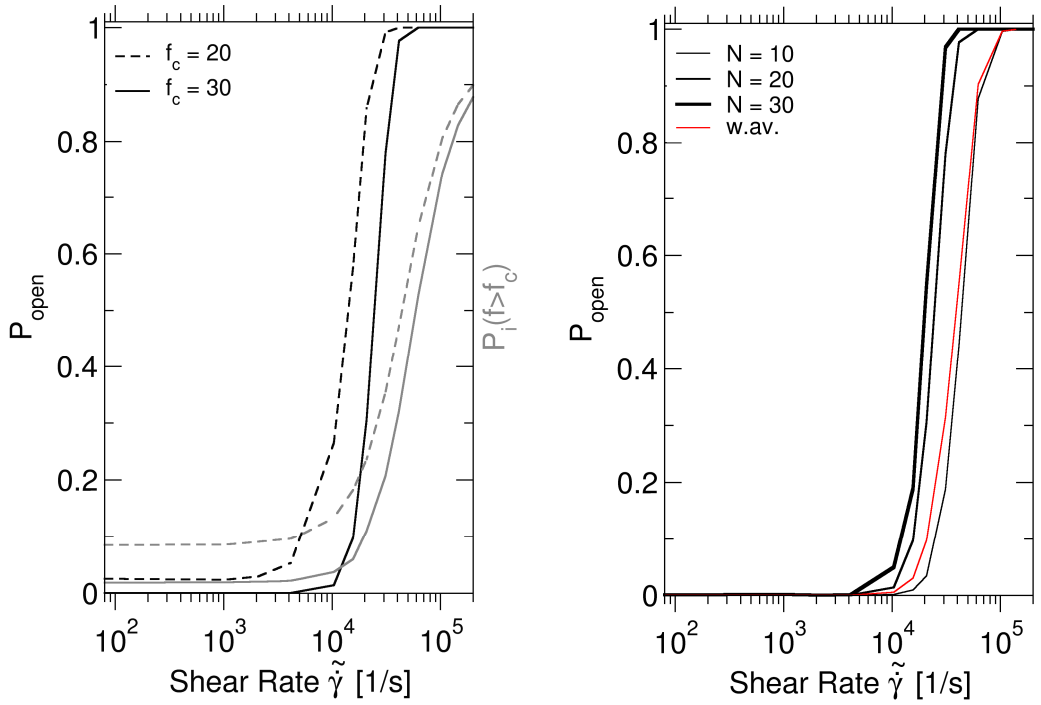

Figure S4: A Opening probability P_{open} of a 20mer (black lines) as a function of shear rate is compared to the probability of a single bead (i=10) to have an accessible cleave site, $P_i(f>f_c)$ (grey lines). P_{open} takes into account all beads and exhibits a steeper increase compared to the single bead opening probability. Dashed lines show the impact of a lower critical force f_c = 20 leading to an abrupt increase at slightly lower shear rates and to a higher opening probability at very low shear rates. **B** P_{open} as a function of shear rate for N=10,20,30 (black lines) and the weighted average (red line) according to the experimentally determined size distribution p^{N-1} with p=0.64.

REFERENCES

[1] Magde D, Elson E, Webb WW (1972) Thermodynamic fluctuations in a reacting system--measurement by fluorescence correlation spectroscopy. *Physical Review Letters* 29(11): 705-708.

[2] Elson EL, Magde D (1974) Fluorescence correlation spectroscopy. I. Conceptual basis and theory. *Biopolymers* 13(1): 1-27.

[3] Magde D, Elson EL, Webb WW (1974) Fluorescence correlation spectroscopy. II. An experimental realization. *Biopolymers* 13(1): 29-61.

[4] Petrov EP, Schwille P (2008) State of the art and novel trends in fluorescence correlation spectroscopy. *Standardization and Quality Assurance in Fluorescence Measurements II*: 145-197.

[5] Lippok S et al. (2013) Exponential Size Distribution of von Willebrand Factor. *Biophysical journal* 105(5): 1208-1216.

[6] Engelke H, Dorn I, Rädler JO (2009) Diffusion and molecular binding in crowded vesicle solutions measured by fluorescence correlation spectroscopy. *Soft Matter* 5(21): 4283-4289.

[7] Thompson N L (1991) *in Topics in Fluorescence Spectroscopy, Volume 1: Techniques.* Plenum Press: New York. pp. 337–378.

[8] Pruss CM, Notley CRP, Hegadorn CA, O'Brien LA, Lillicrap D (2008) ADAMTS13 cleavage efficiency is altered by mutagenic and, to a lesser extent, polymorphic sequence changes in the A1 and A2 domains of von Willebrand factor. *British journal of haematology* 143(4): 552-558.

[9] Rotne J, Prager S (2003) Variational treatment of hydrodynamic interaction in polymers. *The Journal of Chemical Physics* 50(11): 4831-4837.

C

Supplementary Information for "FVIII Binding to PS Membranes Differs in the Activated and Non-Activated Form and Can Be Shielded by Annexin A5"

FVIII Binding to PS Membranes Differs in the Activated and Non-Activated Form and Can Be Shielded by Annexin A5

Supplementary Information

Hanna Engelke[1], Svenja Lippok[1], Ingmar Dorn[2,], Roland R. Netz[3] and Joachim O. Rädler[1 #]

[1] Center for NanoScience (CeNS) and Fakultät für Physik,

Ludwig-Maximilians-Universität, Geschwister-Scholl-Platz 1, 80539 München, Germany

[2] Bayer Technology Services GmbH, E 41, 51368 Leverkusen,

Center for NanoScience (CeNS) and Fakultät für Physik,

[3]Technische Universität München, 85748 Garching, Germany

[#] To whom correspondence should be addressed.

E-mail: joachim.raedler@lmu.de

FCS analysis

The autocorrelation function of the measured intensity as a function of time is defined as:

$$G(\tau) = \frac{\langle I(t) I(t+\tau) \rangle}{\langle I(t) \rangle^2}$$

Equation 1

For a solution containing a single species, the autocorrelation function is fitted with the equation for a Brownian particle in solution:

$$G(\tau) = 1 + \frac{1}{N} \cdot g(\tau, \tau_D) = 1 + \frac{1}{N} \cdot \frac{1}{1 + \frac{\tau}{\tau_D}} \cdot \frac{1}{\sqrt{1 + \frac{\tau}{S^2 \tau_D}}}$$

Equation 2

In solutions with fluorescently-labeled proteins that bind to unlabeled vesicles, the fraction of bound proteins, f_{bound}, was determined from the autocorrelation function according to:

$$G(\tau) = 1 + \frac{1}{N}\left((1 - f_{bound}) \cdot g(\tau, \tau_{Dfree}) + f_{bound}\, g(\tau, \tau_{Dbound}) \right)$$

Equation 3

To enhance fit accuracy, the diffusion times τ_{Dfree} and τ_{Dbound} were determined in separate experiments and kept as fixed parameters. Note that Equation 3 is valid only if bound and unbound proteins display equal molecular intensity. This infers no quenching as well as the assumption that only one protein or less is bound to a vesicle on average. In our experiments, binding was not observed to affect intensity. Secondly the amplitude, i.e. the number of fluorescent proteins did not change significantly. Hence Equation 3 was used without restriction. For the general case of large number of proteins binding to vesicles the reader is referred to reference (S1). Using Equation 3 we determined the fraction of labeled FVIII and FVIIIa bound to PS vesicles for various lipid concentrations. These titrations yielded binding isotherms such as those shown in Figure 2(d). These were then used to determine the molar partition coefficient, i.e. the inverse of the equilibrium dissociation constant. The molar partition coefficient K is defined as:

$$K = \frac{P_{bound}}{L_{free} P_{free}} \qquad \text{Equation 4}$$

where L_{free} is the concentration of free lipids, P_{free} and P_{bound} are the concentrations of free and bound protein, respectively. It is related to the fraction of bound proteins f_{bound} and the total lipid concentration, L, for excess lipid concentrations by the following equation:

$$f_{bound} = \frac{KL}{1 + KL} \qquad \text{Equation 5}$$

Using these equations, the molar partition coefficient of inactivated and activated FVIII binding to PS-vesicles was determined for vesicles with various relative PS-content.

For experiments in blood plasma, scattering and crowding effects have to be considered. Scattering leads to a distortion of the focus, while crowding slows down diffusion. We accounted for possible scattering effects by performing additional calibration experiments in plasma. The slowdown in diffusion was taken into consideration by measuring the diffusion time of each component involved in the binding assay separately and in exactly the solution used for the binding measurements.

For cross-correlation experiments, the sample was additionally illuminated with a 633 nm HeNe-laser. Alexa-647-labeled annexin A5was used. The red emission was separated from the green using a longpass 650 filter; fluorescence intensities were acquired for both red and green channels, and autocorrelation curves of intensities with respect to time were likewise calculated for each. Additionally, the cross-correlation of the two channels was determined using the following function:

$$G(\tau) = \frac{\left\langle I_{green}(t) I_{red}(t+\tau) \right\rangle}{\left\langle I_{green}(t) \right\rangle \left\langle I_{red}(t) \right\rangle} \qquad \text{Equation 6}$$

This cross-correlation function allows for the detection of correlated movements of red- and green-labeled particles. Correlated movement of red and green particles leads to a signal in the cross-correlation function, whereas independent movement will always result in a value of 1 in the cross-correlation.

Antibody labeling

FVIII was indirectly labeled using Alexa-488 tagged ESH2 antibodies (American Diagnostica); antibodies were labeled using a labeling kit (Invitrogen) and were purified using spin-columns. Their purity was checked with FCS to be less than 10% free dye. ESH2 binds to the C2-domain of FVIII and FVIIIa, but does not inhibit binding to PS-containing membranes, allowing the easy, non-invasive labeling of FVIII. However, antibody binding might alter the protein conformation or change its binding behavior (e.g. through sterical hindrance). To exclude any effect of antibody binding, we performed experiments where ESH2 was replaced by ESH8, which binds to a different sequence on the C2-domain (in this case the von Willebrand-Factor binding-site). As described in the main text, the same results are obtained for the two antibody tags. A negative control labeled using ESH4, an antibody that blocks the PS binding site of FVIII, and which consequently inhibits binding to PS membranes, did not exhibit any binding. From these findings, we can conclude that the anomaly in the PS-dependence of FVIIIa membrane binding is not caused by the antibody-label. A further control on labeling as well as activation of FVIII was performed using antibodies binding to the B-domain of FVIII. They did not bind anymore upon activation showing, that activation (upon which the B-domain of FVIII is cleaved off) was successful.

Control experiments using optical thermophoresis

Thermophoresis is a technique that allows for binding experiments in solution independent of FCS measurements (S2). To confirm the FCS experiments and prove the existence of the unusual binding behavior of FVIIIa, we performed optical thermophoresis on our samples. These binding experiments are based on the change of the thermophoretic movement of a particle upon binding to a binding partner. Our experiments were carried out on the Monolith NT.015 (Nanotemper, Germany) thermophoresis instrument and for measurements samples were placed in borosilica glass capillaries (Nanotemper). Titration experiments and their analysis were performed as in the FCS experiments. The results are displayed in Fig. S4 and confirm the peak in the binding behavior of FVIIIa as measured by FCS.

Model of FVIII binding

We present a basic statistical model that derives the existence of a maximum from the assumption that FVIIIa displays discrete binding sites for PS lipid. It is well known that the electrostatic interaction of the PS moiety in the lipid membrane plays a key role in FVIII binding. Firstly, crystallography data show three residual positive charges on the membrane facing side of the protein. Secondly, when the protein binds to the membrane, its surface covers a distinct area of the membrane, which can be estimated to correspond to about 25 lipids. A fraction Φ of the lipids are charged PS lipids and it is assumed that the binding energy is composed out of the binding energy of these charged constituents. The situation is depicted schematically in Fig. S1. We now introduce the very assumption that discriminates the activated and inactivated form in our model. In the inactivated form we assume that the

electrostatic charge of the protein is equally distributed over the contact area and hence all M=25 lipid sites have the same chemical free energy for a PS lipid. Reason for this could be that charges are buried by the B-domain of the protein or that there is a water layer between protein and lipid bilayer. In contrast, in the case of activated FVIIIa we assume the existence of three discrete binding sites for PS, as depicted in Fig. S1. In both cases the binding constant, K, of the protein is determined from the statistical mean of the free energy, F, considering all possible configurations of charged lipids underneath the protein:

$$K = N \cdot \exp(-F/kT) = N \cdot Z(\tilde{\mu}) = N \cdot \sum_{m=1}^{M} P_M(m) e^{m\tilde{\mu}} \qquad \text{Equation 7}$$

where N is a constant normalization factor and $Z(\tilde{\mu})$ denotes the partition function with $P_M(m)$ being the probability that m lipids in the contact area are charged and $\exp(m\tilde{\mu})$ its statistical weight.
To derive the partition function $Z(\tilde{\mu})$ and the binding probability $P_M(m)$, we assume, a protein that binds to the membrane covers M proteins. According to crystallography data M is known to be M=25. The membrane is composed of a fraction of Φ charged lipids and a fraction of (1-Φ) uncharged lipids. Only charged lipids underneath the protein contribute to the binding. The probability P(m) that m out of the M lipids in the contact area of a protein are charged lipids is given by the Bernoulli-distribution:

$$P_M(m) = \Phi^m (1-\Phi)^{M-m} \frac{M!}{m!(M-m)!} \qquad \text{Equation 8}$$

Assuming that each of the m charged lipids contributes $\tilde{\mu}$kT to the binding energy, the weighted probability reads:

$$\tilde{P}_M(m,\mu) = P_M(m) e^{m\tilde{\mu}} = \Phi^m (1-\Phi)^{M-m} \frac{M!}{m!(M-m)!} e^{m\tilde{\mu}} \qquad \text{Equation9}$$

The probability Z that a protein, which hits a membrane binds to it, is then given by the sum over the weighted probabilities of all possible configurations (i.e. amounts of charged lipids in the contact area):

$$Z(\mu) = \sum_{m=1}^{M} P_M(m) e^{m\tilde{\mu}} = \sum_{m=1}^{M} \Phi^m (1-\Phi)^{M-m} \frac{M!}{m!(M-m)!} e^{m\tilde{\mu}} \qquad \text{Equation 10}$$

The probability Z of a binding event is directly proportional to the binding constant K and its logarithm yields the free energy F of the interaction as given by Equation 7.

This allows for description of the PS-dependence of the binding constant K(Φ) via Z(Φ) and a constant normalization factor N.

For inactivated FVIII we assume all charged lipids contribute an equal amount of $\tilde{\mu}$kT per lipid to the binding energy. Hence, we use Z(Φ) as given in equation 9 to fit the data with only $\tilde{\mu}$ and the normalization factor N as free fit parameters. As shown in Fig. S2, K(Φ) of inactivated FVIII can be described well by this model (with $\tilde{\mu}$= 0.4, N = 0.1).

For activated FVIIIa we distinguish between two sorts of lipid positions in the contact region. We assume that K out of the M lipid positions underneath the protein coincide with charge binding sites of the protein. According to crystallography data, FVIII has 3 exposed positively charged sites. These K=3 sites serve as charge binding sites and charged lipids at such sites are attracted and thus contribute a positive amount of $\tilde{\mu}_1$kT to the binding energy. Charged

lipids at the L=M-K sites, which do not correspond to charge binding sites of the protein, contribute a different amount $\tilde{\mu}_2$kT to the binding energy. This contribution is negative since the charged lipids are repulsed from the neutral sites and attracted by the charged binding sites of the protein. Reason for this could be the entropic confinement of the counterions. The contribution of the charged lipids at charge binding sites leads to an increase of binding with increasing fraction of charged lipids at low PS-concentrations up to a certain value, beyond which the repulsion at neutral sites dominates resulting in a decrease of binding with increasing PS-content of the membrane. The discrimination of these two different energy contributions leads to one additional parameter, $\tilde{\mu}_2$, and the probability function $P_M(m)$ splits into the probabilities $P_K(k)$ to find k charged lipids at the K charge binding sites and $P_L(l)$ to find l charged lipids at the L=M-K neutral sites. The binding probability is determined by the probability, that k charged lipids occupy one of the K charge binding sites and that at the same time l charged lipids are positioned at one of the L neutral sites. Consequently, the binding probability Z reads:

$$Z(\mu_1,\mu_2)=\sum_{k=1}^{K}\sum_{l=1}^{L}P_K(k)e^{k\tilde{\mu}_1}\cdot P_L(l)e^{l\tilde{\mu}_2}=\sum_{k=1}^{K}\sum_{l=1}^{L}\Phi^k(1-\Phi)^{K-k}\frac{K!}{k!(K-k)!}e^{k\tilde{\mu}_1}\cdot\Phi^l(1-\Phi)^{L-l}\frac{L!}{l!(L-l)!}e^{l\tilde{\mu}_2}$$

Equation 11

Fig. S2 shows that this discrete binding model reproduces the peak in the PS-dependence of activated FVIIIa with only one additional parameter as compared to the model for inactivated FVIII (with $\tilde{\mu}_1$ = 7.6, $\tilde{\mu}_2$ = -19.8, N = 7.8E-7). However, it reveals only the peak and it fails to describe the increase of the binding constant at high PS-contents. This increase signals cooperative effects, which we implement in the model by addition of a quadratic term $l^2\varepsilon$ in the binding energy per charged lipid at non-charge binding sites. The dashed line in Fig. S2, which was obtained by the model including this extension, reveals the increase of binding at high PS-contents. The experimental data for FVIIIa are more sharply peaked around the maximum than the theoretical model. The agreement could be improved by including higher order terms also for the PS lipids underneath charge sites, which we did not pursue in this paper.

Terms accounting for cooperative effects involving charged lipids at neutral protein sites can be introduced by addition of nonlinear terms in the binding energy per lipid. In principle arbitrary functions $u_1(k)$ and $u_2(l)$ can be used for the binding energies per lipid, but in practice $u_1(k)=\tilde{\mu}_1k+\varepsilon_1k^2$ and $u_2(l)=\tilde{\mu}_2l+\varepsilon_2l^2$ is sufficient. In the case of unspecific binding of the charged lipids at neutral sites, for instance, the binding probability Z is expanded by an energy term quadratic in l:

$$\Omega(\mu_1,\mu_2,\varepsilon)=\sum_{k=1}^{K}\sum_{l=1}^{L}P(k)e^{k\tilde{\mu}_1}\cdot P(l)e^{l\tilde{\mu}_2+l^2\varepsilon}$$

Equation 12

With a positive energy contribution ε, this kind of cooperativity leads to an increase of binding at high fractions Φ of charged lipids as measured for activated FVIIIa.

So far, all cases were calculated explicitly. Although, the system is quite small, we can apply the thermodynamic limit. In this case, we use the Stirling approximation to calculate the free energy F, which is the logarithm of $\tilde{P}(M, m, \mu)$. Determination of the fraction of charged lipids x=m/M per contact area with minimal free energy leads to:

$$x=\frac{\Phi\cdot e^{\mu/kT}}{\Phi\cdot e^{\mu/kT}+(1-\Phi)}$$

Equation 13

Calculation of the exponent of the free energy at this value yields the binding constant in the thermodynamic limit:

$$K = N \cdot \exp(-F(x))$$ Equation 14

Fig. S3 compares the result in the thermodynamic limit with the exact result. Although the numbers M, K, and L, which characterize the system size, are quite small, the thermodynamic limit reveals the binding behavior well.

Quantitative modeling of annexin regulation

Competitive inhibition model:

In the competitive inhibition model, two species, annexin A5 and FVIIIa compete for binding sites on a third species, the membrane. A key parameter for this kind of inhibition is the absolute number of binding sites that each species can occupy. Assuming that annexin A5 exhibits a stronger affinity for membranes than FVIIIa, annexin A5 molecules bound to the membrane reduce the number of free binding sites for FVIIIa, whereas annexin A5 binding is not affected by bound FVIIIa. The effective number of binding sites, L_{eff}, for FVIIIa is then defined by the number of binding sites on the membrane in the absence of annexin A5, L_0, from which the amount of annexin A5-bound lipids, L_a, is subtracted:

$$L_{eff} = L_0 - L_a$$ Equation 15

In the case of excess lipid (i.e. the total lipid concentration is much larger than the number of FVIIIa-bound lipids), the number of bound FVIIIa, f_{bound}, can be calculated as a function of the annexin A5 concentration:

$$f_{bound} = \frac{K(L_0 - L_a)}{1 + K(L_0 - L_a)}$$ Equation 16

with K being the binding constant of FVIIIa in the absence of annexin A5. The assumption that annexin A5 binding to membranes is not influenced by FVIIIa binding allows the direct determination of L_a from the binding isotherm of annexin A5. Considering the high concentrations of annexin A5 used, the limit of excess lipid does not hold true for annexin A5, and L_a has to be calculated explicitly:

$$L_a = \frac{K_A^{-1} + c_A + L_0 - \sqrt{\left(K_A^{-1} + c_A + L_0\right)^2 - 4L_0 c_A}}{2}$$ Equation 17

where c_A is the annexin A5 concentration and K_A, the binding constant of annexin A5.

This yields the equation for the fraction of bound FVIIIa used in generating the curves in Figure 4 (a) and (b) in the main text.

Shielding model:

The shielding model assumes that annexin A5 binding to the membrane shields the charges of the membrane, reducing the relative number of PS detected by FVIIIa, and thus changing the PS content-dependent binding energy of FVIIIa. The fraction of bound FVIIIa, f_{bound}, can then be described by the binding isotherm using a binding constant, $K(PS_{eff}(A))$, as a function of PS content, which, in turn depends on the annexin A5 concentration:

$$f_{bound} = \frac{K\left(PS_{eff}(A)\right) \cdot L_{eff}}{1 + K\left(PS_{eff}(A)\right) \cdot L_{eff}} \qquad \text{Equation 18}$$

To quantify this, the PS-dependence of the molar partition coefficient of FVIIIa binding to membranes, K, is described by a phenomenological fit function applied to the experimental data, K(PS). Next, the shielding of PS by annexin A5 is modeled. The shielding is assumed to be linear with the concentration of bound annexin A5, $Annexin_{bound}$:

$$PS_{eff}(Annexin) = \left(1 - \alpha \cdot Annexin_{bound}\right) \cdot PS_0 \qquad \text{Equation 19}$$

Here, PS_{eff} is the effective PS content; PS_0, the PS-content of the membrane; and α, the molar shielding efficiency. The concentration of bound annexin A5 depends on the total lipid concentration. Since the approximation for excess lipid ($L_{tot} >> L_{bound}$) does not hold for the annexin A5 concentrations used, the concentration of bound annexin A5 has to be explicitly calculated from the binding isotherm:

$$Annexin_{bound} = \frac{K_{Annexin}^{-1} + c_{Annexin} + L - \sqrt{\left(K_{Annexin}^{-1} + c_{Annexin} + L\right)^2 - 4Lc_{Annexin}}}{2} \qquad \text{Equation 20}$$

with $c_{Annexin}$ being the concentration of annexin A5 and $K_{Annexin}$ the molar partition coefficient of annexin A5. $K_{Annexin}$ was determined to be $0.5\mu M^{-1}$ under the experimental conditions used in a separate experiment. Incorporating the phenomenological fit function for the PS-content dependence of FVIIIa binding (where the effective PS-content is annexin A5 dependent) into the equation of the binding isotherm yields the fraction of bound FVIIIa; this fraction is defined as a function of the annexin A5 concentration, according to the shielding model. The function contains one fit parameter, namely the shielding parameter, and was successfully used in describing the data of the interaction between annexin A5 and FVIIIa, as shown in figure 4 (a) and (b). The function was also used to calculate the full 3-D phase diagram shown in figure 4 (c).

References:

S1: Rusu, L., Gambhir, A., McLaughlin, S., Rädler, J., (2004), *Biophys. J.*, **87**, 1044-1053.
S2: Baaske, P., Wienken, C., Reineck, P., Duhr, S. and Braun, D., (2010), *Angewandte Chemie*, **49**, 2238-2241.

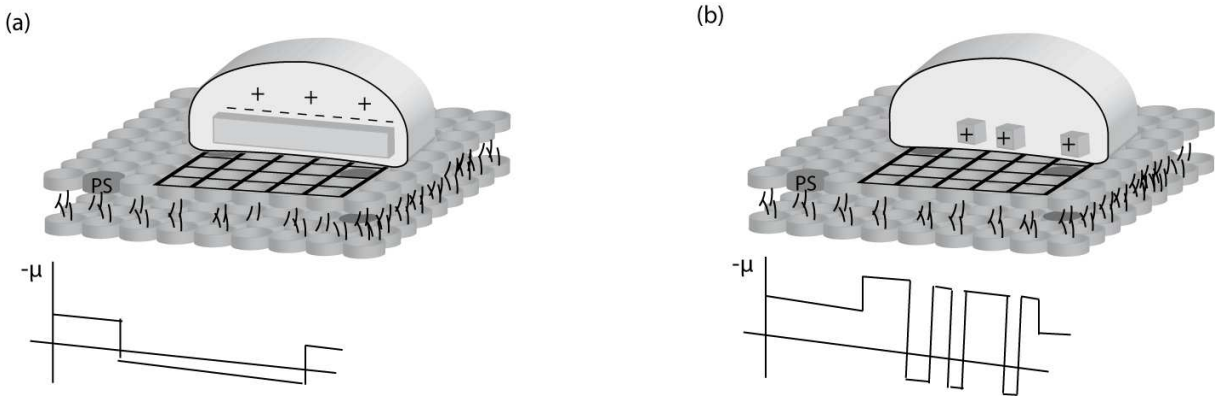

Fig S1

Fig. S1: Schematic drawing of FVIII binding to membranes. (a) Inactivated FVIII is assumed to exhibit an electrostatic charge equally distributed over the contact area of the membrane. The diagram of the potential μ below shows, that the contribution of a PS lipid to the total binding energy is equal on all positions under the protein. (b) Activated FVIIIa exposes three distinct charge binding sites, which attract negatively charged lipids, to the membrane. Hence, the diagram of the potential μ shows an attractive contribution on specific sites under the protein and it is repulsive on all other sites under the protein.

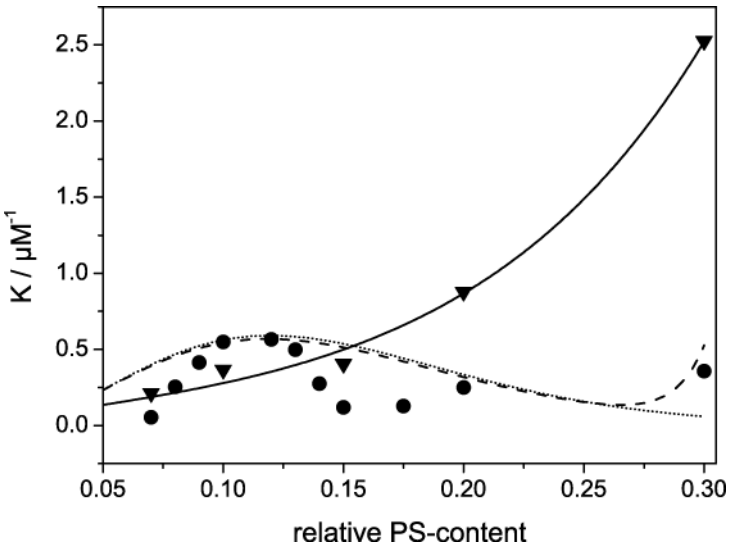

Fig. S2

Fig. S2: Theoretical model and experimental data of the PS-dependence of inactivated and activated FVIII binding. The FVIII binding to membranes (triangles) is well described assuming equal electrostatic interaction of the protein with charged lipids at any position of the contact area (full line, $\tilde{\mu}$= 0.4, N = 0.1). The anomalous peak in the PS-dependence of FVIIIa binding to membranes (full circles) is reproduced by a discrete binding model (dotted line, $\tilde{\mu}_1$ = 7.6, $\tilde{\mu}_2$ = -19.8, N = 7.8E-7) assuming three discrete binding sites within the area of about 25 lipids underneath the protein. Here only one additional parameter that discriminates the discretely bound charged lipids from those at unspecific contact sites is introduced. Addition of a non-linear binding term allows for description of the increase in binding at high PS-contents (dashed line, $\tilde{\mu}_1$ = 6.4563, $\tilde{\mu}_2$ = -10.0321, ε = 0.4989, N = 2.0495E-5).

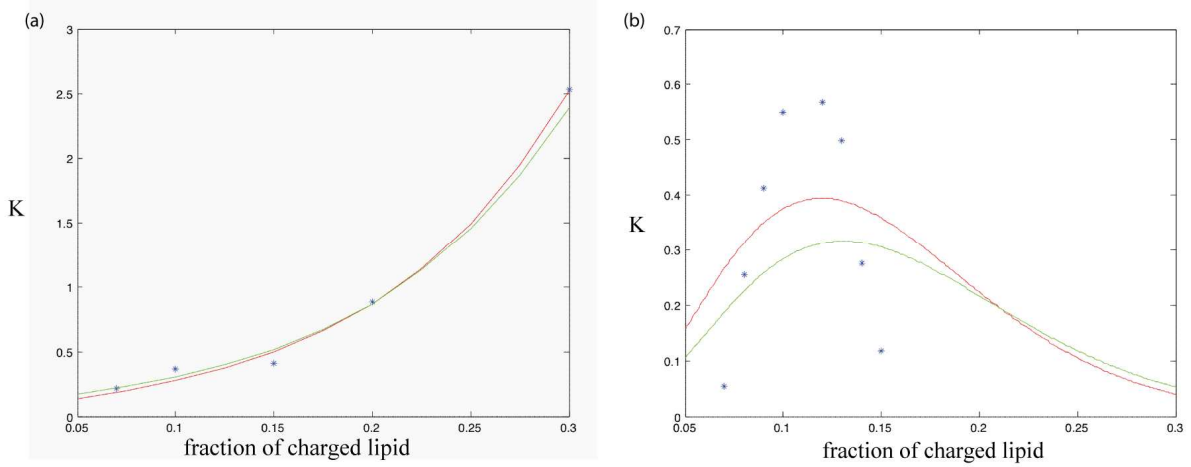

Fig. S3

Fig. S3: Comparison of the exact binding model with the thermodynamic limit. (a) Inactivated FVIII binding fitted according to the exact model (red line, Equation 9) and in the thermodynamic limit (green line, Equation 14). In this case, the two models do not deviate significantly. (b) Activated FVIIIa binding fitted according to the exact model (red line, Equation 11) and in the thermodynamic limit (green line). Both models reproduce the peak in the PS-dependence of the binding constant.

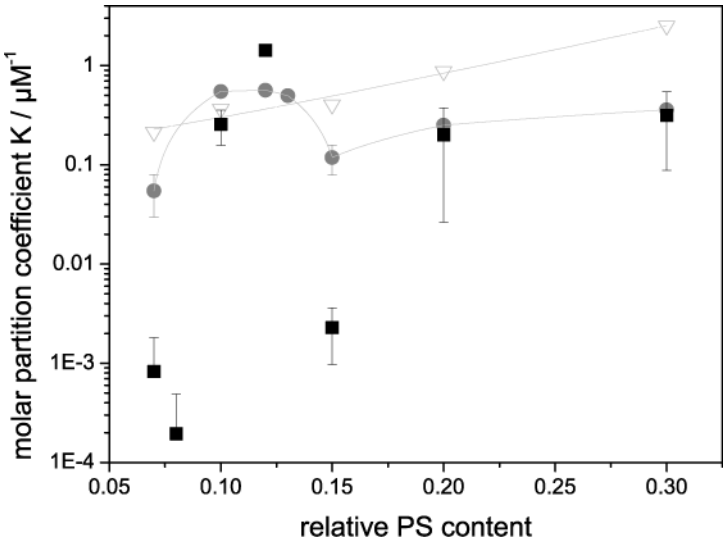

Fig. S4

Fig. S4: Results of the thermophoresis experiments on the binding of FVIIIa to PS-vesicles. The data from experiments using thermophoresis (black squares) reveal the same peak in the binding behavior of FVIIIa as the experiments using FCS (grey circles). For comparison, the binding coefficients of inactivated FVIII measured with FCS are shown as well (grey triangles).

Bibliography

[1] Johann Wolfgang von Goethe. *Faust. Eine Tragödie von Goethe.* J. G. Cotta, 1808.

[2] Geert J. Tangelder, Dick W. Slaaf, Theo Arts, and Robert S. Reneman. Wall shear rate in arterioles in vivo: least estimates from platelet velocity profiles. *American Journal of Physiology*, 254:H1059–H1064, 1988.

[3] George A. Truskey, Fan Yuan, and David F. Katz. *Transport phenomena in biological systems*. Pearson/Prentice Hall Upper Saddle River NJ, 2004.

[4] Lloyd D. Back, John R. Radbill, and Donald W. Crawford. Analysis of pulsatile, viscous blood flow through diseased coronary arteries of man. *Journal of biomechanics*, 10(5):339–353, 1977.

[5] Stefan W. Schneider, Stefan Nuschele, Achim Wixforth, Christian Gorzelanny, Alfredo Alexander-Katz, Roland R. Netz, and Matthias F. Schneider. Shear-induced unfolding triggers adhesion of von Willebrand factor fibers. *Proceedings of the National Academy of Sciences*, 104(19):7899–7903, 2007.

[6] Han-Mou Tsai. Shear stress and von Willebrand factor in health and disease. *Seminars in thrombosis and hemostasis*, 29(5):479–488, 2003.

[7] Volker Huck, Matthias F. Schneider, Christian Gorzelanny, and Stefan W. Schneider. The various states of von Willebrand factor and their function in physiology and pathophysiology. *Thrombosis and Haemostasis*, 111(4):598–609, 2014.

[8] Xinglong Zheng, Dominic Chung, Thomas K. Takayama, Elaine M. Majerus, J. Evan Sadler, and Kazuo Fujikawa. Structure of von Willebrand factor-cleaving protease (ADAMTS13), a metalloprotease involved in thrombotic thrombocytopenic purpura. *Journal of Biological Chemistry*, 276(44):41059–41063, 2001.

[9] Gallia G. Levy, William C. Nichols, Eric C. Lian, Tatiana Foroud, Jeanette N. McClintick, Beth M. McGee, Angela Y. Yang, David R. Siemieniak, Kenneth R. Stark, and Ralph Gruppo. Mutations in a member of the ADAMTS gene family cause thrombotic thrombocytopenic purpura. *Nature*, 413(6855):488–494, 2001.

[10] Kenji Soejima, Noriko Mimura, Masaki Hiroshima, Hiroaki Maeda, Takayoshi Hamamoto, Tomohiro Nakagaki, and Chikateru Nozaki. A Novel Human Metalloprotease Synthesized in the Liver and Secreted into the Blood: Possibly, the von Willebrand Factor-Cleaving Protease? *Journal of Biochemistry*, 130(4):475–480, 2001.

[11] Carsten Baldauf, Reinhard Schneppenheim, Wolfram Stacklies, Tobias Obser, Antje Pieconka, Sonja Schneppenheim, Ulrich Budde, Jing Zhou, and Frauke Gräter. Shear-induced unfolding activates von Willebrand factor A2 domain for proteolysis. *Journal of Thrombosis and Haemostasis*, 7(12):2096–2105, 2009.

[12] Weiqiang Gao, Patricia J. Anderson, Elaine M. Majerus, Elodee A. Tuley, and J. Evan Sadler. Exosite interactions contribute to tension-induced cleavage of von Willebrand factor by the antithrombotic ADAMTS13 metalloprotease. *Proceedings of the National Academy of Sciences*, 103(50):19099–19104, 2006.

[13] J. Evan Sadler. Biochemistry and genetics of von Willebrand factor. *Annual review of biochemistry*, 67(1):395–424, 1998.

[14] Reinhard Schneppenheim and Ulrich Budde. *Von Willebrand-Syndrom und von Willebrand-Faktor: aktuelle Aspekte der Diagnostik und Therapie*. UNI-MED Verlag, 2010.

[15] Erik A. von Willebrand. Hereditär pseudohemofili. *Finska Läkaresällskaptes Handlingar*, 672:7112, 1926.

[16] Erik A. von Willebrand and Rudolf Jürgens. Über ein neues vererbbares Blutungsübel: die konstitutionelle Thrombopathie. *Deutsches Archiv für klinische Medicin*, 175:453–483, 1933.

[17] http://www.vonwillebrand.se/en/von Willebrand-disease/History.

[18] Benjamin Alexander and Robert Goldstein. Dual hemostatic defect in pseudohemophilia. *Journal of Clinical Investigation*, 32:551–557, 1953.

[19] Armand J. Quick and Clara V. Hussey. Hemophilic condition in the female. *Journal of Laboratory and Clinical Medicine*, 42:929–930, 1953.

[20] Inga Nilsson, Margareta Blombäck, and Irene Francken. On an Inherited Autosomal Hemorrhagic Diathesis with Antihemophilic Globulin (AHG) Deficiency and Prolonged Bleeding Times1. *Acta Medica Scandinavica*, 159(1):35–58, 1957.

[21] Theodore S. Zimmerman, Oscar D. Ratnoff, and Arnold E. Powell. Immunologic differentiation of classic hemophilia (factor VIII deficiency) and von Willebrand's disease: with observations on combined deficiencies of antihemophilic factor and proaccelerin (factor V) and on an acquired circulating anticoagulant against antihemophilic factor. *Journal of Clinical Investigation*, 50(1):244, 1971.

[22] David J. Mancuso, Elodee A. Tuley, Lisa A. Westfield, Neil K. Worrall, Beverley B. Shelton-Inloes, James M. Sorace, Yael G. Alevy, and J. Evan Sadler. Structure of the gene for human von Willebrand factor. *Journal of Biological Chemistry*, 264(33):19514–19527, 1989.

[23] Christopher A. Siediecki, Brian J. Lestini, Kandice K. Kottke-Marchant, Steven J. Ep-

pell, David L. Wilson, and Roger E. Marchant. Shear-dependent changes in the three-dimensional structure of human von Willebrand factor. *Blood*, 88(8):2939–2950, 1996.

[24] Xiaohui Zhang, Kenneth Halvorsen, Cheng-Zhong Zhang, Wesley P. Wong, and Timothy A. Springer. Mechanoenzymatic cleavage of the ultralarge vascular protein von Willebrand factor. *Science*, 324(5932):1330–1334, 2009.

[25] Daniel Axelrod. Cell-substrate contacts illuminated by total internal reflection fluorescence. *The Journal of Cell Biology*, 89(1):141–145, 1981.

[26] Edward B. Brown, Robert B. Campbell, Yoshikazu Tsuzuki, Lei Xu, Peter Carmeliet, Dai Fukumura, and Rakesh K. Jain. In vivo measurement of gene expression, angiogenesis and physiological function in tumors using multiphoton laser scanning microscopy. *Nature medicine*, 7(7):864–868, 2001.

[27] Hanna Engelke, Ingmar Dorn, and Joachim O. Rädler. Diffusion and molecular binding in crowded vesicle solutions measured by fluorescence correlation spectroscopy. *Soft Matter*, 5(21):4283–4289, 2009.

[28] Christoph J. Wienken, Philipp Baaske, Ulrich Rothbauer, Dieter Braun, and Stefan Duhr. Protein-binding assays in biological liquids using microscale thermophoresis. *Nature communications*, 1(100):1–7, 2010.

[29] Hoi-Yan Shiu, Hiu-Chi Chong, Yun-Chung Leung, Man-Kin Wong, and Chi-Ming Che. A Highly Selective FRET-Based Fluorescent Probe for Detection of Cysteine and Homocysteine. *Chemistry-A European Journal*, 16(11):3308–3313, 2010.

[30] Eric A. J. Reits and Jacques J. Neefjes. From fixed to FRAP: measuring protein mobility and activity in living cells. *Nature cell biology*, 3(6):E145–E147, 2001.

[31] Timothy A. Springer. Biology and physics of von Willebrand factor concatamers. *Journal of Thrombosis and Haemostasis*, 9:130–143, 2011.

[32] Armando del Rio, Raul Perez-Jimenez, Ruchuan Liu, Pere Roca-Cusachs, Julio M. Fernandez, and Michael P. Sheetz. Stretching single talin rod molecules activates vinculin binding. *Science*, 323(5914):638–641, 2009.

[33] Elias M. Puchner and Hermann E. Gaub. Force and function: probing proteins with AFM-based force spectroscopy. *Current opinion in structural biology*, 19(5):605–614, 2009.

[34] Charles E. Sing and Alfredo Alexander-Katz. Dynamics of collapsed polymers under the simultaneous influence of elongational and shear flows. *The Journal of chemical physics*, 135(1):014902, 2011.

[35] Alfredo Alexander-Katz, Matthias F. Schneider, Stefan W. Schneider, Achim Wixforth, and Roland R. Netz. Shear-flow-induced unfolding of polymeric globules. *Physical review letters*, 97(13):138101–138104, 2006.

[36] Lora Mere, Todd Bennett, Peter Coassin, Paul England, Brian Hamman, Timothy Rink, Susan Zimmerman, and Paul Negulescu. Miniaturized FRET assays and microfluidics: key components for ultra-high-throughput screening. *Drug Discovery Today*, 4(8):363–369, 1999.

[37] Zeno Guttenberg, Andreas Rathgeber, Simon Keller, Joachim O. Rädler, Achim Wixforth, Marcin Kostur, Michael Schindler, and Peter Talkner. Flow profiling of a surface-acoustic-wave nanopump. *Physical Review E*, 70(5):056311, 2004.

[38] Christof B. Mast and Dieter Braun. Thermal trap for DNA replication. *Physical Review Letters*, 104(18):188102, 2010.

[39] Douglas Magde, Elliot Elson, and Watt W. Webb. Thermodynamic fluctuations in a reacting system–measurement by fluorescence correlation spectroscopy. *Physical Review Letters*, 29(11):705–708, 1972.

[40] Douglas Magde, Elliot L. Elson, and Watt W. Webb. Fluorescence correlation spectroscopy.II. an experimental realization. *Biopolymers*, 13(1):29–61, 1974.

[41] Rudolf Rigler, Ülo Mets, Jerker Widengren, and Peet Kask. Fluorescence correlation spectroscopy with high count rate and low background: analysis of translational diffusion. *European Biophysics Journal*, 22(3):169–175, 1993.

[42] Svetlana A. Sukhishvili, Yan Chen, Joachim D. Müller, Enrico Gratton, Kenneth S. Schweizer, and Steve Granick. Materials science: Diffusion of a polymer 'pancake'. *Nature*, 406(6792):146–146, 2000.

[43] Bethe A. Scalettar, John E. Hearst, and Melvin P. Klein. FRAP and FCS studies of self-diffusion and mutual diffusion in entangled DNA solutions. *Macromolecules*, 22(12):4550–4559, 1989.

[44] Dirk Lumma, Simon Keller, Thomas Vilgis, and Joachim O. Rädler. Dynamics of large semiflexible chains probed by fluorescence correlation spectroscopy. *Physical review letters*, 90(21):218301, 2003.

[45] Eugene P. Petrov and Petra Schwille. State of the art and novel trends in fluorescence correlation spectroscopy. *Standardization and Quality Assurance in Fluorescence Measurements II*, pages 145–197, 2008.

[46] Petra S. Dittrich and Petra Schwille. Spatial two-photon fluorescence cross-correlation spectroscopy for controlling molecular transport in microfluidic structures. *Analytical Chemistry*, 74(17):4472–4479, 2002.

[47] Elke Haustein and Petra Schwille. Single-molecule spectroscopic methods. *Current opinion in structural biology*, 14(5):531–540, 2004.

[48] Jerker Widengren and Petra Schwille. Characterization of photoinduced isomerization and back-isomerization of the cyanine dye Cy5 by fluorescence correlation spectroscopy. *The Journal of Physical Chemistry A*, 104(27):6416–6428, 2000.

[49] Nancy L. Thompson. *Topics in Fluorescence Spectroscopy, Volume 1: Techniques*. Plenum Press, New York, 1991.

[50] Prince E. Rouse Jr. A theory of the linear viscoelastic properties of dilute solutions of coiling polymers. *The Journal of Chemical Physics*, 21(7):1272–1280, 1953.

[51] Bruno H. Zimm. Dynamics of polymer molecules in dilute solution: viscoelasticity, flow birefringence and dielectric loss. *The Journal of Chemical Physics*, 24(2):269–278, 1956.

[52] Reinhard Schneppenheim, Hansjoerg Plendl, and Ulrich Budde. Luminography–an alternative assay for detection of von Willebrand factor multimers. *Thrombosis and haemostasis*, 60(2):133–136, 1988.

[53] Ulrich Budde et. al. Detailed von Willebrand factor multimer analysis in patients with von Willebrand disease in the European study, molecular and clinical markers for the diagnosis and management of type 1 von Willebrand disease (MCMDM-1VWD). *Journal of Thrombosis and Haemostasis*, 6(5):762–771, 2008.

[54] Cynthia M. Pruss, Colleen R. P. Notley, Carol A. Hegadorn, Lee A. O'Brien, and David Lillicrap. ADAMTS13 cleavage efficiency is altered by mutagenic and, to a lesser extent, polymorphic sequence changes in the A1 and A2 domains of von Willebrand factor. *British journal of haematology*, 143(4):552–558, 2008.

[55] Svenja Lippok, Tobias Obser, Jochen P. Müller, Valentin K. Stierle, Martin Benoit, Ulrich Budde, Reinhard Schneppenheim, and Joachim O. Rädler. Exponential Size Distribution of von Willebrand Factor. *Biophysical journal*, 105(5):1208–1216, 2013.

[56] Stefan K. Kufer, Mathias Strackharn, Stefan W. Stahl, Hermann Gumpp, Elias M. Puchner, and Hermann E. Gaub. Optically monitoring the mechanical assembly of single molecules. *Nature nanotechnology*, 4(1):45–49, 2008.

[57] Maximilian H. Ulbrich and Ehud Y. Isacoff. Subunit counting in membrane-bound proteins. *Nature methods*, 4(4):319–321, 2007.

[58] Howard A. Barnes, John Fletcher Hutton, and Kenneth Walters. *An introduction to rheology*, volume 3. Elsevier, 1989.

[59] Horace H. Billon. Shear rate determination in a concentric cylinder viscometer. Technical report, DTIC Document, 1996.

[60] Shewaferaw S. Shibeshi and William E. Collins. The rheology of blood flow in a branched arterial system. *Applied rheology (Lappersdorf, Germany: Online)*, 15(6):398, 2005.

[61] Johannes V. Soulis, Olga P. Lampri, Dimitrios K. Fytanidis, and George D. Giannoglou. Relative residence time and oscillatory shear index of non-newtonian flow models in aorta. In *Biomedical Engineering, 10th International Workshop on*, pages 1–4. IEEE, 2011.

[62] Svenja Lippok, Susanne A. I. Seidel, Stefan Duhr, Kerstin Uhland, Hans-Peter Holthoff, Dieter Jenne, and Dieter Braun. Direct detection of antibody concentration and affinity in human serum using microscale thermophoresis. *Analytical chemistry*, 84(8):3523–3530, 2012.

[63] Susanne A. I. Seidel, Patricia M. Dijkman, Wendy A. Lea, Geert van den Bogaart, Moran Jerabek-Willemsen, Ana Lazic, Jeremiah S. Joseph, Prakash Srinivasan, Philipp Baaske, and Anton Simeonov. Microscale thermophoresis quantifies biomolecular interactions under previously challenging conditions. *Methods*, 59(3):301–315, 2013.

[64] Carl Ludwig. *Diffusion zwischen ungleich erwärmten Orten gleich zusammengesetzter Lösung*. Aus der KK Hof-und Staatsdruckerei, in Commission bei W. Braumäller,

Buchhändler des KK Hofes und der K. Akademie der Wissenschaften, 1856.

[65] Stefan Duhr and Dieter Braun. Why molecules move along a temperature gradient. *Proceedings of the National Academy of Sciences*, 103(52):19678–19682, 2006.

[66] Björn Dahlbäck. Blood coagulation. *The Lancet*, 355(9215):1627–1632, 2000.

[67] Christian Hick and Astrid Hick. *Intensivkurs Physiologie*. Elsevier, Urban und Fischer, 2006.

[68] Robert J. Wise, Debra D. Pittman, Robert I. Handin, Randal J. Kaufman, and Stuart H. Orkin. The propeptide of von Willebrand factor independently mediates the assembly of von Willebrand multimers. *Cell*, 52(2):229–236, 1988.

[69] Indrajeet Singh, Harish Shankaran, Mark E. Beauharnois, Zhihua Xiao, Paschalis Alexandridis, and Sriram Neelamegham. Solution structure of human von Willebrand factor studied using small angle neutron scattering. *Journal of Biological Chemistry*, 281(50):38266, 2006.

[70] Philip J. Fay, Yohko Kawai, Denisa D. Wagner, David Ginsburg, David Bonthron, Betsy M. Ohlsson-Wilhelm, Stephen I. Chavin, George N. Abraham, Robert I. Handin, and Stuart H. Orkin. Propolypeptide of von Willebrand factor circulates in blood and is identical to von Willebrand antigen II. *Science*, 232(4753):995–998, 1986.

[71] David R. McCarroll, Eugene G. Levin, and Robert R. Montgomery. Endothelial cell synthesis of von Willebrand antigen II, von Willebrand factor, and von Willebrand factor/von Willebrand antigen II complex. *Journal of Clinical Investigation*, 75(4):1089, 1985.

[72] Thalia Romani de Wit and Jan A. van Mourik. Biosynthesis, processing and secretion of von Willebrand factor: biological implications. *Best Practice & Research Clinical Haematology*, 14(2):241–255, 2001.

[73] Hsieh Chen, Mohammad A. Fallah, Volker Huck, Jennifer I. Angerer, Armin J. Reininger, Stefan W. Schneider, Matthias F. Schneider, and Alfredo Alexander-Katz. Blood-clotting-inspired reversible polymer-colloid composite assembly in flow. *Nature communications*, 4:1333, 2013.

[74] Arnoldo Padilla, Joel L. Moake, Aubrey Bernardo, Chalmette Ball, Yongtao Wang, Maneesh Arya, Leticia Nolasco, Nancy Turner, Michael C. Berndt, and Bahman Anvari. P-selectin anchors newly released ultralarge von Willebrand factor multimers to the endothelial cell surface. *Blood*, 103(6):2150–2156, 2004.

[75] Jing Huang, Robyn Roth, John E. Heuser, and J. Evan Sadler. Integrin avb3 on human endothelial cells binds von Willebrand factor strings under fluid shear stress. *Blood*, 113(7):1589–1597, 2009.

[76] Reinhard Schneppenheim and Ulrich Budde. von Willebrand factor: the complex molecular genetics of a multidomain and multifunctional protein. *Journal of Thrombosis and Haemostasis*, 9(s1):209–215, 2011.

[77] Zaverio M. Ruggeri, Jennifer N. Orje, Rolf Habermann, Augusto B. Federici, and Armin J. Reininger. Activation-independent platelet adhesion and aggregation under

elevated shear stress. *Blood*, 108(6):1903–1910, 2006.

[78] Jongseong Kim, Cheng-Zhong Zhang, Xiaohui Zhang, and Timothy A. Springer. A mechanically stabilized receptor-ligand flex-bond important in the vasculature. *Nature*, 466(7309):992–995, 2010.

[79] Joel L. Moake. von Willebrand factor, ADAMTS-13, and thrombotic thrombocytopenic purpura. *Seminars in Hematology*, 41(1):4–14, 2004.

[80] J. Evan Sadler. Von Willebrand factor, ADAMTS13, and thrombotic thrombocytopenic purpura. *Blood*, 112(1):11–18, 2008.

[81] J.-D. Studt, M. Böhm, U. Budde, J.-P. Girma, K. Varadi, and B. Lämmle. Measurement of von Willebrand factor-cleaving protease (ADAMTS-13) activity in plasma: a multi-center comparison of different assay methods. *Journal of Thrombosis and Haemostasis*, 1(9):1882–1887, 2003.

[82] Maria A. Brehm, Volker Huck, Camilo Aponte-Santamaria, Tobias Obser, Sandra Grässle, Florian Oyen, Ulrich Budde, Sonja Schneppenheim, Carsten Baldauf, Frauke Gräter, Stefan W. Schneider, and Reinhard Schneppenheim. von Willebrand disease type 2A phenotypes IIC, IID and IIE: A day in the life of shear-stressed mutant von Willebrand factor. *Thrombosis and haemostasis*, 112:E–pub ahead of print. 10.1160/TH13–11–0902, 2014.

[83] Hanna Engelke, Svenja Lippok, Ingmar Dorn, Roland R. Netz, and Joachim O. Rädler. FVIII binding to PS membranes differs in the activated and non-activated form and can be shielded by annexin A5. *The Journal of Physical Chemistry B*, 115(44):12963–12970, 2011.

[84] Yan-Feng Zhou, Edward T. Eng, Noritaka Nishida, Chafen Lu, Thomas Walz, and Timothy A. Springer. A pH-regulated dimeric bouquet in the structure of von Willebrand factor. *The EMBO journal*, 30(19):4098–4111, 2011.

[85] Barbara K. Müller, Evgeny Zaychikov, Christoph Bräuchle, and Don C. Lamb. Pulsed interleaved excitation. *Biophysical journal*, 89(5):3508–3522, 2005.

Full List of Publications

S. Lippok, C. Aponte-Santamaría, T. Obser, R. Schneppenheim, C. Baldauf, F. Gräter, U. Budde, J.O. Rädler. "Destabilized recombinant VWF as substrate for highly sensitive ADAMTS13 activity assays." *to be submitted to Journal of Thrombosis and Haemostasis*

S. Lippok, G. König, T. Obser, R. Schneppenheim, J.O. Rädler, M.A. Brehm. "The (patho)-physiological Relevance of Protein Disulfide Isomerase Binding to von Willebrand Factor." *to be submitted to Journal of biological chemistry*

S. Lippok, M. Radtke, T. Obser, L. Kleemeier, R. Schneppenheim, R.R. Netz, J.O. Rädler. "Shear dependency of ADAMTS13-mediated cleavage measured on full-length VWF under blood plasma conditions." *PNAS, under review*

S. Lippok, T. Obser, J.P. Müller, V.K. Stierle, M. Benoit, U. Budde, R. Schneppenheim, J.O. Rädler. 2013. "Exponential Size Distribution of von Willebrand Factor." *Biophysical Journal* 105:1208-1216.

S. Lippok, S.A.I. Seidel, S. Duhr, K. Uhland, H.-P. Holthoff, D. Jenne, D. Braun. 2012. "Direct Detection of Antibody Concentration and Affinity in Human Serum Using Microscale Thermophoresis." *Anal. Chem.* 84:3523-3530.

H. Engelke, **S. Lippok**, I. Dorn, R.R. Netz, J.O. Rädler. 2011. "FVIII Binding to PS Membranes Differs in its Activated and Non-Activated Form and can be Shielded by Annexin A5." *J. Phys. Chem. B* 115:12963-12970.

List of Figures

Danksagung

Für die Betreuung dieser Arbeit möchte ich mich zunächst sehr herzlich bei meinem Doktorvater **Joachim Rädler** für deine Ideen, Unterstützung und Förderung und für das spannende Projekt bedanken. Danke aber auch für die Möglichkeit sehr selbstständig zu arbeiten, die damit verbundenen Freiheiten und dein manchmal fast schon beängstigendes Vertrauen.

Ich danke allen **SHENCs**, inbesondere **Reinhard Schneppenheim**, **Ulrich Budde**, **Martin Benoit**, **Roland Netz**, **Frauke Gräter**, **Carsten Baldauf** und **Matthias Schneider** für den ganzen besonderen Rahmen, in dem ich diese Arbeit verfassen durfte. Euer zahlreiches Feedback bei den Treffen hat mich immer motiviert und viele Ideen geweckt. Danke auch für viele schnelle und unkomplizierte Email-Auskünfte. Ein herzliches Dankeschön geht an die Hamburger **Tobias Obser**, **Maria Brehm**, **Ulrike Klemm** und **Gesa König** für medizinischen Beistand und viel leuchtenden VWF. Maria danke ich insbesondere für das PDI Projekt. **Jochen Müller**, **Matthias Radtke** und **Camilo Aponte-Santamaría** danke ich für schnelle, interessante und verlässliche Kooperationen, die die Projekte spannender und besser gemacht haben.

Beim ganzen **Rädler-Lehrstuhl** möchte ich mich für die lustige, entspannte und freundschaftliche Atmosphäre bedanken. Ich danke meinen Masterleins **Valentin Stierle** und **Lars Kleemeier** für ihren *abgefahrenen* Beitrag an den Projekten. Valentin außerdem dafür, dass er unser Labor letztendlich doch nicht in die Luft gejagt hat. **Margarete Meixner**, **Andrea Cooke**, **Gerlinde Schwake**, **Susanne Kempter**, **Susanne Rappl** und **Max Albert** danke ich dafür, dass sie uns viel abnehmen und den Lehrstuhl vor dem Chaos bewahren. Außerdem danke ich der FCS crew **Hanna Engelke**, **Tobias Stögbauer**, **Tobias Preiss**, **Silvia Milani**, **Judith Mittag** und **Rafal Krzyszton** für geteilte Fehlermeldungen und helfende Diskussionen. Tobi P. auch für die AutoIt Routine, die mir viele Messnächte erspart hat. **IDK**, **NIM** und **DFG** danke ich für die finanzielle Unterstützung und (sehr) viele Reisen. Ich danke den eifrigen **Korrekturlesern** (Volker, Caro, Jochen, Verena, Friederike, Christian, Valentin und Sonja) für den nötigen Schliff. Für den sportlichen Spaß bedanke ich mich darüberhinaus

bei allen **Rennrädlern** und **aktive Pause Damen**, vor allem unserer Lehrerin **Sonja Westermayer** für viel Stütze und Heiterkeit. Unseren Nachbarn, den **Braunies**, danke ich dafür, dass ihr mit eurer goldene Maschine sämtliche Physiker im Umkreis versorgt. Außerdem für das Gefühl immer noch ein Viertel Brauni zu sein (dafür auch und besonders **Dieter Braun**). Ein ganz besonders großes Dankeschön geht an **Carolin Leonhardt**, **Susi Rappl** und **Verena Schüller**, die so viel mehr als nur (Ex-)Kolleginnen sind und die Doktorarbeit zu einer unvergesslichen Zeit haben werden lassen. Allein euch kennenzulernen war die Promotion wert.

Zum Schluss möchte ich vor allem **meiner Familie**, **meinen Freunden** und am allermeisten **Volker** dafür danken, dass ihr mich immer unterstützt, bestärkt und für mich da seid! Ich bin sehr froh, dass ich euch hab. Danke!